UNIVERSITAT DE BARCELONA

Chemical and dynamical analysis of Open Clusters in the context of the Milky Way disc

Laia Casamiquela Floriach

UNIVERSITAT DE BARCELONA
DEPARTAMENT DE FÍSICA QUÀNTICA I ASTROFÍSICA
Programa de doctorat en física
Línia de recerca en astronomia i astrofísica

Chemical and dynamical analysis of Open Clusters in the context of the Milky Way disc

Memòria presentada per
Laia Casamiquela Floriach
per optar al grau de
Doctor en física per la Universitat de Barcelona

Directors de la tesi:
Dra Carme Jordi Nebot
Dr Ricardo Jesús Carrera Jiménez
Tutor de la tesi:
Dr Alberto Manrique Oliva

Barcelona, Abril 2017

CHEMICAL AND DYNAMICAL ANALYSIS OF OPEN CLUSTERS IN THE CONTEXT OF THE MILKY WAY DISC

LAIA CASAMIQUELA FLORIACH

UNIVERSITAT DE BARCELONA

Departament de Física Quàntica i Astrofísica
Facultat de Física
Universitat de Barcelona

April 2017

Laia Casamiquela Floriach, *Chemical and dynamical analysis of Open Clusters in the context of the Milky Way disc,* PhD thesis, © Barcelona, April 2017

DIRECTORS:
Dr Carme Jordi Nebot
Dr Ricardo Jesús Carrera Jiménez

Now that the trees are gone,
I can almost see the forest.

— Gil Grissom

ACKNOWLEDGMENTS

I would like to use these first pages of the thesis to thank all the people that have made this work possible, and those that have shared this journey with me.

I would like to start warmly thanking my supervisors Dr Carme Jordi, Dr Lola Balaguer-Núñez and Dr Ricardo Carrera for giving me the opportunity to develop this thesis and guiding me during these years. Carme i Lola gràcies pel vostre suport, paciència, pels vostres consells tant personals com acadèmics, i sobretot, per creure en mi fins i tot quan jo no hi creia. Ricardo gracias por compartir todos tus conocimientos, por tu motivación y paciencia, y por estar siempre allí cuando me encallaba.

The work I have done during these four years would not have been possible without the collaboration of many other people. Specially I would like to thank Dr Elena Pancino that was my mentor in a wonderful stay in Bologna. Grazie Elena per insegnarmi tante cose pazientemente, per essere sempre disposta a aiutarmi, e anche per la tua onestità. Also to Dr Cristina Chiappini for inviting me to Potsdam. Thank you Cristina for giving me that huge opportunity to see a new way of working, for helping me and for being so close, sincere, and for encouraging me when I needed it most. In special this work would have never been possible without the help of Dr Sergi Blanco-Cuaresma. Sergi, la teva contribució ha estat clau en aquesta feina, però, a més, valoro moltíssim tots els consells i l'ajuda que sempre m'has donat. Ha estat un plaer treballar amb tu! I would like to also thank the observers that have helped in the OCCASO observations. I want to acknowledge the help from Dr Alessio Mucciarelli, thanks for helping and teaching me patiently with `GALA` and `Salvador`.

Vull agraïr a tot el grup *Gaia* de la UB: al Jordi Torra, la Cesca Figueras i al Xavier Luri, així com a la Mercè Romero, el Josep Manel Carrasco, l'Eduard Masana, la Teresa Antoja, la Núria Miret (moltes gràcies a les dues per la feinada de les òrbites!) i el Dani Molina (gràcies per instal·lar-me tants programes impossibles), i també la resta de científics i enginyers. A tots per la seva ajuda i el seu suport científic i moral durant aquests anys. També a la gent del Departament de Física Quàntica i Astrofísica: la Montse, la Rosa, i en especial al JR, per ajudar-me sempre en aquest món de papers en el que tant em perdo, i al Gaby i al Jordi per aguantar les meves ficades de pota amb els ordinadors.

Em fa especial il·lusió agraïr el suport i els bons moments passats amb els becaris/doctorands/post-docs del DAM: la Maria i el Santi per ser sempre a la taula del costat quan necessitava ajuda i per totes les aventures que hem compartit, l'Ignasi per ajudar-me sempre en el que calgui (després de tants anys!), el Víctor per tantes bones estones junts i per deixar-me que el trepitji ballant, el Benito el amigo informatico que ho soluciona tot, el Pere pels seus xists tant enginyosos, la Rosa pels seus

bons consells, el Roger per fer-me sempre obrir els ulls, el Dani per donar-nos suport moral i per sempe saber tot el que diuen les normatives!, el Nico per ser la nova ànima del DAM, el José Luis per ficar-se amb mi però realment ficar-se més amb la Núria, el Xavi, les Núries, el Guillem i el Pol, i tants altres que m'estic deixant, gràcies.

I also want to thank all the people that I have had the luck to know in my formative stays during the PhD. Empezando por Loredana, porque sin ti nada habría sido igual en Bologna, gracias por tus valuosísimos consejos. And also to all other people that I met in Bologna: Davide, Emilio, Carmela, Paolo, Efizio and many others. I want to mention my officemates in the AIP, Kris, Marica and in special, Friedrich, for the inconditional help and the long talks we shared in the institute. También a la gente que he conocido en Canarias, Víctor, Sergio, Inés, Dani, Elena y Alba. Also for the good moments lived together in summer schools: Emiliano, Javi, Paco, Guillaume, Álvaro and Marusa.

Moltes altres persones fora del món acadèmic m'han ajudat a recórrer aquest camí. Als companys del Dir, sobre tot a la Judit, la Sílvia i la Vanessa, per aquestes classes que fan que recuperis tota l'energia. A tota la gent que he conegut durant la carrera: el Jordi, el Genís, el Ricard, l'Ale, la Clàudia, la Mariona i moltíssims més amb els que he compartit una de les millors èpoques de la meva vida. M'agradaria agraïr els bons moments passats amb tots els amics de Castellers de Sants, no acabaria mai de dir noms, gràcies per ensenyar-me una mica més del món dels castells i per transmetre'm tota aquesta il·lusió. Molt especialment vull mencionar: la Núria perquè, sí, ets una magnífica companya de pis, però sobretot gràcies per apuntar les meves frases hater i que no sempre surtin a la llum; l'Albert per les tertúlies inacabables, els magnífics moments que hem passat junts durant tots aquests anys i tot el que m'ha ensenyat; l'Oriol per ajudar incondicionalment en el que faci falta i més; i les nostres crosses preferides, la Marta per haver compartit tantes experiències juntes i les que queden, i la Vicky perquè "nosaltres ens entenem". Gràcies per estar sempre allà nois! Amb especial afecte vull mencionar l'Anna, la Paula i la Coloma per ser sempre el meu suport, i trobar temps per parlar tant en els moments feliços com els difícils.

Concloent, vull agraïr a la meva família, als meus tiets i al meu cosí, Gemma, Cesc i Jan, per fer la vida més divertida, als meus avis Joan i Assutzena per entendre'm i escoltar-me sempre, i, sobretot, a la meva germana Júlia, que tot i les múltiples baralles sabem que en els moments importants podem comptar l'una amb l'altra. Finalment, l'agraïment més especial de tots és pels meus pares, perquè heu confiat en mi, m'heu guiat i heu fet sempre tot el que estava al vostre abast per mi. Us dec a vosaltres haver arribat fins aquí.

This work is based on observations made with the Nordic Optical Telescope, operated by the Nordic Optical Telescope Scientific Association, and the Mercator Telescope, operated on the island of La Palma by the Flemish Community, both at the Observatorio del Roque de los Muchachos, La Palma, Spain, of the Instituto de Astrofísica de Canarias. This work is also based on observations collected at the Centro Astronómico Hispano Alemán (CAHA) at Calar Alto, operated jointly by the Max-Planck Institut für Astronomie and the Instituto de Astrofísica de Andalucía (CSIC).

This research made use of the WEBDA database, operated at the Department of Theoretical Physics and Astrophysics of the Masaryk University, and the SIMBAD, ALADIN and VIZIER database, operated at the CDS, Strasbourg, France. This research made use of the software TOPCAT and STIL (Taylor 2005). This work was supported by the MINECO (Spanish Ministry of Economy) through grant ESP2016-80079-C2-1-R (MINECO/FEDER, UE) and ESP2014-55996-C2-1-R (MINECO/FEDER, UE) and MDM-2014-0369 of ICCUB (Unidad de Excelencia 'María de Maeztu'). I acknowledge financial support from the University of Barcelona under the APIF (2013-2014) grant, and the financial support by the European Science Foundation (ESF), in the framework of the GREAT Research Networking Programme.

CONTENTS

ACRONYMS

4MOST	4-metre Multi-Object Spectroscopic Telescope
AGB	Asymptotic Giant Branch
AMR	Age-Metallicity Relation
APOGEE	Apache Point Observatory Galactic Evolution Experiment
BoCCE	Bologna Open Cluster Chemical Evolution
CAFE	Calar Alto Fiber-fed Echelle spectrograph
CAHA	Centro Astronómico Hispano-Alemán
CMD	Color-Magnitude Diagram
CoRoT	COnvection ROtation et Transits planétaires
DIB	Diffuse Interstellar Band
EW	Equivalent Width
FIES	Fibre-fed Echelle Spectrograph
FWHM	Full Width at Half Maximum
GALAH	GALactic Archaeology with HERMES
GBS	*Gaia* Benchmark Stars
GCE	Galactic Chemical Evolution
GES	Gaia-ESO Survey
GSR	Galactic Standard of Rest
HERMES	High Efficiency and Resolution Mercator Echelle Spectrograph
HFS	Hyperfine Structure Splitting
HJD	Heliocentric Julian Date
HMSFR	High-Mass Star Forming Regions
IDL	Interactive Data Language
IDS	Intermediate Dispersion Spectrograph
IMF	Initial Mass Function
LAMOST	Large Sky Area Multi-ObjectFiber Spectroscopic Telescope
LSR	Local Standard of Rest
LTE	Local Termodynamic Equilibium
MAD	Mean Absolute Deviation
MOONS	Multi-Object Optical and Near-infrared Spectrograph
NLTE	Non Local Termodynamic Equilibium
NOT	Nordic Optical Telescope

OC	Open Cluster
OCCASO	Open Cluster Chemical Abundances from Spanish Observatories
ORM	Observatorio del Roque de los Muchachos
PARSEC	PAdova and TRieste Stellar Evolution Code
RAVE	RAdial Velocity Experiment
RC	Red Clump
RGB	Red Giant Branch
RSR	Regional Standard of Rest
RVS	Radial Velocity Spectrometer
SEGUE	Sloan Extension for Galactic Understanding and Exploration
SFR	Star Forming Rate
SNR	Signal-to-Noise Ratio
SS	Spectral Synthesis
VALD	Vienna Atomic Line Database

RESUM

La present tesi té com a objectiu principal la determinació de la composició química de cúmuls oberts per a l'estudi de les dependències de les seves abundàncies químiques, tant amb la posició en el disc galàctic, com amb l'edat. Els cúmuls oberts són grups d'estrelles que s'observen en el disc de la Galàxia, que van néixer juntes del mateix núvol interestel·lar i encara es mantenen gravitacionalment lligades. Un dels avantatges d'estudiar aquestes entitats és que es pot determinar amb molta precisió la seva distància i edat, les dues quantitats més difícils de derivar en astrofísica. També, l'abundància química es determina amb més precisió que per a les estrelles del camp, en poder fer la mitjana de les diverses estrelles membres del grup. Per tant aquests cúmuls, constitueixen un dels millors traçadors de les propietats del disc galàctic.

Hi ha diversos projectes dedicats a estudiar cúmuls oberts a partir d'observacions espectroscòpiques, principalment centrats a l'hemisferi sud. Al 2012 vam dissenyar un mostreig de $\sim$ 30 cúmuls oberts que cobria els cúmuls visibles des de l'hemisferi nord, OCCASO[1], suportat principalment per aquesta tesi. Aquests cúmuls cobreixen un rang d'edats entre 300 Myr i 10.2 Gyr i un rang de radis galactocèntrics entre $6.8 < R_{GC} < 11$ kpc. A l'hemisferi nord no hi ha disponibles espectròmetres multiobjecte d'alta resolució, per això per a cada cúmul només observem al voltant de 6 estrelles del *red clump*. La instrumentació disponible ens imposa un altre límit: només podem observar estrelles amb magnituds més brillants que 15. Aquestes estrelles es trien a partir de la fotometria de la literatura, i prèvia informació de pertinença al cúmul (velocitats radials i moviments propis), quan hi ha. Un cop triats els membres més probables s'obtenen espectres d'alta resolució i amb alta relació senyal-soroll ($\sim$ 70) per a poder derivar velocitats radials i abundàncies detallades d'una trentena d'elements químics. S'utilitzen els telescopis NOT i Mercator de l'observatori del Roque de los Muchachos (La Palma), i el telescopi de 2.2m del CAHA (Almeria). Durant tres anys i mig s'han realitzat observacions que han permès l'anàlisi de 115 estrelles en 18 cúmuls. A més de les observacions d'estrelles dels cúmuls, s'han fet observacions d'Arcturus i μ-Leo, dues estrelles de referència per a poder validar els nostres resultats. Algunes estrelles s'han observat amb els tres espectròmetres per a poder estudiar sistemàtiques entre la instrumentació. Aquestes observacions i els seus resultats són els que es presenten en aquesta tesi.

El procediment de reducció dels espectres inclou els processos estàndard dissenyats pels propis observatoris per al calibratge de longitud d'ona i mètodes dissenyats explícitament per nosaltres per a la correcció del fons de cel, la normalització, la correcció de les línies tel·lúriques, la correcció heliocèntrica, la combinació dels espectres indi-

1 de les sigles en anglès Open Clusters Chemical Abundance from Spanish Observatories

viduals en un espectre mitjà, i la normalització i la combinació dels diferents ordres. Les precisions de les velocitats radials de cada època són de 0.6 ± 0.1 km s^{-1} per a FIES, 0.8 ± 0.4 km s^{-1} per a HERMES, i 1.2 ± 0.3 km s^{-1} per a CAFE. Les diferències sistemàtiques entre instruments són menors que 0.6 km s^{-1}. S'han obtingut velocitats radials estrella a estrella cosa que ha permès una determinació molt acurada de la pertinença als cúmuls. Les diverses observacions d'una mateixa estrella ens han permès de detectar algunes possibles binàries espectroscòpiques. S'han calculat les velocitats mitjanes de cada estrella i les velocitats mitjanes de cada cúmul. Les dispersions de velocitat dins de cada cúmul són d'entre 0.3 i -11.7 km s^{-1}. Hem fet una comparació extensiva amb la literatura i hem derivat una diferència de 0.2 ± 0.9 km s^{-1}, perfectament consistent amb les precisions obtingudes.

A més, amb aquestes velocitats radials s'ha fet un estudi cinemàtic en el context del disc Galàctic. S'han calculat les velocitats peculiars de cada cúmul respecte del seu estàndard local en repòs, combinant les nostres velocitats radials amb els moviments propis obtinguts de la literatura. Els promitjos dels components d'aquesta velocitats són $\langle U_s \rangle = -7 \pm 20\,\mathrm{km\ s^{-1}}$, $\langle V_s \rangle = 14 \pm 18\,\mathrm{km\ s^{-1}}$, $\langle W_s \rangle = 13 \pm 18\,\mathrm{km\ s^{-1}}$, en molt bon acord amb les expectatives per a una població jove, com és el cas dels nostres cúmuls. Només NGC 6705, NGC 6819, NGC 7762 i NGC 7789 tenen velocitats peculiars superiors a 30 km s^{-1}, però són els cúmuls amb errors més elevats en els moviments propis. S'han traçat les òrbites dels cúmuls utilitzant dos models del potencial gravitatori galàctic: un axisimètric, i un amb barra i braços espirals per tal de poder comparar la posició actual amb les probables posicions en el moment del naixement. Aquest càlcul d'òrbites s'ha fet també per a 12 cúmuls de la part interna del disc (Jacobson et al. 2016) i 9 cúmuls cap a l'anticentre (Cantat-Gaudin et al. 2016). Els paràmetres físics (temperatura efectiva i gravetat superficial) i abundàncies químiques s'han obtingut mitjançant dos mètodes àmpliament utilitzats a la literatura: `DAOSPEC+GALA` (en col·laboració amb l'Osservatorio Astronomico di Bologna), i `iSpec` (en col·laboració amb l'observatori de Ginebra). Un dels avantatges d'aquesta estratègia és estudiar les concordances i diferències entre els resultats proporcionats pels diferents mètodes. Hem realitzat força tests fixant o deixant lliures ara uns paràmetres ara uns altres per poder analitzar l'impacte de cadascun d'ells. Això dóna un valor addicional a l'estudi, molt útil per a la comunitat científica, que posa de manifest la importància d'analitzar grans mostres de manera homogènia per a poder treure conclusions rellevants sobre la Galàxia. Hem aconseguit així una de les mostres més grans que existeixen actualment de cúmuls oberts amb una anàlisi espectroscòpica homogènia d'alta resolució. La comparació amb valors de la literatura dóna unes diferències de 10 ± 92 K i -0.02 ± 0.27 dex en temperatura efectiva i gravetat superficial, respectivament.

S'han determinat les abundàncies del Fe individuals per a cada estrella amb els dos mètodes `GALA` i `iSpec`. La comparació amb la literatura dóna unes diferències de 0.02 ± 0.09 dex (`GALA`) i -0.06 ± 0.09 dex (`iSpec`), perfectament dins del marge de les incerteses de les determinacions. S'han analitzat les primeres implicacions sobre els

models teòrics dels resultats d'OCCASO a partir del gradient d'abundància de Fe en el disc galàctic que tracen els cúmuls oberts en funció del radi galactocèntric i de l'edat. S'ha comparat amb diferents models teòrics d'evolució química de la Galàxia i s'ha vist que els resultats dels cúmuls més vells (entre 4 i 10 Gyr) afavoreixen el model d'evolució químic-dinàmic en front d'un model on es contempli només l'evolució química. S'ha analitzat l'evolució del gradient galactocèntric utilitzant dues mostres recents presumiblement compatibles amb l'anàlisi feta a OCCASO (resolucions i rang en longitud d'ona semblants, models informació atòmica i mètode d'anàlisi semblants). S'ha obtingut un gradient de ~ -0.050 dex kpc^{-1}, força homogeni en tots els rangs d'edat. Amb aquesta mostra també s'ha estudiat la relació edat-metal·licitat. No s'ha trobat cap gradient significatiu a la part interna de la Galàxia $R_{GC} < 10$ kpc, però, en canvi, a la part externa s'hi ha trobat una tendència marcada amb pendent semblant en dos anells de radi galactocèntric: -0.029 ± 0.011 i -0.026 ± 0.014 dex Gyr^{-1} a $10 < R_{GC} < 13$ kpc i $13 < R_{GC} < 22$ kpc, respectivament. El gradient en l'anell més extern és l'únic que canviaria significativament en cas de considerar les probables posicions dels cúmuls en el moment del naixement i no la posició actual.

S'han obtingut també abundàncies d'altres elements: Ni, Cr (elements del pic del ferro), Si, Ti, Ca (elements α). Amb aquests resultats s'ha obtingut una visió completa dels patrons d'abundància que presenten els cúmuls. Excepte pel cúmul NGC 6791 (pel quan tenim més incerteses) s'han obtingut dispersions petites en les proporcions d'abundàncies dels diferents elements respecte al ferro, sent les màximes: 0.03 en [Ni/Fe], 0.06 en [Cr/Fe], 0.05 en [Si/Fe], 0.07 en [Ca/Fe], 0.05 en [Ti/Fe] dex. En particular, s'ha estudiat en detall els resultats del cúmul NGC 6705, un cúmul molt jove pel qual hem obtingut una sobre-abundància d'elements α respecte al que s'esperaria donada la seva edat. Hem derivat abundàncies per dos elements α addicionals, el Mg i l'O, cosa que ens ha fet corroborar que el cúmul és sobre-abundant en elements α. S'han investigat a fons les possibles trajectòries que podria haver seguit el cúmul dins el disc, que poguessin explicar aquestes abundàncies, per exemple una migració des de la part més interna de la Galàxia. Els diferents models explorats i diferents valors de moviments propis i distàncies donen com a resultat un radi galactocèntric per al naixement de $6.5 - 7.8$ kpc, la qual cosa implica una migració relativament petita. Això descarta l'escenari proposat per Chiappini et al. (2015) que el cúmul podria provenir de l'extrem de la barra al centre galàctic.

Finalment, la tesi inclou les perspectives de feina futura i el llegat observacional dels espectres d'alta resolució d'OCCASO, tant per als nostres propis temes d'interès com per a d'altres aspectes com la contribució als models d'evolució estel·lar i estudi de les bandes d'absorció difuses.

1

INTRODUCTION

Back to 1609 Galileo Galilei performed the first documented telescope observations. Among other outstanding studies (e. g. the discovery of the largest satellites of Jupiter, confirmation of the phases of Venus, analysis of sunspots) he observed the diffuse band seen in the night skies called Milky Way, and discovered that could be resolved into innumerable stars. Therefore the Milky Way could not any longer be attributed to a celestial way to Valhalla or the road to Rome: it became a stellar system. Around 50 years later Isaac Newton was the first to understand that the colors produced when white light goes though a prism is a property of the nature of light, not an artifact of the prism. These facts meant the beginning of the study of our Galaxy and the understanding of the nature of the stars. After that revolutionary epoch for astronomy, our knowledge has greatly improved by using larger telescopes, more precise instruments and techniques, and the development of physical theories and models.

In this introductory chapter we include the basic and general concepts that are going to be used throughout this thesis. In Section 1.1 we qualitatively explain the formation and evolution of stars. We include the description of a stellar spectrum and we describe the formation of it in the stellar atmosphere. With this we can understand which information can be obtained from stellar spectroscopy. In Section 1.2 we give a general picture of the nucleosynthesis of the different elements, and specially in which type of stars each chemical species is formed. In Section 1.3 we include a view of the general properties of the Galactic disc, in which this thesis focuses. In particular we describe how clusters of stars can trace the properties of the Galactic disc. In Section 1.4 we explain several ongoing spectroscopic surveys that are/will help improve our knowledge of the Milky Way, and specifically, of the disc. Finally, we present the motivation of the thesis in Section 1.5 and the thesis outline in Section 1.6.

1.1 STARS AND STELLAR SPECTROSCOPY

Stars are the building blocks of galaxies, the largest structures in the Universe, thus they are the key to understand it. Stars can simply be thought as self-gravitating balls of gas of a given mass, which most of its life obey four equilibrium equations: the continuity of mass (m) along the different layers of the star, the hydrostatic equilibrium

where pressure (P) is balanced with gravity (g), the luminosity (L) balance depending on the produced energy (ε), and the type of energy transport (convective, radiative or conductive) from the core to the surface of the star that constrains the temperature gradient. Also required are other essential equations: the equation of state that relates pressure as a function of local variables (temperature, density), and the nuclear fusion rates. See Collins (2003, chapter 2), for a detailed explanation.

1.1.1 *Formation and evolution*

Stars are born from massive clouds that collapse due to gravitational instabilities and are fragmented into several cores. A collapsing core grows acquiring mass from the surrounding envelope during the protostellar phase, to end up as a pre-main sequence star. These objects radiate their energy from gravitational contraction, and it finally becomes a main sequence star when it reaches enough temperature and density in the core to begin nuclear fusion of hydrogen. There is evidence that most of the stars are formed in groups from the same molecular cloud forming a stellar cluster (Lada 2010), though most of these groups dissolve after few Myr. In particular Open Clusters (OCs), which typically span ages from few Myr to some Gyr, are very valuable targets to study many astrophysical topics, star formation and evolution among them.

During their lifes and depending on their mass, stars go through different evolutionary stages as their energy source changes. This results in changes in their temperatures (color) and luminosities (radiated energy per second). Ejnas Hertzprung and Henry Noris Russel proposed in 1910 the so-called Hertzprung-Russel (HR) diagram, which allows us to visually inspect these changes for stars of different masses: stellar evolutionary tracks (see Fig. 1.1). Using this diagram the stars can be classified in "spectral classes", which depend on temperature, and luminosity types which depend on luminosity.

After the core hydrogen fusion phase, very low-mass stars ($m \lesssim 0.5 M_\odot$) cannot evolve to giant stages, and get rid of the outer layers to become helium white dwarfs sustained by electron degenerate pressure. On the other hand, stars with $m \gtrsim 0.5 M_\odot$ begin to fuse hydrogen in a thick layer above the core, while the helium core is still in thermal equilibrium. This is the subgiant phase where any additional energy production from the shell fusion is consumed inflating the envelope and the star cools but does not increase in luminosity. When the helium core starts the contraction to maintain thermal equilibrium the outer layers are expanded and the star gets more luminous. This is called the Red Giant Branch (RGB) phase. During this stage all the stars draw a path upwards in the HR diagram, ascending the RGB. Not all stars go up to the RGB, the more massive ones ($m \lesssim 8 - 12 M_\odot$, depending on the metallicity) have large hot convective envelopes and shell hydrogen fusion and core helium fusion begin very quickly, so they experience a very quick subgiant phase to become a supergiant before the star reaches the RGB.

Shell hydrogen burning has fed the helium core that will eventually start He fusion to C and O. Depending on the mass of the star, helium burning can start gradually when temperature is high enough to initiate the triple α process (intermediate mass stars), or it will start helium fusion through an explosive process, the so-called helium flash, if the star immediately develops an electron-degenerate He core after leaving the main sequence (low mass stars). Once the helium process begins the star reaches a new equilibrium stage where He-fusing core and H-fusing shell are the sources of energy, it is the called horizontal branch phase (for low metallicities) and Red Clump (RC) phase (for high metallicities).

An analog process to the RGB is produced when after a few million years, He fusion in the core stops. The C+O core contracts and the fusion is produced in two shells, one around the core burning He into C+O, and another external one burning H into He. This process makes the star larger and cooler and suffers from thermal pulses produced by sequential He flashes in the shell, it is called the Asymptotic Giant Branch (AGB) phase. The core is fed from the He-fusing shell, and if its mass does not grow above the Chandrasekhar limit ($m \lesssim 1.4M_\odot = M_{Ch}$) it will end up in a degenerate C+O white dwarf. Otherwise it will start Carbon fusion to Neon, and then to Magnesium following a similar schema, ending up in white dwarfs of different composition depending on the initial mass of the star.

The highest mass stars ($m \lesssim 8-12M_\odot$) do not suffer from core electron degeneracy in any stage, but form subsequent burning shells surrounding an iron core. These end up into a core-collapse supernova explosion.

The net effect of the stars evolution is that they lock material from the interstellar medium where they are born, change this material during their lives, and whatever evolutionary track they follow, they will return at least some of the processed material into the interstellar medium from which new stars will be formed.

1.1.2 *Stellar spectroscopy*

Most of our knowledge of stars is derived from spectroscopy, which in turn, offers a wealth of information on different aspects of stellar astrophysics: temperatures, surface gravities, chemical compositions, etc. Spectroscopy is the technique that studies the wavelength distribution of radiation emitted or absorbed uniquely by an object. It forms the link between astrophysics and fundamental physics at atomic and molecular levels. Using spectroscopy is how we really see the Universe in all its glory.

Frederick William Herschel realized that spectra contain quantitative information on the source and tried to establish how and what from flame spectroscopy. He also discovered the infrared radiation of the sunlight in 1800. William Wollaston was the first to observe absorption spectral lines in 1802. He noticed dark gaps in a Solar spectrum seen through a prism. These noticeable gaps included the Na I D lines and the Ca II H&K lines. Joseph von Fraunhofer rediscovered the dark lines in 1814 and

Figure 1.1. Schematic evolutionary tracks in an HR diagram for stars of 1, 5, and 25$M_\odot$. From http://astronomy.nju.edu.cn/~lixd/GA/AT4/AT420/HTML/AT42004.htm.

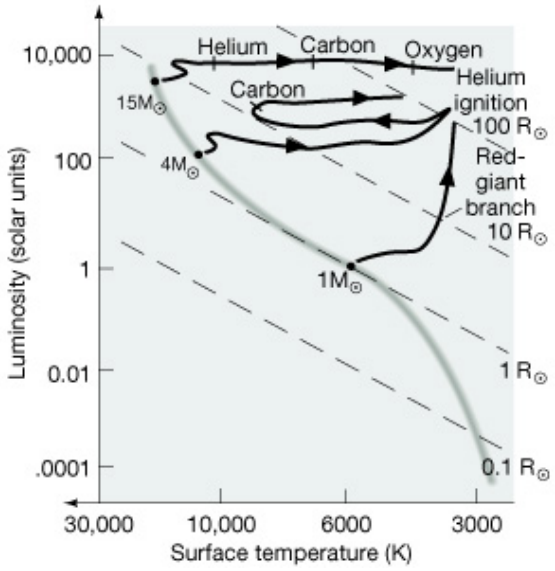

Figure 1.2. Drawing of the Solar spectrum, the Fraunhofer lines are indicated. From Arcimis (1901).

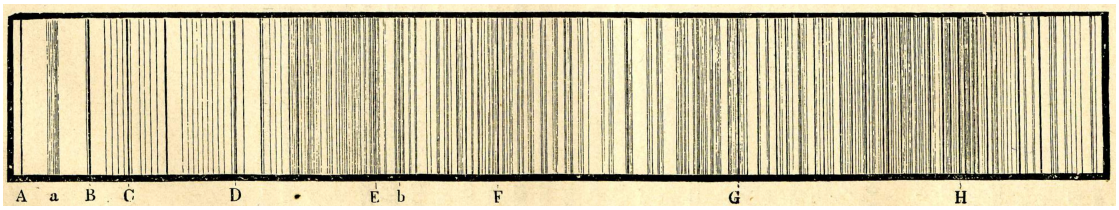

labeled the darkest ones alphabetically. We still use this notation for the *Fraunhofer lines*: D for the Na I D, H&K for the Ca II, G for a CH band in the bluest part of the spectrum, and b for the Mg I triplet. In Fig. 1.2 the Fraunhofer lines from a Solar spectrum are carefully drawn.

The formation of a stellar spectrum depends on atomic processes that emit or absorb electromagnetic radiation. The variety of atomic interactions determines the observed spectral features that are divided into two components: (i) a continuum defining the background radiation, and (ii) a superposition of lines that add or subtract energy to or from the continuum, characterized by emission or absorption, respectively. The continuum of a stellar spectrum resembles the Planck law for the blackbody radiation, which depends on the temperature of the source. The Planckian shape is modified by spectral lines, which are produced in the way from the deep of the stellar photosphere to the observer. This means that the spectral lines that one can observe from a stellar

spectrum can be produced in different layers of the stellar atmosphere, in the interstellar medium, or even in the Earth atmosphere. All these processes modify the stellar spectrum in a different way.

The constituents of a stellar plasma are in general electrons, protons and trace elements in various ionization stages. The diversity of atom-photon interactions which cause the spectral features depends on the abundance of the atoms involved in the process, and the conditions of the plasma such as temperature and density. The dominant atomic processes in stars usually are: photoionization and radiative recombination, electron impact ionization, autoionization, ion-atom collisions, among others (see Pradhan and Nahar 2011, for details). Spectral analysis is often complicated and it is difficult to determine the probability at which each process occurs, and the energies involved, to figure out the final shape and strength of the spectral lines.

One of the first quantities that can be obtained from spectroscopy is the temperature, which determines the peak of the spectral energy distribution of the spectra, as well as a measure of the total energy output of the source, and the strength of the spectral lines. Another useful parameter that can be derived is its composition in terms of the amount of 'metals' or *metallicity*[1]. For late-type stars (K and M spectral types) the metallicity is generally inferred using the iron abundance which is one of the most abundant elements of the metals and more importantly, can provide hundreds of observable spectral lines. It is not the same case for early type stars (O, B, A spectral types) where the usual indicator of metallicity is C and/or O abundances.

1.1.2.1 *Spectral lines*

Spectral lines are used to infer a wide variety of intrinsic quantities of stars, from rotational velocity to chemical composition. However, there are external agents that can modify the appearance of the spectrum such as the interstellar medium or the Earth atmosphere. Also, the radial velocity of a star respect to the observer due to its motion across the Galaxy, or due to gravitational effects from a binary companion, shifts the overall spectrum via Doppler effect.

Photons coming from the nuclear reactions in the stellar interiors reach the photosphere, where spectral lines are formed at different layers, each one characterized by its opacity. The detailed shapes and strengths of spectral lines is determined by the radiative transfer equation which characterizes the stellar atmosphere. Solving this equation is not straight forward. For this reason, usually, one solves the radiative transfer equation to derive intensity as a function of wavelength, under the assumption of Local Termodynamic Equilibium (LTE). This means that material particles of the gas are assumed to be characterized by a single temperature, locally. Under these conditions the populations of various levels of atoms in the gas are given by the Maxwell-Boltzmann statistics, and the ionization equilibrium is given by the Saha

1 Metals in the astronomical context means the amount of chemical elements heavier than helium.

equations. Departures from LTE (from the analytical Saha and Boltzmann equations) lead to a huge increase of complexity of the physics. Non Local Termodynamic Equilibium (NLTE) effects need to be taken into account depending on the line, usually through coefficients that correct the effect on the abundance (see Collins 2003, chapter 15). Also, to computationally simplify the problem it is usually assumed 1D geometry where gas-dynamical effects are neglected. However, this assumption has severe effects in the derivation of stellar properties from the spectra, in particular in abundance determinations (e. g. Ludwig et al. 2014). To partially compensate for the incomplete description of convection in 1D models, the microturbulence (ξ) is usually introduced as an effective parameter that provides an additional broadening. Due to all these problems, in the latest years some 3D atmosphere grids came to existence. One of the most important outcomes are the 3D abundance corrections, i. e. differences that can be applied to 1D abundance determinations to correct from 3D effects.

Spectral lines are not infinitesimally narrow, they have a finite width described by a line profile. There are several sources of broadening: natural broadening, due to the time-energy uncertainty; thermal broadening and convection, due to the motion of the atoms in the hot gas; collisional broadening, due to collisions between atoms; rotational broadening, because in a rotating star light from the receding limb is redshifted and light from the approaching limb is blueshifted. A correct reproduction of the line profile is needed to extract the physical information that the line provides.

Absorption lines are widely used as abundance indicator. For the purpose of abundance determination it is mandatory to know that a given line is formed by a determined ionic specie and via a well defined atomic transition. To compute the abundance of a given specie from an absorption line the main atomic parameters required are: the excitation potential χ, which is the difference of energies of the two involved atomic states, and the oscillator strength $\log gf$, which is the transition probability of the line from Einstein coefficients[2].

For an isolated absorption line the area between the line profile and the continuum is related to (i) the number of absorbers along the line of sight, and (ii) the strength of the transition. We define a quantity related to this area, the Equivalent Width (EW), which is the width a line would have if it was completely rectangular (see Fig. 1.3):

$$W_{\lambda_o} = \int_{\lambda_1}^{\lambda_2} \frac{F_c - F_\lambda}{F_c} d\lambda \tag{1.1}$$

where F_c and F_λ are the measured continuum and line fluxes, respectively, W_{λ_o} denotes the EW of the line at the nominal wavelength λ_o, and λ_1, λ_2 are the edges of the line.

2 The Einstein coefficients measure the probability of absorption or emission of light by an atom. There are three coefficients that describe three processes: spontaneous emission, induced emission and photon absorption. The three coefficients are atomic properties, do not depend on the state of the gas where the atoms are part of.

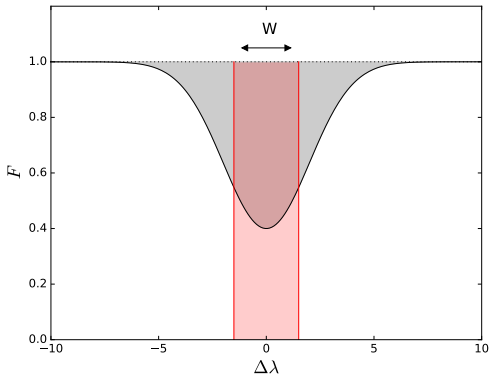

Figure 1.3. Spectral line energy relative to the continuum flux. W is the equivalent width. The two shaded areas are equal.

Generally, fixing all the parameters of the model, the EW of a given line increases with the abundance of the chemical specie. If the number of absorbers was large enough, then *all* the flux at the line center would be absorbed, leading to the saturation of the line. However, the saturation of the line is never produced at flux 0, since there exists a dependence of the flux with temperature which yields that the flux is zero only at zero temperature.

The behaviour of the EW as a function of temperature and density is described by the so-called *curve of growth* (see Pradhan and Nahar 2011). If one plots the EW as a function of the abundance, one finds three different regimes (see Fig. 1.4):

1. Linear part: EW increases linearly with the number of atoms $W \propto N$.
2. Saturated part: when the number of atoms is sufficient to absorb nearly all the continuum photons at the line center, any further increase in density results in a slow increase $W \propto \sqrt{\ln N}$.
3. Damped part: when the central core is saturated, ions absorb photons in the line wings, and the EW growth expands with the line wings, $W \propto \sqrt{N}$.

The curve of growth can be used to compute abundances. However, a far more rigorous methodology has been developed to solve the radiative transfer equations (see Rutten 2003, for details) in a stellar atmosphere. Radiative transfer codes usually work under the assumption of LTE to compute detailed spectra, e. g. `TURBOSPECTRUM` (Plez 2012), `SYNTHE` (Kurucz 1993).

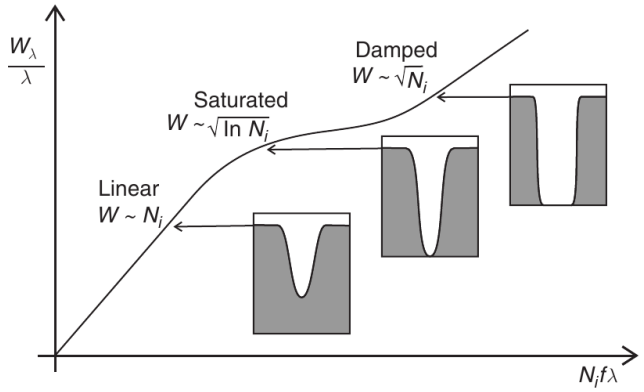

Figure 1.4. Curve of growth relating the EW of an absorption line to the number density of atoms of a given species along the line of sight. The three possible regimes are indicated. From Pradhan and Nahar (2011).

1.1.2.2 *Notation*

A roman numeral after the chemical symbol of a given element denotes its ionization state. E. g. Li I and Li II correspond to the neutral and singly ionized lithium atoms, respectively.

The lightest and most abundant element in the Universe is hydrogen (H). The abundances of other elements are commonly expressed relative to H, which has the most common spectroscopic features in most astronomical sources. The abundance of an element X is defined as:

$$A_X = \log\left(\frac{N_X}{N_H}\right) + 12 \tag{1.2}$$

where N_X is the number of absorbers of the element, and N_H is the number of hydrogen atoms.

Usually, the abundances are expressed relative to the Sun using the notation:

$$[X/H] = A_{X_*} - A_{X_\odot} = \log\left(\frac{N_X}{N_H}\right)_* - \log\left(\frac{N_X}{N_H}\right)_\odot \tag{1.3}$$

Then $[X/H]_\odot = 0$ by definition.

Under the observational point of view one measures abundances using the number of absorbers of the given chemical species. However, abundances can also be quantified using the mass fraction of a given element. Metallicity Z is the fraction of mass of a system that is not hydrogen (X) or helium (Y). Then by definition: $X + Y + Z = 1.0$. These two ways of expressing the metal content of a star are related through:

$$[M/H] = \log\left(\frac{Z/X}{Z_\odot/X_\odot}\right) \tag{1.4}$$

extensive to any chemical species.

1.2 CHEMICAL ABUNDANCES IN THE UNIVERSE

The analysis of high resolution spectra provides the most direct way to measure abundances of chemical elements in stars. Thanks to the great improvement both in the theoretical model atmospheres and synthetic spectra, and the technical development of efficient high resolution spectrographs, a large amount of data has been useful to constrain chemical evolution and nucleosynthesis theories.

For many years scientists thought that all elements, in the proportions that we see them nowadays, were formed in the early dense universe during primordial nucleosynthesis. This hypothesis collapsed with further studies of the Big Bang conditions and the nucleosynthetic channels that were involved in it (see a detailed review in Zuckerman and Malkan 1996). The chemical abundances predicted by the Big Bang nucleosynthesis agree quite well with what is seen in the most primordial gas and stars: about $^3/_4$ of hydrogen, about $^1/_4$ of helium-4, with one or two atoms in every hundred thousand of ^{2}H and ^{3}He, and one ^{7}Li atom among 10 billion atoms. Elements beyond these are synthesised by different processes (see Fig. 1.5) in stellar cores during different phases of stellar evolution, in explosive supernovae events, or under special conditions such as strong stellar winds, collisions with cosmic rays (*spallation*), among others.

Light elements He and ^{7}Li are produced in stars, and ^{6}Li, ^{9}Be,^{10}B and ^{11}B are produced from spallation. Sequential nuclear burning in star cores of H, He, C, Ne, O, and Si produce mainly: He, C+O, Ne+Na, O+Mg+Si, Si+P+S, Ni+Co+Fe, respectively. This is a very simplified picture of stellar nucleosynthesis, we refer to Matteucci (2001) and references therein for a more detailed explanation of the production ratios.

On the other side, explosive nucleosynthesis in supernovae produces other ratios of elements. In core-collapse supernovae (high-mass stars) a shock wave is generated in the core and propagates through the different layers producing explosive nucleosynthesis. The fuels for this nucleosynthesis are mostly α-elements (C, O, Mg, Si, S), and since the timescale for the explosion is very short, few β-decays can be produced favouring nuclei that have the same number of protons and neutrons. Explosive Si burning mainly produces Fe-peak elements; and O, Ne and C explosive burning from the outer shells produce mainly α-elements plus traces of other elements like Na, Ni or Fe. Another type of explosive nucleosynthesis is produced in type Ia supernovae where a C+O or O+Ne white dwarf in a binary system can achieve the Chandrasekhar limit and explode by C-deflagration. These supernovae produce mostly Fe-peak elements, mainly Fe, Ni and Co (Hillebrandt and Niemeyer 2000).

Elements heavier than the Fe group are mainly produced by neutron captures. The r-process occurs (probably) in core collapse supernovae where temperature and neutron densities are high enough to accumulate neutron captures rapidly, so neutron rich

elements are produced before decaying to the valley of stability. On the contrary, if neutron captures happen at low rate, then nuclei are able to β-decay before they are hitted by another neutron. Conditions for s-process are probably achieved for low-mass AGB stars. Typical s-process elements are Ba, La, Sr, and typical r-process elements are Eu, Ir, Pt. However, it is generally believed that most s- and r-process elements have a contribution from both processes.

There is a third way of synthesizing heavy elements, the p-process. Elements that are proton rich, i. e. that lay on the left extreme of the valley of stability (e. g. Cu, Zn, Se), cannot be produced by a beta decay because the path is blocked by stable isotopes. Their formation requires adding a proton to the nucleus, thus overcoming the Coulomb barrier. This requires extremely high proton densities that would only be reached in few layers of type II supernovae (Arnould and Goriely 2003).

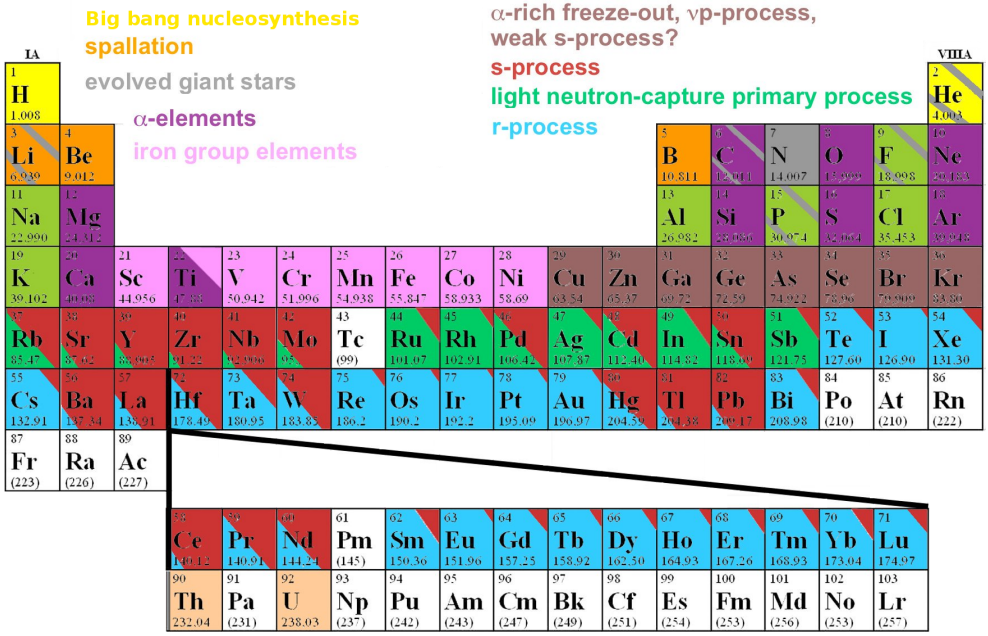

Figure 1.5. Periodic table with the chemical elements colored depending on the process where are produced. From https://pbs.twimg.com/media/CkxqJEfWgAAFCef.jpg.

1.3 STUDY OF THE GALACTIC DISC

Discs are the most prominent stellar component of most of spiral galaxies, including the Milky Way. Discs contain a substantial fraction of the baryonic matter and angular momentum of their galaxies, also they hold most of their evolutionary activity such as star formation, spiral arms, and bars (see van der Kruit and Freeman 2011, for a review). Understanding the formation and evolution of discs is, therefore, one of the key goals of galaxy formation research.

Enormous efforts have been expended to unravel the Galaxy's chemodynamical history. The disc evolution is fossilized in the distribution of stars, their chemical composition and ages as a function of the position of birth. One of the most used observables to constrain the Galaxy evolution models is the variation of chemical abundances across the Galactic disc (see Fig. 1.6 for an example). Different tracers have been used in the literature to adress this question: H II regions (e.g. Balser et al. 2011), B-type stars (e.g. Daflon et al. 2009), planetary nebulae (e.g. Stanghellini and Haywood 2010), Cepheids (e.g. Lemasle et al. 2013; Andrievsky et al. 2013; Korotin et al. 2014; Genovali et al. 2015), main sequence (e.g. Nordström et al. 2004; Cheng et al. 2012; Mikolaitis et al. 2014) or giant field stars (e.g. Hayden et al. 2014; Huang et al. 2015; Anders et al. 2016), or OCs (e.g. Friel et al. 2002; Carrera and Pancino 2011; Yong, Carney, and Friel 2012; Frinchaboy et al. 2013; Cantat-Gaudin et al. 2016), among others. Because each tracer has a distinct nature, they allow for the investigation of different age/position ranges.

Although all tracers agree on the existence of a radial metallicity gradient in the sense that stellar populations are more metal rich towards the inner disc, there are discrepancies about how this gradient behaves. While the radial gradient described by OCs flattens at large Galactocentric distances (e.g. Carrera and Pancino 2011; Frinchaboy et al. 2013; Cantat-Gaudin et al. 2016), Cepheids and planetary nebulae seem not to show a slope change in the outer disc (e.g. Lemasle et al. 2013; Henry et al. 2010).

The stellar disc population from the chemical point of view shows a clear bimodal distribution in ([Fe/H], [α/Fe]) with two sequences of high- and low-[α/Fe] (Fuhrmann 2011; Adibekyan et al. 2012; Nidever et al. 2014), see Fig. 1.7. It has been seen that the high-[α/Fe] is more prominent in the inner disc, while the low-[α/Fe], and in particular its metal-poor end, dominates in the outer disc (see Fig. 1.8). Mainly two scenarios are proposed to explain this bimodality: (i) thick disc stars are formed thick at high redshifts during a collapse of gas with a large scale-height from turbulent and clumpy discs (e. g. Forbes, Krumholz, and Burkert 2012), or deposited at large scale-heights during the accretion of satellite galaxies (Abadi et al. 2003). In the latter case thick disc stars have an extragalactic origin. Or (ii) that thick disc stars where vertically heated from a pre-existing thin disc by minor mergers (Villalobos and Helmi 2008; Di Matteo et al. 2011), in this case the thick disc should contain stars of either the heated thin disc and the merged galaxy.

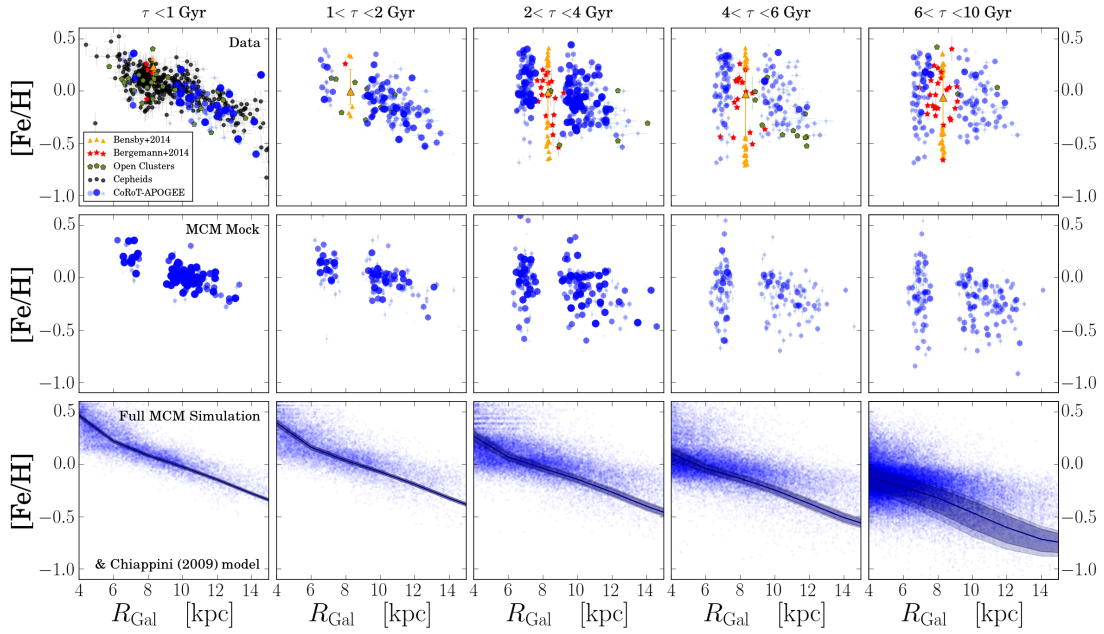

Figure 1.6. [Fe/H] vs R_{GC} distribution near the Galactic plane in five bins of age from Anders et al. (2016). Top row shows the data compilation: CoRoT-APOGEE sample, OC compilations of Genovali et al. (2014) and Magrini et al. (2015), subgiant sample from Bergemann et al. (2014), Cepheid sample from Genovali et al. (2014), and FG dwarf sample from Bensby, Feltzing, and Oey (2014). The second row shows a mock catalogue from the chemodynamical simulation of Minchev, Chiappini, and Martig (2013, 2014), and the bottom row shows the full simulation and the underlying chemical evolution model. Figure from Anders et al. (2016).

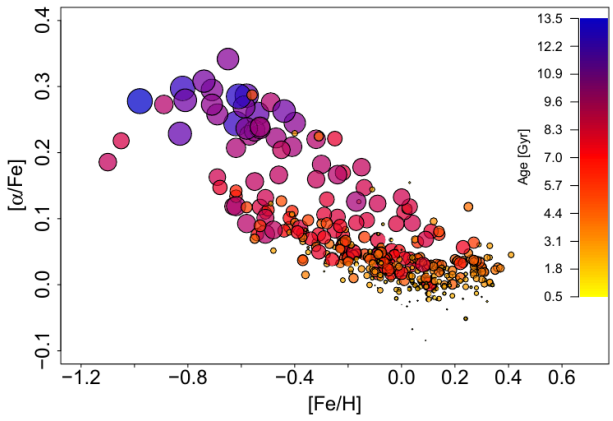

Figure 1.7. [α/Fe] vs [Fe/H] distribution of a subsample of stars of Adibekyan et al. (2012) for which ages were derived following a bayesian method based on isochrone fitting in Haywood et al. (2013). The color and the size of the symbols code the age of the stars, to emphasize the age stratification of the distribution of stars within this plane. Figure from Haywood et al. (2013).

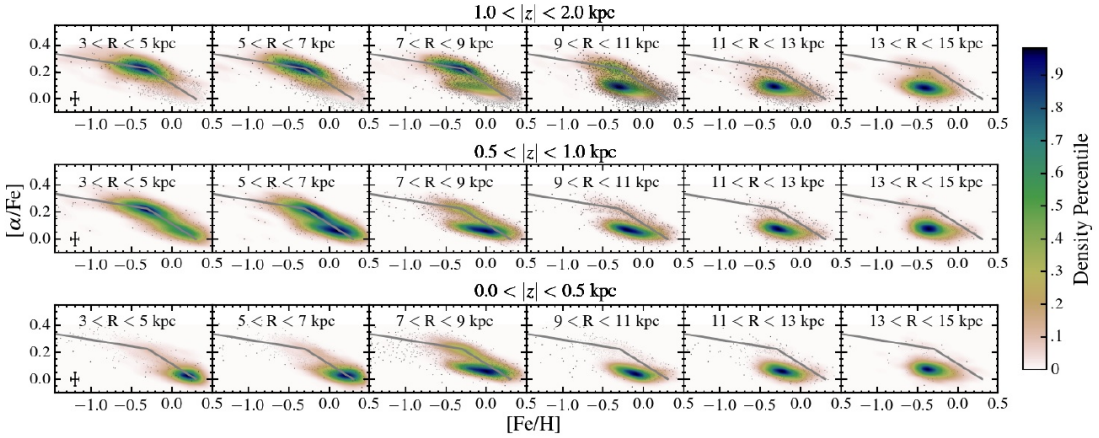

Figure 1.8. [α/Fe] vs [Fe/H] distribution of stars from Apache Point Observatory Galactic Evolution Experiment (APOGEE) as a function of different Galactocentric radius and height above the plane. Figure from Hayden et al. (2015).

Most detailed Galactic Chemical Evolution (GCE) models are able to reproduce the present-day radial distribution of chemical elements derived from young objects such as Cepheids (Genovali et al. 2013, 2015). However, different assumptions mainly in the distribution of the Star Forming Rate (SFR) as a function of Galactocentric distance, and in the nature and timescale of the material falling onto the disc (e. g. monolithic collapse, two infall), lead to different predictions of the evolution of the gradient with time.

Abundance gradients not only reflect the formation of the disc but also the stellar nucleosynthesis. Gradients traced by different chemical elements can be different from one another due to the different stellar origin. See table 6.3 in Matteucci (2001) as an example of the prediction of the gradients for different chemical elements.

Numerous studies have tried to understand how this gradient evolves with time (e. g. Chiappini, Matteucci, and Romano 2001; Cescutti et al. 2007; Magrini et al. 2009; Lépine et al. 2011) exploring different Initial Mass Function (IMF), SFR, supernovae yields and infall processes. In general, models can predict either a steepening or a flattening of the gradient. Models that assume an inside-out formation of the disc with long infall timescales in the outermost regions predict a steepening of the gradient. On the other hand, models that consider infall negligible at late times tend to produce a flattening.

The existence of the Age-Metallicity Relation (AMR) is another important issue for developing GCE models. The first to derive an AMR was Twarog (1980) from $uvby$ photometry for the Solar neighbourhood, finding that metallicity increases from [Fe/H]=−1 at 13 Gyr to −0.03 at the Solar age with a dispersion of ±0.1 dex at any given age. Edvardsson et al. (1993) derived elemental abundances from high-resolution spectroscopy surprisingly finding great scatter in the AMR (~ 0.15 dex at

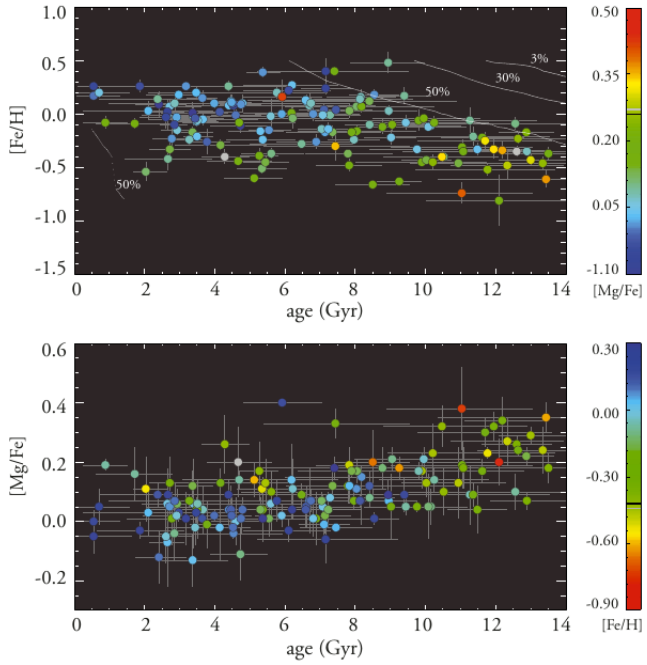

Figure 1.9. [Fe/H] (top) and [Mg/Fe] (bottom) vs age distribution of Gaia-ESO Survey (GES) disc stars. Contours indicate the relative sample completeness, i. e.percentage of stars that would remain in the sample due to the GES selection functions. Figure from Bergemann et al. (2014).

almost any given age), implying that there is a weak correlation between age and metallicity. Other observational studies still found clear AMR (e. g. Rocha-Pinto et al. 2000; Soubiran et al. 2008), but more recent studies obtain a flat AMR with large scatter suggesting that it may not exist (e. g. Bergemann et al. 2014, see Fig. 1.9). Haywood et al. (2013) found a tighter and steeper (~ 0.15 dex Gyr^{-1}) correlation between metallicity and age for thick disc stars than for thin disc stars (~ 0.025 dex Gyr^{-1}), that would imply a decrease by a factor of $5-6$ in the production of iron at 8 Gyr (see Fig. 1.10). Part of the discrepancies seen could be explained by the large uncertainties in deriving precise stellar ages.

Recently a more complex vision of the Galaxy taking into account dynamical effects have been provided by N-body chemodynamical simulations (Minchev, Chiappini, and Martig 2013, 2014; Kubryk, Prantzos, and Athanassoula 2015, among others). These take into account that stars can migrate across significant Galactocentric distances due to the resonant scattering with transient spiral arms (Roškar et al. 2008), or due to resonance overlap of the bar with the spiral structure (Minchev and Famaey 2010). The effects in the observables would be mainly a wipe-out of the radial gradient of metallicity, and the flattening of the AMR at each Galactocentric radius.

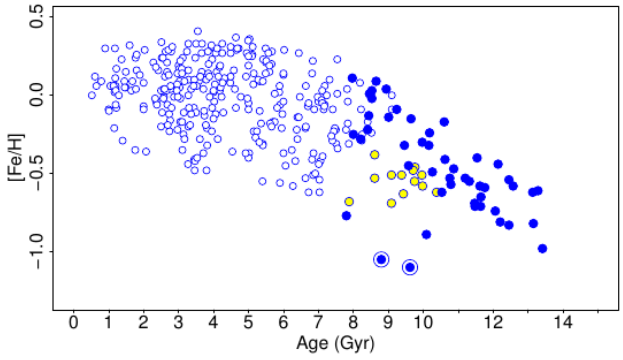

Figure 1.10. [Fe/H] vs age distribution. Symbols: thick disc (filled blue circles), thin disc (empty blue circles), thin disc metal-poor stars are indicated in yellow symbols and not considered in the analysis, two objects at [Fe/H]< -1 dex are treated as outliers. Figure from Haywood et al. (2013).

1.3.1 *Open Clusters as tracers of the Galactic disc*

As explained in Section 1.3 several tracers have been used to infer the metallicity gradient, and they do not always agree in its shape. Part of the uncertainties that difficult the validation of the models is the multitude of different spectroscopic methods, atmosphere models, Solar abundances and tracers adopted to derive the chemical abundances. To tackle this kind of problem is mandatory to pursue homogeneity in the spectroscopic analysis. In this context, the large spectroscopic surveys like APOGEE (Frinchaboy et al. 2013) and GES (Gilmore et al. 2012; Randich, Gilmore, and Gaia-ESO Consortium 2013) are playing a major role.

In comparison to other tracers, OCs provide the most reliable ages and distances from photometry (see Friel 1995), and they cover a wide range of age and Galactocentric radius. These properties make OCs very valuable objects to study the chemical profiles of the Galactic disc and their evolution with time. However, the radial gradient traced by OCs is still in debate since different authors reach a diversity of conclusions: a single linear gradient, a two-function gradient, a step-function, etc.

The first use of OCs to trace the chemistry of the Galactic disc was by Janes (1979), who observed a negative metallicity radial gradient. Other works in the same line confirmed and extended these results: Friel (1995), Twarog, Ashman, and Anthony-Twarog (1997), Friel et al. (2002), Magrini et al. (2009), Pancino et al. (2010), Lépine et al. (2011), Frinchaboy et al. (2013), Magrini et al. (2015), Cantat-Gaudin et al. (2016), among others. In particular, Twarog, Ashman, and Anthony-Twarog (1997) suggested that the metallicity distribution traced by OCs could be described as a step function with transition near the solar circle. A steeper gradient is generally seen in the inner

disc, and a flat or shallow gradient in the outer disc beyond ~ 10 kpc (−0.2 and −0.02 dex kpc^{-1}, respectively Frinchaboy et al. 2013).

As part of the GES results on OCs Magrini et al. (2015) analysed four inner disc OCs finding metallicities in agreement with simple model expectations, but with peculiarities in the abundances of α-elements. Latest results from Jacobson et al. (2016) of iron abundances in 12 GES inner OCs ($5.5 < R_{GC} < 7$ kpc) point to a gradient of -0.10 ± 0.02 dex kpc^{-1}. This result does not support the idea that the gradient steepens towards the inner disc. In the same work they find an age-metallicity relation in the range $0.1 <$ Age < 1.6 Gyr of 0.06 dex between two groups of age. However, this difference is at the level of their uncertainties in Fe abundance. Cantat-Gaudin et al. (2016) investigate ten outer disc OCs analysed similarly as in GES, and suggested that there is a shallow but not flat negative gradient in the outer disc of slope -0.027 ± 0.007 dex kpc^{-1}.

1.4 SPECTROSCOPIC SURVEYS

Our understanding of the Milky Way in general and the Galactic disc in particular, is going to change significantly in the next years with the *Gaia* space mission (Gaia Collaboration et al. 2016). *Gaia* is a full-sky scanning satellite observing all stars down to 20th magnitude with precisions at the μas level. Parallaxes and proper motions of individual stars will be as precise as 1% for the OCs up to a distance of 1.5 kpc, and 10% for almost all known clusters. Importantly, the faint limiting magnitude and the high precision will allow the discovery of distant clusters. However, spectroscopic capabilities to derive radial velocities and chemical abundances are limited due to the low resolution, the limiting magnitude $V \sim 16$, and the small wavelength coverage of the *Gaia* Radial Velocity Spectrometer (RVS) (Katz et al. 2004).

Gaia space observations are being complemented with several ongoing and forthcoming ground-based spectroscopic surveys. Low- and medium-resolution spectroscopic surveys ($R < 10,000$), such as RAdial Velocity Experiment (RAVE) (Conrad et al. 2014), Sloan Extension for Galactic Understanding and Exploration (SEGUE) (Lee et al. 2008), and Large Sky Area Multi-ObjectFiber Spectroscopic Telescope (LAMOST) (Li et al. 2015) survey, provide radial velocities, together with rough information about the chemical content of the studied stars. Large high-resolution spectroscopic surveys ($R \gtrsim 20,000$) such as APOGEE (Frinchaboy et al. 2013), GES (Gilmore et al. 2012; Randich, Gilmore, and Gaia-ESO Consortium 2013), GALactic Archaeology with HERMES (GALAH) (De Silva et al. 2015) and the forthcoming WEAVE (Dalton et al. 2012, installed in the William Herschel Telescope in the Observatorio del Roque de los Muchachos (ORM)) will provide detailed information about the chemical composition, in addition to radial velocities. APOGEE-S has been recently installed in the du Pont 2.5m telescope in Las Campanas Observatory (Chile), and will provide the Southern hemisphere counterpart of APOGEE. Future large surveys are planned to start opera-

Table 1.1. Details of the high-resolution spectroscopic surveys.

Survey	Sky coverage	Spectral resolution	Wavelength range	Magnitude limit	Observation period
APOGEE-1	North	22,500	$1.51 - 1.70\,\mu m$	$H = 12.2$	2011-2014
APOGEE-2	South	22,500	$1.51 - 1.70\,\mu m$	$H = 12.2$	2014-2020
GES (UVES)	South	45,000	$300 - 1,100$ nm	$V = 15.5$	2011-2016
GALAH	South	28,000	$470 - 790$ nm	$V = 14$	2013-2016
WEAVE	North	20,000	$400 - 950$ nm	$V = 17$	2019-

tions in the next 5 years: 4-metre Multi-Object Spectroscopic Telescope (4MOST) and Multi-Object Optical and Near-infrared Spectrograph (MOONS) in the VISTA and VLT telescopes, respectively, at Paranal, Chile, and MaunaKea Spectroscopic Explorer in the Canada-France-Hawaii Telescope, at Mauna Kea, Hawaii.

However, not all the large high-resolution spectroscopic surveys have dedicated observations to OCs. Except for a few systems observed for calibration purposes, OC stars are targeted only when they fall in the field of view of other targets. This means that the results for most of the studied clusters are based on observations of one or two members only. Currently, APOGEE is the only survey sampling the Northern hemisphere with high-resolution spectra in the infrared H band. GES and GALAH are operating in the South, and WEAVE is defining the OCs targets and will start operations in 2018.

There are other long-term projects dedicated to the study of the OCs. The Bologna Open Cluster Chemical Evolution (BoCCE) project (Bragaglia and Tosi 2006) uses both color-magnitude diagram synthesis and high-resolution spectra to infer cluster properties such as age, distance, and chemical composition. The WIYN Open cluster study (von Hippel and Sarajedini 1998) is also obtaining photometry, astrometric and spectroscopic data for few nearby OCs.

1.5 MOTIVATION AND GOALS OF THE THESIS

The chemical evolution of the Milky Way is not well understood despite the great efforts invested during the last decades in acquiring precise observational data and building detailed GCE models. It is clear that uncertainties in deriving detailed abundances from high-resolution spectroscopy, stellar ages and distances, radial velocities and proper motions, play a major role and prevent detailed investigations to reach strong conclusions. Also, probably there is a need to enrich theoretical models to be able to reproduce the apparent complexity of the Galactic evolution. It is mandatory to account for dynamical effects of structures such as spiral arms and bars, and explore different possibilities in the SFR, IMF and infall assumptions.

In the observational field OCs provide the most precise ages and distances derived from photometry. Moreover, the possibility of averaging results for several member stars to derive mean chemical abundances, radial velocities and proper motions, derives in better quality data that helps to strongly constrain models. The main drawback when using OCs is that they exist in a limited number and they have a restricted coverage in ages and through the Galactic disc. This may introduce an unavoidable observational bias.

As mentioned above GES has dedicated observations to OCs with high-resolution in the South, but we do not have a GES-UVES counterpart in the North covering the anticenter direction. Lacking of multi object spectrographs in the North, in 2012 we started the Open Cluster Chemical Abundances from Spanish Observatories (OCCASO) survey aiming to study a sample of $\sim$ 25 OCs with the facilities available in Spanish observatories.

1.6 THESIS OUTLINE

This thesis is organized as follows. After this first introductory chapter, we detail the observations that we performed in this work in Part I. Chapter 2 presents the used observational facilities, target selection and observational strategy of the OCCASO survey. In Chapter 3 we give the details of the observational runs, and the data reduction pipeline.

In Part II we include the analysis and the results of the spectroscopic analysis, it is divided in four main chapters. First, we present the results of radial velocities obtained from the spectroscopic analysis in Chapter 4. Our results are combined with proper motions to provide a kinematic view of the sample of OCs in the context of the Galactic disc. Additionally we use a dynamical model of the Milky way to reconstruct the orbits of the OCs and extrapolate their birth place. In Chapter 5 we describe the derivation of the atmospheric parameters of the OCs stars from spectroscopy (with two methods) and from photometry. We also do an extensive comparison with previous results in the literature. In Chapter 6 we focus on the chemical abundance determination. We describe the two methods used to derive chemical abundances and we present the results of Fe-peak, and α-elements. We derive mean cluster abundances for these elements using bona-fide member stars. We analyse the abundance ratios respect to iron of each OC.

In Part III we present the main implications that can be extracted from the radial velocities and abundances, and we summarize the general conclusions of the thesis, the future work and perspectives. Chapter 7 contains the results of the radial and vertical trends of [Fe/H] abundance in the Galactic disc extracted from the OCCASO sample. We use two additional samples of OCs to explore a further range in Galactocentric radius and the existence of an AMR. We also use the results of the orbit computation in Chapter 4 to analyse how the Galactic trends could have been if the clusters would not

have moved from its original position. We also analyse in more detail the abundance patterns derived for NGC 6705, emphasizing its α-enhancement and the possible explanations for it. Finally, we summarize the general conclusions of the thesis and the future work and perspectives in Chapter 8.

At the end we include the Appendix A where we present the main results of the work done in the workshop "Opening the black box of stellar spectroscopy". There we test the performance of six methods of spectroscopic analysis to investigate the effects and usual assumptions that have more impact in the abundance results. In the Appendix B we add long tables cited in the text.

Part I

THE OCCASO SURVEY

2

OBSERVATIONAL FACILITIES AND CLUSTER SELECTION

This chapter describes the OCCASO survey. The used observational facilities (instrument/telescope) are described in Section 2.1, and the observational strategy is detailed in Section 2.2. We give details of the selected clusters in Section 2.3 where we also explain the selection of the target stars in each cluster. Finally in Section 2.4 we list several scientific topics in which OCCASO data can contribute.

OCCASO is an on-going spectroscopic survey designed to observe OCs in the Northern hemisphere. It provides homogeneous radial velocities, atmospheric parameters, and individual abundances of 30 chemical species from high-resolution spectroscopy ($R \geqslant 65,000$) of RC stars in OCs. OCCASO was designed in 2012 where no other survey was dedicating observations to Northern OCs aside from APOGEE (see Section 1.4) with much lower resolution and in the infrared. In few years WEAVE will provide further results on OCs chemical abundances, though at much lower resolution than OCCASO. OCCASO was created to be developed in parallel to the GES-UVES observations of Southern OCs. The observational strategy and the data analysis of both surveys are similar. Moreover, there are several OCs in common between both surveys to provide a way to assess homogeneity.

2.1 OBSERVATIONAL FACILITIES

There is no easy access for the European community to a spectrograph with similar multi-object capabilities as UVES, in the Northern hemisphere. However, at Spanish Observatories there are several echelle high-resolution spectrographs available with resolutions and wavelength coverage ranges similar to, or larger than UVES. In particular, for OCCASO we have selected: the Calar Alto Fiber-fed Echelle spectrograph (CAFE) at the 2.2 m telescope in the Centro Astronómico Hispano-Alemán (CAHA), the Fibre-fed Echelle Spectrograph (FIES) at the 2.5 m Nordic Optical Telescope (NOT) telescope in the ORM, and the High Efficiency and Resolution Mercator Echelle Spectrograph (HERMES) at the 1.2 m Mercator telescope also in the ORM. See Table 2.1 for a summary of the instrument characteristics.

FIES (Telting et al. 2014) is a cross-dispersed echelle spectrograph mounted at the 2.5 m NOT, and located in the ORM in the island of La Palma (Spain). FIES is mounted in a heavily isolated building separated from the NOT building. It is connected to the Cassegrain focus of the telescope with a fiber bundle offering a maximum resolution

of $R \sim 67,000$. The wavelength coverage of the output spectra is $3700 - 7300$ Å without gaps.

HERMES (Raskin et al. 2011) is a fibre-fed prism-cross-dispersed echelle spectrograph at the 1.2 m Mercator telescope in the ORM as well. It is mounted in a temperature-controlled room and fibre-fed from the Nasmyth A focal station through an atmospheric dispersion corrector. The size of the detector enables a coverage of the $3770 - 9000$ Å wavelength range, with a maximum resolution of $R \sim 85,000$.

CAFE (Aceituno et al. 2013) is an instrument constructed at the 2.2 m telescope in the CAHA, Almería (Spain). CAFE is installed in a temperature and vibration controlled room. It offers a maximum resolution of $R \sim 62,000$, and a spectral coverage of $3900 - 9500$ Å.

2.2 OBSERVATIONAL STRATEGY

Since only one star can be observed at once in each of the selected spectrographs, we distribute our observations among the three different telescopes/instruments according to the magnitude of the stars. This allows us to develop OCCASO on a timeline similar to GES. The brightest targets ($V \leqslant 13$) are assigned to HERMES@Mercator, and the faintest stars ($V > 13$) are assigned mainly to FIES@NOT. Primarily, the faintest stars were also assigned to CAFE@2.2mCAHA, but our observations demonstrated that its current efficiency is lower than expected, and all the faint stars were finally moved to FIES.

All stars are observed in at least three exposures lasting $80 - 3600$ s, depending on their magnitude, until a global Signal-to-Noise Ratio (SNR) of around 70 per pixel at $\lambda \sim 6000$ Å is reached, enough for the precision in abundance that we require ($\lesssim 0.05$ dex). For the faintest targets ($V \geqslant 14$), this condition is relaxed to a SNR~ 50. In each run we take a sky exposure to subtract the sky emission lines and, when relevant, the sky background level. Hot, rapidly rotating stars were observed twice per run to remove sky absorption features, like telluric bands of O_2 and H_2O. Standard calibration images (flat, bias and arcs) were all taken at the beginning and end of each night.

In general, we assign each OC to one instrument to maximize the precision in our measurements. In order to guarantee the homogeneity of our whole sample, at the beginning of the survey we have repeated observations of a set of few stars with the three instruments. Additionally, Arcturus (α-Bootes) and μ-Leo, two extensively studied stars, part of the *Gaia* Benchmark Stars (GBS) (Jofré et al. 2014; Blanco-Cuaresma et al. 2014b; Heiter et al. 2015b) and the APOGEE reference stars (Smith et al. 2013), were observed with the three telescopes for the sake of comparison. We distribute the target stars among the observing runs (see Section 3.1) taking into account their magnitudes, the quality of the nights and the characteristics of the instruments.

Table 2.1. Characteristics of the instruments and telescopes used for the OCCASO Survey.

Telescope/Instrument	Diameter	Spectral range	Resolution
NOT/FIES	2.5 m	$3700 - 7300$ Å	$67,000$
Mercator/HERMES	1.2 m	$3770 - 9000$ Å	$85,000$
2.2mCAHA/CAFE	2.2 m	$3900 - 9500$ Å	$62,000$

2.3 CLUSTER SELECTION AND MEMBERSHIP

We select OCs to observe in OCCASO according to the following criteria:

i. Visible from the Northern hemisphere

ii. Ages $\gtrsim 0.3$ Gyr, since intermediate-age and old OCs are excellent probes of the structure and chemo-dynamical evolution of the Galactic disc.

iii. With six or more stars in the expected position of the RC area of the Color-Magnitude Diagram (CMD)[1]. In general, RC stars are clearly identified even in sparsely populated CMDs. In some cases, however, it is not easy to differentiate a RC star from a RGB star in OCs, so for simplicity we refer them as RC from now on. Selecting RGB stars instead of RC would not imply abundance changes except maybe for light elements, e. g. C or N. Spectra of this type of Red Giants are less line-crowded and therefore, easier to analyse than those of the brighter giants. Moreover, targeting objects in the same evolutionary state avoids measuring distinct abundances for some elements due to effects of stellar evolution. The requirement of six stars has been chosen to have reasonable statistics for the chemical abundances of each cluster.

iv. With RC magnitude brighter than $V \sim 15$ mag, constrained by the available instruments/telescopes.

v. Prioritizing those OCs with ages, metallicities, heights from the plane, or Galactocentric distances lying in poorly studied regions of the R_{GC}-[Fe/H], Age-[Fe/H], z-[Fe/H] diagrams. In this way, we will improve the sampling homogeneity of the Galactic disc.

vi. Some clusters with previous high-resolution studies in the literature (e.g. Carrera and Pancino 2011; Carrera 2012b; Bragaglia and Tosi 2006), and OCs selected in other surveys (GES, APOGEE) for comparison purposes.

Following the outlined criteria, we selected a list of 33 candidate OCs, distributed in the [Fe/H]-R_{GC}, [Fe/H]-Age, [Fe/H]-z diagrams as seen in Figs. 2.1 to 2.3.

1 Actually, some bright clusters not fulfilling this condition were added to be observed during nights of non optimal weather conditions.

Table 2.2. Completed clusters of OCCASO by the end of August 2016. We list Galactic longitude and latitude, distance from the Sun D from Dias et al. (2002), Galactocentric radius R_{GC} and height above the plane z are calculated assuming $R_\odot = 8.5$ kpc. We list the V magnitude of the RC and the number of stars observed. The photometry used to select the target stars is indicated as a footnote.

Cluster	l (deg)	b (deg)	D (kpc)	R_{GC} (kpc)	z (pc)	Age (Gyr)	V_{RC}	Stars
IC 4756[1]	36.381	5.242	0.484	8.12	44	0.8[a]	9	7
NGC 188[2]	122.843	22.384	1.714	9.54	652	6.3[a]	12.5	6
NGC 752[3]	137.125	−23.254	0.457	8.84	−180	1.2[a]	9	7
NGC 1817[4]	186.156	−13.096	1.972	10.46	−446	1.1[a]	12.5	5
NGC 1907[5]	172.619	0.306	1.800	10.29	9	0.4[b]	9	6
NGC 2099[6]	177.635	3.091	1.383	9.88	74	0.4[c]	12	7
NGC 2420[7]	198.107	19.634	2.48	10.88	833	2.2[a]	12.5	7
NGC 2539[8]	233.705	11.112	1.363	9.37	262	0.7[d]	11	6
NGC 2682[9]	215.696	31.896	0.808	9.17	426	4.3[a]	10.5	8
NGC 6633[10]	36.011	8.328	0.376	8.2	54	0.6[e]	8.5	4⋆
NGC 6705[11]	27.307	−2.776	1.877	6.89	−90	0.3[f]	11.5	7
NGC 6791[12]	69.959	10.904	5.035	8.26	952	10.2[a]	14.5	7
NGC 6819[13]	73.978	8.481	2.403	8.17	354	2.9[a]	13	6
NGC 6939[14]	95.903	12.304	1.80	8.87	383	1.3[g]	13	6
NGC 6991[15]	87.39	1.60	0.70	8.5	19	1.3[h]	10	6
NGC 7245[16]	101.368	−1.852	3.467	9.79	−112	0.4[i]	13	6
NGC 7762[14]	117.210	5.851	0.78	8.88	79	2.5[j]	12.5	6
NGC 7789[17]	115.432	−5.385	1.795	9.41	−168	1.8[a]	13	7

[1]Alcaino (1965); [2]Platais et al. (2003); [3]Johnson (1953); [4]Harris and Harris (1977); [5]Pandey et al. (2007); [6]Kiss et al. (2001); [7]Anthony-Twarog et al. (1990); [8]Choo et al. (2003); [9]Montgomery, Marschall, and Janes (1993); [10]Harmer et al. (2001); [11]Sung et al. (1999a); [12]Stetson, Bruntt, and Grundahl (2003); [13]Rosvick and Vandenberg (1998); [14]Maciejewski and Niedzielski (2007); [15]Kharchenko et al. (2005); [16]Subramaniam and Bhatt (2007); [17]Mochejska and Kaluzny (1999) and McNamara and Solomon (1981).
[a]Salaris, Weiss, and Percival (2004); [b]Subramaniam and Sagar (1999); [c]Nilakshi and Sagar (2002); [d]Vogel et al. (2003); [e]Jeffries et al. (2002); [f]Cantat-Gaudin et al. (2014b); [g]Andreuzzi et al. (2004); [h]Kharchenko et al. (2005); [i]Subramaniam and Bhatt (2007); [j]Carraro, Semenko, and Villanova (2016)
⋆It has only 4 stars in the RC but was included for observation in a night with non optimal weather conditions.

Table 2.3. Clusters selected in OCCASO but still to finish observations. We list the same properties as in Table 2.2 adding the number of observed stars.

Cluster	l (deg)	b (deg)	D (kpc)	R_{GC} (kpc)	z (pc)	Age (Gyr)	V_{RC}	Stars
Be 17	175.65	−3.65	2.70	11.19	−171	10.00	14.6	5
Be 31	206.26	5.12	8.30	16.36	740	2.04	14.5	0
Be 32	207.97	4.40	3.10	11.33	237	3.39	15	0
Col 74	199.031	−10.389	2.51	10.90	−452	8.91	14	0
Col 110	209.649	−1.978	1.95	10.24	−67	9.12	13.5	0
King 1	119.76	1.690	1.90	9.59	56	2.00	14.5	3
NGC 559	137.17	−23.26	0.46	8.84	−181	1.12	14	1
NGC 2112	205.90	−12.60	0.94	9.35	−205	1.78	13.5	0
NGC 2158	186.64	1.76	5.07	13.55	155	1.05	15	0
NGC 2192	173.415	10.65	2.50	10.99	462	2.00	14	0
NGC 2266	187.79	10.29	3.40	11.88	607	0.63	13.7	0
NGC 2355	203.39	11.80	2.20	10.56	449	0.71	12.7	4
NGC 6603	18.31	−18.41	3.60	5.21	−1136	0.20	13.5	1
NGC 7142	105.42	9.45	1.69	9.10	277	1.91	14	2
NGC 7226	101.41	−0.6	2.62	9.38	−27	0.28	13	0

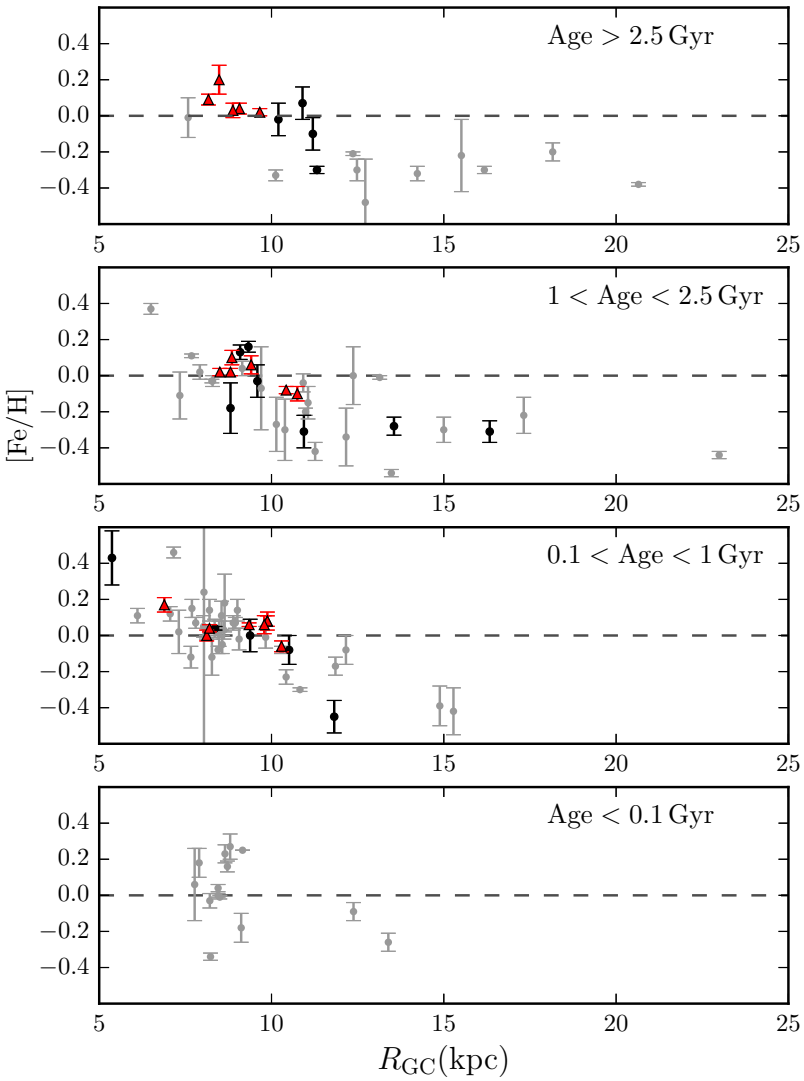

Figure 2.1. [Fe/H] as a function of R_{GC} in four bins of age. Grey dots correspond to the high-resolution data of OCs compiled by Carrera and Pancino (2011). Red triangles are the 18 OCs analysed in this thesis ([Fe/H] from OCCASO). Black dots are the rest of OCs within OCCASO but not observed yet (metallicities from different authors). Dashed line indicates the Solar metallicity.

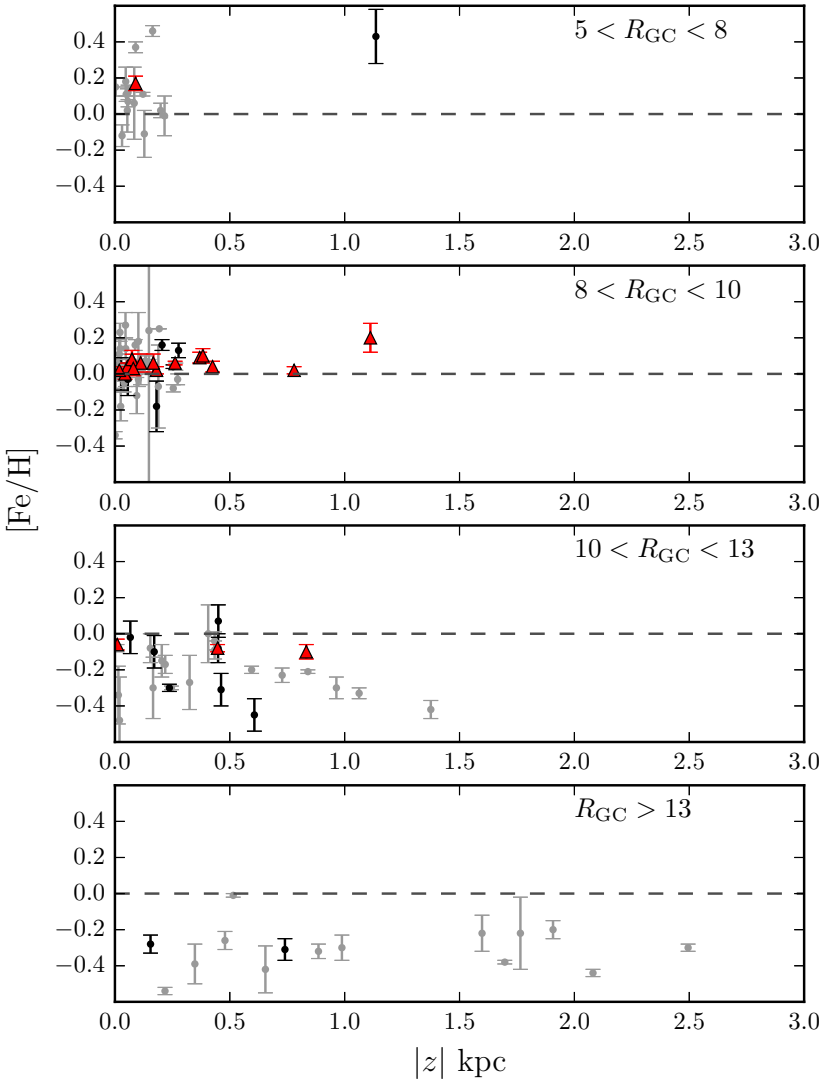

Figure 2.2. [Fe/H] as a function of z in four bins of R_{GC}. The symbols are the same as in Fig. 2.1.

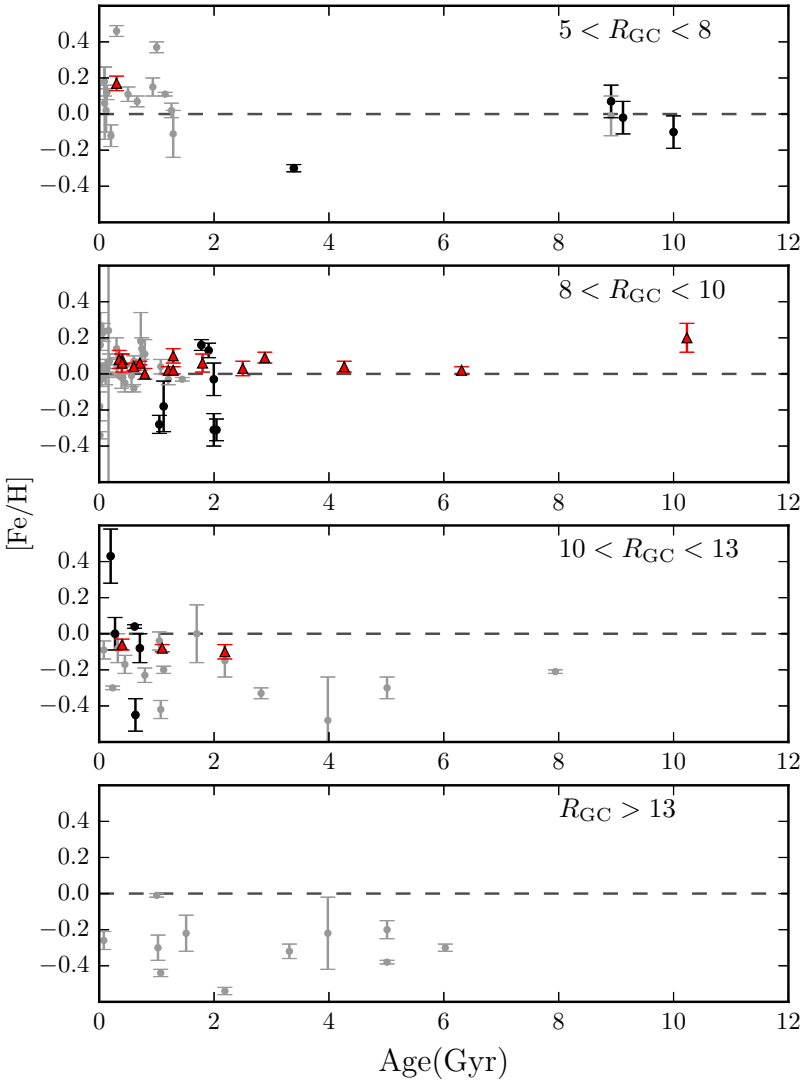

Figure 2.3. [Fe/H] as a function of Age in four bins of R_{GC}. The symbols are the same as in Fig. 2.1.

To select individual stars within each cluster we use the available literature information, with the following procedure:

i. the targets are first selected among the stars located in the expected position of the RC in the CMD from the available photometries (see Fig. 2.4);

ii. membership information based on radial velocities and proper motions, if available, is taken into account;

iii. stars already flagged as non-members or spectroscopic binaries are avoided.

When membership information is not available (poor photometry, no prior information about radial velocities or proper motions), we acquire complementary medium-resolution spectroscopy using Intermediate Dispersion Spectrograph (IDS) instrument in the 2.54 m Isaac Newton Telescope (ORM). The strategy is to obtain radial velocities and overall metallicities for a large selection of objects in the line of sight of the cluster, to constrain the selection of members (see Carrera et al. 2015, 2017, for further details).

During the observational runs described in Section 3.1 we have finished observations for 18 OCs. Their general properties are summarized in Table 2.2. CMDs from the available photometries are plotted in Fig. 2.4, where targeted stars and probable non-members derived from our analysis are indicated. The clusters pending to finish are listed in Table 2.3.

2.4 LEGACY VALUE

The OCCASO survey has been designed to study the chemical evolution of the Galactic disc through OCs. Observations and analysis strategies have been optimized for this purpose. However, OCCASO observational data and results can also contribute to our understanding of other astrophysical questions:

i. *Galactic disc kinematics.* The same reasons that make OCs good chemical tracers of the Galactic disc justify their use to investigate Galactic dynamics. The rotation curve described by OCs is similar to that derived from other thin disc populations such as Cepheids, H II regions or molecular clouds (e.g. Hron 1987; Scott, Friel, and Janes 1995; Glushkova et al. 1998; Friel et al. 2002). There are several OCs with unusual kinematics that keep them away from the disc or the inner regions of the Galaxy. It has been suggested that several OCs in the outer disc could have been accreted during a dwarf galaxy merger. In this sense, two OCs Saurer 1 and Berkeley 29 have been related to the Galactic anticenter stellar structure, also known as Monoceros stream (Frinchaboy et al. 2006). An extragalactic origin has also been proposed for the most metal-rich known OC, NGC 6791 (Carraro et al. 2006a). However, accurate proper motions derived from

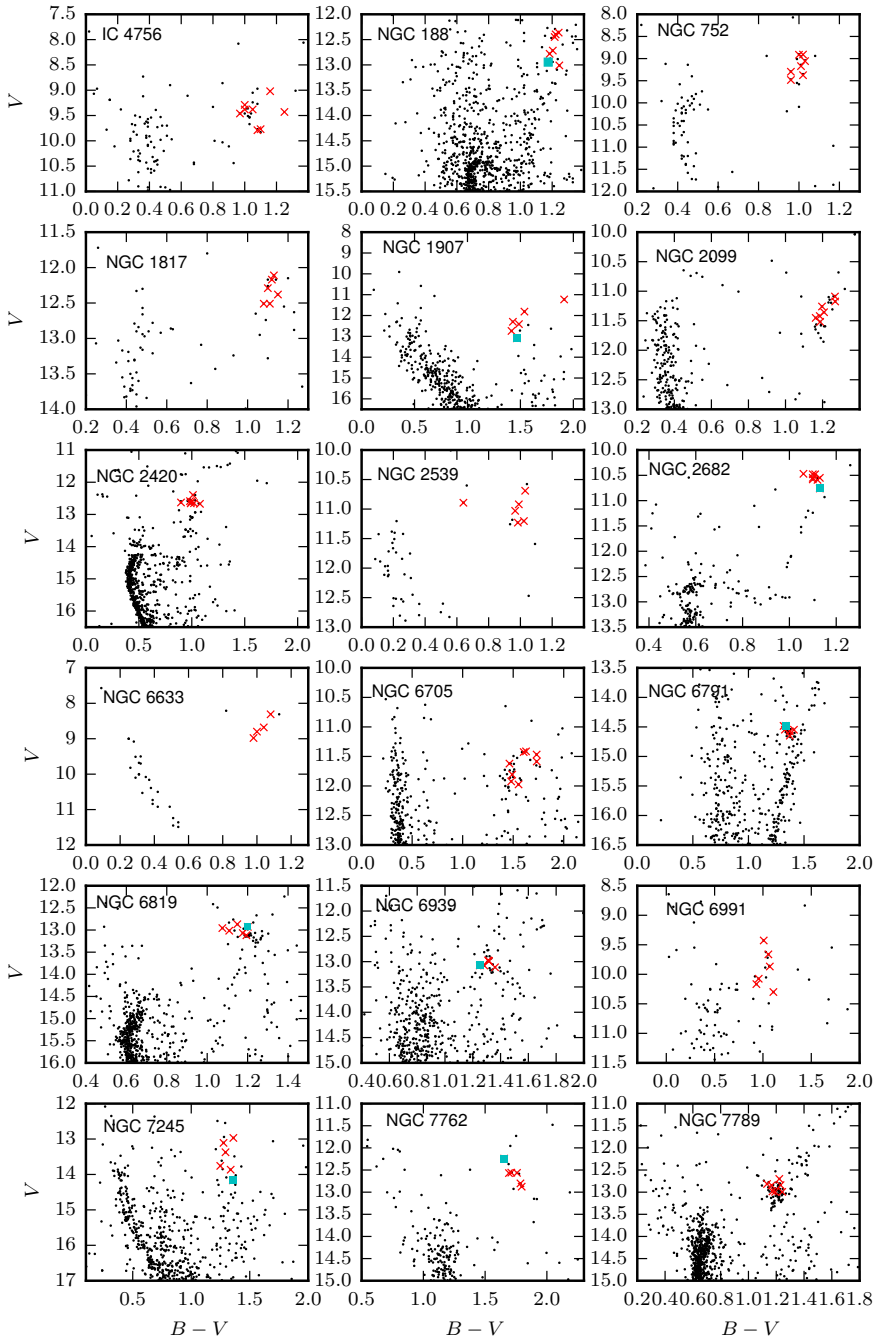

Figure 2.4. (B-V), V CMDs of the analyzed clusters (references are listed in Table 2.2). The red crosses indicate target stars, and cyan squares indicate stars that we have found to be probably non-members or spectroscopic binaries from the radial velocity study.

Hubble Space Telescope data suggest that this cluster was formed near the Galactic bulge (Bedin et al. 2006). In addition to the chemical abundances OCCASO will provide radial velocities for observed stars with uncertainties of about 500 m s^{-1} (see Section 4.1.3). These radial velocities together with the proper motions provided by the *Gaia* mission will allow us to study the three-dimensional kinematics of the OCs, trace their orbits and relate them to the spiral structure of the Galactic disc.

ii. *S*tellar evolution laboratories. OCs have been widely used to check the applicability of stellar evolutionary models and the validity of their physical parameters and prescriptions such as convective overshooting (e.g. Pietrinferni et al. 2004), and rotation (e.g. Carlberg 2014; Lanzafame and Spada 2015). In spite of the progress performed in last years, current evolutionary models are not able to completely reproduce the color-magnitude diagrams of many OCs independently of their metallicities (e.g. Ahumada et al. 2013). A possible explanation could be that each cluster has different abundance ratios (Gallart, Zoccali, and Aparicio 2005). Stellar evolutionary models for different chemical compositions besides the iron and α-elements have not been available until very recently (e.g. VandenBerg et al. 2012). The chemical abundances provided by OCCASO will help to constrain their parameters.

iii. *D*iffuse interstellar bands. In spite of the discovery of the Diffuse Interstellar Bands (DIBs) occurred as early as 1922 (Heger 1922), their origin is still not well understood. They were originally suspected of being produced on or in the interstellar grains, because the strength of some DIBs (but not all) shows a correlation with the interstellar extinction. Current evidences favours free polyatomic molecules (Herbig 1995), being the large carbon-bearing molecules the most likely candidates. Kos et al. (2014) have derived a pseudo-three-dimensional map of the strength of the DIB at 8620 Å, one of the DIBs with a strong correlation with the reddening. Despite a similar distribution in the Galactic plane, the DIB 8620 carrier has a significantly larger vertical scale height than the dust. The census by Jenniskens and Desert (1994)[2] contains 185 DIBs with certain identification in the wavelength range of our observations, 31 of them with Full Width at Half Maximum (FWHM) larger than 5 Å. Being our spectra of a higher resolution than those in other surveys like GES, APOGEE and the future WEAVE and 4MOST, and covering a larger wavelength interval too, they constitute an excellent observational material to investigate the correlations among DIBs and with the interstellar medium.

OCCASO could also contribute in the understanding of a variety of topics such as the study of the internal dynamics of old (highly evolved) OCs (e.g. Bonatto and

2 Updated catalogue: https://leonid.arc.nasa.gov/DIBcatalog.html

Bica 2003; Davenport and Sandquist 2010), and the detection of signs of the existence of multiple stellar populations (Geisler et al. 2012; Carrera 2012a; Cunha et al. 2015). However, the small number of stars sampled in each cluster difficults these kind of studies from OCCASO data only.

3

OBSERVATIONAL MATERIAL AND DATA REDUCTION

This chapter contains in Section 3.1 the description of the observational runs in the different observational facilities dedicated to OCCASO. In Section 3.2 we detail the observational material used in the thesis, in one side the data of the OC stars obtained from the observations, and also the sample of the GBS retrieved from a high-resolution spectral library. Finally, in Section 3.3 we describe the data reduction process and, in particular, the data reduction pipeline specifically designed for OCCASO.

3.1 OBSERVATION RUNS

This work is based on observational material from the spectrographs: FIES, HERMES, CAFE (see Section 2.1). OCCASO observations started in April 2013 in the ORM, then the project earned a long term program in NOT and Mercator telescopes granting 5 nights per telescope and semester, for two years. After that, we continued observations in the two telescopes for one more year. We also regularly applied for service time in the 2.2m CAHA telescope, and the NOT Spanish and Swedish service time. Until August 2016 we have completed a total of 81 nights of observations. The number of nights, dates and instruments of each run are summarized in Table 3.1 together with the percentage of time lost due to bad weather and a description of the quality of the sky. In this time we have finished observations of 18 OCs which comprise a total of 115 stars, together with Arcturus and μ-Leo used for comparison purposes.

There are two additional runs: one with HERMES which material is pending to analyse, and one with IDS devoted to do complementary observations at intermediate resolution with (see Section 2.3). Data from these two runs is not used for this work.

3.2 OBSERVATIONAL MATERIAL

3.2.1 *Open Clusters*

With 81 nights of observations we were able to complete observations for 115 stars in 18 OCs plus two of the GBS and APOGEE reference stars: Arcturus and μ-Leo. From 17 stars out of these 117 we have repeated observations with more than one instrument,

Table 3.1. Runs devoted to the project. Observations from the runs 1-19 are included in this thesis. Data from run 20 is pending to analyze, data from run 21 was devoted to do complementary observations (see text).

Run	Period	Instrument	# nights	Time lost	Q[1]
1	1-2 Apr 2013	FIES	2	50%	2
2	25-29 Jul 2013	HERMES	5	0%	1
3	23-25 Sep 2013	FIES	3	50%	2
4	1-6 Oct 2013	HERMES	5	30%	1
5	25-29 Nov 2013	FIES	5	40%	2
6	3-7 Jan 2014	CAFE	5	100%	3
7	26 Jan 2014[2]	FIES	1	0%	2
8	29-30 Jan 2014	CAFE	2	100%	3
9	21-25 May 2014	HERMES	5	15%	1
10	14-15 Jul 2014	CAFE	2	0%	2
11	6-8/10-11 Sep 2014	FIES	5	10%	2
12	7-11 Oct 2014	FIES	5	25%	1
13	18-22 Dec 2014	HERMES	5	15%	1
14	1-3 Jan 2015	CAFE	3	0%	1
15	27 Apr-02 May 2015	HERMES	5	0%	1
16	28 Aug-02 Sep 2015	FIES	5	0%	1
17	16-20 Dec 2015	FIES	5	10%	1
18	14-21 Jan 2016	FIES	8	30%	2
19	5-9 Aug 2016	FIES	5	0%	1
20	9-13 Feb 2017	HERMES	5	80%	2
21	18-20 Jul 2014	IDS	3	0%	1

[1]Quality of the night: 1: good seeing ($< 1''$), no clouds; 2: medium seeing ($1 - 2''$), disperse thin clouds, low dust, we were forced to observe stars 1-2 mag brighter than expected; 3: bad seeing ($> 2''$), clouds, no observations.
[2]Shared period, only a fraction of the night was used for this project.

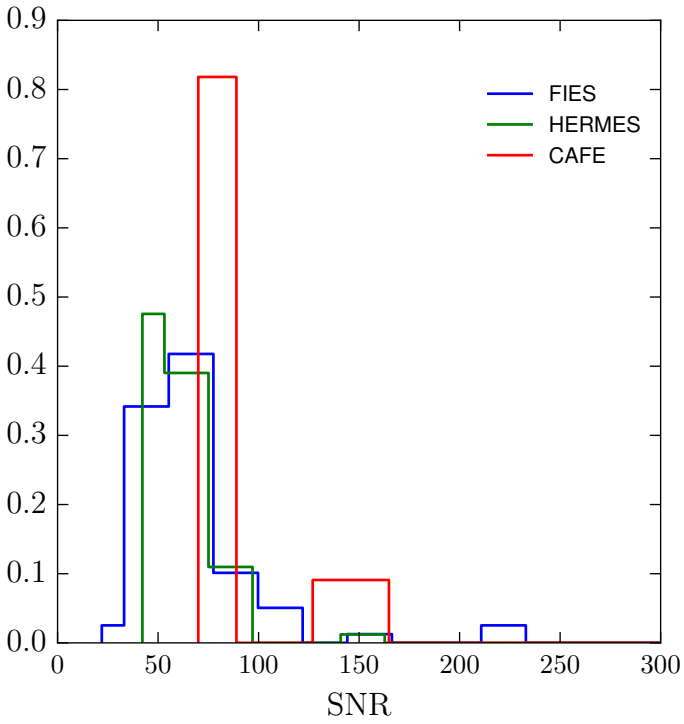

Figure 3.1. SNR distribution of the observed stars per instrument. The histograms are normalized to allow a better visualization. Arcturus and μ-Leo observed with the three instruments fall out of the plot with SNR> 300.

for comparison purposes. In total we have analyzed 154 spectra: 62 corresponding to FIES, 81 to HERMES, and 11 to CAFE.

We plot the distribution of SNR of the observed stars per instrument in Fig. 3.1.

3.2.2 *Benchmark stars*

Aside of our own observational material, we also analyse a sample of GBS to assess our results. The GBS are a set of calibration stars, covering different regions of the HR diagram and spanning a wide range in metallicity. For these stars there exists enough data to determine effective temperature and surface gravity independently from spectroscopy by using their angular diameter measurements and bolometric fluxes. These determinations and related uncertainties are fully described in Heiter et al. (2015b). Reference metallicities also exist for these stars, and are determined from a careful spectroscopic study by Jofré et al. (2014).

We retrieved the data from the library of high-resolution optical spectra of the GBS (Blanco-Cuaresma et al. 2014b). This library includes 100 high SNR spectra of 34 stars

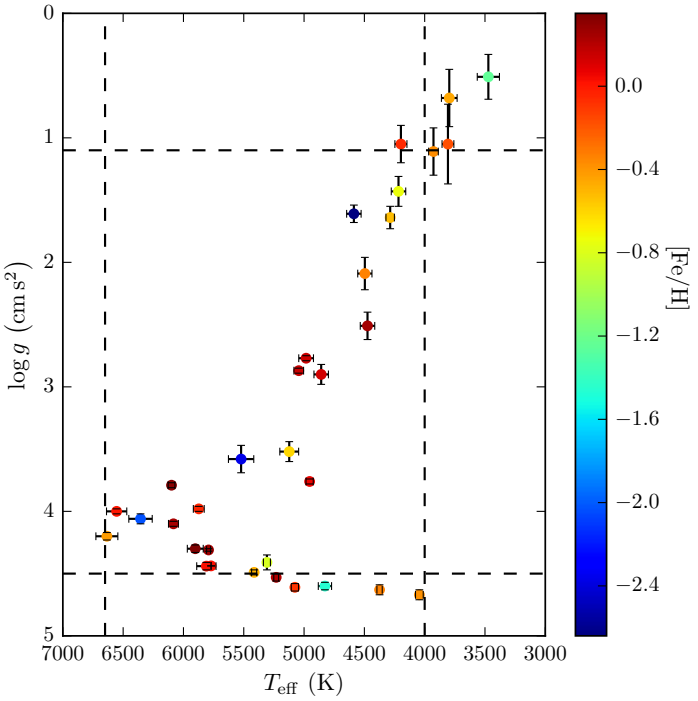

Figure 3.2. CMD of the whole sample of the GBS. T_{eff} and log g from Heiter et al. (2015b), metallicity from Jofré et al. (2014). The dashed lines indicate the cuts that define the subsample used in OCCASO, the cut in metallicity is [Fe/H]$\geqslant -1.5$.

from the spectrographs HARPS, NARVAL, UVES, and ESPaDOnS, which cover the visual spectral range ($4800 \leqslant \lambda \leqslant 6800$ Å). Taking into account our target stars, we have selected the GBS that covered the portion of the parameter space of the typical OCs Red Giants: $4000 \leqslant T_{eff} \leqslant 6650$ (K), $1.1 \leqslant \log g \leqslant 4.5$, [Fe/H]$\geqslant -1.5$. 23 GBS fulfill these criteria (see Fig. 3.2). We degradated the resolution of the spectra to a common resolution of 62,000 (the lowest in OCCASO) to analyse them homogeneously with our OCCASO spectra.

3.3 DATA REDUCTION

An example of how a typical raw image of a spectrum looks like is shown in Fig. 3.3. The first part of the reduction process consists in bias subtraction, flat-field normalization, order tracing and extraction and wavelength calibration. This step is performed with the dedicated pipelines for each instrument: HERMESDRS (Raskin et al. 2011), FIESTool (Telting et al. 2014), and the pipeline developed by J. Maíz-Apellániz for

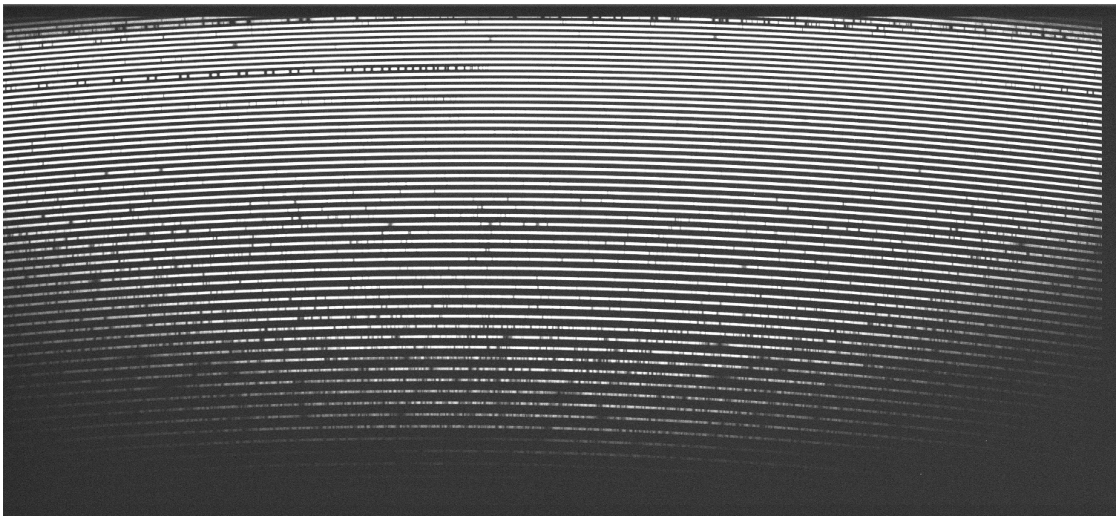

Figure 3.3. Raw image of an individual exposure of Arcturus taken with HERMES.

CAFE used in Negueruela et al. (2014). We checked that the results from the pipelines are appropriate: the spectra are correctly extracted, calibration in λ is realistic.

After these initial steps of reduction, the spectra from HERMES/FIES and CAFE are handled in different ways.

For CAFE spectra the pipeline used in Negueruela et al. (2014) merges the orders. After that, we manually perform the subtraction of sky lines, normalization by fitting the continuum with a polynomial function using `DAOSPEC` (Stetson and Pancino 2008, see details in Chapter 4), and correction of telluric features using the `IRAF`[1] task *telluric*. The heliocentric correction to account for observer's motion is obtained with the `IRAF` task *rvcorrect*. Finally, the combination of the single normalized spectra of the same star and telescope is done using the `IRAF` task *scombine* with a median algorithm and a sigma-clipping rejection.

For HERMES and FIES spectra we have built our own data reduction pipeline instead of using the latest steps of the telescope pipelines. We detected that the order merge procedure used by these pipelines yield wiggles in the overlap regions between the orders that are difficult to correct with the normalization algorithm (top left panel of Fig. 3.5). Moreover, these wiggles cause that the core of some lines get values below zero after normalization. This has a high impact in the chemical abundance analysis. Additionally, we have detected that the standard procedures used for emission sky and absorption telluric lines subtraction leave large residuals in several cases (top right panel of Fig. 3.5). All together, these issues motivated us to develop a new data

1 `IRAF` is distributed by the National Optical Astronomy Observatory, which is operated by the Association of Universities for Research in Astronomy (AURA) under a cooperative agreement with the National Science Foundation.

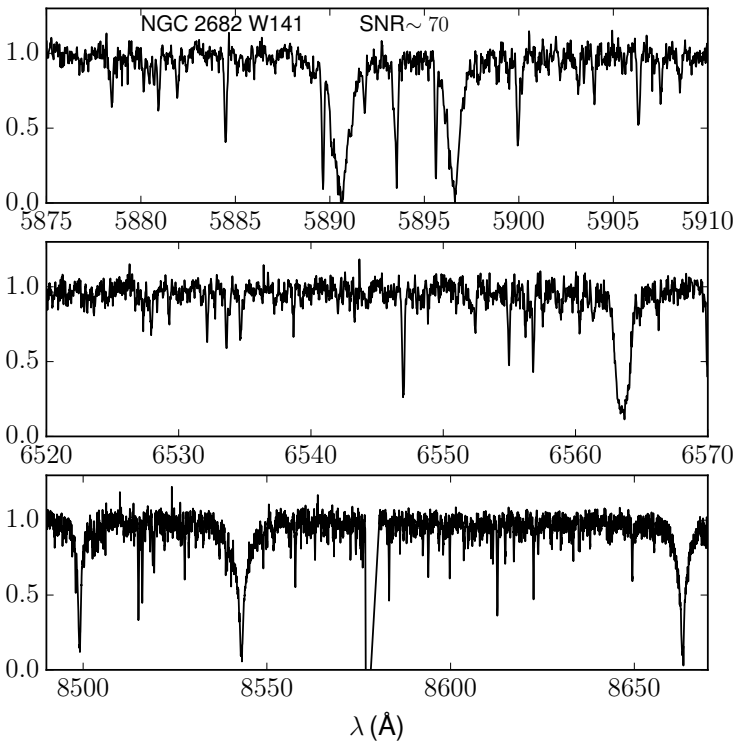

Figure 3.4. The Ca I triplet (bottom), Hα (middle) and the Na I doublet (top) regions of the final combined and normalized spectrum of the star NGC 2682 W141, from HERMES instrument. A small gap from the order merging can be seen at 8580 Å.

reduction protocol. In this way we aim to improve the quality of the spectra (see next subsection).

As an example of the results of the reduction protocol, we show three regions of the combined and normalized spectrum of the star NGC 2682 W141 in Fig. 3.4. One can clearly identify the Ca I lines, the Hα line, and the Na I doublet together the interstellar medium one (wider) shifted about 1 Å.

3.3.1 *Data reduction pipeline*

After the wavelength calibration and order merge performed by the dedicated pipelines there are several steps that need to be done: (i) sky subtraction, (ii) normalization, (iii) subtraction of telluric features, (iv) apply the heliocentric correction, and (v) combine the spectra of an object obtained with each instrument. In the first OCCASO data release (Casamiquela et al. 2016, Paper I hereafter) we described in detail the reduction of the data where we perform these steps after the whole telescope pipeline run.

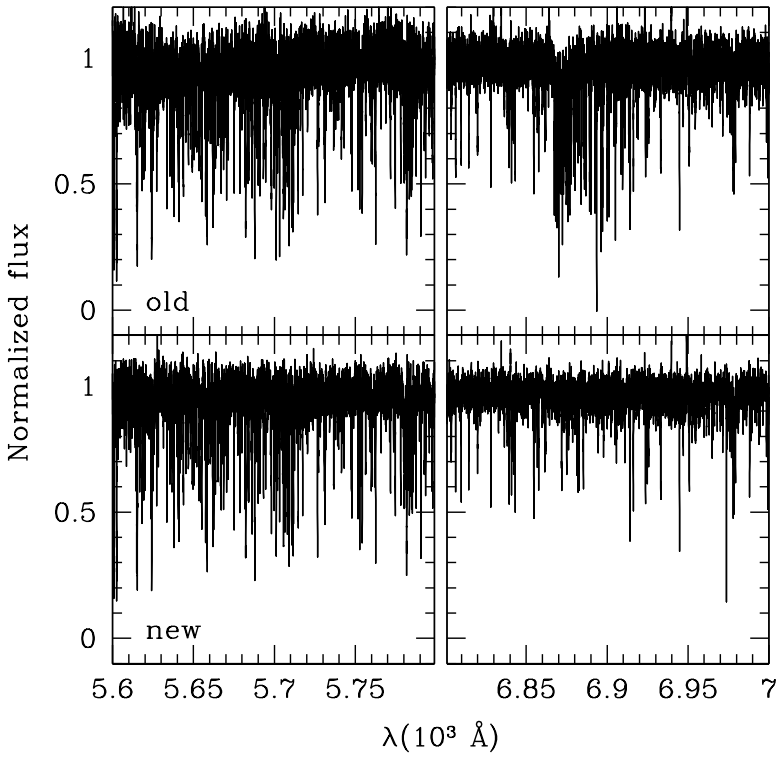

Figure 3.5. Comparison between the old (top) and new (bottom) data reduction procedures for star NGC 6939 W230 observed with HERMES in two differences wavelength regions (see text for details).

The procedure designed here does not modify the wavelength calibration derived by the individual instrument pipelines which could introduce noise in the radial velocity determination, but improves the order merging and the sky and telluric lines subtraction, key for abundance determination.

In Paper I, we were using the final 1D spectra pipelines products with the orders merged. Order merging is one of the causes of the issues described above, so we start the new protocol from an intermediate pipeline product where the spectra have been wavelength calibrated but still separated by orders. We do not start the data reduction from the beginning, e.g. bias subtraction, order tracing and extraction, etc. This is because these steps are very dependent of the instrument and the pipelines have been specifically designed to handle the particularities of each of them. From this point the procedure followed is:

i. Sky subtraction. With the spectrum still divided into orders the sky emission lines are subtracted following a similar procedure that used in Carrera et al. (2017, submitted to A&A). Each order in the object individual exposure and in the sky exposure obtained in the same observing run with similar sky conditions

are divided into two components: continuum and line. To obtain the continuum of both sky and object spectra we used a nonlinear median filter with k-sigma clipping. The line spectrum is obtained by subtracting the continuum. The sky- and object-line components are compared to search for the scale factor that minimizes the sky line residuals over the wavelength range covered by each order. This optimum scaling factor is the value that minimizes the L1 norm. The object-continuum component is wavelength updated and added back to the sky-subtracted object-line spectrum. Finally, the sky-continuum is subtracted assuming that the scale factor is the same as for the sky-line component.

ii. Telluric subtraction. We have followed the same procedure that in the case of the sky subtraction described above taken into account that, in contrast with emission sky lines, telluric ones are always in absorption.

iii. Heliocentric correction. The wavelength solution is modified to account for the observer's motion at the moment of each observation.

iv. Combine different exposures of the same object. Still with the spectra divided by orders, the different exposures of the same object acquired with a given instrument are combined scaling individual exposures by their median and weighting by their SNR. We applied an averaged sigma clipping algorithm which rejects those pixels with values larger than three times the sigma about the median.

v. Normalization of each order. The continuum of each order is iteratively fitted with a low order polynomial. When the relative variation from the first to the last iteration is small, the order of the polynomial is selected to define the continuum. The selected orders are used to fit a smooth polynomial. The final continuum is derived from the interpolation for the rest of the orders.

vi. Merging of the orders. Finally, the orders are merged to obtain a final 1D spectrum. To do that, overlapping regions are simply averaged.

An example of the obtained final spectra is shown in bottom panels of Fig. 3.5. All the software used for the new data reduction pipeline is exclusively implemented in Interactive Data Language (IDL)[2].

2 A product of Exelis Visual Information Solutions formerly ITT Visual information Systems and research Systems, Inc.

Part II

ANALYSIS

4

KINEMATICS OF OPEN CLUSTERS IN THE GALACTIC DISC

This chapter presents radial velocities derived for each of the 18 completed clusters, and the reference stars Arcturus and μ-Leo. Using mean cluster radial velocities we do a kinematic analysis in the context of the Galactic disc.[1]

In Section 4.1 we describe the results of epoch and mean radial velocities of the target stars, which let us perform a selection of bona-fide member stars. We include a comparison of the results among instruments. We compute cluster average radial velocities and we perform an extensive comparison with previous determinations of some stars in the literature. In Section 4.2 we use the calculated radial velocities together with proper motions determinations to calculate spatial velocities of the OCs and analyse them in the context of the Galactic disc. In Section 4.3 we use the velocities of the clusters and two models of the Galactic potential to determine their orbits, and in particular, their position of birth.

4.1 RADIAL VELOCITY

All radial velocities are measured using `DAOSPEC` (Stetson and Pancino 2008). `DAOSPEC` is a Fortran code that identifies absorption lines in a stellar spectrum, fits the continuum, match these lines from a provided linelist, and measures EWs. `DAOSPEC` also provides a radial velocity estimate using a cross-correlation procedure based on the line centers and on their reference laboratory wavelengths in the linelist (i. e., a sort of line mask cross-correlation). To run `DAOSPEC` we used the `DOOp` code (Cantat-Gaudin et al. 2014a), an algorithm that optimizes its most critical parameters in order to obtain the best measurements of EWs. In brief, it fine tunes the FWHM and the continuum placement among other parameters, through a fully automatic and iterative procedure.

The linelist used in this step is the same as the one used to calculate atmospheric parameters and abundances, and it is explained in Section 5.1.

We compute radial velocities from both individual and combined exposures for each star. Using the combined exposures, we perform a comparison among the three instruments, and we compute the final values per star. We perform a membership selection after which we compute the average radial velocity for each of the 18 clusters. Details are given in the following subsections.

1 The results for the first 12 OCs were published in Paper I.

4.1.1 *Wavelength calibration accuracy*

Wavelength calibration accuracy is key for radial velocity determination. This step is performed with dedicated pipelines (Section 3.3). To re-assess it, we calculate the radial velocity offsets of sky emission lines.

For each run we measure the radial velocities of the skylines at: 6300.304, 6363.78, 6863.95, 7276.405, 7913.708, 8344.602 and 8827.096 Å, when visible, in the sky exposures and/or in target stars exposure. This is done before applying the heliocentric correction. Therefore, the measured radial velocities are expected to be zero.

We include the mean values and standard deviations of the measured skylines radial velocity obtained for each run in Table 4.1. We can conclude the following:

i. All FIES runs have negligible offset except for run#1, for which it has a value of $5.09 \pm 0.44\,\mathrm{km\ s^{-1}}$. The pipeline could not be run in the telescope during the observing run, and it was run a posteriori using a version built to be used outside the NOT. The origin of the offset could be related to the use of inappropriate calibration images when running the pipeline. We have corrected the individual spectra of this run using this value.

ii. All HERMES offsets are compatible with $0\,\mathrm{km\ s^{-1}}$ within 3σ. The mean value is $-0.29 \pm 0.11\,\mathrm{km\ s^{-1}}$. This offset can be neglected given the spectral resolution of the instrument.

iii. Both runs from CAFE present a roughly constant offset of unknown origin, with a mean value and standard deviation of $2.55 \pm 0.62\,\mathrm{km\ s^{-1}}$. We have shifted all the spectra from these runs by $-2.55\,\mathrm{km\ s^{-1}}$.

4.1.2 *Epoch v_r*

We measure radial velocities from individual exposures after applying the offsets calculated in the previous section, and once heliocentric corrections are applied. The values obtained are listed in Table 4.2. The first, second and third columns denote the star identifier (taken from WEBDA[2]), night of observation, and instrument, respectively; the fourth column indicates the Heliocentric Julian Date (HJD) of the observation; and the fifth column lists the measured radial velocity and the uncertainty. The quoted uncertainties are those calculated by `DAOSPEC`, which correspond to the line-by-line radial velocity dispersion.

The uncertainties on the individual radial velocities are constrained by the resolution and wavelength range (which limits the number of lines used) of the instrument, and the SNR of the spectrum. The distribution of uncertainties is shown in Fig. 4.1, with

2 http://webda.physics.muni.cz/

Table 4.1. Mean radial velocity offsets and standard deviations for each run (number as in Table 3.1) from visible skylines in the spectra (see text for more details).

Run	Instrument	v_r (km s^{-1})	# measured lines
1	FIES	5.09 ± 0.44	9
3	FIES	0.09 ± 0.26	5
5	FIES	0.07 ± 0.24	6
7	FIES	-0.04 ± 0.17	7
11	FIES	-0.5 ± 0.7	6
12	FIES	0.00 ± 0.19	7
16	FIES	-0.14 ± 0.33	6
17	FIES	0.12 ± 0.34	6
18	FIES	-0.42 ± 0.36	6
19	FIES	-0.28 ± 0.63	4
2	HERMES	-0.16 ± 0.28	9
4	HERMES	-0.26 ± 0.77	7
9	HERMES	-0.42 ± 0.72	7
13	HERMES	-0.29 ± 0.89	7
15	HERMES	-0.32 ± 0.14	8
10	CAFE	2.45 ± 0.52	6
14	CAFE	2.64 ± 0.72	7

median values of 0.6 ± 0.1 km s^{-1} for FIES, 0.8 ± 0.4 km s^{-1} for HERMES, and 1.2 ± 0.3 km s^{-1} for CAFE.

Although our observations are not designed to look for spectroscopic binaries[3], we can detect them by comparing the radial velocity obtained from different exposures of the same star. Individual radial velocities for all stars agree within the errors but two:

i. NGC 6819 W983, with a radial velocity of 3.2 ± 0.8 km s^{-1} from the exposure in the night 25 Jul 2013, and -8.3 ± 0.8 km s^{-1} from the three consecutive exposures in the night 29 Jul 2013. We flag this star as possible spectroscopic binary (see next section for further discussions).

ii. NGC 7245 W0045, has a radial velocity of ~ -61.4 km s^{-1} in the two exposures from Aug 2015, and ~ -34.4 km s^{-1} in the six exposures from Dec 2015. We also flag this star as possible spectroscopic binary.

There can be other single-line spectroscopic binaries within our sample that we are not detecting because in most cases we have taken the individual exposures in the same night. In this case we would only detect them if the period is very short.

NGC 6791 W2604 has a particularly large dispersion in radial velocity. Although we did not see anything unexpected in the individual radial velocities, we performed

3 in many cases observations are consecutive

Table 4.2. Radial velocities from individual spectra. The complete version of the table can be retrieved under request.

Star	Night	Instr	HJD	$v_{r,indiv}$ (km s^{-1})
IC4756 Woo42	20130729	HERMES	2456503.42986657	-24.7 ± 0.6
IC4756 Woo42	20130729	HERMES	2456503.4350752	-24.7 ± 0.6
IC4756 Woo42	20130729	HERMES	2456503.44028436	-24.7 ± 0.6
IC4756 Woo42	20140521	HERMES	2456799.71796826	-24.5 ± 0.7
IC4756 Woo42	20140521	HERMES	2456799.72317693	-24.5 ± 0.7

a cross-correlation with a radial velocity standard. We saw a clear secondary peak at 100 ± 0.1 km s^{-1}, this means that a possible faint companion is contributing to the spectrum. We have discarded this star from our analysis.

4.1.3 *Mean v_r*

The final values of the radial velocities are obtained running `DOOp` on the combined spectra. The results of each star and instrument are specified in columns 9, 10 and 11 (for FIES, HERMES and CAFE, respectively) of Table B.1. The radial velocity uncertainties are smaller than the ones from individual spectra due to the higher SNR, as shown in the lower pannel of Fig. 4.1. Now the median dispersion values for each instrument are: 0.5 ± 0.1 km s^{-1} for FIES, 0.7 ± 0.3 km s^{-1} for HERMES, and 0.93 ± 0.07 km s^{-1} for CAFE.

We use the final combined spectra of the repeated stars to make a comparison among instruments (see Fig. 4.2). Fifteen stars were observed with both FIES and HERMES, nine stars observed with both CAFE and FIES, and five stars observed with both HERMES and CAFE. We notice:

i. For HERMES-FIES comparison, we find a mean offset and dispersion of $\langle \Delta v_r \rangle = -0.10 \pm 0.12$ km s^{-1}.

ii. For CAFE-FIES, we find a mean offset of $\langle \Delta v_r \rangle = 0.40 \pm 0.20$ km s^{-1}.

iii. For the CAFE-HERMES case, we find a mean offset of $\langle \Delta v_r \rangle = 0.60 \pm 0.28$ km s^{-1}.

All offsets are in agreement within the observational uncertainties and follow the expectations from sky emission lines results (see Table 4.1).

For the cases of stars observed with several instruments we adopt the weighted mean of all the determinations, and the mean of the nominal errors as the uncertainty. These final values are found in column 12 of Table B.1.

In general, stars have compatible radial velocities within the same cluster. This is because they were already pre-selected to be very likely cluster members, as explained

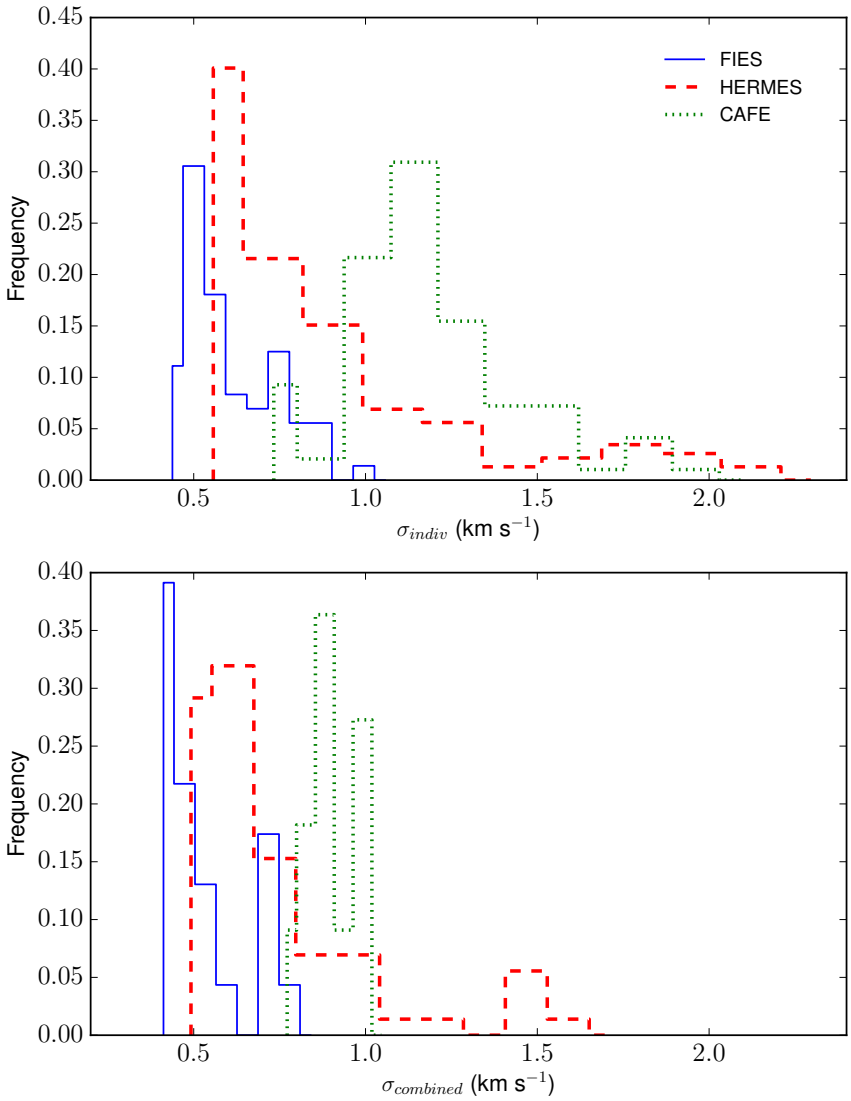

Figure 4.1. Radial velocity uncertainty distributions from the individual spectra (top panel), and the combined spectra (bottom panel), for each instrument. The histograms are scaled to facilitate the visualization.

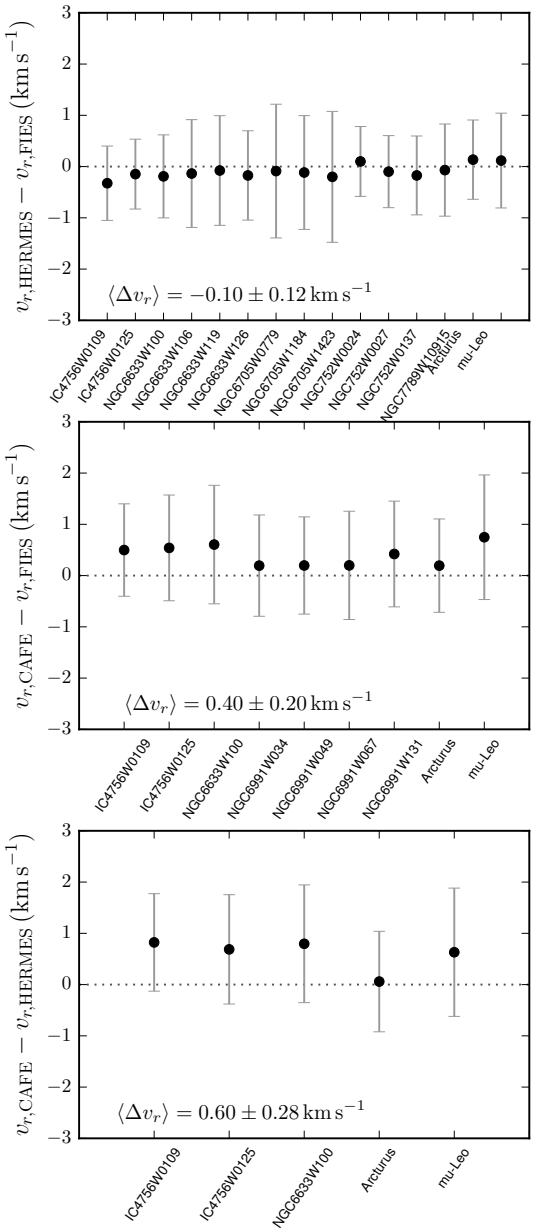

Figure 4.2. Differences in v_r obtained for the stars in common between HERMES and FIES (top panel), CAFE and FIES (central panel), and CAFE and HERMES (bottom panel).The error bars are the sum in quadrature of the two uncertainties.

in Section 2.3. However, a re-analysis of membership is performed. We flag as non-members those stars which have v_r not compatible at 3σ level of the radial velocity of the cluster. We have used the median and the Mean Absolute Deviation (MAD). We iterate this by rejecting non-members and recalculating the median radial velocity, until we find a sample of compatible stars. Under this criterion we flag the following seven stars:

i. NGC 1907 W2087 has a significant difference of $\sim 60\,\mathrm{km\ s^{-1}}$ with respect to the other stars from the same cluster. The four values from individual exposures of this star are compatible with each other, so probably it is a non-member star or a large period spectroscopic binary. There is no other measurement in the literature for comparison.

ii. NGC 2539 W233 has a radial velocity of $34.8 \pm 1.1\,\mathrm{km\ s^{-1}}$, which is $5.4\,\mathrm{km\ s^{-1}}$ above the median of the other five stars. It was already flagged as spectroscopic binary by Mermilliod, Mayor, and Udry (2008). They obtain a variability with the maximum at 28.3 ± 1.1 km s^{-1}. This value is compatible with ours within 3σ.

iii. NGC 2682 W224 has a radial velocity of $6.5\,\mathrm{km\ s^{-1}}$ under the median of the cluster. The four individual spectra were taken in two consecutive days and the individual radial velocities are in agreement. It was already flagged as member spectroscopic binary by Jacobson, Pilachowski, and Friel (2011) and Geller, Latham, and Mathieu (2015).

iv. NGC 6819 W983 has a variable radial velocity as discussed in Section 4.1.2. For this reason we do not give a final value of the radial velocity, and we do not include it in Table B.1. Neither Hole et al. (2009) nor Milliman et al. (2014) identify this star as a radial velocity variable, obtaining a final radial velocity of 2.36 ± 0.20 km s^{-1}. Both studies are based in the same spectra (6 observations) and classify this star as single member for having $e/i < 4$ (external error divided by internal error).

v. NGC 6939 W130 has a radial velocity of -29.33 ± 2.0 km s^{-1}, this is more than 10 km s^{-1} below the cluster mean, and outside 3σ. We do not see any apparent variability in the individual exposures, but they were observed during the same night. This star has not been targeted in previous studies in the literature. Since the dispersion found in radial velocity is larger than that of the other stars from the same OC, we consider that it could be a spectroscopic binary or a non-member.

vi. NGC 7245 W045 has a variable radial velocity as discussed in Section 4.1.2. For this reason we do not give a final value of the radial velocity, and we do not

include it in Table B.1. It was flagged by Carrera et al. (2015) as a cluster non-member, though from its variability range in radial velocity it can be a spectroscopic binary member.

vii. NGC 7762 W0084 has a large difference of $\sim 40\,\mathrm{km\ s^{-1}}$ with respect to the other stars of the same cluster. Radial velocities obtained from the three individual spectra acquired in two consecutive nights are consistent within the uncertainties. There is a radial velocity study of the cluster (Carraro, Semenko, and Villanova 2016) but this star was not targeted.

Special attention must be paid to NGC 7789. Following the iterative procedure described above, two stars should be rejected: W08260 and W07714. Radial velocities of all stars in this OC compare well with the literature for stars in common (Gim et al. 1998; Jacobson, Pilachowski, and Friel 2011, see Table B.1), which considers all of them as members. Moreover, Jacobson, Pilachowski, and Friel (2011) reported that they find a broader dispersion compared with other OCs. Taking into account the OC mean radial velocity and dispersion from the three large samples in the literature (Table 4.3), all the seven stars studied here fall inside the distribution. Therefore, we have decided to keep these two stars as members.

The rest of studied stars from the observed clusters are compatible with being members of their parent cluster. We point out that stars NGC 1907 W0133, NGC 6819 W978, and NGC 7762 W0003, have radial velocities outside of the 3MAD margin of the cluster, but when also considering the uncertainties on these radial velocities, these stars are still within the cluster distributions, and are included as members in our sample (see Fig. 4.3). The doubtful cases of membership will be probably solved when doing the abundance analysis (Chapter 6).

4.1.4 *Clusters v_r*

The sample of non-spectroscopic binaries and bona-fide member stars is used to compute the cluster radial velocity. Median values and MADs are found in Table 4.3 and plotted in Fig. 4.3. We also list in Table 4.3 previous determinations of the OCs radial velocity, for those references where a mean value is given. All values from literature are compatible within 3σ with the ones derived here. Carrera et al. (2015) gives the largest difference with us ($8.7\ \mathrm{km\ s^{-1}}$), probably because their study is at low resolution ($R \sim 8,000$).

The radial velocity dispersions within each cluster are found between $0.3 - 1.7\,\mathrm{km\ s^{-1}}$. The quoted dispersions are the result of (a) the precision that we have in our radial velocity determinations (Table B.1), which is computed as the line-by-line radial velocity variance found by `DAOSPEC`, (b) a fraction of undetected binaries, and (c) the intrinsic internal dispersion of each cluster. In most of the cases the dispersions in Table 4.3 are at the level of the quoted precisions. Only, the dispersion for NGC 6705

is very well above the uncertainties (1.7 km s^{-1}). This can be indicative that either this cluster has a larger fraction of undetected binaries, or that this is indeed the intrinsic radial velocity dispersion, and that this OC is kinematically hot. Given that the star by star comparison of this cluster with the literature is coherent within the uncertainties (Fig. 4.4, Table B.1), we tend to think that this is due to the intrinsic velocity dispersion. Moreover, this OC is the most massive and youngest cluster in the sample. Cantat-Gaudin et al. (2014b) selected bona-fide members and found a mean radial velocity of 34.1 ± 1.5 km s^{-1} from 21 stars (UVES targets), and 35.9 ± 2.8 km s^{-1} from 536 stars (GIRAFFE targets). Our result confirms the high intrinsic velocity dispersion of this cluster. See Section 7.3 for a further analysis of this cluster.

4.1.5 *Comparison with literature*

We compared our final values for each star (column 12 of Table B.1), with previous measurements in the literature, when available (column 13 of Table B.1). Since in most cases our individual exposures are taken during the same night, this external comparison is also useful to identify potential spectroscopic binaries.

Calculated differences with each author are shown in Table B.1 (column 14) and illustrated in Fig. 4.4. We exclude from this comparison the confirmed spectroscopic binaries already described in Section 4.1.3 (NGC 6819 W983, NGC 7245 W045, NGC 2539 W233, and NGC 2682 W224). The mean differences with each author are shown in Table 4.4.

We find good agreement with literature except for five stars:

i. IC 4756 W0081: we find a difference of 4.8 km s^{-1} with Valitova et al. (1990), and a difference of only 0.1 km s^{-1} with Mermilliod, Mayor, and Udry (2008). Given the small differences of the other stars in common with Valitova et al. (1990), we consider this case an outlier in this comparison and we exclude it to calculate the mean difference with these authors (Table 4.4). Our three individual measurements are taken within the same night (Table 4.2), so we cannot know if this star is a spectroscopic binary. A large set of measurements from Mermilliod, Mayor, and Udry (2008) do not show variability.

ii. NGC 188 W2051: there is a difference of 1.4 and 2.8 km s^{-1} with Friel, Jacobson, and Pilachowski (2010) and Geller et al. (2008), respectively. We see no hint of variable radial velocity in the 5 exposures taken between the 18-22 December 2014. It could be a large period spectroscopic binary.

iii. NGC 1907 W0062: we find a difference of 4.68 km s^{-1} with Glushkova and Rastorguev (1991). We have three other stars from the cluster NGC 1907 in common with these authors, with differences of: 0.53, 2.98, 1.35 km s^{-1}. Their uncertainties are of the order of 1 km s^{-1}. The mean difference with these

Table 4.3. Radial velocities (in km s^{-1}) of each cluster calculated as the median of the non-spectroscopic binaries and bona-fide member stars. The MAD is assigned as the uncertainty, the number of stars considered as members and used to derive the cluster radial velocity are written in parentheses. Other determinations of the cluster radial velocity are shown in column 3, and the reference is listed in column 5. Difference between OCCASO and literature is computed as $\Delta v = v_r - v_{r,lit}$.

Cluster	v_r	$v_{r,lit}$	$\Delta v_{r,lit}$	Reference
IC 4756	-24.7 ± 0.7 (7)	-25.0 ± 0.2 (15)	0.3	Valitova et al. (1990)
		-25.15 ± 0.17 (17)	0.45	Mermilliod, Mayor, and Udry (2008)
NGC 188	-41.8 ± 0.8 (6)	-42.4 ± 0.6 (473)	0.6	Geller et al. (2008)
NGC 752	5.6 ± 0.4 (7)	5.04 ± 0.08 (16)	0.56	Mermilliod, Mayor, and Udry (2008)
		4.82 ± 0.20 (10)	0.78	Böcek Topcu et al. (2015)
NGC 1817	65.7 ± 0.3 (5)	65.3 ± 0.5 (31)	0.4	Mermilliod, Mayor, and Udry (2008)
NGC 1907	2.3 ± 0.5 (5)	0.1 ± 1.8 (4)	2.2	Glushkova and Rastorguev (1991)
NGC 2099	8.6 ± 0.6 (7)	8.30 ± 0.20 (30)	0.3	Mermilliod, Mayor, and Udry (2008)
NGC 2420	73.7 ± 0.1 (7)	73.6 ± 0.6 (18)	0.1	Mermilliod, Mayor, and Udry (2008)
NGC 2539	29.4 ± 0.7 (5)	28.89 ± 0.21 (11)	0.51	Mermilliod, Mayor, and Udry (2008)
NGC 2682	33.9 ± 0.5 (7)	33.52 ± 0.29 (23)	0.38	Mermilliod, Mayor, and Udry (2008)
		33.73 ± 0.83 (110)	0.17	Pasquini et al. (2011)
		33.3 ± 0.6 (22)	0.6	Jacobson, Pilachowski, and Friel (2011)
		33.67 ± 0.09 (141)	0.23	Yadav et al. (2008)
		33.74 ± 0.12 (77)	0.16	Pasquini et al. (2012)
NGC 6633	-28.6 ± 0.3 (4)	-28.95 ± 0.09 (6)	0.35	Mermilliod, Mayor, and Udry (2008)
NGC 6705	34.5 ± 1.7 (7)	35.08 ± 0.32 (15)	-0.58	Mermilliod, Mayor, and Udry (2008)
		34.1 ± 1.5 (21)	0.4	Cantat-Gaudin et al. (2014b)
NGC 6791	-47.0 ± 1.7 (7)	-47.4 ± 1.1 (101)	0.4	Tofflemire et al. (2014)
NGC 6819	3.0 ± 0.5 (5)	2.45 ± 1.02 (566)	0.55	Milliman et al. (2014)
NGC 6939	-18.5 ± 0.5 (5)	-18.9 ± 0.9 (20)	0.4	Milone (1994)
NGC 6991	-12.3 ± 0.6 (6)	-	-	
NGC 7245	-74.0 ± 1.4 (5)	-65.3 ± 3.2 (5)	-8.7	Carrera et al. (2015)
NGC 7762	-45.7 ± 0.3 (5)	-46.5 ± 0.8 (8)	0.8	Carraro, Semenko, and Villanova (2016)
NGC 7789	-53.6 ± 0.6 (7)	-54.9 ± 0.9 (50)	1.3	Gim et al. (1998)
		-54.7 ± 1.3 (26)	1.1	Jacobson, Pilachowski, and Friel (2011)
		-54.6 ± 1.0 (29)	1.0	Overbeek et al. (2015)

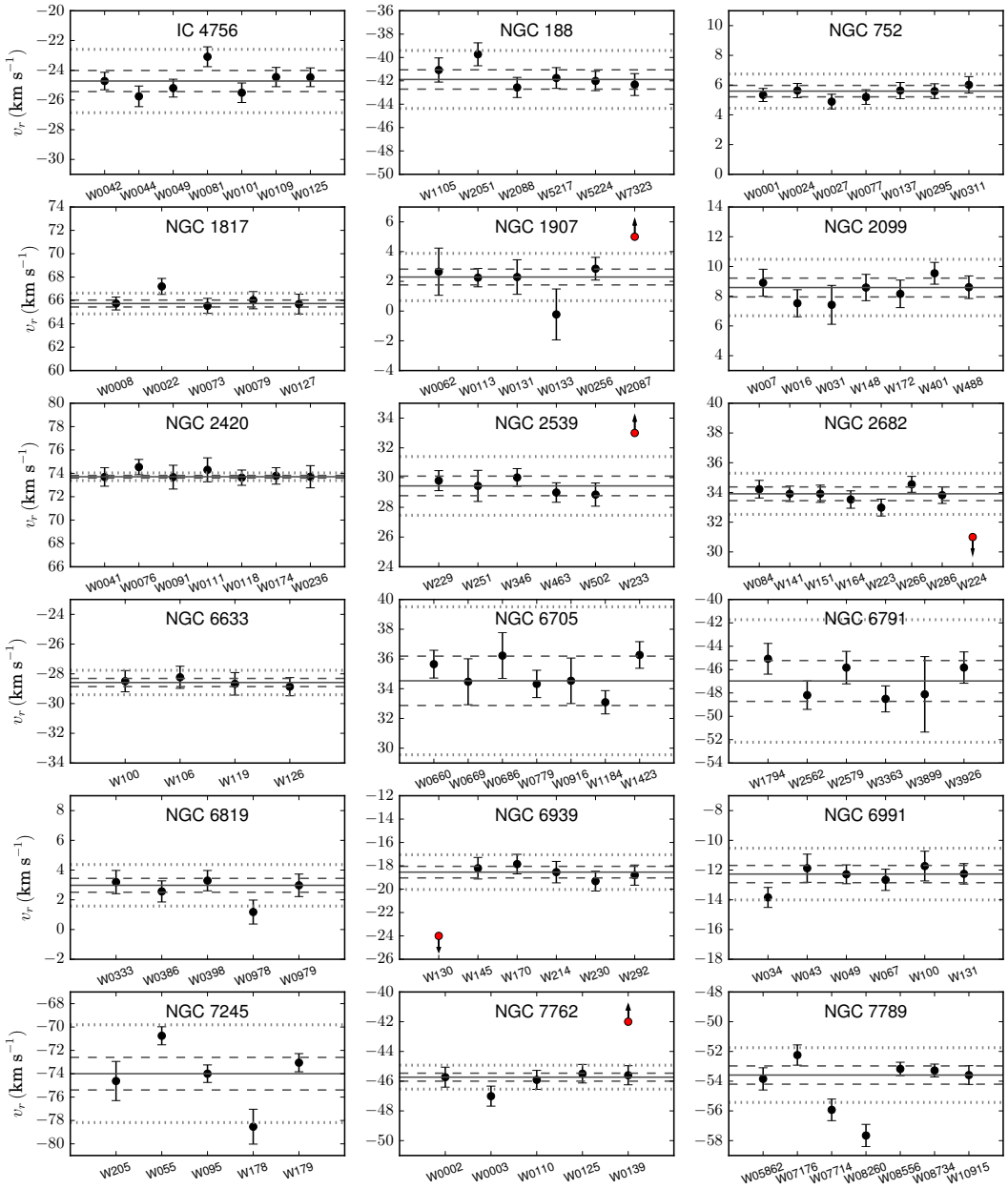

Figure 4.3. Radial velocities of the stars in the 18 open clusters. In red the stars considered as non members or spectroscopic binaries (see text). The arrow indicates that the point falls out of the plot limits. The solid line corresponds to the median radial velocity of the cluster (calculated with the considered member stars), the dashed lines correspond to the mean absolute deviation level 1MAD, and the dotted lines show the 3MAD level.

authors is large (2.4 ± 1.6 km s^{-1}), even if we do not consider the star W0062 (1.6 ± 1.0 km s^{-1}). Glushkova and Rastorguev (1991) reported large uncertainties in their final values due to large errors in the observational data.

iv. NGC 2682 W286: we find significant differences of 8.1 km s^{-1} and -5.1 km s^{-1} with Mermilliod, Mayor, and Udry (2008) and Pancino et al. (2010), respectively. Since we find differences smaller than 1 km s^{-1} for the same star with six other authors (Pasquini et al. 2011; Jacobson, Pilachowski, and Friel 2011; Pasquini et al. 2012; Alam et al. 2015; Mészáros et al. 2013; Mathieu et al. 1986), we consider this case as outlier, and we exclude it to calculate the mean difference with Mermilliod, Mayor, and Udry (2008) and Pancino et al. (2010) in Table 4.4.

v. NGC 6791 W2562: has quite a large difference of -2.7 km s^{-1} with Smolinski et al. (2011). Looking at our 6 individual exposures, which comprise two observational runs, we cannot see any variability. We point out that we obtain quite high offsets with this author.

vi. NGC 6791 W3899 has a compatible radial velocity with the other stars in this cluster. However, `DAOSPEC` finds a large line-by-line dispersion when calculating the radial velocity: 3.2 km s^{-1} compared with 1-2.3 km s^{-1} obtained with the other cluster stars. Also, the mean FWHM measured for its lines is significantly higher (13 pixels approximately), compared with the other stars 8.5-10 pixels. A cross-correlation done with `iSpec`, using a template shows two clear peaks, which indicates that it is probably an spectroscopic binary. We discard it in the abundance analysis.

vii. NGC 6819 W0333: there is a discrepancy of -2.11 km s^{-1} with Bragaglia et al. (2001), of 0.43 km s^{-1} with Milliman et al. (2014), and 8.8 km s^{-1} with Alam et al. (2015), which is the Data Release 12 of APOGEE. We find a difference of only 0.7 km s^{-1} with Mészáros et al. (2013), which is the Data Release 10. This star is reported to have "high persistency"[4] in the APOGEE detector by Alam et al. (2015). Given the low differences of the other stars in common, this effect could be the explanation for the discrepancy. From a set of 5 measurements Milliman et al. (2014) identify this star as single member.

viii. NGC 6819 W0978: there is a difference of -4.76 km s^{-1} with Bragaglia et al. (2001), and a small difference with the two APOGEE data releases, -0.4 and -0.1 km s^{-1}, respectively. Also we see a small difference of 0.41 km s^{-1} with Milliman et al. (2014), which identify this star as single member. Bragaglia et al. (2001) have used a spectral resolution of $R = 40,000$. They do not specify their errors, but they report that they were not interested in obtaining precise radial velocities.

4 The APOGEE detector suffers of the persistence effect, where the amount of charge deposited can be affected by the previous exposure. This is further explained in Nidever et al. (2015).

Table 4.4. Mean offsets and dispersions calculated for each author from the values in Table B.1. Offsets (second column) are in the direction OCCASO-literature, the number of stars for each paper is listed in the third column.

Reference	Δv_r(km s^{-1})	N
Mathieu et al. (1986)	0.2 ± 0.18	14
Valitova et al. (1990)[1]	0.3 ± 0.39	6
Glushkova and Rastorguev (1991)	2.16 ± 1.59	4
Milone (1994)	-0.08 ± 0.46	8
Gim et al. (1998)	0.35 ± 0.49	6
Bragaglia et al. (2001)	-0.47 ± 2.04	2
Carraro et al. (2006b)	0.28 ± 0.09	2
Geller et al. (2008)	0.6 ± 0.88	6
Mermilliod, Mayor, and Udry (2008)[2]	0.2 ± 1.11	52
Yadav et al. (2008)	0.0 ± 0.08	3
Friel, Jacobson, and Pilachowski (2010)	0.6 ± 0.77	2
Pancino et al. (2010)[3]	-0.9 ± 0.79	4
Jacobson, Pilachowski, and Friel (2011)	0.3 ± 0.35	28
Pasquini et al. (2011)	0.16 ± 0.36	7
Sakari et al. (2011)	0.0 ± 0.0	1
Smolinski et al. (2011)	0.85 ± 0.89	4
Pasquini et al. (2012)	0.15 ± 0.06	7
Reddy, Giridhar, and Lambert (2012)	-0.8 ± 0.3	2
Mészáros et al. (2013)	-0.21 ± 0.23	11
Reddy, Giridhar, and Lambert (2013)	0.3 ± 0.0	2
Blanco-Cuaresma et al. (2014b)	0.28 ± 0.09	2
Cantat-Gaudin et al. (2014b)	1.0 ± 0.21	6
Milliman et al. (2014)	0.43 ± 0.53	3
Alam et al. (2015)[4]	0.13 ± 0.32	10
Böcek Topcu et al. (2015)	0.57 ± 0.5	7
Geller, Latham, and Mathieu (2015)	0.11 ± 0.06	5

[1]excluded IC 4756 W0081, [2]excluded NGC 2682 W286, [3]excluded NGC 2682 W286, [4]excluded NGC 6819 W0333.

We can state that large differences are found for few specific authors and stars. Given that for the same stars we find compatible values with other authors, we do not interpret these discrepancies as due to binarity but some spurious measurements in the literature.

Arcturus and μ-Leo are compared with the values given by Blanco-Cuaresma et al. (2014b) for the GBS. These are two stars with very precise determination of the radial velocity because they are taken as standard stars for the *Gaia* mission wavelength calibration. We find a difference of 0.19 and 0.37 km s^{-1}, respectively. We also compare for the same stars with the results for the APOGEE Data Release 12 (Alam et al. 2015), which are -0.28 and 0.19 km s^{-1}, respectively. All differences are lower than our quoted uncertainties.

We compare the 6 stars in common with GES for the cluster NGC 6705 with Cantat-Gaudin et al. (2014b), finding a mean offset of 0.95 ± 0.21 km s^{-1}.

Besides, regarding APOGEE stars, we have 7 stars in common with Alam et al. (2015), and 8 stars in common with Mészáros et al. (2013). To make an overall comparison we do not take into account the star NGC 2682 W224 and NGC 6819 W0333 for the reasons already discussed. We find a mean offset of 0.06 ± 0.34 km s^{-1} with Alam et al. (2015), and -0.27 ± 0.25 km s^{-1} with Mészáros et al. (2013).

All the computed mean differences with literature estimates are listed in Table 4.4. The largest offset is found for Glushkova and Rastorguev (1991) and is already commented above. The mean of the differences with the other authors is 0.2 ± 0.9 km s^{-1}. This means that the accuracy with the overall literature is formally consistent with the quoted uncertainties.

4.2 KINEMATICS IN THE DISC CONTEXT

Galactic disc kinematics is one of the science topics of OCCASO. This section is devoted to an analysis using the 18 studied OCs. Our analysis here is limited to the range of Galactocentric distances of the 18 OCs, mainly in the range 8–10 kpc. Most of the OCs studied here are located in the vicinity of the Local arm. Seven of them in the Perseus arm, and only NGC 6705, is located in the Sagittarius arm (see Fig. 4.5).

4.2.1 *Radial velocity with respect to the Standards of Rest*

It is well known that the Galactocentric velocity of any source in the Galactic disc can be described using two components: (a) the velocity associated to a circular orbit around the Galactic center, constrained by the Galactocentric distance and defining the Regional Standard of Rest (RSR), and (b) an additional peculiar velocity, the velocity with respect to such RSR. The velocity with respect to RSR tells us how much the motion of the cluster differs from the Galactic disc rotation.

One can compute the velocity with respect to the Galactic Standard of Rest (GSR) by adding the spatial velocity of the Sun to the measured heliocentric velocity. This spatial velocity of the Sun is described in the same two components: its velocity with respect to the Local Standard of Rest (LSR), and the circular motion of the LSR. Considering only the line-of-sight component:

$$v_{GSR} = v_r + U_\odot \cos l \cos b + (\Theta_o + V_\odot) \sin l \cos b + W_\odot \sin b \tag{4.1}$$

where v_r is the heliocentric radial velocity, ($U_\odot$, $V_\odot$, $W_\odot$) are the components of the motion of the Sun with respect to the LSR, and Θ_0 is the circular velocity at the Galactocentric distance of the Sun R_0.

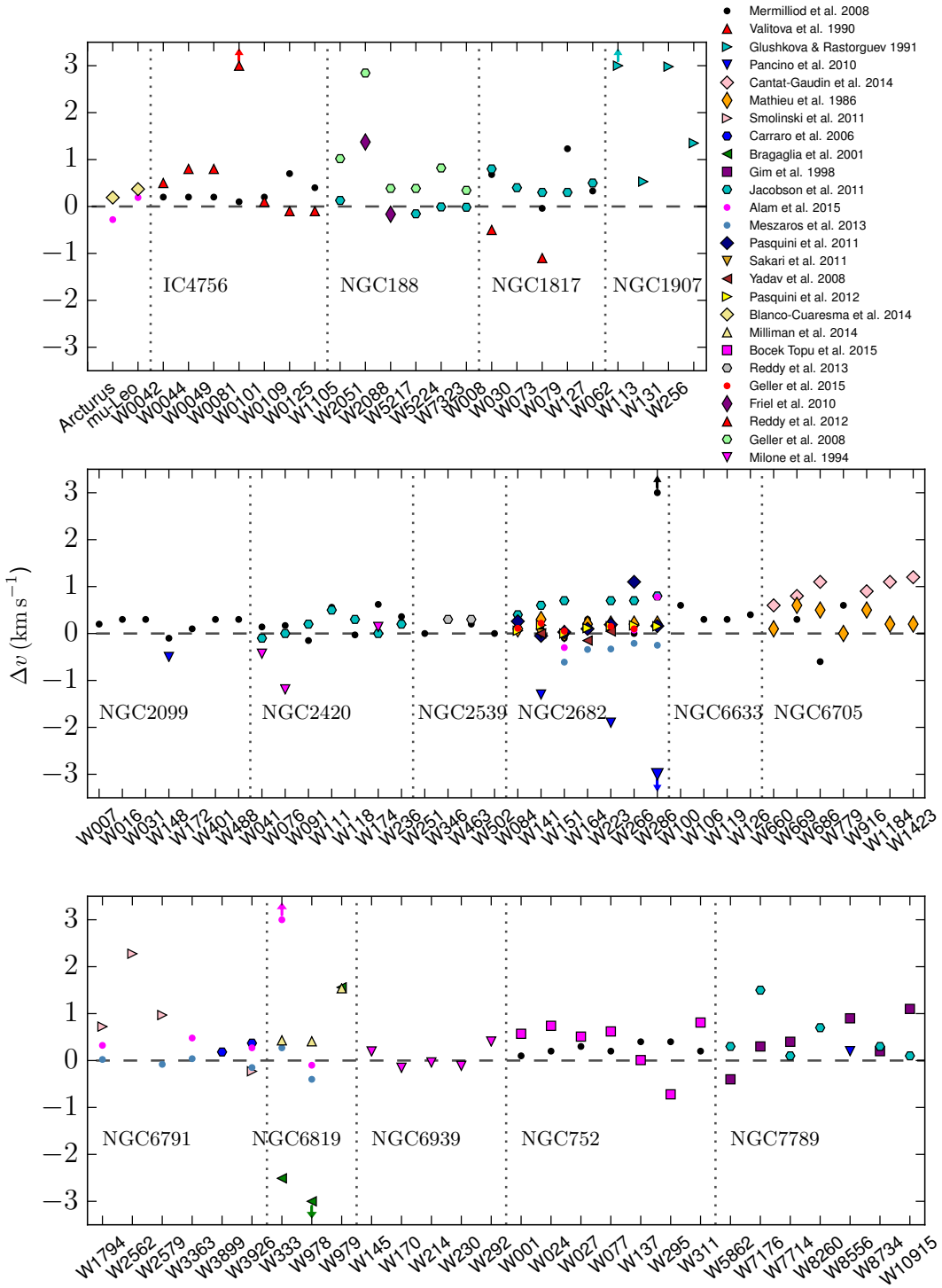

Figure 4.4. Radial velocity comparison with literature. Stars are grouped by cluster. Differences, in the direction OCCASO-literature, are plotted for each star. Different points in the same x-coordinate denote different literature values for the same star. Points out of the set y-limits are marked with an arrow. Possible spectroscopic binaries as explained in Section 4.1.3 are not plotted. Uncertainties are specified in Table B.1.

The line-of-sight velocity with respect to the RSR can be computed by subtracting the circular motion of the RSR projected onto the line-of-sight:

$$v_{RSR} = v_{GSR} - \Theta_R \frac{R_0}{R} \sin l \cos b \tag{4.2}$$

where Θ_R is the circular velocity at the Galactocentric distance of the cluster R. In first order aproximation (enough for the R of our clusters) Θ_R is computed as

$$\Theta_R = \Theta_o + \frac{d\Theta}{dR}(R - R_0) \tag{4.3}$$

Assuming the Sun motion derived by Reid et al. (2014)[5] ($U_\odot$, $V_\odot$, $W_\odot$)=(10.7, 15.6, 8.9) km s^{-1}, and their values of the Galactic rotation curve Θ_o = 240 km s^{-1}, R_0 = 8.34 kpc and $d\Theta/dR = -0.2$ km s^{-1}kpc^{-1}, we derive v_{GSR} and v_{RSR} for each cluster. Galactocentric distances R are computed from heliocentric distances in Dias et al. (2002)[6] (see Table 2.2). Since no error estimates are given for those distances, we adopted an uncertainty of 0.2 mag in distance modulus, rather typical when determining distances from isochrone fitting. The errors in v_{GSR} are computed taking into account errors in v_r, and the motion of the Sun: Θ_o, $U_\odot$, $V_\odot$, and $W_\odot$. The errors in v_{RSR} are computed taking into account also the errors in distance modulus.

Fig. 4.6 presents v_{GSR} as a function of Galactic longitude[7]. The values corresponding to circular orbits at different radii have been overplotted. There is a good correlation between the Galactocentric distance of each cluster and the corresponding circular orbits, meaning that line-of-sight v_{RSR} are small. The obtained values of v_{RSR} and v_{GSR} are listed in Table 4.5. The v_{RSR} are in the range of -64.5 to $+24.7$ km s^{-1}, typical values for the disc populations. Mean v_{RSR} of the ten clusters located in the Local arm is -6 km s^{-1} with an standard deviation of 17 km s^{-1}. Again, rather typical.

We have also computed v_{RSR} using different assumptions for the Galactic rotation and Sun's location taken from Antoja et al. (2011) and Sofue, Honma, and Omodaka (2009). The mean differences of v_{RSR} from the different assumptions are smaller than 0.4 km s^{-1}, well within uncertainties due to the errors in radial velocity and distances. Therefore, our v_{RSR} do not favour one or another Galactic rotation curve or location of the Sun.

4.2.2 *Spatial velocity with respect to RSR*

Cluster line-of-sight velocities were combined with proper motions to derive full spatial velocities. To do so, mean proper motions were taken from Dias et al. (2014) and are listed in Table 4.6. Dias et al. (2014) compared their mean proper motions

5 Values obtained by their model A5.
6 Available at http://irsa.ipac.caltech.edu
7 OCs at b > 15 deg (NGC 2682 and NGC 752) are not plotted since at these latitudes the line-of-sight component of the velocity is not in the Galactic plane.

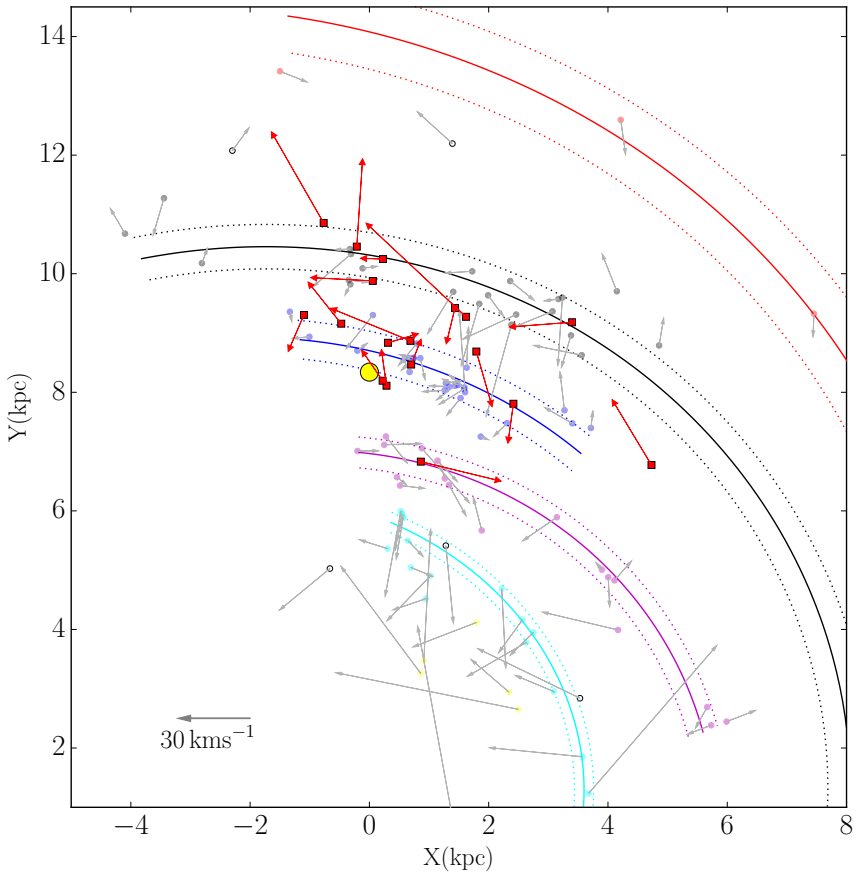

Figure 4.5. Spatial distribution of the 18 studied clusters (red squares). The Sun (big yellow circle) is at $(0, 8.34)$ kpc. The Galaxy's spiral arms positions and widths (coloured solid and dashed lines) are obtained from Reid et al. (2014). Coloured circles show the locations of High-Mass Star Forming Regions (HMSFR) studied in Reid et al. (2014). Circles are coloured according to the spiral arm to which are assigned to, as described in Reid et al. (2014). The arrows show the spatial velocity with respect to the RSR projected onto the plane for the HMSFR from Reid et al. (2014) (in grey), and for the OCs from this study (red).

Table 4.5. Radial projections of the velocities with respect to the RSR v_{RSR}, and the Galactic Standard of Rest v_{GSR}.

Cluster	v_{GSR} (km s^{-1})	v_{RSR} (km s^{-1})
Saggitarius arm:		
NGC 6705	151.9 ± 5.2	$24.7^{+3.3}_{-2.9}$
Local arm:		
IC 4756	123.8 ± 6.4	$-13.1^{+1.0}_{-1.1}$
NGC 752	142.1 ± 6.7	$10.7^{+0.6}_{-0.6}$
NGC 2539	-161.4 ± 8.4	$-5.6^{+1.7}_{-1.6}$
NGC 2682	-85.6 ± 5.4	$14.8^{+0.9}_{-0.8}$
NGC 6633	118.3 ± 6.3	$-15.2^{+0.5}_{-0.6}$
NGC 6791	195.3 ± 2.1	$-35.6^{+3.5}_{3.1}$
NGC 6819	230.8 ± 10.0	$12.2^{+0.8}_{-0.8}$
NGC 6939	230.7 ± 0.5	$-0.8^{+0.8}_{0.8}$
NGC 6991	223.6 ± 10.5	$3.8^{+0.7}_{-0.7}$
NGC 7762	156.7 ± 9.3	$-27.0^{+1.0}_{-1.1}$
Perseus arm:		
NGC 188	155.0 ± 0.8	$-59.8^{+1.1}_{1.0}$
NGC 1817	26.6 ± 0.3	$-59.4^{+0.4}_{0.4}$
NGC 1907	21.7 ± 2.5	$-1.2^{+1.2}_{-1.2}$
NGC 2099	7.9 ± 2.0	$0.2^{+0.7}_{-0.7}$
NGC 2420	-7.4 ± 0.1	$-56.3^{+1.1}_{1.1}$
NGC 7245	174.1 ± 1.4	$-64.5^{+1.5}_{1.6}$
NGC 7789	152.0 ± 9.6	$-24.0^{+2.6}_{-2.7}$

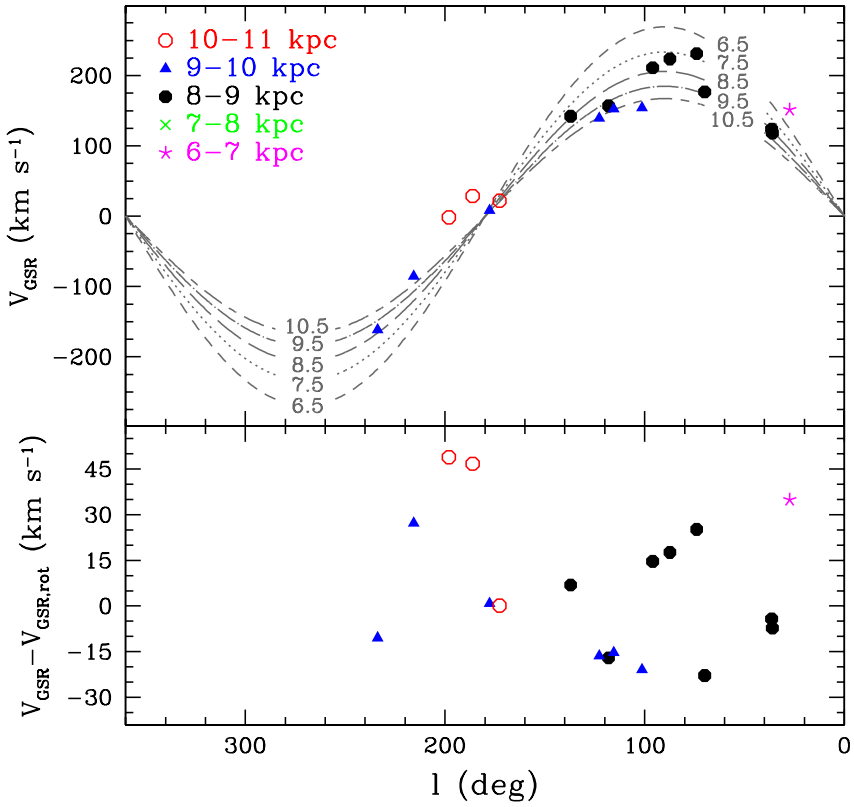

Figure 4.6. Upper panel: distribution of the studied clusters in the $l - v_{GSR}$ plane. The symbols change as a function of Galactocentric radius. v_{GSR} has been computed assuming ($U_\odot$, $V_\odot$, $W_\odot$)=(10.7, 15.6, 8.9) km s^{-1} and Θ_o=240 km s^{-1} from Reid et al. (2014). Lines represent circular orbits at different radii showing the rotation curve derived by Reid et al. (2014). Errors in v_{GSR} are not plotted since they are smaller than the point size (see Table 4.5). Lower pannel: differences between the velocities of the clusters with respect to the GSR and the circular velocity at the position of each cluster $v_{GSR} - v_{GSR,rot}$.

with other values in the literature and concluded that mean differences and standard deviation were among 1.4–1.7 mas yr^{-1}. We have assumed uncertainties of 1.5 mas yr^{-1} in each proper motion coordinate. The velocity with respect to RSR in a Cartesian Galactocentric frame, (U_s, V_s, W_s), was computed as (more details of the derivation in Reid et al. 2009):

$$\begin{pmatrix} U_s \\ V_s + \Theta_R \\ W_s \end{pmatrix} = R_z(-\beta) \left[\begin{pmatrix} U_\odot \\ V_\odot + \Theta_0 \\ W_\odot \end{pmatrix} + R_z(-l)\, R_y(b) \begin{pmatrix} v_r \\ D\,\mu_l \cos b \\ D\,\mu_b \end{pmatrix} \right] \tag{4.4}$$

where U_s points towards the Galactic Center, V_s towards Galactic rotation, and W_s towards the North Galactic Pole, R_z and R_y are rotations of a certain angle on the z and y axis respectively, β is the angle formed by Sun - Galactic Center - Cluster, μ_l and μ_b are the proper motions in the l, b directions.

The uncertainty has been derived from classical Markov chain Monte Carlo simulation with 10,000 random realizations for each cluster.

Taking the values from Table 4.6 we find mean values and standard deviations of $\langle U_s \rangle = -7 \pm 20\,\mathrm{km\ s^{-1}}$, $\langle V_s \rangle = 14 \pm 18\,\mathrm{km\ s^{-1}}$, $\langle W_s \rangle = 13 \pm 18\,\mathrm{km\ s^{-1}}$. Studies of velocity dispersions as a function of age such as Holmberg, Nordström, and Andersen (2009, fig. 7) indicate that for stars of ages $0.8 - 2.5$ Gyr we expect σ_U and σ_V between $15 - 25$ $\mathrm{km\ s^{-1}}$. So, this is well verified in our sample. There are only four OCs, NGC 6705, NGC 6819, NGC 7762 and NGC 7789, with velocities with respect to their RSR larger than about $30\,\mathrm{km\ s^{-1}}$ and are the ones with the larger errors. Particularly remarkable is NGC 6819 with a vertical velocity of $71.73 \pm 23.10\,\mathrm{km\ s^{-1}}$.

IC 4756 and NGC 6633, both in the Local arm, are located close together and have similar age and spatial non-circular velocity. Taken together, this may indicate some relationship in their formation. Better uncertainties in proper motions like the ones that *Gaia* will provide, and comparison of chemical abundances, (which is the main purpose of OCCASO) will clarify this issue.

Finally, in Fig. 4.5 we have plotted the spatial distribution of the 18 OC in the Galactic plane. The location of the spiral arms, as derived by Reid et al. (2014), and the (U_s, V_s) components for each cluster have been overplotted. HMSFR studied by Reid et al. (2014) are also included. We have calculated mean values and dispersions of the HMSFR $\langle U_s \rangle$, $\langle V_s \rangle$, $\langle W_s \rangle$ in each arm. And we have computed differences between the OC components and these mean values (see last three columns in Table 4.6), to see if there exists a hint of dynamical relationship between our OCs and the arms. In general, the differences fall inside the 3σ margin except for the clusters NGC 7789 (Perseus arm), NGC 7762 and NGC 6819 (Local arm), and NGC 6705 (Saggitarius arm). We do not find correlations with age, but our sample is limited in number. Again, precise proper motions of *Gaia* can help on the interpretation of the kinematics of the studied clusters.

4.3 ORBIT INTEGRATION

Using radial velocities calculated in Section 4.1.4 and proper motions from Dias et al. (2014) we reconstruct the orbit of the OCs and integrate backwards until the time of birth. We also reconstruct the orbits from 12 inner disc OCs in Jacobson et al. (2016) and 9 anticenter OCs from Cantat-Gaudin et al. (2016) (to analyse them as a whole sample in Section 7.2).

To do so one basically needs: 3D positions (l, b, and heliocentric distance d), 3D velocities (proper motions and radial velocity $\mu_\alpha \cos\delta$, μ_δ, v_r), and to assume a certain gravitational potential for the Milky Way[8]. This method can carry large uncertainties: (i) errors coming from the assumed distances, motions and age; (ii) inaccuracies the assumed model of the gravitational potential, (e. g. axisymmetric, featuring the bar and/or spiral arms), and the free parameters involved in them; (iii) for the old OCs the assumption of a static model of the potential is not a correct approximation taking into account that typical pattern speeds of the dynamic structures can change in few Gyr.

We have computed orbits of the 37[9] OCs analyzed in the previous section. Proper motions of Jacobson et al. (2016) OCs are from Dias et al. (2002), and radial velocities from Jacobson et al. (2016). Proper motions and radial velocities of the 9 anticentre OCs are those calculated by Cantat-Gaudin et al. (2016) (from the MWSC catalogue Kharchenko et al. 2013).

To integrate the orbit back in time we have assumed two gravitational potentials: an axisymmetric model (Allen and Santillan 1991), and a model that includes Galactic bar and spiral arms resembling those of the Milky Way. We employ the prolate bar model from Pichardo, Martos, and Moreno (2004) with a pattern speed of 46 km s^{-1} kpc^{-1} from the determination of Antoja et al. (2014), a mass of 9.84×10^9 $M_\odot$ and an orientation with respect to the Sun of 20 deg. The spiral arms are the ones from the PERLAS model in Pichardo et al. (2003) with a pattern speed of 18 km s^{-1} kpc^{-1}, the locus of Drimmel and Spergel (2001) and a mass of 3.42×10^9 $M_\odot$ (that is 0.04 times the disc mass). We refer to the cited references for details of the model and of the parameters that best fit the Milky Way.

We show the projection of the orbits to the Galactic disc plane in Figs. 4.7 and 4.8 for the axisymmetric potential, and in Figs. 4.9 and 4.10 for the potential that features bar and spiral arms. The orbits of OCCASO clusters set are relatively circular in both assumed gravitational potentials. NGC 2682, NGC 6791, NGC 6819, NGC 6991 and NGC 7762 describe orbits with a larger spread of galactocentric radius with the non-axisymmetric potential than with the axisymmetric one. NGC 7789 show a larger eccentricity with the non-axisymmetric potential than with the axisymmetric one.

8 Other parameters are needed like Sun position and velocity, Galactic rotation, among others

9 From the 40 OCs, 2 are the common ones between Jacobson et al. (2016) and OCCASO, and from the 10 anticenter OCs Ruprecht 7 from Cantat-Gaudin et al. (2016) does not have proper motions in the literature

The OCs from Jacobson et al. (2016) show orbits relatively circular like the OCCASO clusters, without big differences in the comparison of the results from the two potentials. The outer clusters of Cantat-Gaudin et al. (2016) have orbits with large eccentricities (except Rup 4 and Tom 2) and large inclinations (except Rup 4) above the Galactic plane. For those clusters, a small error in the estimation of the ages translates into large uncertainties in the location of the birth place.

We have compared the birth and current positions (Galactocentric radius and height above the plane) of this set of clusters in Fig. 4.11. The clusters with high eccentricity and high inclination (Be 20, Be 22, Be 29, Be 66, Be 73, Be 75, Sau 1 and Tom 2) are not included due to the large uncertainty mentioned. The mean and standard deviation of the differences $R_{birth,non-a} - R_{birth,a}$ is of -0.2 ± 0.6 kpc with no dependence on age, current or birth positions.

There are seventeen clusters for which the current and birth Galactocentric radius do not differ more than 0.5 kpc. Those that show the largest migration outwards are NGC 2099, NGC 7245. They have current Galactocentric positions at $\sim$ 10 kpc with a birth radius of $\sim 7-8$ kpc in both axisymmetric and non-axisymmetric models. Being relatively young ($\sim$ 0.4 Gyr) the assumption of a static potential is not an issue. The migration inwards (by $2-3$ kpc) in both potentials is experimented by Be 8 and Tr 20, with ages of 0.9 and 1.5 Gyr. The staticity of the potential can still be assumed. The most critical elements in all these cases are probably the uncertainty in the age and the accuracy of the proper motions. NGC 188, NGC 2682 and NGC 7762 also migrate outwards according to the two potentials, but their ages range $2.5-6$ Gyr and the potentials may have changed during their life. NGC 752 experiments a modest migration inwards of $0.6-0.8$ kpc, depending on the potential. Its age is of 1.2 Gyr.

NGC 3532, NGC 4815, NGC 6791 and NGC 6819 suffer migration inwards/outwards or no -migration depending on the assumed potential. NGC 6791 is the oldest cluster in OCCASO sample with and age of 10 Gyr, which makes any prediction fully uncertain. On the other hand, NGC 3532 is relatively young (0.3 Gyr) and it does not migrate according to the axisymmetric potential and migrates inwards by 0.7 kpc in the non-axisymmetric case.

4.4 CONCLUSIONS

The radial velocity analysis has been performed for 115 stars in 18 OCs. We have derived radial velocities from 401 individual exposures. With these values we have found two new possible spectroscopic binaries NGC 6819 W983 and NGC 7245 W045, which have never been identified as multiple systems. We have derived radial velocities from the combined spectra with SNR$\geqslant$ 70, obtaining uncertainties of $0.5-0.9\,\mathrm{km\ s^{-1}}$. We have used these values of the radial velocities to confirm or discard membership from our sample of stars and compute a median radial velocity for each OC. In particular, we have obtained radial velocities for OCs never studied before with high-resolution

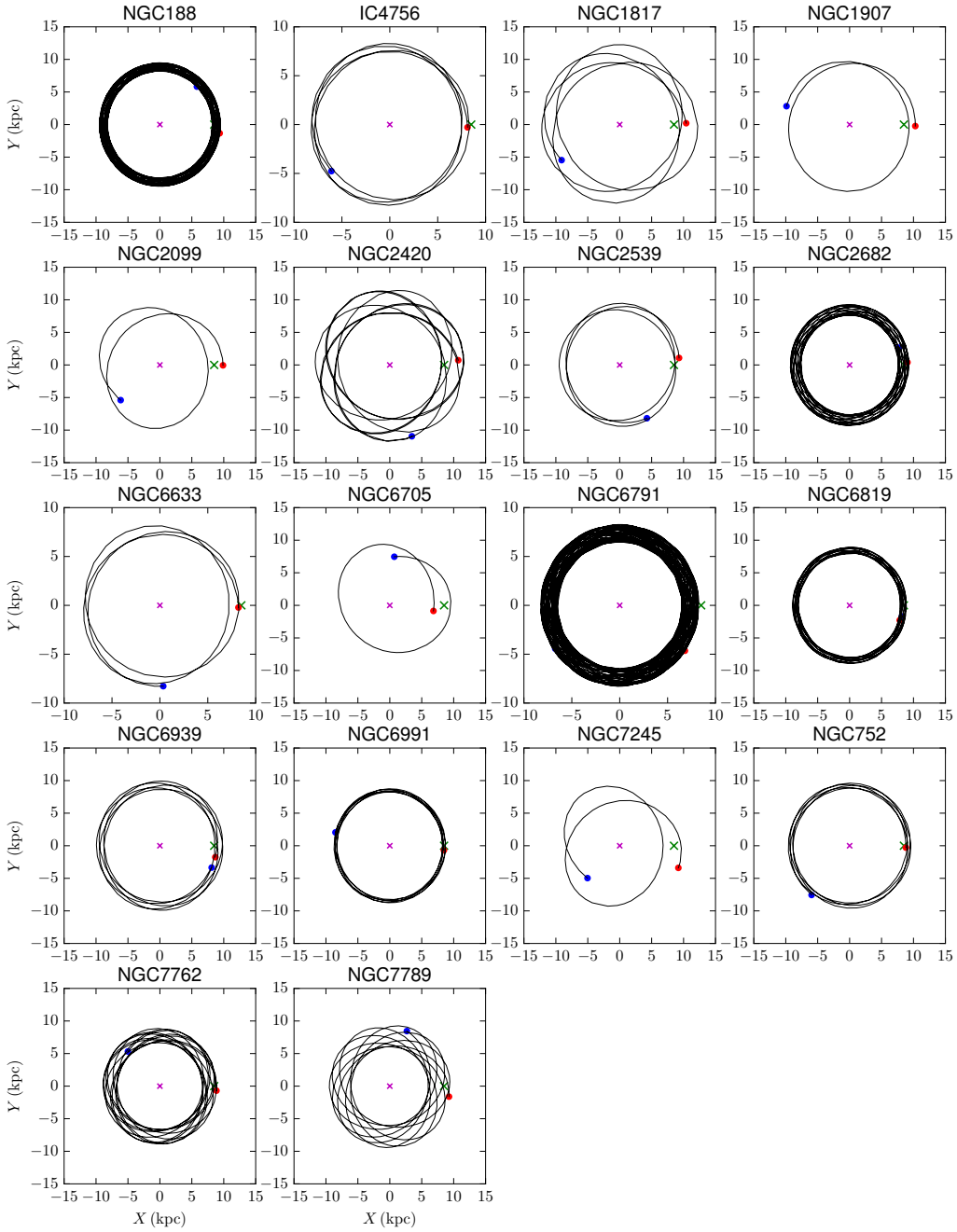

Figure 4.7. 2D projection onto the Galactic disc plane of the OCCASO OCs. The Galactic center and the Sun position are indicated with a violet and green crosses, respectively. The present day and birth positions are indicated with a red and blue dots, respectively.

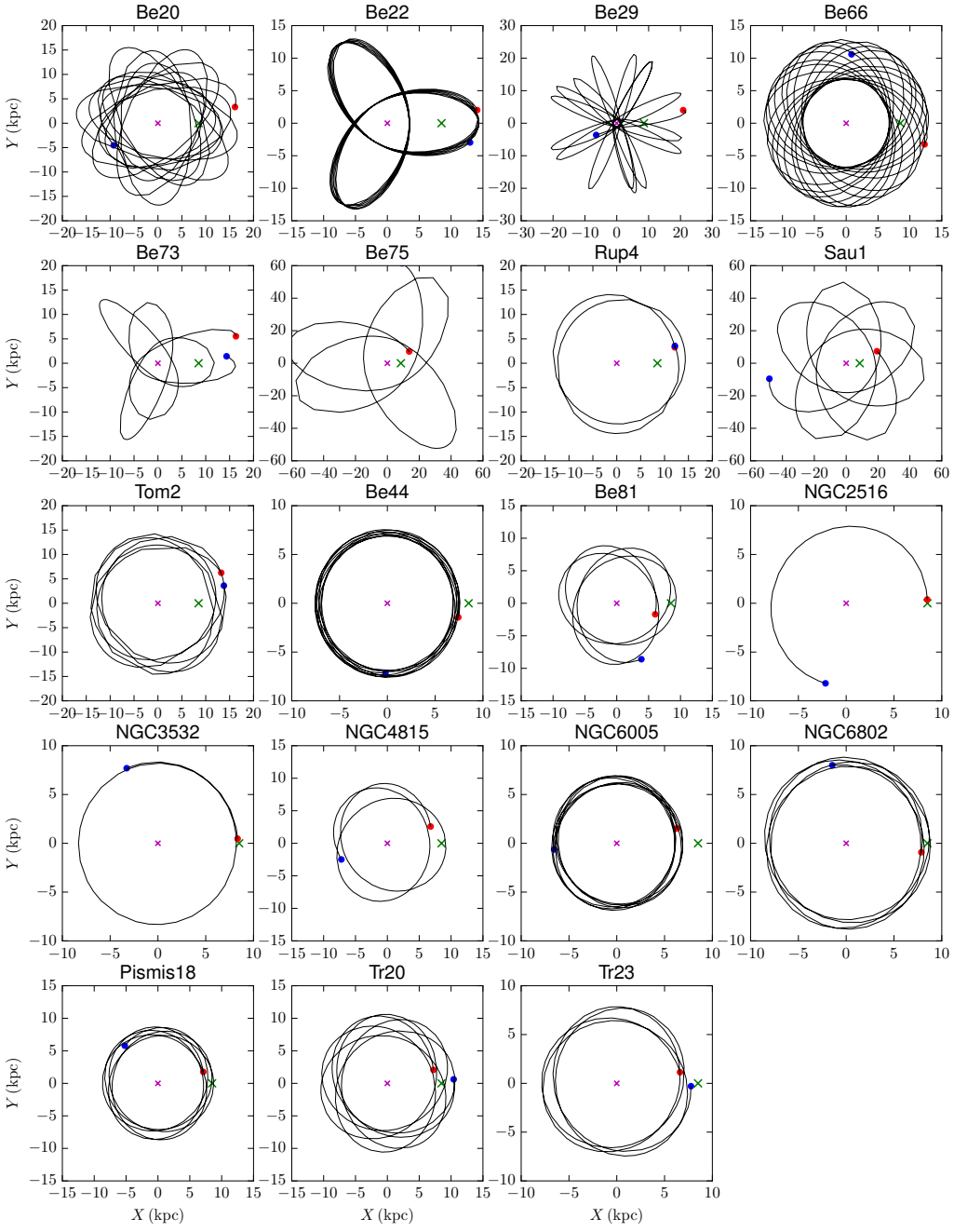

Figure 4.8. 2D projection onto the Galactic disc plane of the inner and anticenter OCs. Symbols are the same as in Fig. 4.7.

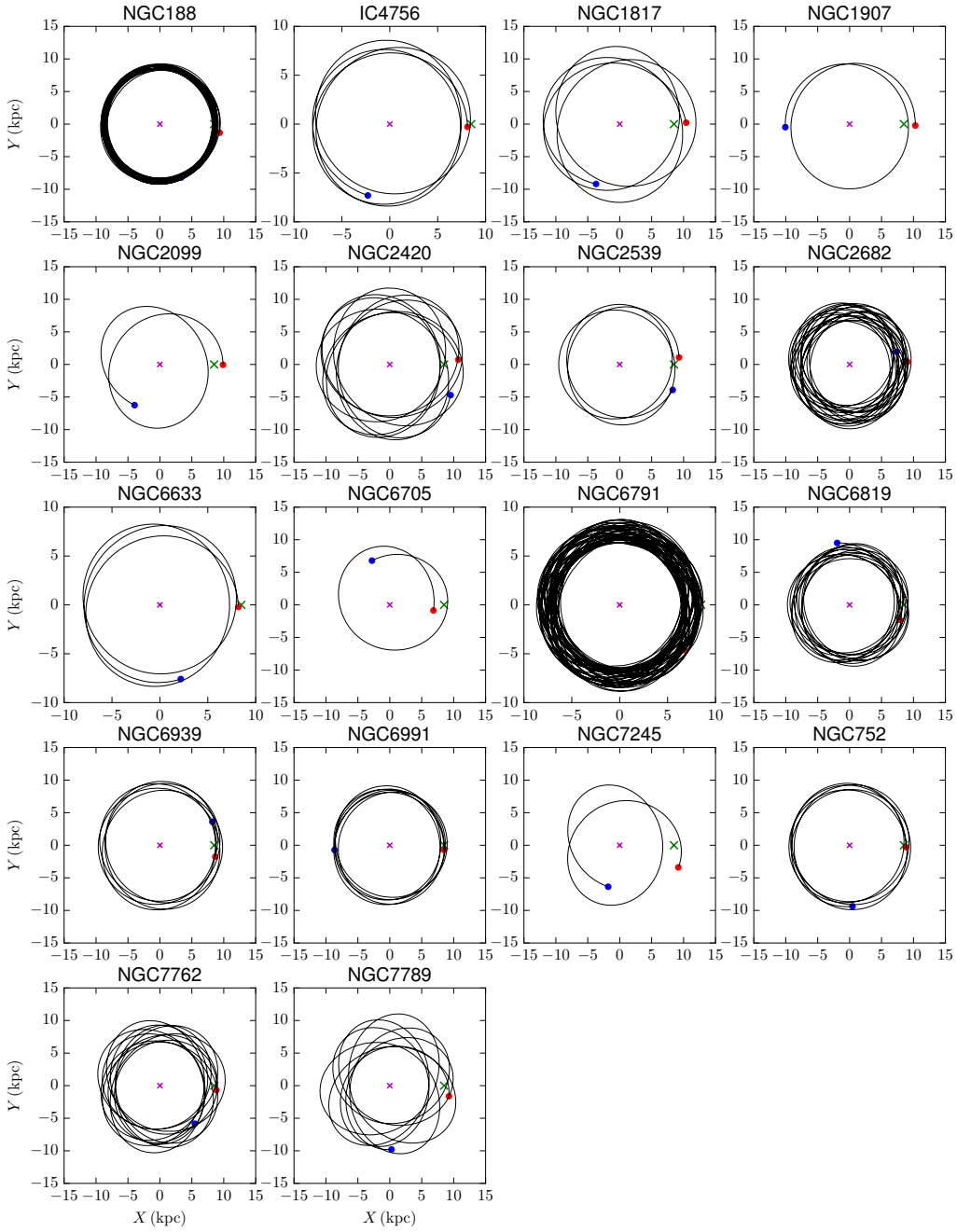

Figure 4.9. The same as in Fig. 4.7 with the non-axisymmetric model.

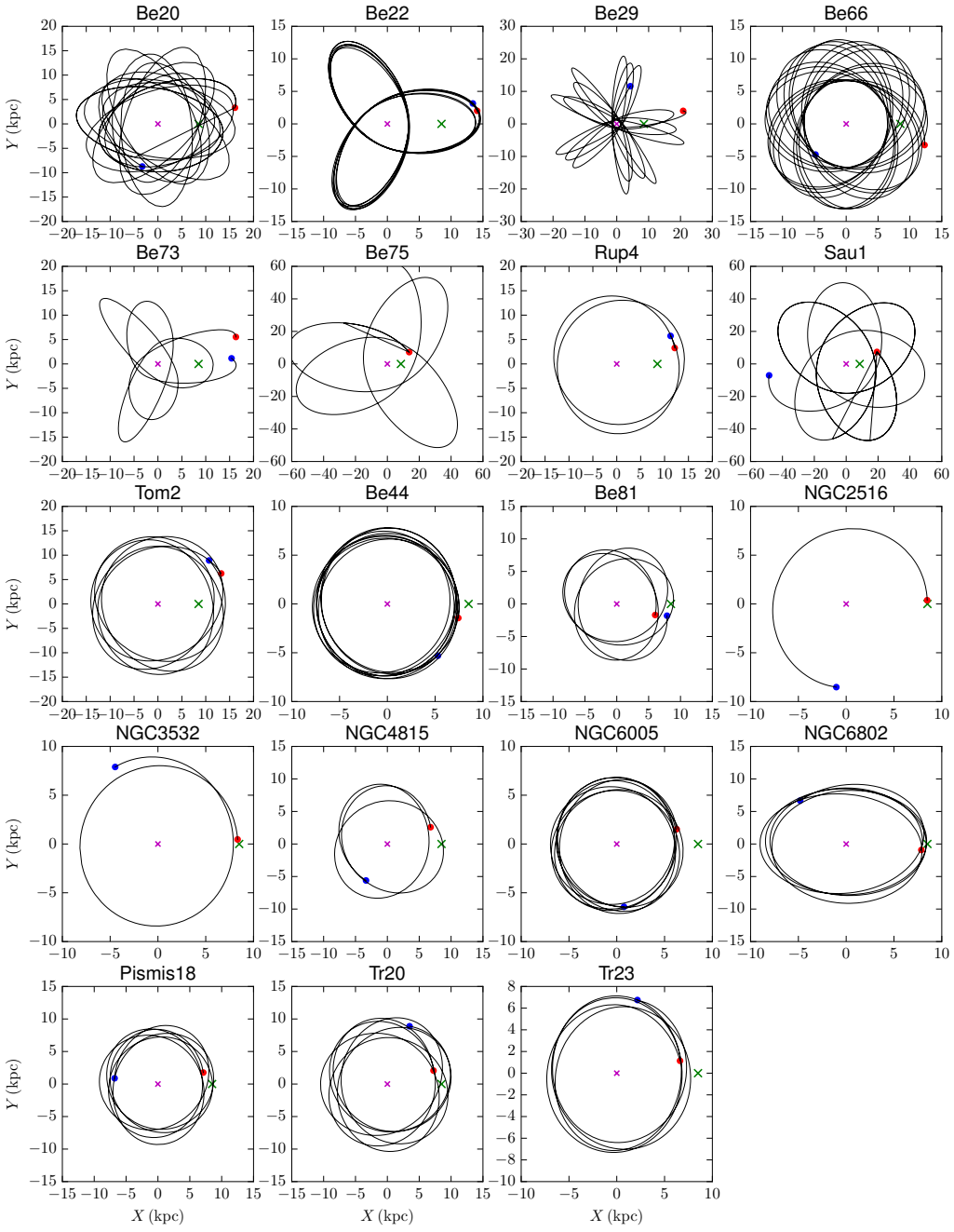

Figure 4.10. The same as in Fig. 4.8 with the non-axisymmetric model.

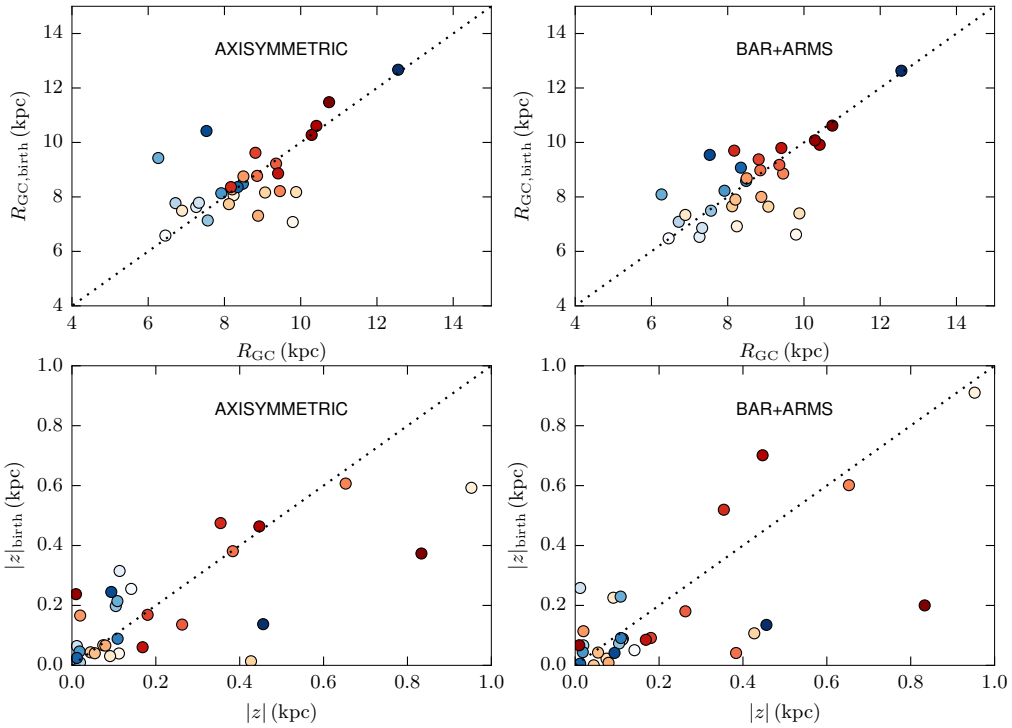

Figure 4.11. Top: birth Galactocentric radius vs current one from the axisymmetric model (left) and the one that includes bar and spiral arms (right). Bottom: the same but for height above the plane. The red set of colors are for OCCASO clusters color-coded by age (light to dark red: from young to old). The same for the blue set of colors which stand for the other clusters from (Cantat-Gaudin et al. 2016; Jacobson et al. 2016, see text).

spectroscopy: NGC 1907 ($v_r = 2.3 \pm 0.5$ km s^{-1}), NGC 6991 ($v_r = -12.3 \pm 0.6$ km s^{-1}) and NGC 7245 ($v_r = -74.0 \pm 1.4$ km s^{-1}).

The radial velocities obtained here agree with the values from previous authors within the uncertainties, except for few cases. We have compared the stars in common with other two large spectroscopic surveys: GES, 6 stars in common with an average difference of $\Delta v_r = 0.95 \pm 0.21$ km s^{-1}; and APOGEE, 7 stars in common with Mészáros et al. (2013) a mean difference $\Delta v_r = -0.27 \pm 0.25$ km s^{-1}, and 7 stars in common with Alam et al. (2015) a mean difference of $\Delta v_r = 0.06 \pm 0.34$ km s^{-1}.

Median radial velocities for each OC have been used to study their kinematics in relation to the disc and the spiral arms. It is shown that all of the studied clusters follow the expected rotation of the Milky Way assuming the rotation curve derived by Reid et al. (2014).

Adding information of proper motions from Dias et al. (2002) we have derived full spatial velocities, and we have compared the non-circular velocities among them. There seems to be no clear relation of the peculiar velocities among the OCs from the same spiral arm (except for IC 4756 and NGC 6633), nor with the peculiar velocities of the high-mass star-forming regions (Reid et al. 2014) from the same arms. From our sample we calculate the dispersion in the two components of the plane velocity: σ_U and $\sigma_V = 20$ and 18 km s^{-1}, which is expected for a population of ages 0.8–2.5 Gyr as seen in Holmberg, Nordström, and Andersen (2009).

We have used radial velocities from OCCASO and proper motions from the literature to integrate back in time the orbits of the OCs using two gravitational potentials for the Milky Way: an axisymmetric model, and a model featuring the bar and the spiral arms. We have also done this process for 19 OCs in the inner disc and the anticenter direction. We have recovered the birth radius R_{GC} and the height above the plane z to be analysed in Chapter 7.

Table 4.6. U_s, V_s and W_s are the components of the non-circular velocity at the position of each cluster. These are computed from proper motions (Dias et al. 2014) and our radial velocities, using the values for the motion of the Sun with respect to the LSR from Reid et al. (2014). Mean values and dispersions of the non-circular velocity for the HMSFR studied by Reid et al. (2014) are indicated for each arm. The last three columns list the differences in the direction OCCASO - ⟨HMSFR⟩.

Cluster	$\mu_\alpha \cos\delta$ (mas yr^{-1})	μ_δ (mas yr^{-1})	U_s (km s^{-1})	V_s (km s^{-1})	W_s (km s^{-1})	ΔU_s (km s^{-1})	ΔV_s (km s^{-1})	ΔW_s (km s^{-1})
		Saggitarius arm:	4.18 ± 9.99	2.89 ± 11.31	-4.03 ± 6.41			
NGC 6705	-1.23	1.31	3.7 ± 7.8	39.1 ± 11.1	22.4 ± 13.6	-0.5	36.2	26.4
		Local arm:	-0.72 ± 10.12	-4.27 ± 4.48	1.58 ± 8.57			
IC 4756	-0.60	-1.69	-15.1 ± 2.2	-2.7 ± 2.7	6.1 ± 3.4	-15.8	1.5	4.5
NGC 752	1.81	-3.90	-4.2 ± 2.9	12.1 ± 3.1	0.4 ± 3.1	-4.9	16.3	-1.1
NGC 2539	-3.20	-1.24	14.8 ± 7.4	-8.5 ± 6.8	-7.4 ± 9.9	14.0	-4.2	-8.9
NGC 2682	-9.40	-4.87	-19.3 ± 4.4	-14.0 ± 5.2	-8.3 ± 5.9	-20.0	-9.7	-9.8
NGC 6633	-2.27	-4.95	-12.7 ± 1.7	-9.1 ± 2.2	4.4 ± 2.6	-13.4	-4.8	2.8
NGC 6791	-0.83	-4.91	-14.5 ± 11.5	-32.4 ± 4.1	-28.2 ± 5.3	-15.2	-28.1	-29.7
NGC 6819	-6.07	-3.57	17.1 ± 21.0	2.6 ± 3.3	71.7 ± 23.1	16.3	6.8	70.1
NGC 6939	-2.37	-5.29	23.0 ± 5.4	11.9 ± 1.6	13.3 ± 1.5	22.2	16.1	11.7
NGC 6991	-1.50	1.94	-10.4 ± 6.0	3.0 ± 0.6	18.4 ± 6.5	-11.1	7.2	16.8
NGC 7762	3.44	-2.21	-10.4 ± 12.8	-38.5 ± 7.9	-10.3 ± 6.3	-11.1	-34.2	-11.8
		Perseus arm:	6.96 ± 14.07	-3.92 ± 11.55	-4.14 ± 8.15			
NGC 188	-0.21	0.17	15.6 ± 16.6	-1.4 ± 14.0	-5.0 ± 1.6	8.6	2.52	-0.86
NGC 1817	-1.79	-2.17	-41.4 ± 0.7	3.5 ± 1.1	-31.2 ± 2.5	-48.3	7.42	-27.06
NGC 1907	-0.85	-4.22	-0.0 ± 1.5	-7.9 ± 13.6	-17.8 ± 14.9	-6.9	-3.98	-13.66
NGC 2099	2.08	-6.40	-1.3 ± 0.9	-28.2 ± 11.2	1.7 ± 11.2	-8.2	-24.28	5.84
NGC 2420	-1.76	-2.38	-45.1 ± 0.5	-21.7 ± 1.8	4.0 ± 2.7	-52.0	-17.78	8.14
NGC 7245	-1.98	-1.76	12.1 ± 7.4	-26.0 ± 4.8	18.8 ± 5.2	5.1	-22.08	22.94
NGC 7789	2.86	-0.74	-36.5 ± 18.8	-55.5 ± 13.9	-1.6 ± 13.4	-43.4	-51.58	2.54

5

ATMOSPHERIC PARAMETERS

This chapter describes the determination of the atmospheric parameters from high resolution spectra for the stars belonging to 18 OCs in OCCASO, plus Arcturus and μ-Leo as reference. We also calculate T_{eff}, log g and [Fe/H] for a set of GBS for comparison. The content of this chapter corresponds to Casamiquela et al. (2017).

In Section 5.1 we summarize the analysis strategy: used linelist, adopted model atmospheres, and analysis methods, and in Section 5.2 we describe the results and associated uncertainties of the two used methods, in Section 5.3 we compare the results with the values derived from photometry, and in Section 5.4 we describe the final values of the atmospheric parameters adopted and we compare with previous values in the literature.

5.1 DERIVATION FROM SPECTROSCOPY

The final goal of OCCASO is to calculate detailed abundances from the spectra. The high-resolution and large wavelength coverage of the spectra allows for the determination of a large number of astrophysical quantities: effective temperature (T_{eff}), surface gravity (log g), microturbulence (ξ), overall stellar metallicity [M/H], and individual abundances for more than 30 chemical species. The adopted procedure is to first determine atmospheric parameters: T_{eff}, log g, ξ and [M/H], and then derive individual abundances from a fixed model atmosphere for each line/species. We use the two methods described below. This determination is a key point in any spectroscopic analysis, since inaccurate atmospheric parameters unavoidably introduce biases in the derived chemical abundances.

5.1.1 *Linelist*

We have used the GES linelist which is a compilation of experimental and theoretical atomic and molecular data that is being updated and improved regularly. It is convenient for our study because it covers the wavelength range of our instruments, it has been extensively used in the literature, and its atomic parameters are recent. Details of this compilation and the full linelist are provided in Heiter et al. (2015a).

In this thesis, we have used version 5, which covers a wavelength range between $4200 \leqslant \lambda \leqslant 9200$ Å. Collisional broadening by hydrogen is treated considering the theory by Anstee, Barklem and O'Mara (Anstee and O'Mara 1991; Barklem and O'Mara 1998). It contains atomic information for 35 different chemical species: Li, C, N, Al, K and Na (light and odd-Z elements); Mg, O, Si, S, Ca and Ti (α-elements); Sc, V, Cr, Mn, Fe, Co and Ni (Fe-peak elements); Cu and Zn (p-process elements); Rb, Sr, Y, Zr, Ba and La (s-process elements); Sm, Eu , Ru, Mo and Dy (r-process elements); and other neutron capture elements like Ce, Pr and Nd.

5.1.2 *Model atmospheres*

We adopted the MARCS grid[1] model atmospheres of Gustafsson et al. (2008). It is an extensive grid of 10^4 spherically-symmetric models (supplemented with plane-parallel for the highest surface gravities) for stars with $2500 \leqslant T_{\rm eff} \leqslant 8000$ K, $0 \leqslant \log g \leqslant 5$ (cgs) with various masses and radii, and $-5 \leqslant [M/H] \leqslant +1$. Underlying assumptions in addition to 1D stratification (spherical or plane-parallel) include hydrostatic equilibrium, mixing-length convection and LTE. The standard MARCS models assume Solar abundances of Grevesse, Asplund, and Sauval (2007) and α—enhancement at low metallicities.

5.1.3 *Analysis methods*

There are two state-of-the-art methodologies currently employed in the literature: EW and Spectral Synthesis (SS). We use these two approaches to determine atmospheric parameters and abundances. The strategy of applying multiple pipelines to determine atmospheric parameters and abundances is applied in other surveys such as the GES (Gilmore et al. 2012), as explained in Smiljanic et al. (2014). This strategy has the advantage that allows the investigation of method-dependent effects, different sources of uncertainty, and provides an estimation of up to which level derived absolute parameters and abundances can be trusted.

Both methods run independently on the same spectra, with the common master linelist and model atmospheres to guarantee internal consistency. Although the master linelist is the same, each method chooses independently the most suitable lines (see the details of this choice in the next subsections).

EW: DAOSPEC+GALA

`DAOSPEC+GALA` is our EW method. It consists in two steps performed by two different codes. First, EWs are measured using `DOOp` (Cantat-Gaudin et al. 2014a) which is an automatic wrapper for `DAOSPEC` (Stetson and Pancino 2008) (see Section 4.1, for details).

1 http://marcs.astro.uu.se/

The determination of the atmospheric parameters is done with the GALA code (Mucciarelli et al. 2013). It is based on the set of Kurucz abundance calculation codes (Kurucz 2005; Sbordone et al. 2004). GALA optimizes atmospheric parameters (T_{eff}, log g, ξ, [M/H]) using the classical spectroscopic method based on iron lines. The T_{eff} is optimized by minimizing the slope of the iron abundance versus excitation potential. The difference of abundances between neutral iron Fe I and ionised iron Fe II lines is used to constrain the surface gravity. The angular coefficient in the iron abundance-EW is used to optimize the microturbulence. And the average Fe abundance to constrain the global metallicity of the model. GALA measures the line abundances and performs a rejection of lines of the same chemical species using a threshold on too weak or too strong lines (we use $-5.9 \lesssim \log(^{EW}/_{\lambda}) \lesssim -4.7$), a limit in the EW error measured by DAOSPEC (we choose $\sim 15\%$ depending on the SNR of the star), and finally performing a σ clipping rejection in abundance (we choose 2.5σ). An example of an output from GALA can be seen in Fig. 5.1.

The linelist used for EW is cleaned to have a selection of lines that provide consistent abundances, and get rid of blends or lines with bad atomic parameters. This is done in two steps. Firstly, Fe I and Fe II lines detected by DAOSPEC in less than three stars are rejected. This provides a better determination of the FWHM and the continuum placement. Afterwards, Fe I and Fe II lines that are rejected by GALA in all the stars, or that give systematically discrepant abundances with respect to the mean Fe abundance are discarded. This procedure is also done a posteriori when calculating abundances of other chemical species, to obtain robust mean abundances.

SS: iSpec

iSpec (Blanco-Cuaresma et al. 2014a) is a tool that can be used to perform spectroscopic operation such as determine or correct radial velocities, normalize and degrade the spectral resolution. And more importantly, it also offers the possibility to derive atmospheric parameters and chemical abundances by using the EW method and the SS fitting technique with many different atomic line lists, model atmosphere and radiative transfer codes.

In this work, iSpec was used to prepare the custom library of GBS (as described in Section 3.2.2) and a customized pipeline was developed to analyse OCCASO targets using the synthetic spectral fitting technique. iSpec compares regions of the observed spectrum with synthetic ones generated on-the-fly. A least-square algorithm minimizes the differences between the synthetic and observed spectra until it converges into a final set of atmospheric parameters.

In the analysis by iSpec, the line selection is done based on the automatic detection of absorption lines in the NARVAL Solar spectrum included in the GBS. Each line is cross-matched with the atomic line list and we derive line-by-line chemical abundances using the reference atmospheric parameters for the Sun. Good lines will lead to abundances similar to the Solar ones (i.e. Grevesse, Asplund, and Sauval 2007), thus

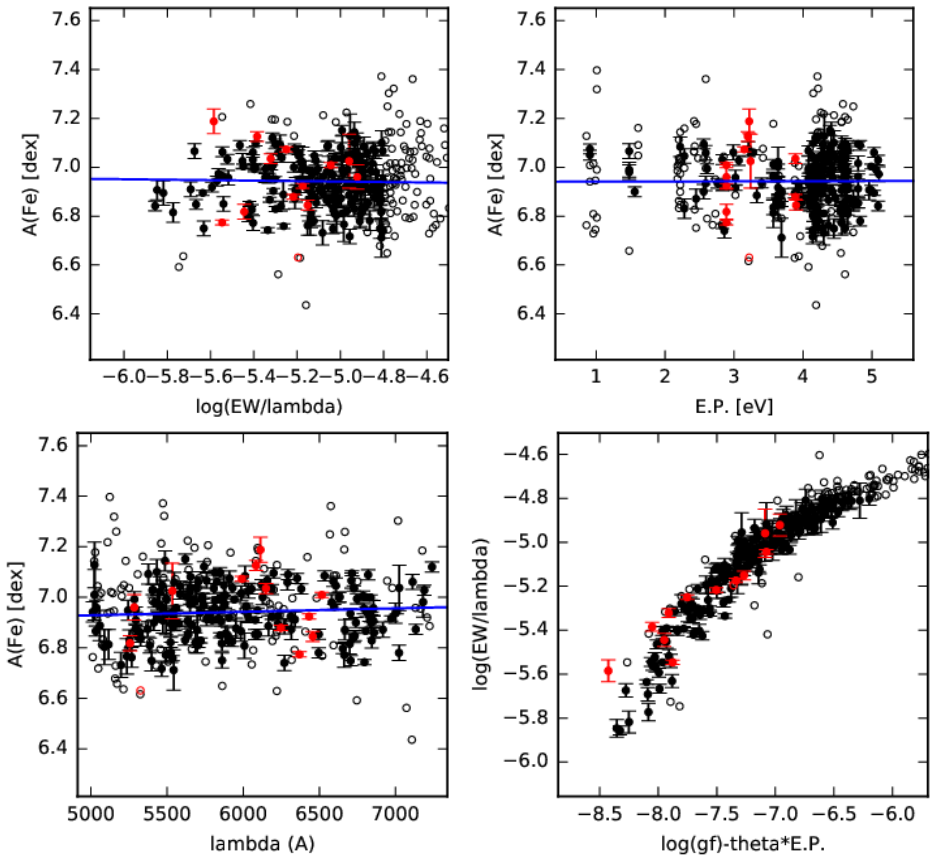

Figure 5.1. Example of the optimization done by GALA following the classical spectroscopic method based on Fe I (black symbols) and Fe II lines (red symbols). Empty symbols are the lines rejected after the iterative process. Top right: abundance as a function of excitation potential to constrain T_{eff}, top left: abundance as a function of reduced EW to constrain ξ, bottom right: empirical curve of growth that relates reduced EW vs a theoretical optical depth (*theta*= $1/T_{eff}$), bottom left: abundance as a function of wavelength.

we select all lines with an abundance that falls in the range ±0.05 dex. Additionally, in our analysis we use the wings of Hα/β and Mg triplet, which helps us to break degeneracies of the parameters in the abundance determination.

5.2 RESULTS FROM EACH METHOD

Both methods have analysed the full OCCASO dataset of 154 spectra letting all the atmospheric parameters free. Fig. 5.2 shows the comparison of the resulting T_{eff} and log g with `GALA` and `iSpec`. The dispersion in effective temperature (78 K) is roughly compatible with the errors estimated by `GALA`, 68 K in average, but not with `iSpec` ones, 14 K (mean errors are drawn in the plot). The dispersion in surface gravity (0.23 dex) is large considering the mean errors (0.04 and 0.11, drawn in the plot). It is well known that gravity is the most difficult quantity to derive from spectroscopy. Comparing the results of `GALA` and `iSpec` we obtain differences similar to other studies in the literature, like GES iDR1 and iDR2 node-to-node dispersions (Smiljanic et al. 2014).

We also plot in Fig. 5.2 the comparison of the microturbulences ξ, derived by the two methods. There is an offset of $-0.19 \pm 0.14\,\mathrm{kms}^{-1}$. This offset is above the dispersion, and above the quoted errors by the methods: 0.02 and $0.07\,\mathrm{kms}^{-1}$, for `iSpec` and `GALA`. However, we know that the microturbulent velocity is not a physical parameter, but an effective parameter used to compensate the *wrong* assumptions of the models. Therefore, it is widely known that each analysis may lead to different values of this parameter. In Table B.2 we list the T_{eff}, log g and ξ and their errors, derived by the two methods.

Arcturus and μ-Leo

As explained in previous chapters, among the OCCASO data we have observations of two GBS (Arcturus and μ-Leo) representative of the parameter space covered by the targeted OCs. As explained in Section 3.2.2, the GBS have determinations of atmospheric parameters independently from spectroscopy, and reference metallicities. We compare the obtained results from the two methods with the reference values in Table 5.1. We computed the mean value and standard deviation for each parameter from all the spectra. We also list in parentheses the mean error reported by each method. These two determinations of the internal error of the method are roughly of the same order. For both stars, `GALA` is reporting larger errors and also finds larger dispersions than `iSpec` in T_{eff} and log g, but not in metallicity.

From the comparison with the reference values from Heiter et al. (2015b) we obtain an excellent agreement in effective temperature. Differences in gravity are of the same order in both methods: for μ-Leo both methods underestimate by aproximately the same amount; for Arcturus, `iSpec` underestimates it but `GALA` overestimates it. However, Arcturus has a large uncertainty in log g as a GBS, and as quoted by the authors

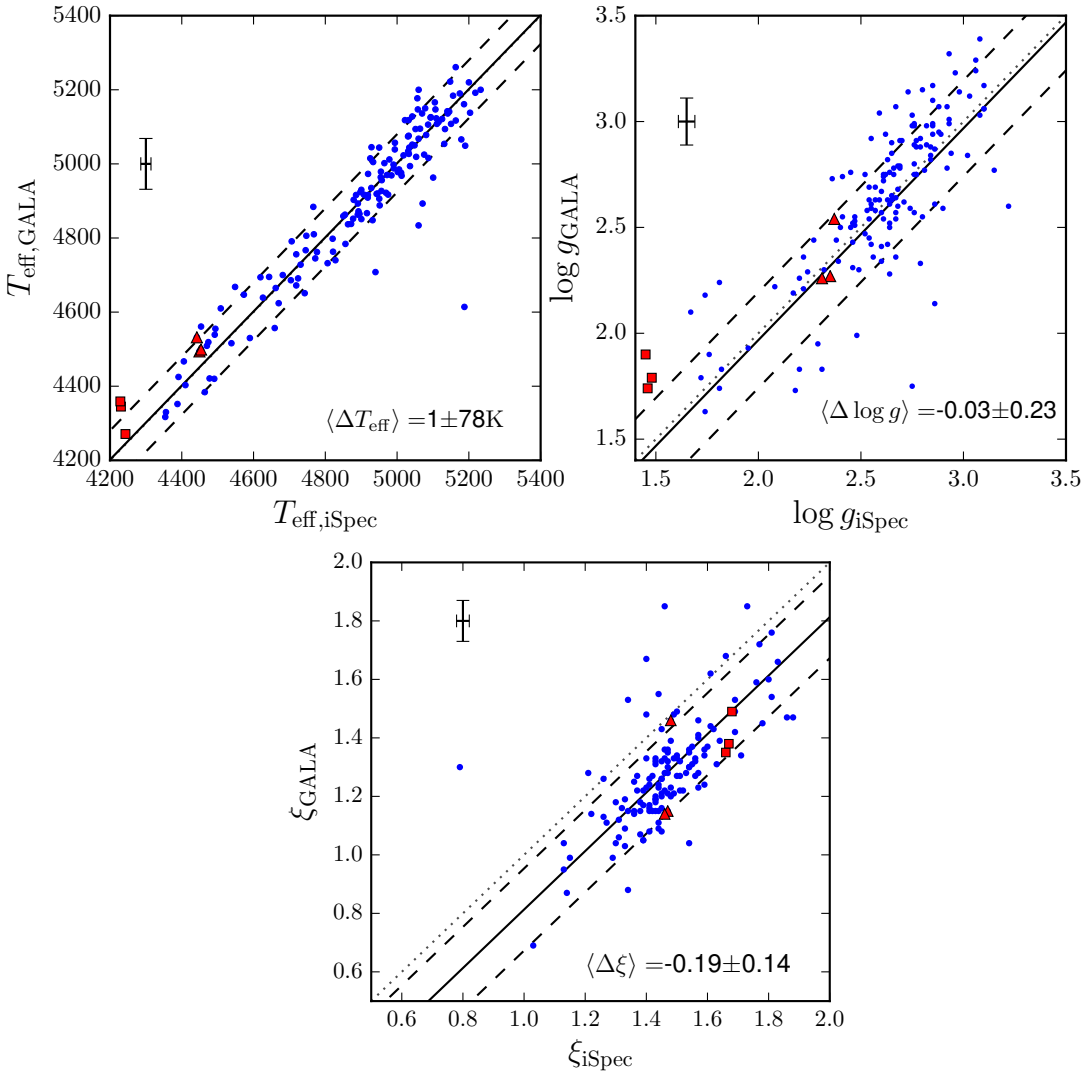

Figure 5.2. Comparison of the effective temperature, surface gravity and microturbulence from `GALA` and `iSpec` analysis. Red symbols indicate the values of Arcturus (squares) and μ-Leo (triangles). The solid line stands for the mean difference, and the dashed lines indicate the 1σ level. The dotted line is the 1:1 relation. In the top left corner of each panel we plot the mean errors in X and Y axis.

Table 5.1. Effective temperature (in K), surface gravity and [Fe/H] for Arcturus and μ-Leo obtained from OCCASO data using GALA and iSpec. The errors indicate the dispersion found between the spectra of the three instruments, and in parenthesis the mean of the errors reported by the methods. The reference values are from Heiter et al. (2015b) and Jofré et al. (2014). The differences (iSpec/GALA-Reference) are in the last three columns.

Star	Origin	T_{eff}	log g	[Fe/H]	ΔTeff	Δlog g	Δ[Fe/H]
Arcturus	Ref	4286 ± 35	1.64 ± 0.09	-0.52 ± 0.01			
	iSpec	4234 ± 8 (5)	1.46 ± 0.02 (0.02)	-0.55 ± 0.04 (0.01)	−52	−0.18	−0.03
	GALA	4325 ± 47 (54)	1.81 ± 0.08 (0.14)	-0.54 ± 0.03 (0.01)	39	0.17	−0.02
μ-Leo	Ref	4474 ± 60	2.51 ± 0.11	0.25 ± 0.02			
	iSpec	4448 ± 6 (5)	2.34 ± 0.03 (0.02)	0.13 ± 0.05 (0.02)	−26	−0.17	−0.12
	GALA	4508 ± 20 (98)	2.36 ± 0.16 (0.20)	0.27 ± 0.06 (0.01)	34	−0.15	0.02

(Heiter et al. 2015b) it can be used for validation purposes only if the large error is taken into account. The differences found in atmospheric parameters are compatible with the quoted errors.

The differences in iron abundances are compatible within 3σ with the dispersions found between the three instruments but not compatible with the mean errors quoted by the methods. In the case of Arcturus both methods slightly underestimate the abundance. For μ-Leo GALA slightly overestimates the abundance and iSpec underestimates it by 0.12 dex. It is worth noting that the GBS reference metallicities were obtained based on a spectroscopic analysis where several methods were averaged. μ-Leo is a metal rich star with many blended lines, thus, EW methods which are not able to reproduce blends as good as SS methods, tend to provide higher abundances.

5.2.1 *Gaia Benchmark stars*

As a sanity check to ensure the reliability of our analysis we have analysed 69 spectra from the 23 GBS described in Section 3.2.2 using the same linelist, atmosphere models and strategy as in the case of OCCASO stars.

We compare the results of our analysis with the reference ones described in Heiter et al. (2015b) in Fig. 5.3. We remark with vertical green lines the Arcturus and μ-Leo spectra, the two GBS also observed in OCCASO. We obtain overall offsets which are compatible at 1σ level with the dispersions in both T_{eff} and log g. The results are available in Table B.3.

We have also tested the iron abundances derived by the two methods with the GBS sample. Each pipeline has analysed the spectra of the selected GBS using its own atmospheric parameters. In Fig. 5.4 we compare the [Fe/H] abundance results from

GALA and iSpec, with the reference values in Jofré et al. (2014). Both methods show good agreement considering the errors.

We have calculated the dispersion in each parameter of the different observations of the stars that have more than one spectra. The mean value of these dispersions are T_{eff}: 9 K, 24 K; $\log g$: 0.02 dex, 0.06 dex; and [Fe/H]: 0.01 dex, 0.01 dex (iSpec and GALA, respectively). All are smaller than the dispersions of the comparison with reference values.

5.3 DERIVATION FROM PHOTOMETRY

We have done an additional independent check of the spectroscopic results by performing a comparison with T_{eff} and $\log g$ determined from photometry. We have used precise BVI Johnson photometry (Stetson 2000) for two clusters in the sample, NGC 2420 and NGC 6791. These are one of the most metal-rich and one of the most metal-poor clusters in the sample.

Photometric T_{eff} is obtained using Alonso, Arribas, and Martínez-Roger (1999) colour-temperature empirical relations as a function of the dereddened colour $(B-V)_0$ and the metallicity (Eq. 4 from their Table 2). Photometric surface gravity is derived from T_{eff} using fundamental relations:

$$\log\left(\frac{g}{g_\odot}\right) = 0.4(M_{bol} - M_{bol,\odot}) + \log\left(\frac{m}{m_\odot}\right) + 4\log\left(\frac{T_{eff}}{T_{eff,\odot}}\right) \tag{5.1}$$

where $\log g_\odot$, $M_{bol,\odot}$, $m_\odot$ and $T_{eff,\odot}$ are the surface gravity, bolometric magnitude, mass and effective temperature of the Sun respectively[2], and m is the mass of the star derived from the isochrone fitting [3]. The bolometric magnitude of the star is calculated from the bolometric correction for giants using Alonso, Arribas, and Martínez-Roger (1999) prescriptions: $M_{bol} = V + BC_V$.

We also derive parameters from $(V-I)$ colour. To do so we calculate extinction in $V-I$ assuming $\frac{A_I}{A_V} = 0.479$ (Cardelli, Clayton, and Mathis 1989). A similar relation as for $(B-V)_0$ is provided for $(V-I)_0$ by Alonso, Arribas, and Martínez-Roger (1999) to derive T_{eff}. Surface gravity is derived in the same way using these temperatures.

We compare the photometric results with the spectroscopic ones in Fig. 5.5. The adopted input parameters for the two clusters: reddening $E(B-V)$, distance modulus $(V_0 - M_V)$, age and metallicity, are indicated in Table 5.2. For the two clusters we compute the mean T_{eff} and $\log g$, from the spectroscopic and photometric analysis in Table 5.3. The dispersion of the spectroscopic parameters within each cluster is around 1.7 and 5.7 times higher (in T_{eff} and $\log g$, respectively) than the photometric one. This

2 We assume $\log g_\odot = 4.438$, $M_{bol,\odot} = 4.74$ and $T_{eff,\odot} = 5772$ K following the IAU recommendations (Prša et al. 2016).

3 We have used PAdova and TRieste Stellar Evolution Code (PARSEC) isochrones (Bressan et al. 2012)

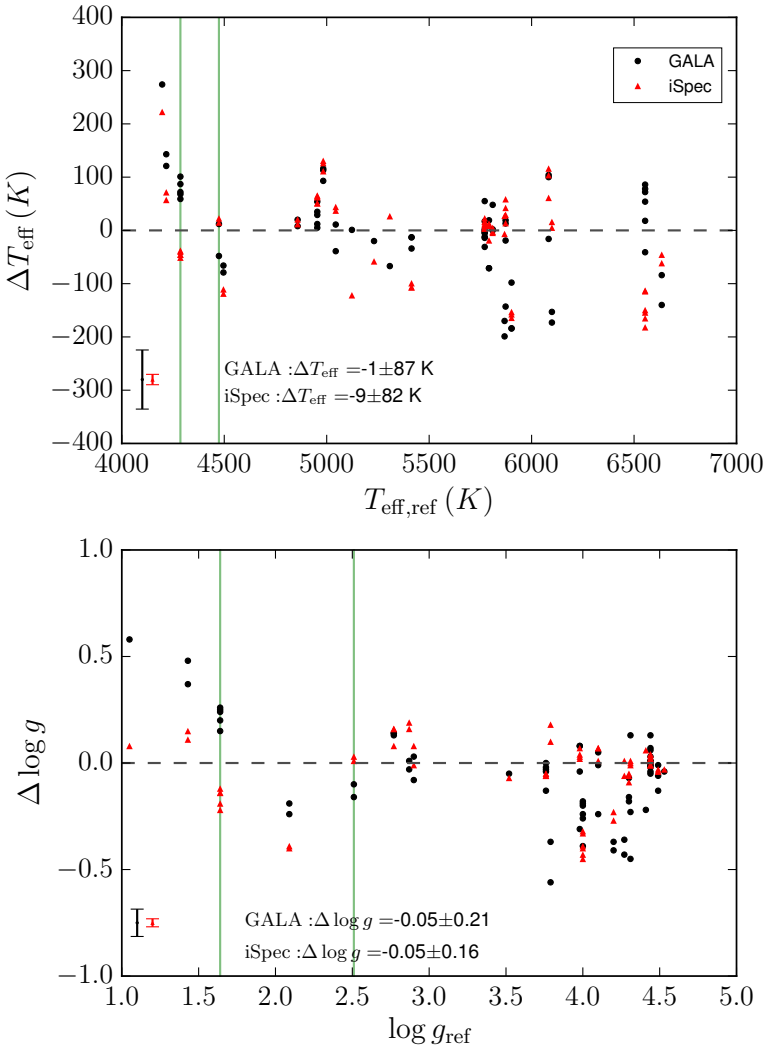

Figure 5.3. Differences in effective temperature (top panel) and surface gravity (bottom panel), between GALA and reference value (black dots), and iSpec and reference value (red triangles), for GBS spectra. The two vertical green lines indicate Arcturus and μ-Leo. Mean error bars are plotted on the bottom-left of each pannel. Differences are calculated in the direction: this study - reference. Reference values are taken from Heiter et al. (2015b).

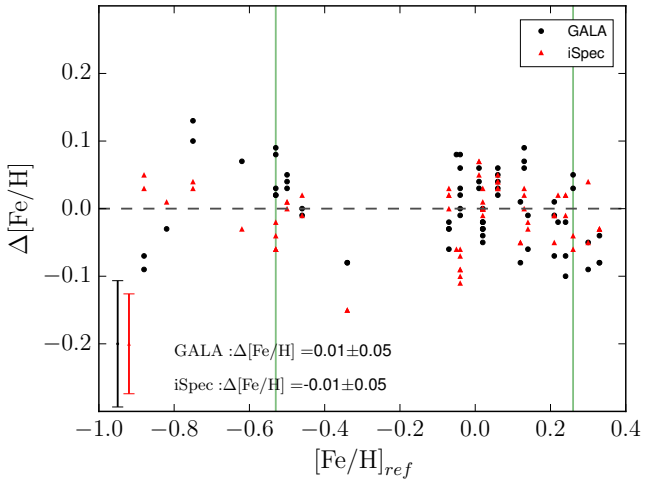

Figure 5.4. Differences in iron abundances between GALA and reference value (black dots), and iSpec and reference value (red triangles), for GBS spectra. The two vertical green lines correspond to Arcturus and μ-Leo. Mean errorbars are plotted on the left of the pannel. Differences are calculated in the direction: this study - reference. Reference values are taken from Jofré et al. (2014).

is compatible within 1σ and $2-3\sigma$, respectively, with the mean uncertainties of the methods.

Both determinations are compatible within $1-2\sigma$, though we find systematic differences which are not the same for the two analysed clusters. Photometric results are very sensitive to the assumed cluster parameters. Any variation in reddening, distance or age within the given errors change the overall offset with respect to spectroscopic parameters. However, the internal dispersion among the stars of the same cluster remains constant. We have assigned as error the dispersion in photometric parameters when changing $E(B-V)$, $(V_0 - M_V)$ and [Fe/H] by their errors $\pm\sigma_i$.

5.4 ADOPTED T_{EFF} AND $\log g$

The analysis in the previous sections include comparisons of the method performances among the OCCASO stars and GBS, and comparisons with photometry. From there, we conclude that the results derived by GALA and iSpec are compatible and the differences are at the level of the expected uncertainties of the analysis. We decided to fix T_{eff} and $\log g$ to the average results from both methods to do the chemical analysis. This approach is a statistically consistent way to combine two results of the same physical quantity that do not show any systematic offset. Moreover, this helps to disentangle the discrepancies in the determination of chemical abundances from those due to the propagation of errors from different T_{eff} or $\log g$. Additionally, this strategy allows us

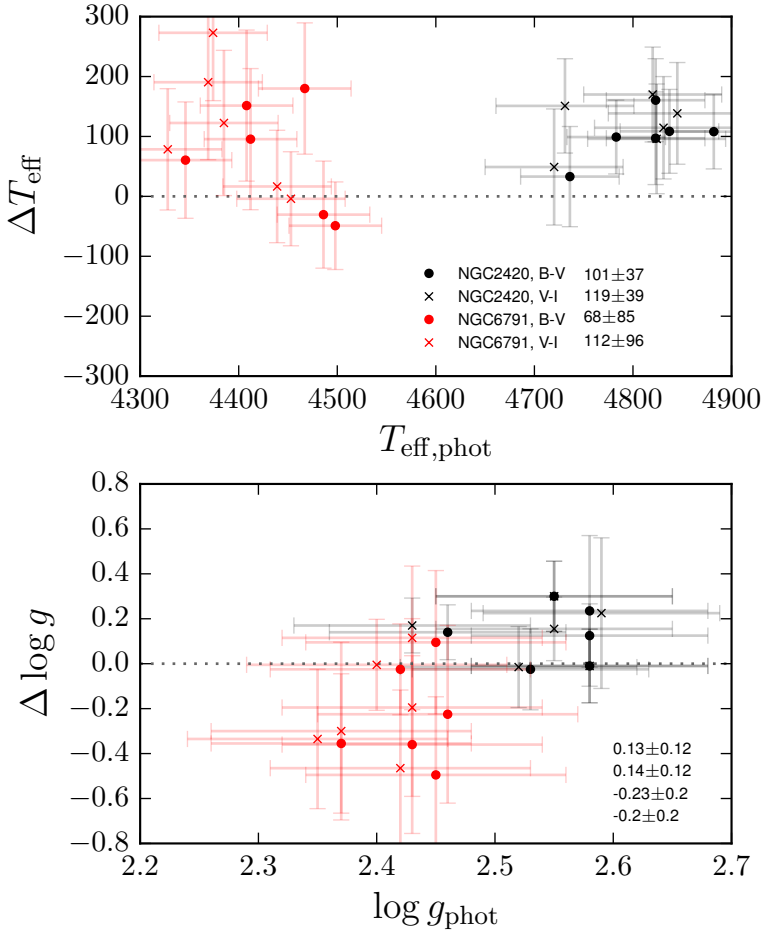

Figure 5.5. Differences in effective temperature and surface gravity from spectroscopy (mean of GALA and iSpec results) and from photometry for the individual stars in NGC 2420 (in black) and NGC 6791 (in red). Mean differences and dispersions for the two OCs and the two photometries are at the bottom right.

Table 5.2. Adopted input cluster parameters to calculate photometric temperature and surface gravity.

Cluster	$E(B-V)$	$(V_0 - M_V)$	logAge (Gyr)	[Fe/H]
NGC 2420[1]	0.04 ± 0.03	11.88 ± 0.27	9.47 ± 0.17	-0.20 ± 0.06
NGC 6791[2]	0.12 ± 0.03	13.25 ± 0.35	9.91 ± 0.20	$+0.30 \pm 0.02$

[1]Reddening, distance modulus and age from Pancino et al. (2010), calculated as average measurements of different authors, metallicity from Jacobson, Pilachowski, and Friel (2011), calculated as average of 9 stars.
[2]Reddening as a mean of all previous determinations (Sandage, Lubin, and VandenBerg (2003), Stetson, Bruntt, and Grundahl (2003), Anthony-Twarog, Twarog, and Mayer (2007), Brogaard et al. (2012), Geisler et al. (2012)), distance modulus from Sandage, Lubin, and VandenBerg (2003), age and metallicity from Brogaard et al. (2012).

Table 5.3. Means and standard deviations of effective temperatures (K) and gravities for the two clusters analysed with photometry. Results from spectroscopy of `GALA` and `iSpec`, and from $B-V$ and $V-I$ photometry.

Cluster		$T_{eff,spectr}$	$\log g_{spectr}$		$T_{eff,phot}$	$\log g_{phot}$
NGC 2420	`GALA`:	4899 ± 87	2.69 ± 0.20	$B-V$:	4814 ± 45	2.55 ± 0.04
	`iSpec`:	4931 ± 64	2.66 ± 0.12	$V-I$:	4795 ± 50	2.54 ± 0.05
NGC 6791	`GALA`:	4507 ± 94	2.07 ± 0.34	$B-V$:	4436 ± 53	2.43 ± 0.03
	`iSpec`:	4502 ± 81	2.34 ± 0.12	$V-I$:	4391 ± 43	2.40 ± 0.03

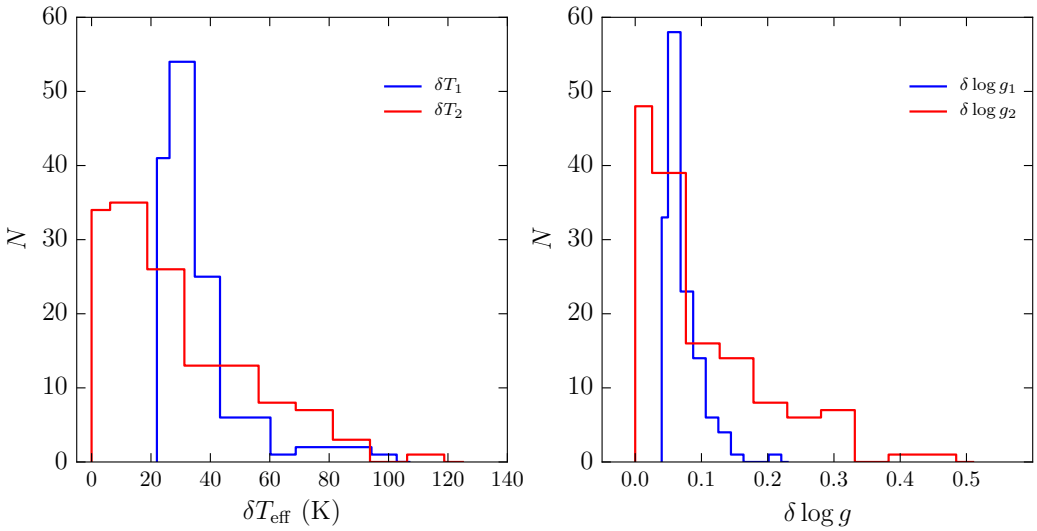

Figure 5.6. Histogram of the distribution of errors in T_{eff} and log g. For both parameters δ_1 stands for the mean of the errors quoted by the methods (in blue), and δ_2 is the dispersion found between the two results (in blue).

to provide an estimation of the external uncertainty (method-dependent) for each star, aside of the error quoted by each pipeline in the derivation of these parameters.

In Table B.2 we list the average results of the two parameters. We indicate two sources of errors: the mean of the errors quoted by the methods δ_1, and the standard deviation between the two values δ_2. In Fig. 5.6 we plot the distribution of these two estimations of the error. When the errors are low, we see that the estimation of errors done by the methods is larger than the dispersion between the two results, both in T_{eff} and log g. On the contrary, when errors are large this is reversed with the methods providing lower errors than the found dispersions. This last behaviour is more defined in log g, where a long tail towards large dispersions is not reproduced by the nominal errors of the methods.

5.4.1 *Literature comparison of OCCASO stars*

Previous works have analysed stars in common with our sample providing results obtained using different methodologies, resolution, and quality of the spectra. A comparison of our results with those available in the literature provides an independent consistency test for our analysis. We compared the averaged values of T_{eff}, log g. This is shown in Fig. 5.7.

In general we find good agreement in effective temperature and surface gravity, with negligible offsets and expected dispersions: 10 ± 92 K, -0.02 ± 0.27 dex. Although not a perfect agreement should be expected because of the methods and assumptions done

by the different authors, this comparison shows that as a whole, our derived values are within the values found in the literature.

There are discrepant cases in particular stars and with some authors, mostly in $\log g$:

i. Jacobson, Friel, and Pilachowski (2007) obtained gravities around 0.5 dex lower than ours for IC 4756. However, for the same cluster Santos et al. (2009) and Pace et al. (2010) obtain gravities 0.25 dex higher than us.

ii. For NGC 6791 Carraro et al. (2006b) finds gravities about 0.6 dex higher than ours (2 stars in common), and Mészáros et al. (2013) finds similar values for those stars and high dispersion in the whole cluster. However, Mészáros et al. (2013) finds higher gravities respect to us in the whole sample of common stars. On the contrary, Gratton et al. (2006) finds very similar results as us for the three stars in common.

iii. Pancino et al. (2010) find discrepant gravities, around 0.4 dex higher than us, for the cluster NGC 2682, and more compatible values for the stars in common in: NGC 2099, NGC 2420 and NGC 7789. We also find a quite discrepant value of temperature (400 K higher than them) for the star NGC 2099 W148.

iv. We find systematically discrepant gravities with Mészáros et al. (2013) with a mean difference of -0.30 ± 0.16 dex. This authors discuss differences in $\log g$ between $0 - 0.3$ dex in OCs comparing their values with isochrones and with asteroseismic gravities from Kepler. They suggest that the derived gravities are too high by a few tenths of a dex.

We remark that this is the first time that atmospheric parameters and abundances have been derived for the clusters NGC 6939, NGC 6991, NGC 7245, NGC 7762.

5.5 CONCLUSIONS

We have computed atmospheric parameters (T_{eff}, $\log g$, ξ) of the stars in the OCCASO sample. We have used two methods representative of two of the procedures extensively used in the literature: EW and SS. We have also used the same procedure to derive atmospheric parameters of the GBS.

We made an extensive comparison of the results of both methods to assess our internal consistency and the reliability of the quoted errors:

i. The comparison between methods of T_{eff} and $\log g$ per star for the OCs and Arcturus and μ-Leo shows that there exists no systematic offsets.

ii. The comparison of the results obtained by the two methods with the reference values of the GBS also indicates that there are no systematic differences.

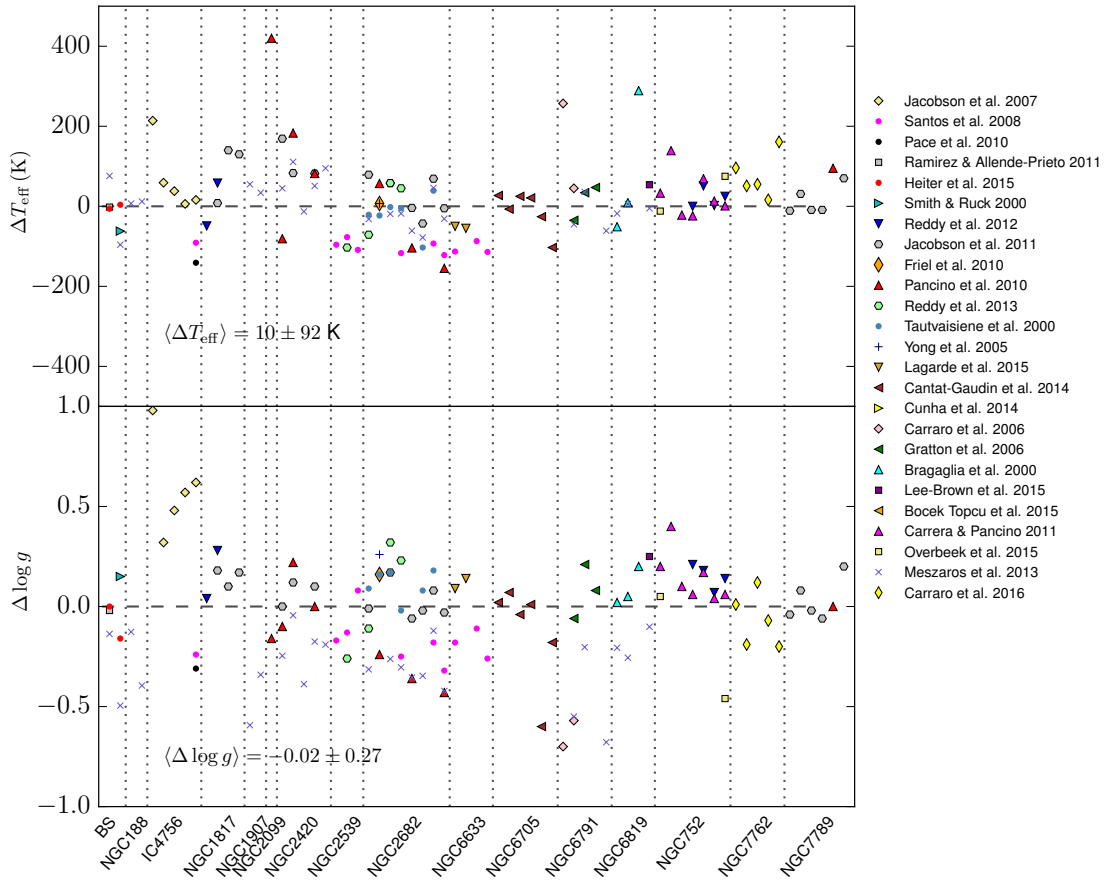

Figure 5.7. Comparison of the derived atmospheric parameters from this study (average values between GALA and iSpec), and previous determinations in the literature. Differences are in the direction this study − literature.

iii. We calculate atmospheric parameters using Johnson BVI photometry for two OCs: NGC 2420 and NGC 6791. The systematic differences found in the comparison with spectroscopy are inside the errors when varying the assumed $E(B-V)$, $(V_0 - M_V)$ and [Fe/H], to do the photometric analysis.

In all the comparisons we found dispersions of ~60-80 K, 0.15-0.20 dex in T_{eff} and log g, respectively.

6

ABUNDANCE DETERMINATION

In this chapter we determine chemical abundances of all OCCASO stars using the average values of T_{eff} and $\log g$ calculated in the previous chapter (Table B.2). In Section 6.1 we calculate iron abundances per star with two methods, we do an assessment of the precision of the results, and we analyse the performance of the methods when deriving abundances under different assumptions. We also perform an analysis cluster by cluster with an extensive comparison with literature. In Section 6.2 we derive abundances of two Fe-peak elements (Ni and Cr) and three α-elements (Si, Ca, Ti). We also compute cluster mean abundances and the respective abundance ratios respect to iron. We specifically discuss the results obtained for Arcturus and μ-Leo and compare them with previous literature values. With this results we have a complete view of the abundance patterns of the 18 studied clusters

6.1 IRON

In this section we derive Fe abundances using `iSpec` and `DAOSPEC+GALA` (see more details of the methods in Section 5.1). This allows a comparison of the results obtained with the two methods, to assess the precision and accuracy of our analysis. We also check the performances of the methods using the GBS, and do an external comparison with literature, similarly to the cases of radial velocities and atmospheric parameters in previous chapters.

6.1.1 *Results and precision*

We take the mean values of T_{eff} and $\log g$ (Section 5.4) to perform the second step in the analysis: calculate the chemical abundances of the whole sample of 154 spectra, 62 from FIES, 81 from HERMES, and 11 from CAFE.

We have followed a global differential approach relative to the Sun. As Solar abundance we derived $A(Fe)_{\odot,GALA} = 7.46 \pm 0.01$, $A(Fe)_{\odot,iSpec} = 7.39 \pm 0.02$ using the Solar spectra provided in the GBS library (Blanco-Cuaresma et al. 2014b). In this way we are sure that the two methods have the same Sun reference.

The average iron abundances derived from each method, the spread in the line abundances and the number of used lines are listed in Table B.2. We also include

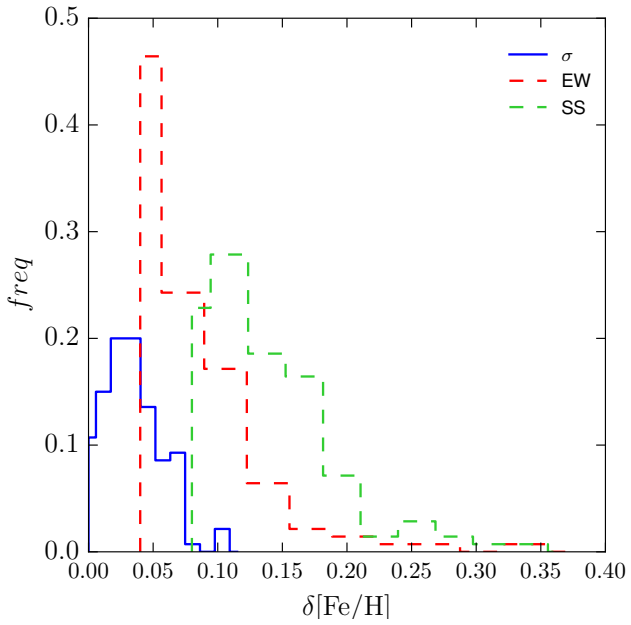

Figure 6.1. Distribution of: errors given by the methods (spread in the line-by-line abundances) and the standard deviation derived by the two methods σ[Fe/H].

in Table B.2 the standard deviation of the abundance derived by the two methods σ[Fe/H]. This last value provides a *less* method-dependent estimation of the error, and has a distribution plotted in Fig. 6.1. It has a mean value of 0.04. We consider that a good approximation of the error in [Fe/H] derived by the two methods is be the squared sum of the spread of line-by-line abundance divided by the square root of the number of lines, and this fixed value 0.04.

We have calculated the errors in [Fe/H] due to the choice of the atmospheric parameters: T_{eff}, log g and ξ. To do so, we have recomputed iron abundances varying the three input parameters within their uncertainties $\pm\sigma_i$. We have used as errors of T_{eff} and log g the square root of the quadratic sum of δ_1 and δ_2 in Table B.2. We have done this process with the two methods and for 5 stars covering the range in metallicity. The mean values of the variation in abundance for the five stars are summarized in Table 6.1. They range from −0.04 to 0.03 dex in `GALA`, and −0.02 to 0.02 dex in `iSpec` well within the mean uncertainties of the methods.

6.1.2 *Performance of the methods*

The comparison of the iron abundances obtained by the two methods is plotted in Fig. 6.2. The plotted errorbar is an average for all the spectra of the quadratic sum

Table 6.1. Mean variation obtained in the [Fe/H] computed by each method when altering atmospheric parameters by their errors $\pm\sigma_i$ for 5 representative stars.

Parameter	GALA	iSpec
$\frac{d\,[Fe/H]}{d\,T_{eff}}$	$^{+0.027}_{-0.023}$	$^{+0.022}_{-0.018}$
$\frac{d\,[Fe/H]}{d\,\log g}$	$^{+0.019}_{-0.024}$	$^{+0.012}_{-0.010}$
$\frac{d\,[Fe/H]}{d\,\xi}$	$^{-0.036}_{+0.034}$	$^{+0.004}_{-0.010}$

of the spread divided by the square root of the number of lines, and the mean of the σ[Fe/H] from Table B.2. The average difference between the two determinations of 0.07 ± 0.05 (GALA-iSpec). Similar differences between spectroscopic methods have been studied in detail (Hinkel et al. 2016; Blanco-Cuaresma et al. 2016, 2017; Jofre et al. 2016).

To better illustrate the differences between the methods for our particular case, we used iSpec capabilities to perform synthesis and equivalent width analysis. We configured iSpec to use SPECTRUM (Gray and Corbally 1994) for spectral synthesis, which is the same radiative transfer code used in this thesis (see Section 5.1), and WIDTH9 (Kurucz 1993; Sbordone et al. 2004) for the equivalent width derivation (which is the code used by GALA). Then we derived the [Fe/H] for the GBS considering four different scenarios as shown in Fig. 6.3:

i. We fix T_{eff} and $\log g$ to their reference values and we derive the rest of parameters with each method independently.

ii. Like in the previous case but we also fix the microturbulence.

iii. Like in the previous case but we use only lines in common between both methods.

iv. Like in the previous case but forcing the synthesis method not to synthesize blends.

The first case coincides with the strategy followed in our study and its average difference (SPECTRUM - WIDTH9= -0.05 ± 0.04) is comparable to our results. If we fix the microturbulence parameter, the dispersion per star does not improve and the overall mean difference worsens (-0.09 ± 0.06). The microturbulence is a parameter used to compensate errors and assumptions in the models and this compensation depends on the method, thus fixing it does not improve the agreement between both methods, as expected.

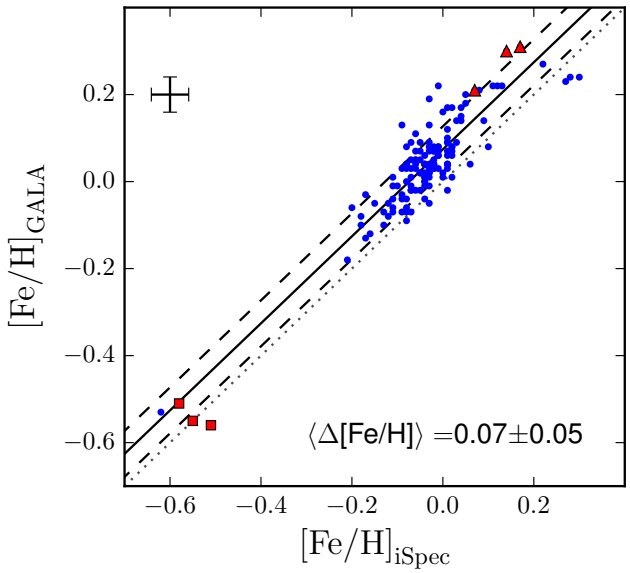

Figure 6.2. Results of iron abundance from `GALA` and `iSpec` analysis. Red squares and red triangles indicate the values of Arcturus and μ-Leo (3 spectra each), respectively. The solid line stands for the mean differences, and the dashed lines indicate the 1σ level. The dotted line is the 1:1 relation. In the top left corner we plot the mean errors in X and Y axis. The mean offset between the two determinations is 0.07 ± 0.05 (`GALA-iSpec`). The star that has a very low [Fe/H]~ −0.6 is NGC 1907 W2087 (not member of the cluster, see Section 6.1.3).

When we use the same lines, there are three stars that get excluded from the analysis because no overlapping lines were found. Lines that are good enough for methods based on synthesis might not be convenient for EW (e. g., blended lines), thus the line selection is different for each method and it can be challenging to find lines in common (specially for metal poor stars). Nevertheless, the agreement between both methods (SPECTRUM - WIDTH9= -0.04 ± 0.04) is almost the same as in the first case.

In the fourth case, we forced the synthetic method to only synthesize the lines being analysed (ignoring the atomic lines around it) to make it more similar to the equivalent width method. This is the case with a higher level of agreement (SPECTRUM - WIDTH9= -0.02 ± 0.02).

In all the four cases there is no dependence in T_{eff} or [Fe/H] as seen in Fig. 6.3.

This analysis shows that the differences between methods are intrinsic to how each technique works. This is further discussed in Appendix A, where we test several assumptions of six different analysis methods to try to measure its influence on the abundance determinations. There, it is shown that EW and SS methods can be affected differently by the different assumptions. For example, the presence of blends is a weak point of EW methods for which we found differences up to 0.15 dex, while SS methods can cope better with this when the blends are known. On the other side, while EW methods are robust for shifts in the wavelength, SS methods can be significantly affected and easily yield differences of 0.2 dex. Other effects such as the Hyperfine Structure Splitting (HFS)[1] in some elements can produce very large differences in abundances (e. g. up to 0.4 dex for Mn lines in giants), so it is important to be aware of which elements are more affected by this. The treatment of the continuum is also important and different methods may require different normalization procedures.

Based on our analysis we argue that the derivation of abundances must be properly documented, where input parameters and method assumptions have to be provided to the community for better reproducibility of results, understanding of uncertainties and correct use of the data.

6.1.3 *Cluster-by-cluster analysis*

We calculate cluster averaged [Fe/H] using only trustful member stars. This means that we exclude those stars with discrepant radial velocities, possible non-members or spectroscopic binaries (see Chapter 4), or stars that give unreliable values in the spectroscopic analysis. These stars are marked in red in Fig. 6.4.

We plot in Fig. 6.4 the two determinations (`GALA` and `iSpec`) of [Fe/H] obtained for the stars in each OC. For the stars that have determinations with the different instruments, we plot the mean value. We draw special attention to the following stars:

1 The HFS is due to the interaction of the nuclear spin of the atom with the electron spin splitting of the energy levels. The separation between these spectral lines is tiny, and usually cannot be resolved.

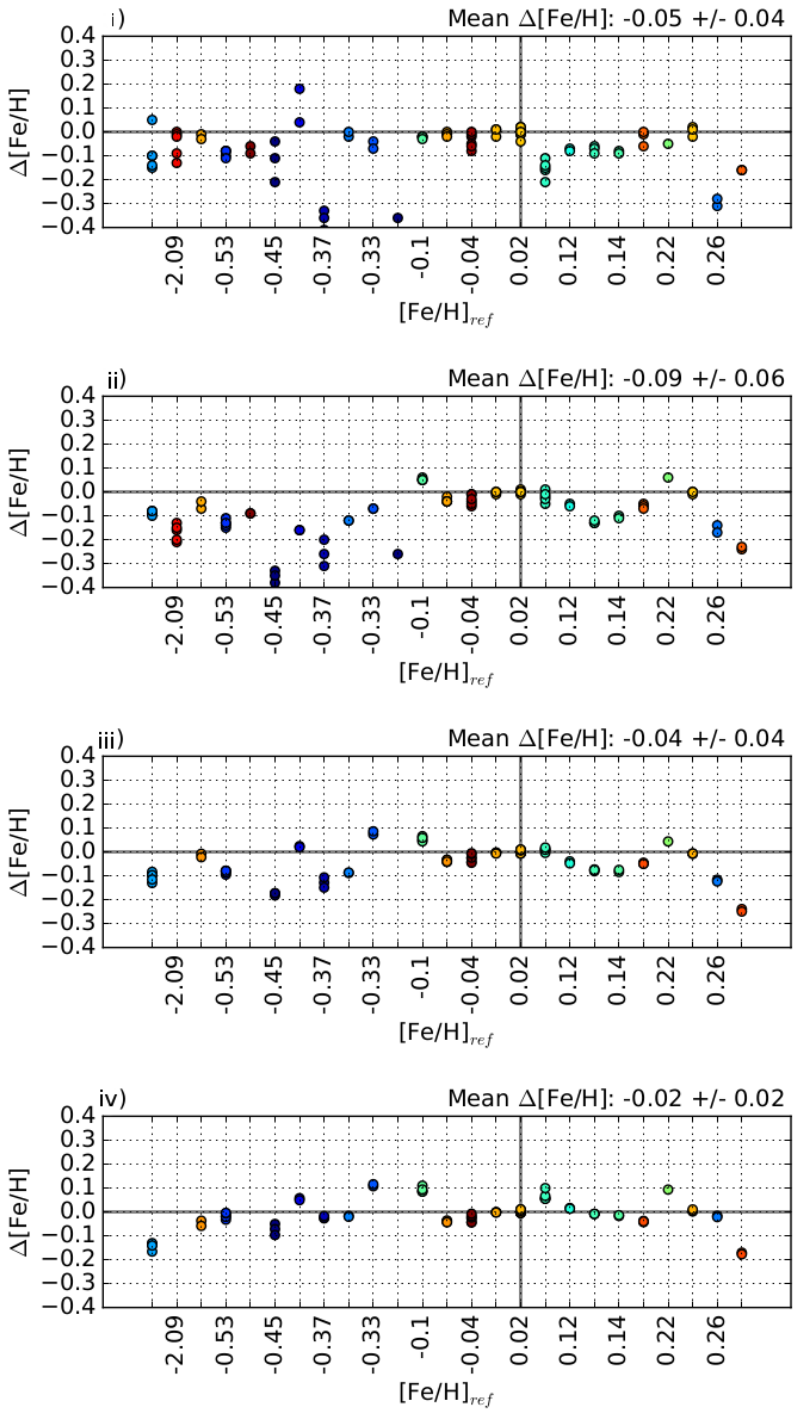

Figure 6.3. Differences in iron abundance obtained for the GBS analysis between SPECTRUM - WIDTH9. The four panels stand for the four cases mentioned in the text (Section 6.1.2). The colours represent the reference temperature where blue is cold and red is hot. The Sun is indicated with a vertical grey line.

i. NGC 188 W2051 has a radial velocity slightly above the mean of the cluster, but compatible within 3σ. GALA derives a higher [Fe/H] compared with the rest of the stars in the OC. However, iSpec finds it compatible with the rest of the stars. For safety we consider it as possible non-member.

ii. NGC 1907 W2087 was flagged as non-member in Chapter 4 for having a significant difference in radial velocity with respect to the other stars in the cluster. Moreover, both GALA and iSpec obtain a [Fe/H] which differs in more than 0.5 dex from the other stars of the cluster. The chemical abundances confirm that this star is not a cluster member.

iii. NGC 2539 W233 was flagged as spectroscopic binary in Chapter 4, and previously in the literature. It gave inconsistent results in the analysis by the two methods: very high gravity and temperature (4.5 dex, 6500 K) in iSpec, and very low microturbulence in GALA compared to the other stars. This is probably because the spectral lines have a distorted shape due to the companion star. Therefore, we do not consider it in the cluster analysis. The star is not included in Fig. 6.4.

iv. NGC 2682 W224 has a discrepant radial velocity in Chapter 4. It was flagged as member spectroscopic binary by Jacobson, Pilachowski, and Friel (2011) and Geller, Latham, and Mathieu (2015). The spectral analysis with both GALA and iSpec give results in agreement and compatible with being a member. Therefore, we consider its results of abundances in the analysis.

v. NGC 6791 W3899 has a compatible radial velocity with the other stars in this cluster but as showed in Chapter 4 it is a possible spectroscopic binary. Its results of the abundances have large errors and are quite discrepant with the other stars of the cluster. We discard its abundance to calculate the cluster mean and we do not plot it.

vi. NGC 6819 W983 was flagged as spectroscopic binary in Chapter 4 for having variable radial velocity. We could analyse this star by shifting the individual exposures to a common reference frame. It gives satisfactory results with both methods, and compatible Fe abundance with the rest of members. For this reason we consider it in the cluster abundance analysis.

vii. NGC 6939 W130 has a more than 3σ discrepant radial velocity with respect to the other cluster members in Chapter 4. It gives around 2σ discrepant value of the [Fe/H]. It is probably a non-member so we discard it to do the mean of abundances.

viii. NGC 7245 W0045 was detected as spectroscopic binary in Chapter 4. In Fig. 6.4 it is seen that its abundance is higher than the rest of the stars by more than 3σ. So this star is possibly a non-member.

ix. NGC 7762 W0084 had a more than 3σ discrepant radial velocity in Chapter 4, pointing out that it could be a non-member. By its abundance results we cannot confirm it as non-member but in any case we do not use its abundance values to compute the cluster averages.

The sample of bona fide member stars is used to compute the cluster mean iron abundance. This value and its dispersion is indicated in Table 6.2. The internal dispersions within each cluster are found in the range 0.01-0.05 dex from both analysis excluding NGC 6791. The largest dispersion for both methods corresponds to NGC 6791 0.08 and 0.11 dex for EW and SS, respectively. This is the faintest OC in our sample with SNR~ 50, while for the others we reach SNR~ 70. This may partly explain the large dispersion, though it also has large dispersions in radial velocity (Table 4.3).

The most metal-rich OCs are NGC 6791 and NGC 6705 according to `GALA` results, and NGC 6705 is not metal-rich according to `iSpec`. On the other hand, the most metal-poor clusters are NGC 2420, NGC 1817 and NGC 1907, for both `GALA` and `iSpec`. We note that this is the first time chemical abundances are derived from high-resolution spectroscopy for the clusters NGC 6939, NGC 6991 and NGC 7245.

In Section 4.2.2 we noticed that IC 4756 and NGC 6633 have very similar ages, locations and non-circular spatial velocities. Their [Fe/H] is 0.00 ± 0.01 and 0.04 ± 0.01 (`GALA`), -0.05 ± 0.01 and -0.03 ± 0.01 (`iSpec`)[2], respectively. The results of both clusters are compatible within 1σ for `iSpec` and within 2σ for `GALA`, so we cannot discard a common origin.

6.1.4 *Comparison with literature*

Previous works have analysed stars from our sample providing results obtained using different methodologies, resolutions, and qualities of the spectra. A comparison of our results with those available in the literature provides an independent consistency test for our analysis. We compare the two determinations of [Fe/H] obtained in this thesis with previous measurements in the literature in Fig. 6.5.

Both methods have the same dispersion in comparison with literature with offsets in opposite directions: 0.02 ± 0.09 dex (`GALA`), -0.06 ± 0.09 dex (`iSpec`). These offsets are fully compatible with the quoted dispersions. More importantly, they are consistent with the comparison done in Section 6.1.1, since we find a systematic difference of 0.07 dex between the two methods. Most of the literature analyses are done with EW method, and therefore there is no surprise if the EW results agrees more with literature than the SS one. NGC 6791 is the cluster that presents largest differences. However, this is the most metal rich cluster and it is known that deriving abundances from metal rich stars can be difficult (e. g. Liu et al. 2017).

2 Here we give the errors in [Fe/H] as the dispersion divided by the square root of the number of stars: $\sigma/\sqrt{N}$

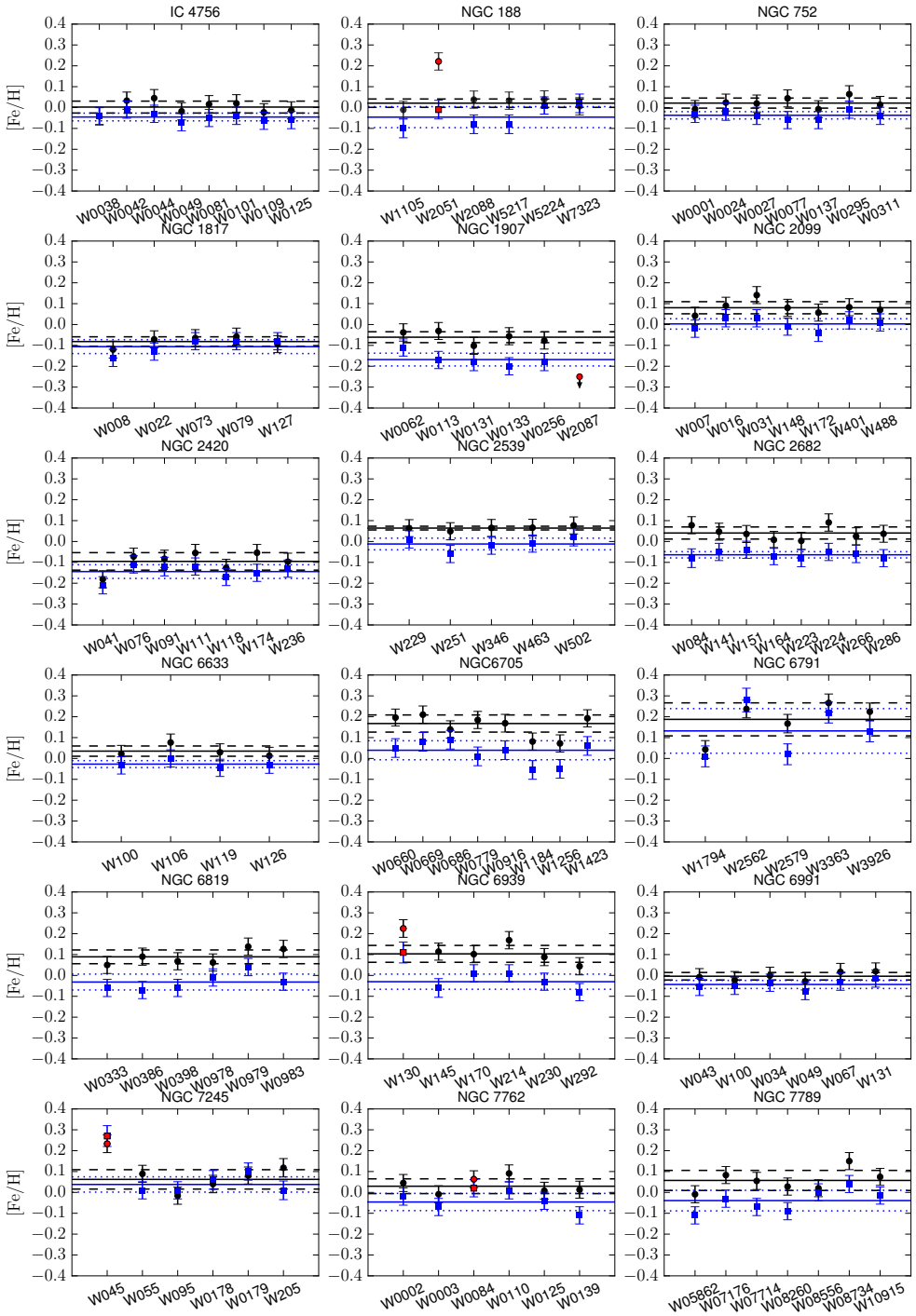

Figure 6.4. Iron abundances obtained for the 18 studied OCs. In black GALA results, in blue iSpec results. Red symbols indicate probable non members or detected spectroscopic binaries not used for the computation of the mean [Fe/H]. NGC 1907 W2087 is indicated with an arrow because it falls out of the plot. The black solid and dashed lines indicate the mean and 1σ level of GALA iron abundance, respectively. The blue solid and dotted lines indicate the mean and 1σ level of iSpec iron abundance.

Table 6.2. Iron abundances from GALA and iSpec analysis of the 18 OCs computed as the mean of the bona fide member stars. Dispersions are listed as errors. The number of stars to compute the mean in each cluster is indicated.

Cluster	$[Fe/H]_{GALA}$	$[Fe/H]_{iSpec}$	Stars
IC 4756	0.00 ± 0.03	-0.05 ± 0.02	8
NGC 188	0.02 ± 0.02	-0.05 ± 0.05	5
NGC 752	0.02 ± 0.02	-0.04 ± 0.02	7
NGC 1817	-0.08 ± 0.02	-0.11 ± 0.03	5
NGC 1907	-0.06 ± 0.03	-0.17 ± 0.03	5
NGC 2099	0.08 ± 0.03	0.00 ± 0.02	7
NGC 2420	-0.10 ± 0.04	-0.14 ± 0.03	7
NGC 2539	0.06 ± 0.01	-0.01 ± 0.03	5
NGC 2682	0.04 ± 0.03	-0.06 ± 0.01	8
NGC 6633	0.04 ± 0.02	-0.03 ± 0.02	4
NGC 6705	0.17 ± 0.04	0.04 ± 0.05	8
NGC 6791	0.19 ± 0.08	0.13 ± 0.11	5
NGC 6819	0.09 ± 0.03	-0.03 ± 0.04	6
NGC 6939	0.10 ± 0.04	-0.03 ± 0.04	5
NGC 6991	0.02 ± 0.02	-0.04 ± 0.02	6
NGC 7245	0.06 ± 0.05	0.04 ± 0.04	5
NGC 7762	0.03 ± 0.04	-0.05 ± 0.04	5
NGC 7789	0.06 ± 0.05	-0.05 ± 0.04	7

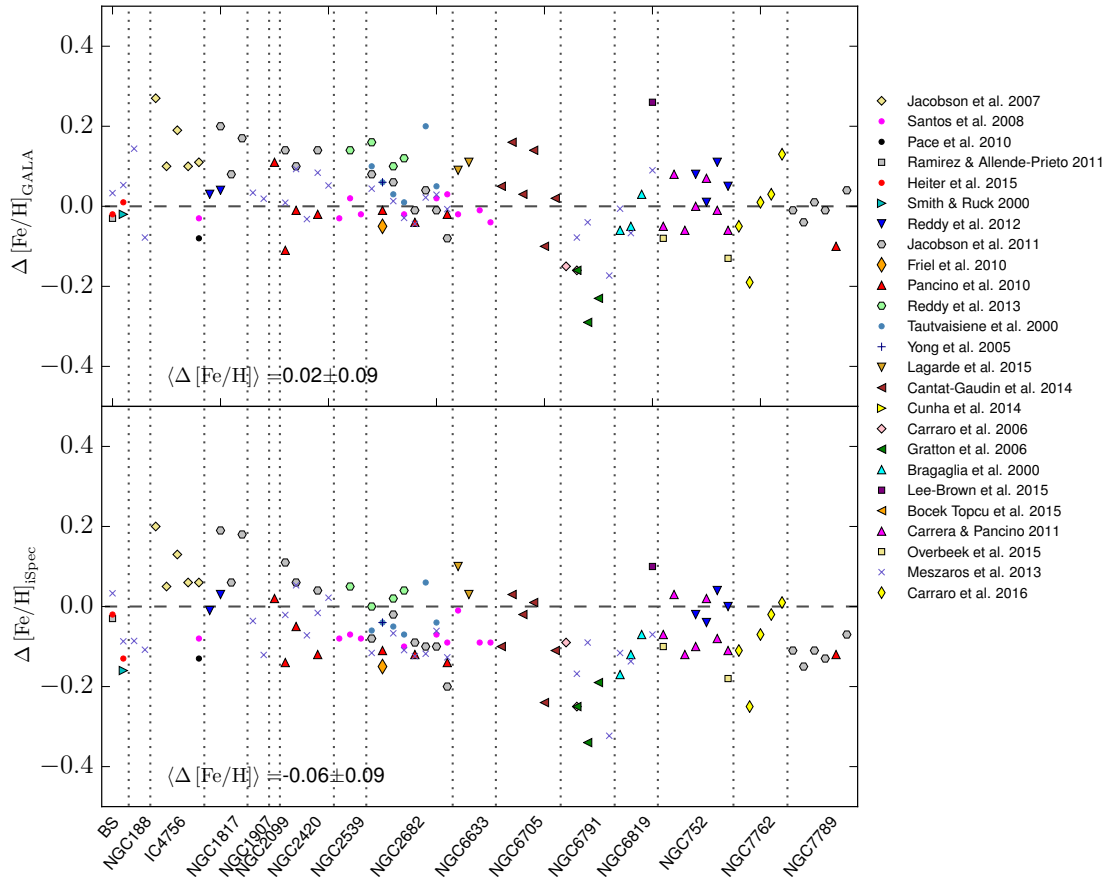

Figure 6.5. Comparison of star-by-star iron abundances obtained in this study and previous determinations in the literature. In the top pannel we compare values from GALA, in the bottom pannel determinations from iSpec. Differences are in the direction this study − literature.

6.2 FE-PEAK AND α-ELEMENTS

We determine abundances from EW analysis for several elements (Ni, Cr, Si, Ca, Ti) selected to perform the analysis with confidence. This is, mainly if they have enough lines to perform a statistical line cleaning, basically to get rid of blendings. This is important because the most critical aspect of EW techniques is that they perform a comparison of the EW of a line and the theoretical strength of the line, changing the abundance of the model until they match. The theoretical line profile is calculated taking into account the continuum opacity sources but neglecting neighbouring lines (Kurucz 2005). Another important point is that we must exclude elements which suffer from HFS. This affects odd-Z atoms, and spectral lines that involve penetrating electron orbits in atoms with large nuclear spin. V, Mn, Co and Cu are typical elements that suffer from HFS.

We use the linelist described in Section 5.1. We do a line cleaning for the five elements using HERMES spectra, for having the largest wavelength range of our instruments. We reject the lines that are not found in less than eight spectra (10% of the total number of spectra), or that give systematically discrepant abundances respect to the mean abundance of the chemical species. We iterate the process twice. First, lines that differ more than 0.2 dex from the mean abundance, or that give a dispersion of more than 0.27 dex are rejected. In the second iteration we are more restrictive rejecting those at more than 0.1 dex from the mean, and that give more than 0.2 dex in dispersion.

Using the same strategy followed for iron in Section 6.1.3 we have computed the Ni, Cr, Si, Ca, Ti abundances of individual stars, and the mean cluster abundances using bona fide member stars. The results are plotted in Figs. 6.6 to 6.10. We assume Solar abundances by Asplund et al. (2009): $A\,(\mathrm{Ni})_\odot = 6.20 \pm 0.01$, $A\,(\mathrm{Cr})_\odot = 5.64 \pm 0.01$, $A\,(\mathrm{Si})_\odot = 7.51 \pm 0.01$, $A\,(\mathrm{Ca})_\odot = 6.29 \pm 0.02$, $A\,(\mathrm{Ti})_\odot = 4.91 \pm 0.03$. In the figures we indicate the number of lines used to do the calculation, and the mean value of [X/H]. If a star was observed with different instruments we plot the different values in grey, and the mean value in black. The errors are computed in the same way as for [Fe/H], with the square sum of the spread in abundance divided by the square root of the number of lines, and a fixed value representative of the method-dependent error[3]. The distribution of these errors is plotted in Fig. 6.11. Typically, errors in [X/H] are around $0.04 - 0.05$ dex in all elements. Cr and Ni have a very similar distribution with all errors lower than 0.14 dex, and Si, Ca and Ti have a long tail up to 0.2 dex. Ca in particular has slightly higher errors than the other elements. We have computed the abundance ratios per star for the five studied elements, and their errors as the quadratic sum of the error in [X/H] and the error of [Fe/H]. The values of [X/H] and [X/Fe] with their errors, per spectra are listed in Table B.4.

3 We use as characteristic method-dependent error the mean of the σ[Fe/H], which is 0.04, as done by [Fe/H] see Section 6.1.1.

We obtain the cluster average [X/Fe] using the member stars. The cluster average and dispersions are listed in Table 6.4. We plot the abundance ratio distributions of the OCs as a function of the [Fe/H] abundance in Figs. 6.12 to 6.16. These are calculated using bona fide member stars, and the average of the abundances given by the different instruments if applicable. In general, except NGC 6791, clusters show homogeneous abundance patterns with very small dispersions in [X/Fe]: $0.01 - 0.03$ (Ni), $0.01 - 0.06$ (Cr), $0.01 - 0.05$ (Si), $0.01 - 0.07$ (Ca), $0.01 - 0.05$ (Ti). NGC 6791 has larger dispersions for several elements such as Cr o Si 0.08 and0.09, respectively. This is also seen for [Fe/H], and can be partly explained because the SNR of the spectra is lower than the other clusters. However, we do not discard that this OC has a intrinsic higher dispersion than the others.

In Fig. 6.17 we show the [X/Fe] abundance ratios as a function of the [Fe/H] of the studied clusters. The clusters with [Fe/H]> 0.1 are NGC 6705 and NGC 6791, and those with [Fe/H]< -0.05 are NGC 2420, NGC 1907 and NGC 1817. In general, [Cr/Fe] and [Ni/Fe] are below zero for all the clusters except the metal rich ones for Ni. The mean of [Si/Fe] is also slightly below zero except for the two metal rich ones again. Ca and Ti seem to roughly follow Fe, but Ca with more spread.

In Fig. 6.18 we show the mean abundance of the studied α-elements (Si, Ca and Ti) as a function of [Fe/H]. Here we can see a decreasing dependency of [α/Fe] between -0.1 and 0.1. NGC 6791 would be compatible with this trend because of the large errorbars, though slightly above it. NGC 6705 has an [α/Fe] content very well above the expectations. We do a further insight to this cluster in Section 7.3, where we investigate other α-elements like Mg and O.

Several papers have been devoted to investigate if the Sun could have been born in M 67 because it is a close by cluster with very similar age and chemical composition (e. g. Pasquini et al. 2008; Pichardo et al. 2012). We obtain a [Fe/H]$= 0.04 \pm 0.03$ for the EW analysis and -0.06 ± 0.01 for SS. As judged by our results of abundance ratios all elements seem to follow iron except for Cr (which is below zero like the rest of the OCs) Some studies point out that Cr lines could suffer from NLTE effects (e. g. Sobeck, Lawler, and Sneden 2007).

6.2.1 *Arcturus and μ-Leo*

We have analysed the α- and Fe-peak elements for the two GBS (Arcturus and μ-Leo) observed in OCCASO. Both stars were observed with the three instruments FIES, HERMES and CAFE. We compare the obtained results with the reference values in Table 6.3. We computed the mean value and standard deviation for each element from the mean of the three spectra. We also list in parentheses the mean error reported by the EW method. Usually the dispersion between the three instruments is lower than the quoted errors.

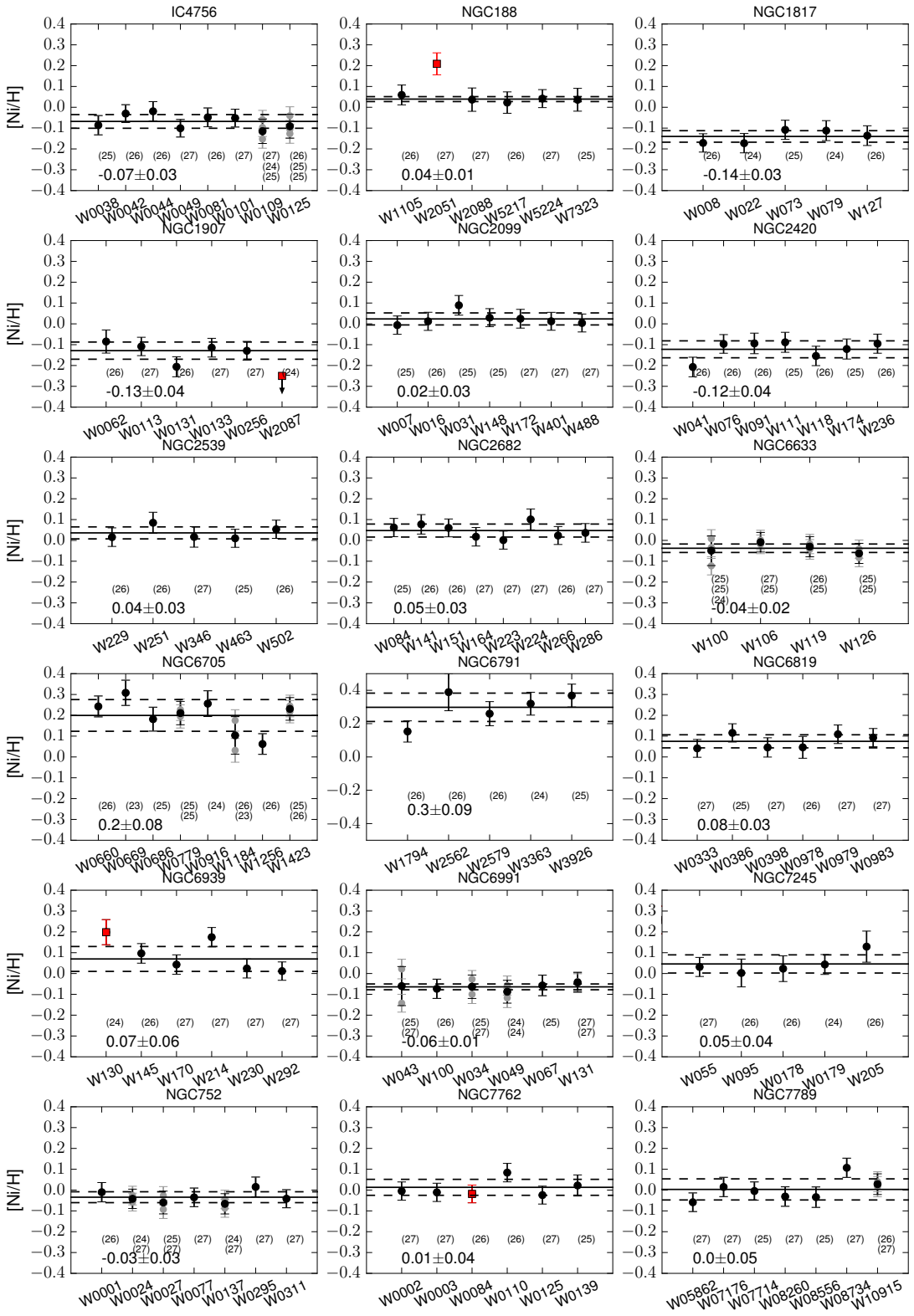

Figure 6.6. Ni abundances obtained for the 18 studied OCs using the EW analysis. Grey symbols indicate the values obtained for the different instruments. The number of used lines is indicated in parentheses. The other symbols are the same as in Fig. 6.4.

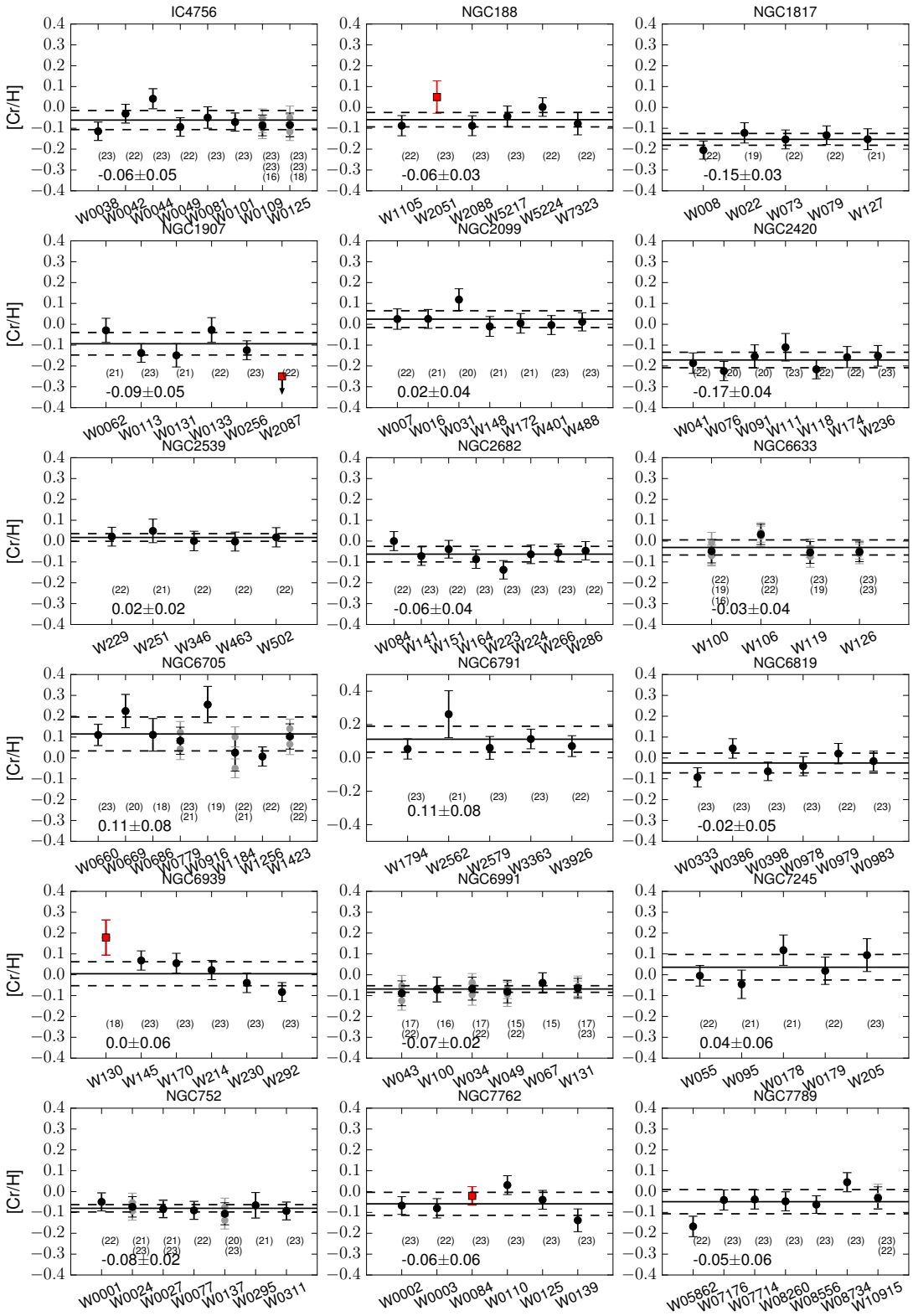

Figure 6.7. As in Fig. 6.6, for Cr.

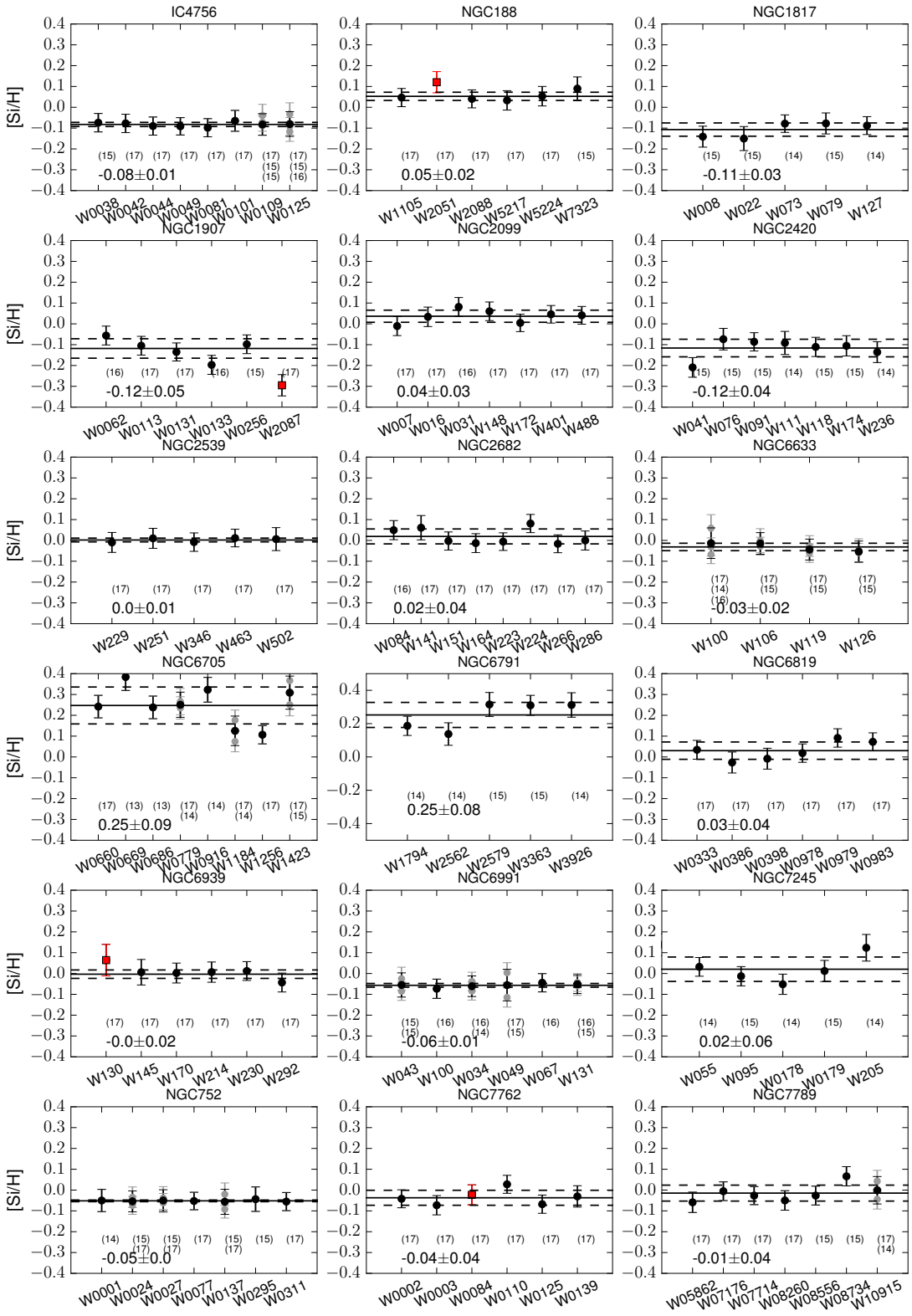

Figure 6.8. As in Fig. 6.6, for Si.

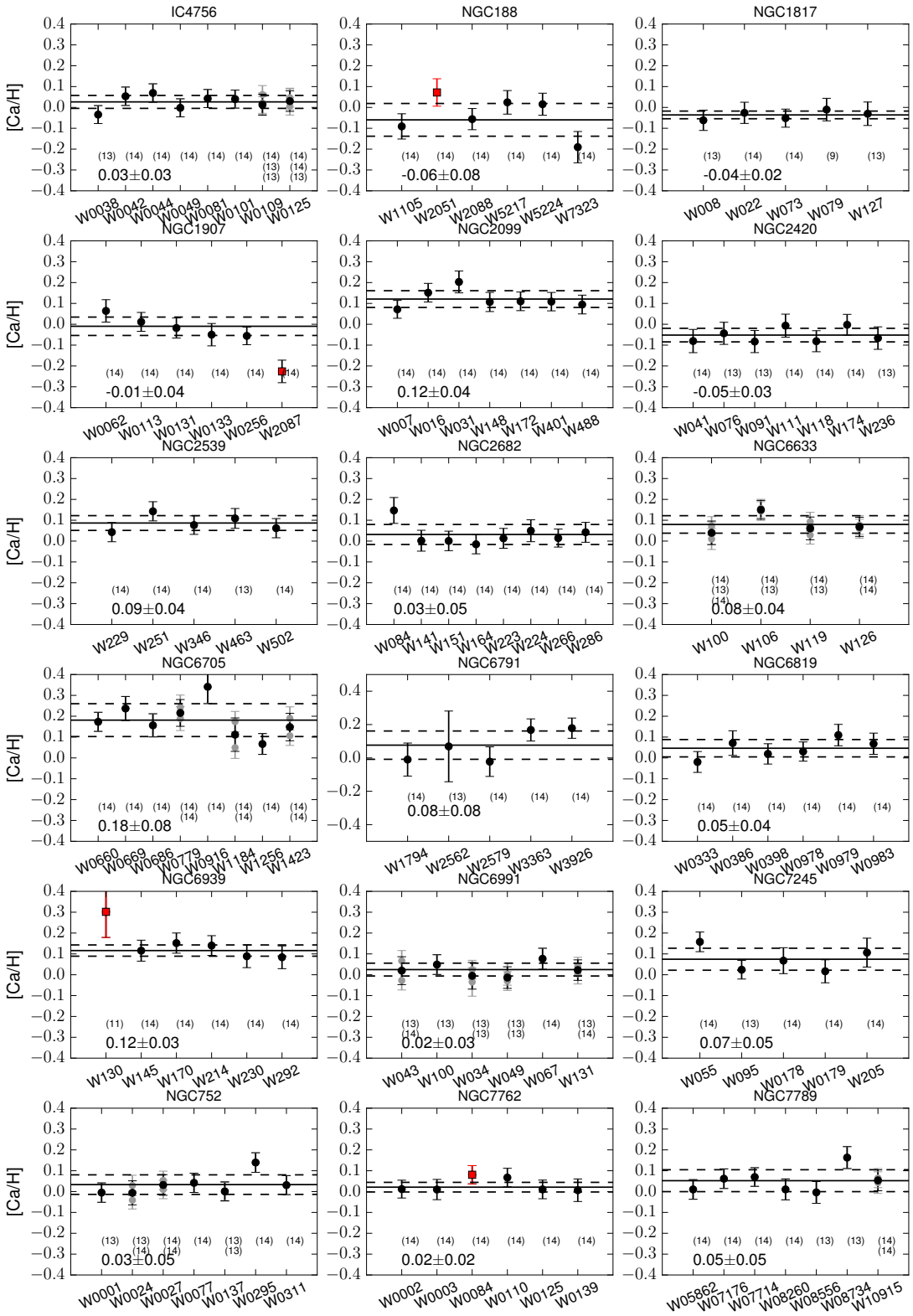

Figure 6.9. As in Fig. 6.6, for Ca.

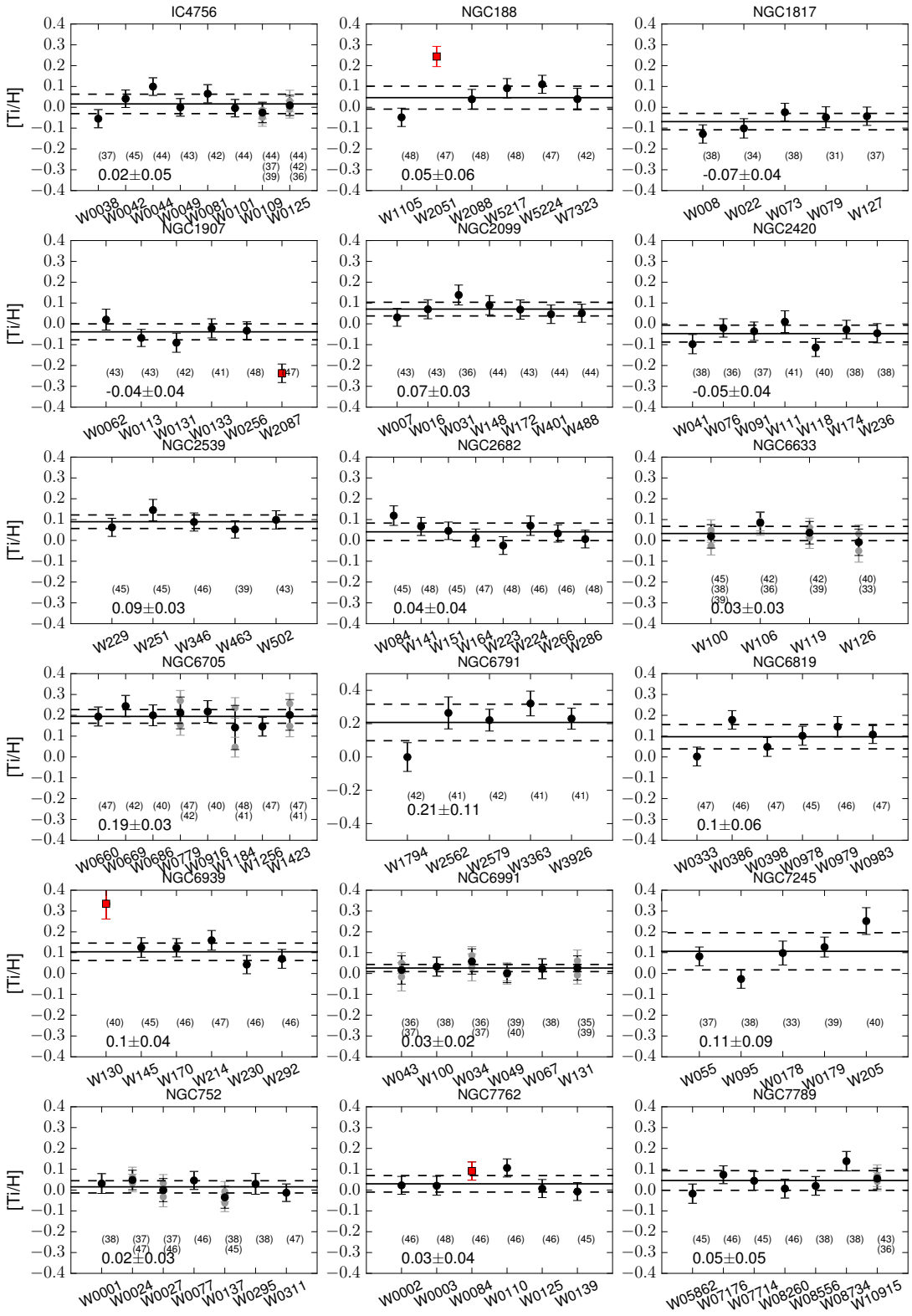

Figure 6.10. As in Fig. 6.6, for Ti.

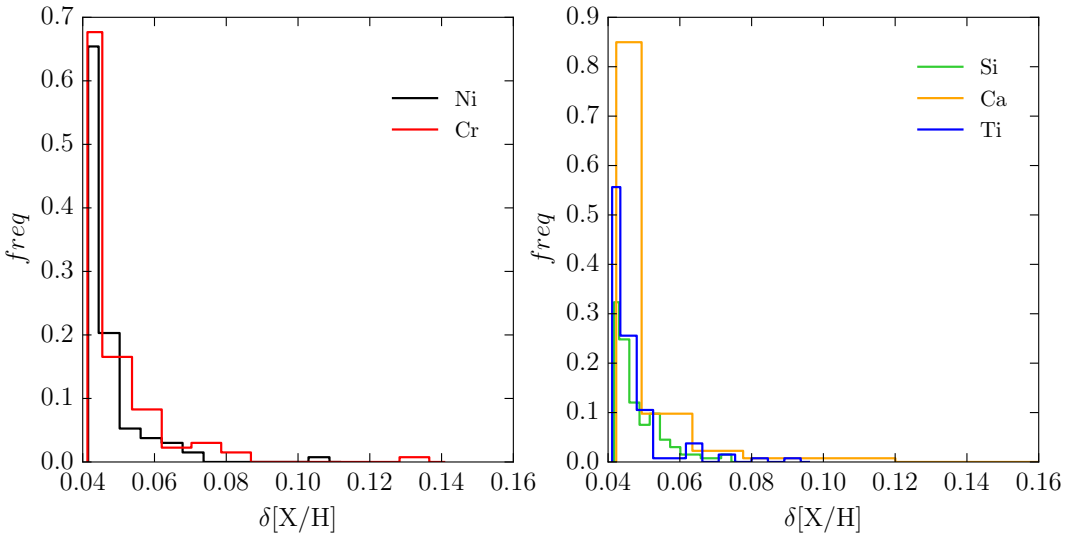

Figure 6.11. Normalized distribution of Ni, Cr, Si, Ca and Ti errors in abundance for all the spectra.

From the comparison with the reference values from Jofré et al. (2015) in general we obtain an excellent agreement within 1σ of the uncertainties, this means differences at the level of 0.05 dex. Cr and Si present the highest discrepancies. For Cr we obtain a difference of 0.1 and 0.17 dex for Arcturus and μ-Leo, respectively, in the direction reference−OCCASO. We also find, only for μ-Leo, a difference in Si of 0.17 dex. The values from Jofré et al. (2015) are calculated under LTE assumption, yet they list NLTE corrections which are lower than 0.09 dex for these two elements and stars. We have not found a convincing explanation for this though the determination of abundances in μ-Leo can be difficult for its high metallicity. Previous values in the literature for Cr and Si in Arcturus and μ-Leo:

– [Cr/H] in Arcturus. Ramírez and Allende Prieto (2011) find −0.57, Luck and Heiter (2005) find −0.55, and Thevenin (1998) find −0.2. This points towards a slight underestimation of our Cr abundance (−0.68) in Arcturus

– [Cr/H] in μ-Leo. Luck and Heiter (2005) find 0.37 and Thevenin (1998) find 0.1. Our value of 0.17 is in between them.

– [Si/H] for μ-Leo. Luck and Heiter (2005) find 0.54, Thevenin (1998) find 0.45, and McWilliam (1990) find 0.69. Comparing our result of 0.35 with all the rest, we find again a slight underestimation in μ-Leo. [Si/H] in Arcturus is much more consistent with Jofré et al. (2015), and also with previous values.

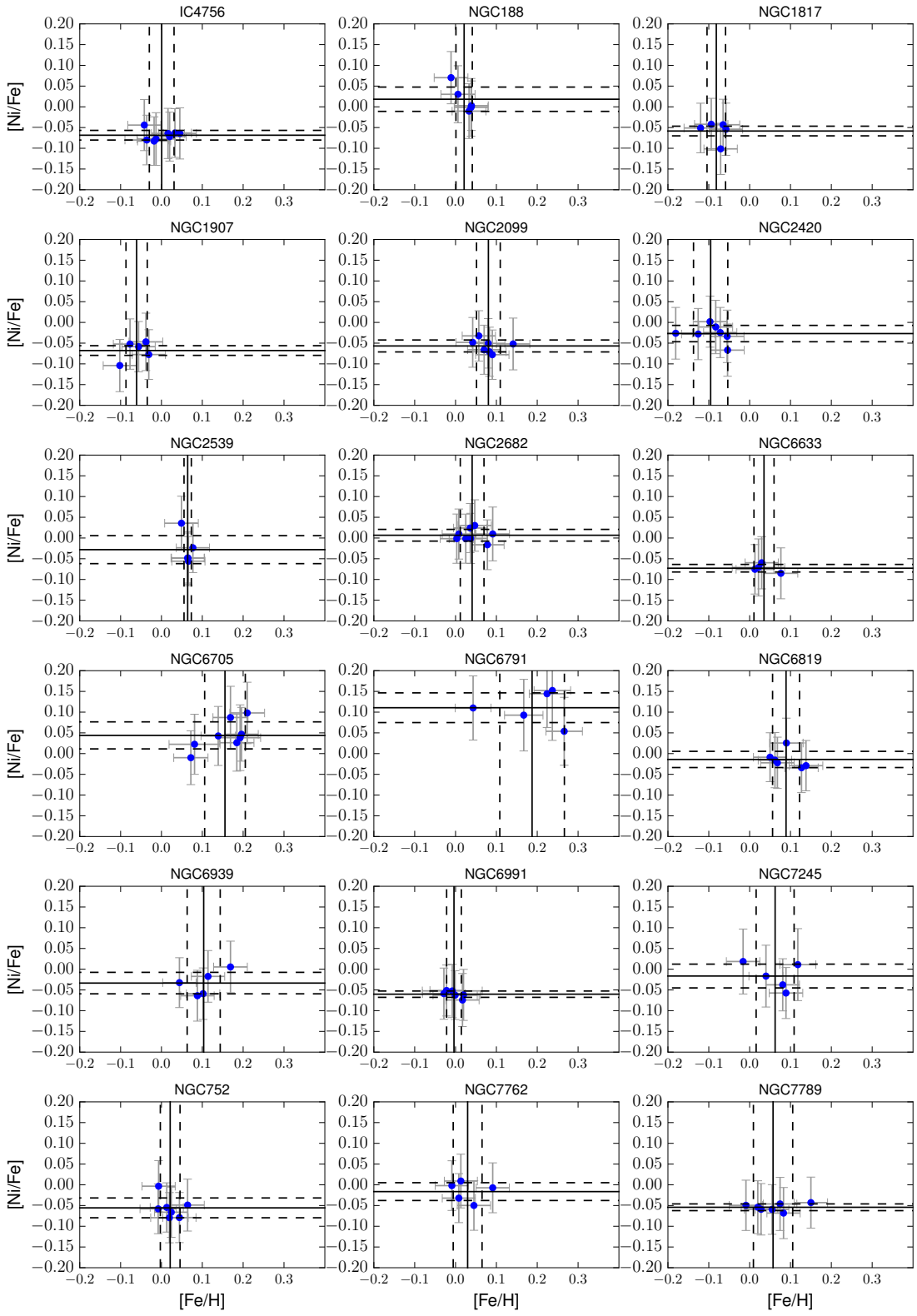

Figure 6.12. Ni abundance ratios obtained for the 18 studied OCs as a function of Fe abundance. The black solid and dashed lines indicate the mean and 1σ level of abundance.

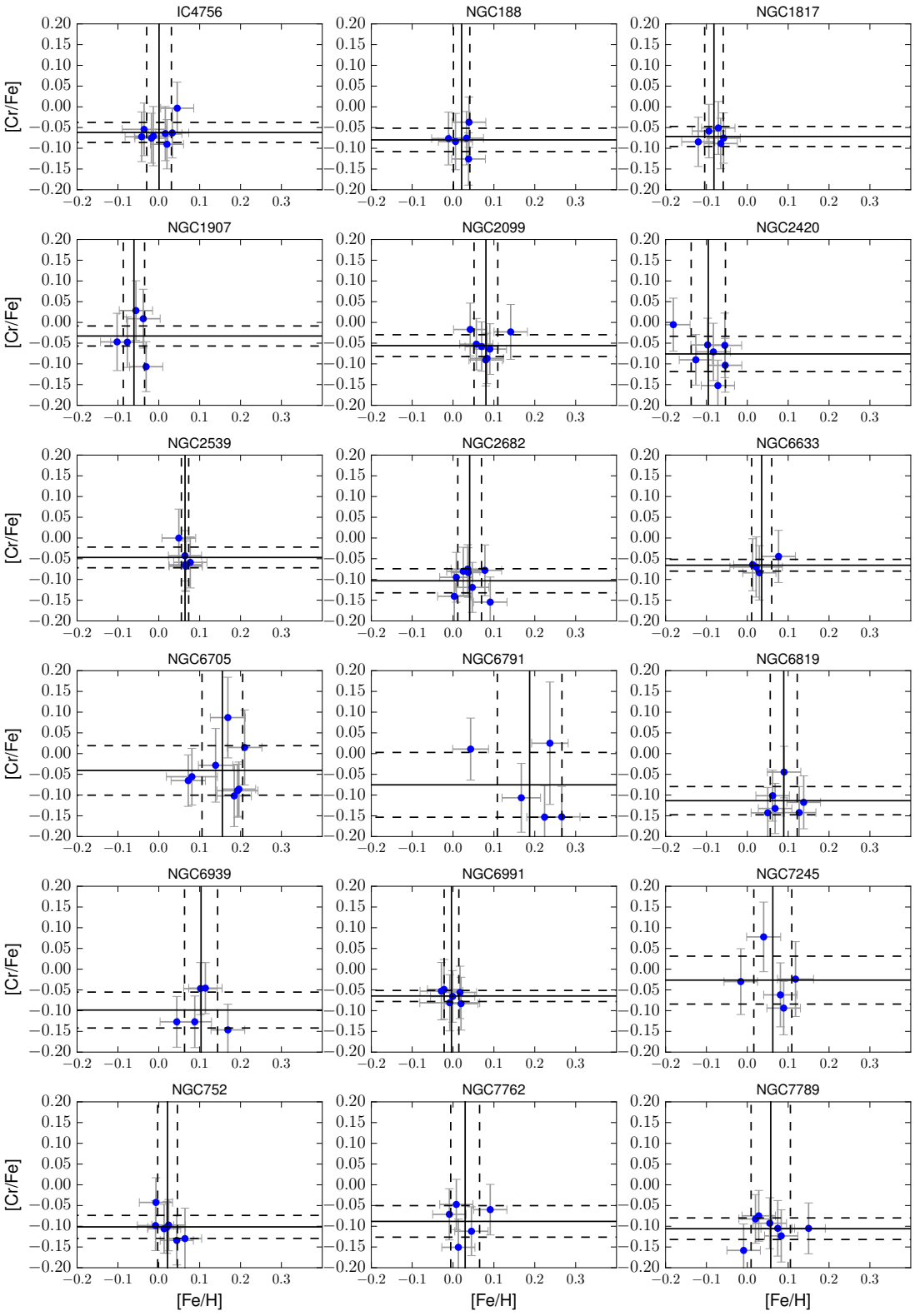

Figure 6.13. As in Fig. 6.12, for Cr.

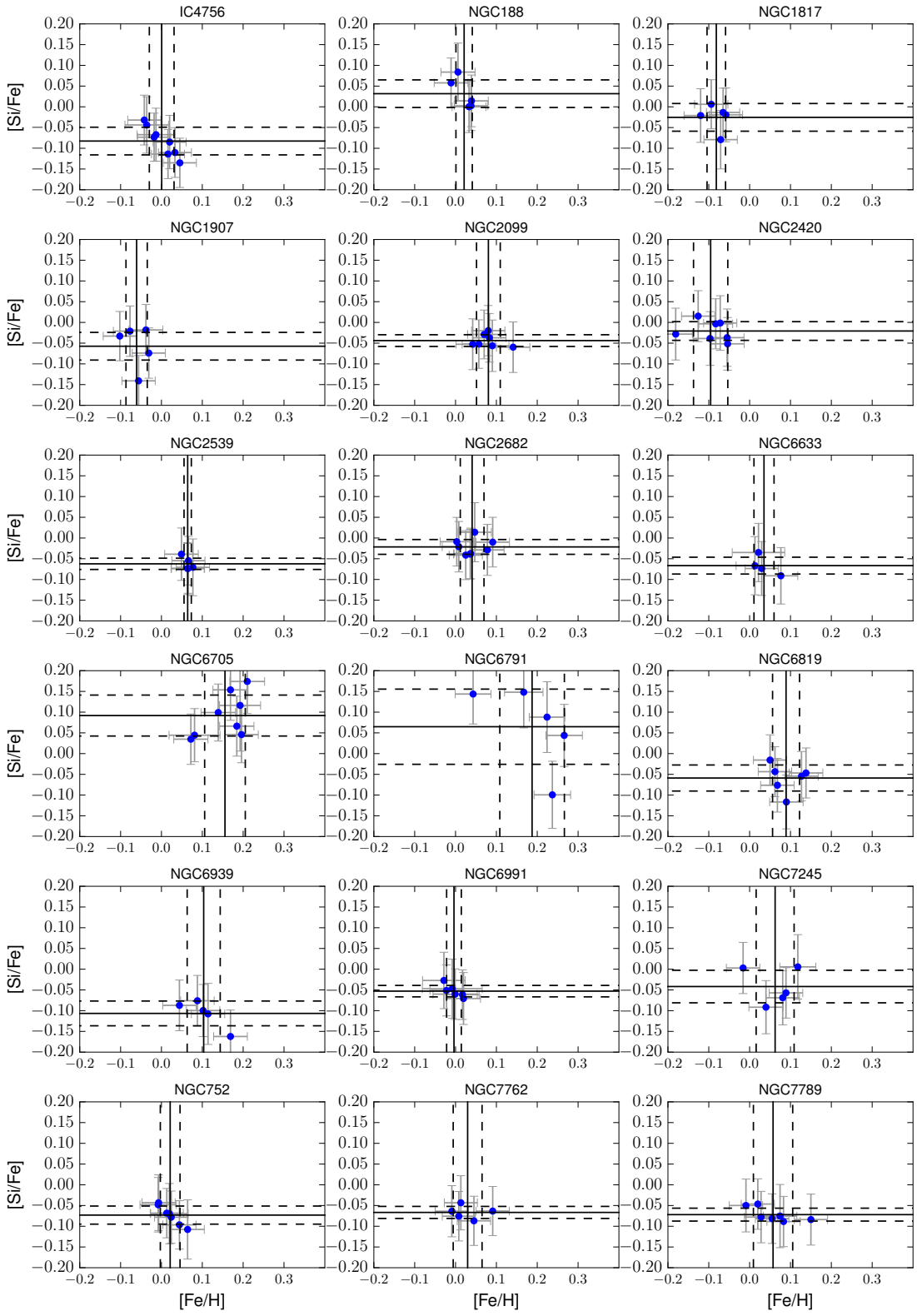

Figure 6.14. As in Fig. 6.12, for Si.

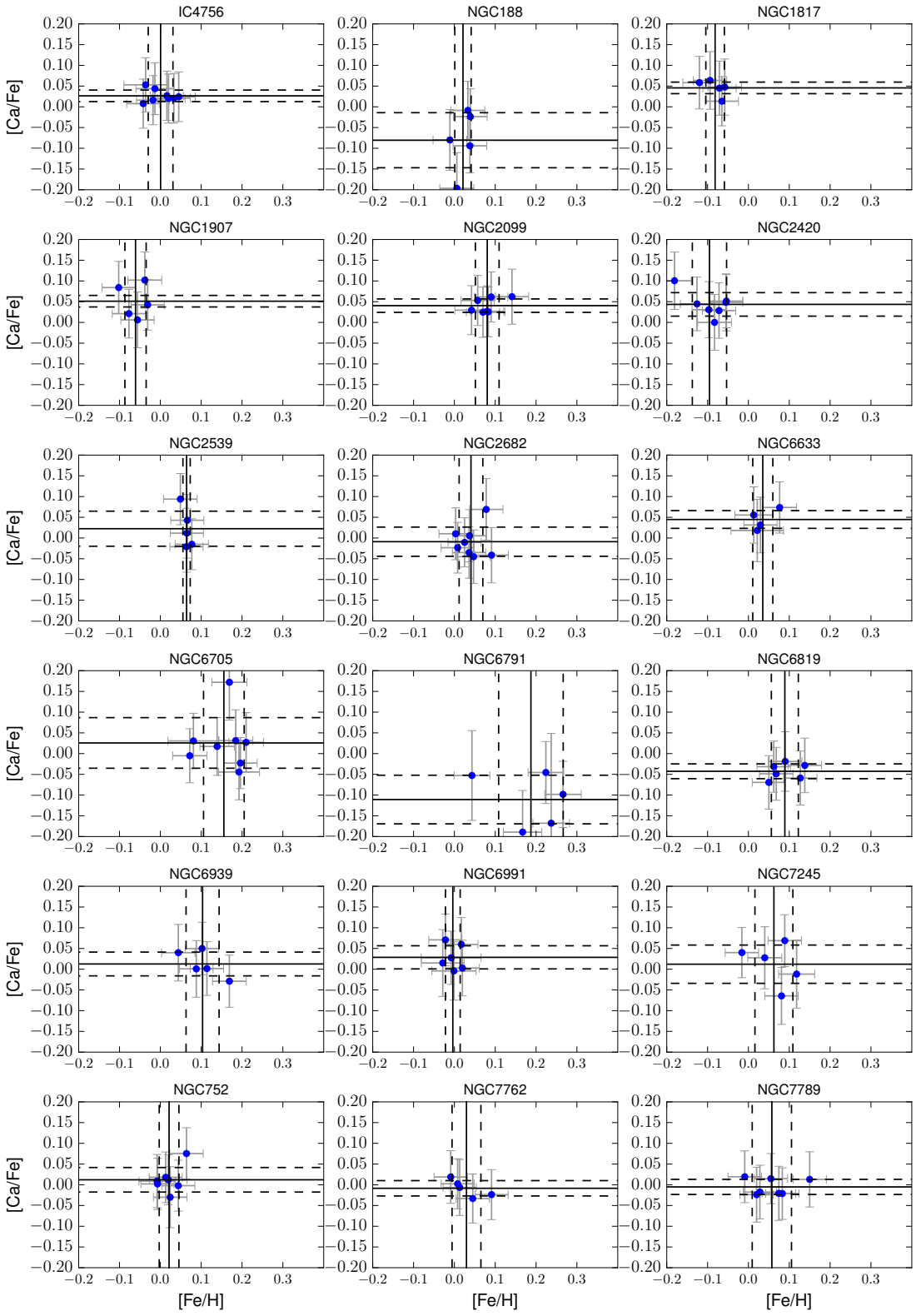

Figure 6.15. As in Fig. 6.12, for Ca.

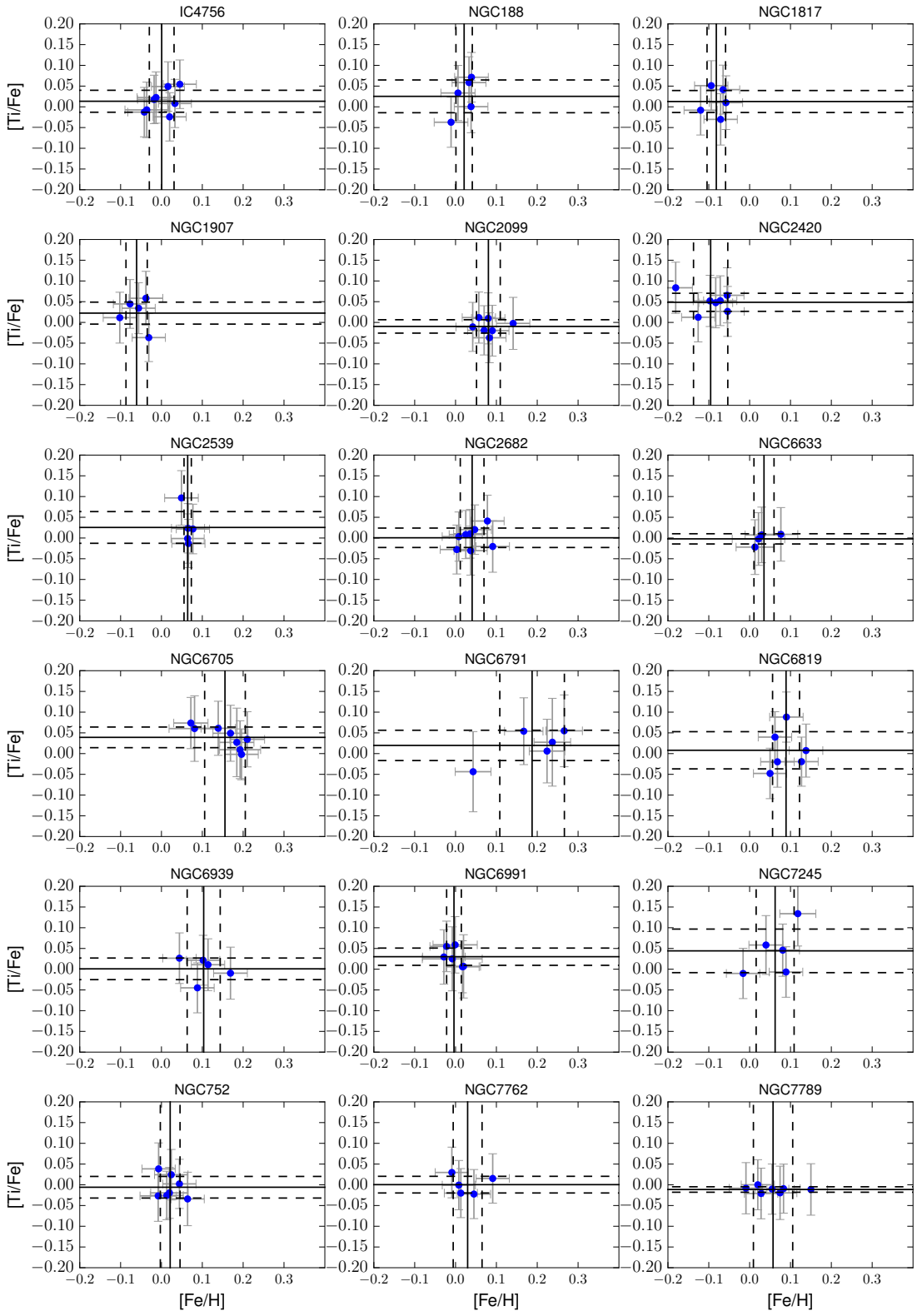

Figure 6.16. As in Fig. 6.12, for Ti.

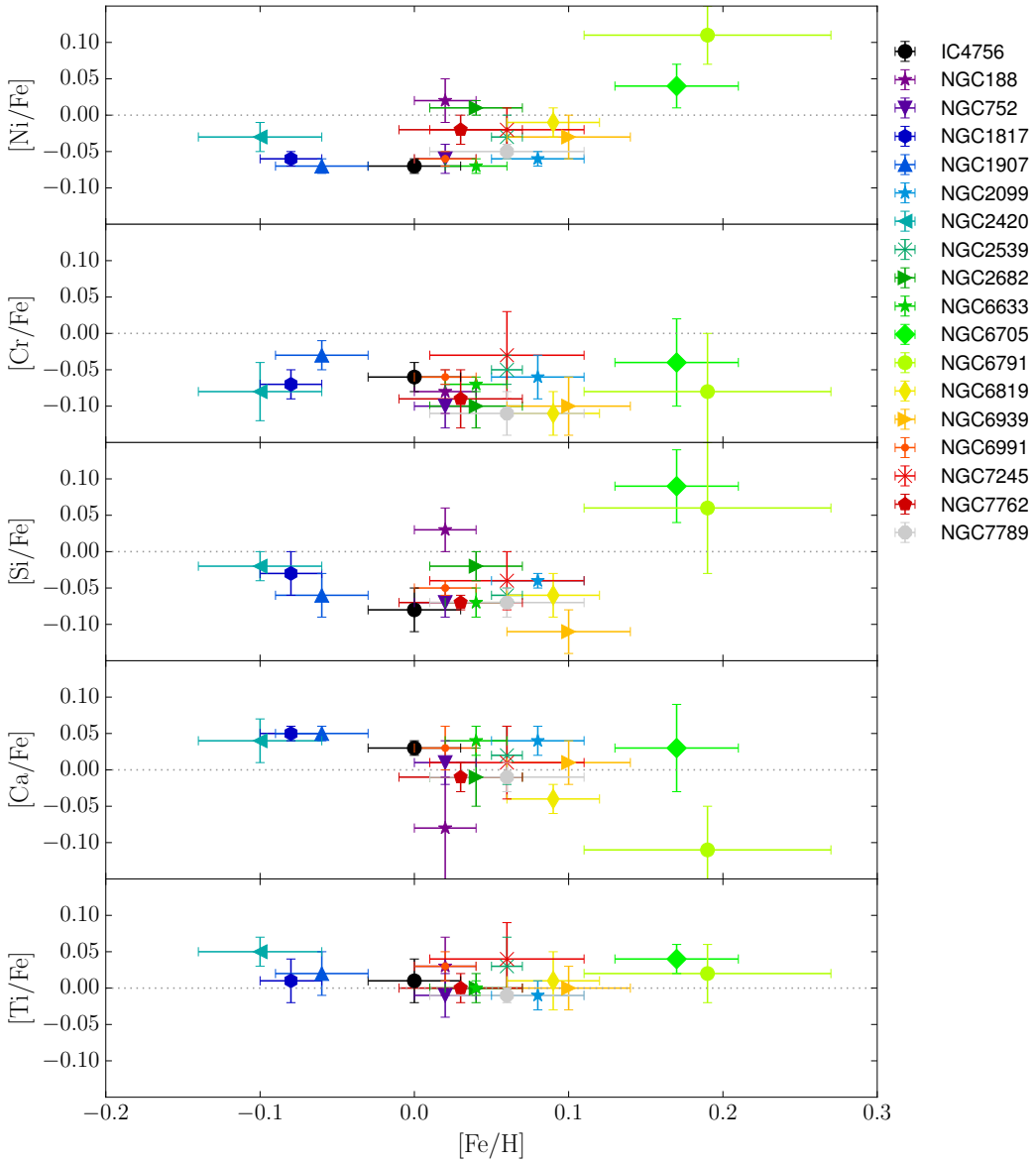

Figure 6.17. Abundance ratios [Ni/Fe], [Cr/Fe], [Si/Fe], [Ca/Fe], [Ti/Fe] as a function of the [Fe/H] of the studied clusters.

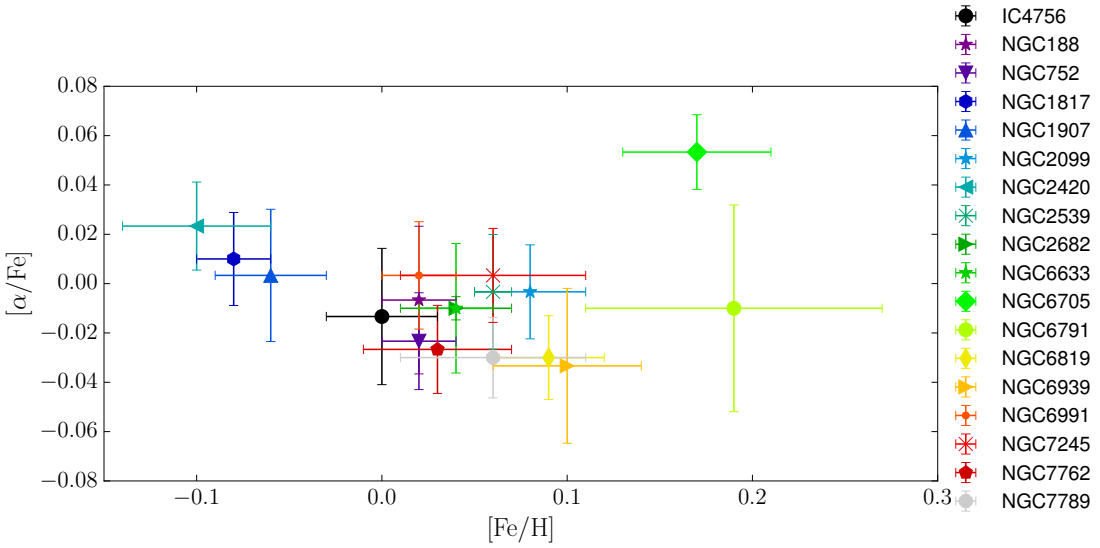

Figure 6.18. [α/Fe] abundances (calculated as the mean of [Si/Fe], [Ca/Fe] and [Ti/Fe]) as a function of the [Fe/H] of the studied clusters.

Table 6.3. Ni, Cr, Si, Ca and Ti abundances for Arcturus and μ-Leo obtained from OCCASO data using the EW method. The errors indicate the dispersion found between the three instruments, in parentheses the mean of the quoted errors for the three instruments. The reference values are from Jofré et al. (2015), the listed errors from reference are their line scatter divided by the square root of the number of lines.

Star	Orig	[Ni/H]	[Cr/H]	[Si/H]	[Ca/H]	[Ti/H]
Arcturus	Ref	-0.487 ± 0.020	-0.582 ± 0.018	-0.252 ± 0.013	-0.405 ± 0.044	-0.313 ± 0.013
	here	-0.51 ± 0.02 (0.06)	-0.68 ± 0.03 (0.06)	-0.29 ± 0.02 (0.06)	-0.43 ± 0.02 (0.06)	-0.28 ± 0.02 (0.06)
μ-Leo	Ref	0.324 ± 0.058	0.335 ± 0.022	0.522 ± 0.029	0.280 ± 0.067	0.322 ± 0.022
	here	0.39 ± 0.04 (0.06)	0.17 ± 0.07 (0.07)	0.35 ± 0.01 (0.07)	0.25 ± 0.08 (0.08)	0.35 ± 0.08 (0.07)

Table 6.4. Ni, Cr, Si, Ca, Ti mean results from EW analysis of the 18 OCs computed as the mean of the bona fide member stars. Dispersions are listed as errors. The number of stars to compute the mean in each cluster is indicated.

Cluster	[Ni/H]	[Cr/H]	[Si/H]	[Ca/H]	[Ti/H]	[Ni/Fe]	[Cr/Fe]	[Si/Fe]	[Ca/Fe]	[Ti/Fe]	Stars
IC4756	-0.07 ± 0.03	-0.06 ± 0.05	-0.08 ± 0.01	0.03 ± 0.03	0.02 ± 0.05	-0.07 ± 0.01	-0.06 ± 0.02	-0.08 ± 0.03	0.03 ± 0.01	0.01 ± 0.03	8
NGC188	0.04 ± 0.01	-0.06 ± 0.03	0.05 ± 0.02	-0.06 ± 0.08	0.05 ± 0.06	0.02 ± 0.03	-0.08 ± 0.03	0.03 ± 0.03	-0.08 ± 0.07	0.03 ± 0.04	5
NGC752	-0.03 ± 0.03	-0.08 ± 0.02	-0.05 ± 0.00	0.03 ± 0.05	0.02 ± 0.03	-0.06 ± 0.02	-0.10 ± 0.03	-0.07 ± 0.02	0.01 ± 0.03	-0.01 ± 0.03	7
NGC1817	-0.14 ± 0.03	-0.15 ± 0.03	-0.11 ± 0.03	-0.04 ± 0.02	-0.07 ± 0.04	-0.06 ± 0.01	-0.07 ± 0.02	-0.03 ± 0.03	0.05 ± 0.01	0.01 ± 0.03	5
NGC1907	-0.13 ± 0.04	-0.09 ± 0.05	-0.12 ± 0.05	-0.01 ± 0.04	-0.04 ± 0.04	-0.07 ± 0.01	-0.03 ± 0.02	-0.06 ± 0.03	0.05 ± 0.01	0.02 ± 0.03	5
NGC2099	0.02 ± 0.03	0.02 ± 0.04	0.04 ± 0.03	0.12 ± 0.04	0.07 ± 0.03	-0.06 ± 0.01	-0.06 ± 0.03	-0.04 ± 0.01	0.04 ± 0.02	-0.01 ± 0.02	7
NGC2420	-0.12 ± 0.04	-0.17 ± 0.04	-0.12 ± 0.04	-0.05 ± 0.03	-0.05 ± 0.04	-0.03 ± 0.02	-0.08 ± 0.04	-0.02 ± 0.02	0.04 ± 0.03	0.05 ± 0.02	7
NGC2539	0.04 ± 0.03	0.02 ± 0.02	0.00 ± 0.01	0.09 ± 0.04	0.09 ± 0.03	-0.03 ± 0.03	-0.05 ± 0.02	-0.06 ± 0.01	0.02 ± 0.04	0.03 ± 0.04	5
NGC2682	0.05 ± 0.03	-0.06 ± 0.04	0.02 ± 0.04	0.03 ± 0.05	0.04 ± 0.04	0.01 ± 0.01	-0.10 ± 0.03	-0.02 ± 0.02	-0.01 ± 0.04	0.00 ± 0.02	8
NGC6633	-0.04 ± 0.02	-0.03 ± 0.04	-0.03 ± 0.02	0.08 ± 0.04	0.03 ± 0.03	-0.07 ± 0.01	-0.07 ± 0.01	-0.07 ± 0.02	0.04 ± 0.02	-0.00 ± 0.01	4
NGC6705	0.20 ± 0.08	0.11 ± 0.08	0.25 ± 0.09	0.18 ± 0.08	0.19 ± 0.03	0.04 ± 0.03	-0.04 ± 0.06	0.09 ± 0.05	0.03 ± 0.06	0.04 ± 0.02	8
NGC6791	0.30 ± 0.09	0.11 ± 0.08	0.25 ± 0.08	0.08 ± 0.08	0.21 ± 0.11	0.11 ± 0.04	-0.08 ± 0.08	0.06 ± 0.09	-0.11 ± 0.06	0.02 ± 0.04	5
NGC6819	0.08 ± 0.03	-0.02 ± 0.05	0.03 ± 0.04	0.05 ± 0.04	0.10 ± 0.06	-0.01 ± 0.02	-0.11 ± 0.03	-0.06 ± 0.03	-0.04 ± 0.02	0.01 ± 0.04	6
NGC6939	0.07 ± 0.06	0.00 ± 0.06	-0.00 ± 0.02	0.12 ± 0.03	0.10 ± 0.04	-0.03 ± 0.03	-0.10 ± 0.04	-0.11 ± 0.03	0.01 ± 0.03	0.00 ± 0.03	5
NGC6991	-0.06 ± 0.01	-0.07 ± 0.02	-0.06 ± 0.01	0.02 ± 0.03	0.03 ± 0.02	-0.06 ± 0.01	-0.06 ± 0.01	-0.05 ± 0.01	0.03 ± 0.03	0.03 ± 0.02	6
NGC7245	0.05 ± 0.04	0.04 ± 0.06	0.02 ± 0.06	0.07 ± 0.05	0.11 ± 0.09	-0.02 ± 0.03	-0.03 ± 0.06	-0.04 ± 0.04	0.01 ± 0.05	0.04 ± 0.05	5
NGC7762	0.01 ± 0.04	-0.06 ± 0.06	-0.04 ± 0.04	0.02 ± 0.02	0.03 ± 0.04	-0.02 ± 0.02	-0.09 ± 0.04	-0.07 ± 0.01	-0.01 ± 0.02	0.00 ± 0.02	5
NGC7789	0.00 ± 0.05	-0.05 ± 0.06	-0.01 ± 0.04	0.05 ± 0.05	0.05 ± 0.05	-0.05 ± 0.01	-0.11 ± 0.03	-0.07 ± 0.02	-0.01 ± 0.02	-0.01 ± 0.01	7

6.3 CONCLUSIONS

We calculate [Fe/H] abundances for all OCCASO stars with both methods GALA and iSpec, using the average values of T_{eff} and $\log g$ calculated in Chapter 5. We assess the precision we obtain for the final abundances, and we compare the results obtained from both methods for all OCCASO spectra.

We do several additional tests to investigate the performance of the two methods when calculating iron abundances. We use the GBS sample to derive [Fe/H] in different conditions: (a) fixing T_{eff} and $\log g$ to their reference value in Heiter et al. (2015b); (b) fixing also the microturbulence; (c) only using the lines in common to calculate [Fe/H]; (d) only use the common lines and force the synthesis method not to reproduce blends. We found the best agreement in the (d) case with an offset of -0.02 ± 0.02. In all cases uncertainties are small, being the worst case 0.09 dex, when fixing the microturbulence parameter.

We discuss the [Fe/H] abundances obtained for each OC to perform an accurate membership selection. From bona fide member stars we obtain a final value of [Fe/H] per OC using each method. We obtain cluster dispersions ranging 0.01-0.08 dex from the EW analysis, and 0.01-0.11 dex from the SS analysis. NGC 6791 and NGC 6705 are the most metal-rich clusters in our analysis with [Fe/H]$= 0.19 \pm 0.08$ and 0.17 ± 0.04, respectively from GALA analysis, and [Fe/H]$= 0.13 \pm 0.11$ and 0.04 ± 0.05 from iSpec analysis. The most metal poor clusters are NGC 2420, NGC 1817 and NGC 1907 with [Fe/H]$= -0.10 \pm 0.04$, -0.08 ± 0.02 and -0.06 ± 0.03, respectively from GALA analysis, and [Fe/H]$= -0.14 \pm 0.03$, -0.11 ± 0.03 and -0.17 ± 0.03 from iSpec analysis.

We make an extensive comparison with literature values which provides an independent consistency test for our analysis in spite of the inhomogeneity of the literature. We found overall offsets of 0.02 ± 0.09 dex (EW), -0.06 ± 0.09 dex (SS), well within the uncertainties.

Using an accurate linelist we calculate Ni, Cr, Si, Ca and Ti abundances using the EW method. We specifically compare the results of [X/H] from Arcturus and μ-Leo with previous values in the literature obtaining very good agreement in all elements except for Cr. We derive cluster average results of [Ni/H], [Cr/H], [Si/H], [Ca/H] and [Ti/H] and its abundance ratios with respect to Fe. We also calculate abundance ratios respect to iron star by star of all elements. We see that all clusters present homogeneous abundance patters except NGC 6791 (for which we have larger errors also). The largest dispersions in [X/Fe] excluding this cluster are 0.03 (Ni), 0.06 (Cr), 0.05 (Si), 0.07 (Ca), 0.05 (Ti). We analyse the average cluster [α/Fe] abundances respect to [Fe/H], which shows a decreasing trend between [Fe/H] -0.1 and 0.1 dex. NGC 6705 is very well above this trend showing a clear α-enhancement. This cluster is further analysed in Chapter 7.

Part III

CHEMICAL EVOLUTION OF THE DISC AND GENERAL CONCLUSIONS

7

CHEMICAL EVOLUTION OF THE GALACTIC DISC

In this Chapter we analyse the obtained results of radial velocities (Chapter 4) and abundances (Chapter 6) of the OCCASO OCs in the context of the Galactic disc. First, in Section 7.1 we inspect the radial and vertical gradients of iron abundance, and we do a comparison with chemical evolution models. Since OCCASO OCs have a limited range in age and distance to the Galactic center, in Section 7.2 we select two complementary samples of 12 inner disc and 10 anticenter OCs analysed similarly as in OCCASO to explore a wider range in the iron gradient. We also use the age span of this whole sample of 40 OCs to explore the age-metallicity relation. We use our results from Chapter 4 concerning orbits to help analysing the gradients here. In Section 7.3 we analyse in detail the abundance patterns of NGC 6705 (M 11) given its α-enhancement derived in the previous chapter. We include an extensive inspection of two additional α-elements (Mg and O). To investigate the origin of the α-enhancement we do a detailed analysis of the possible orbits of this OC to trace its most probable place of birth.

7.1 GLOBAL TRENDS USING OCCASO RESULTS

The trends in the chemical abundances with Galactocentric radius provide strong constrains on the models of Galactic chemical evolution as far as the disc formation mechanism is concerned. A far stronger constrain is the variation of this trend with age. In the previous chapters we have derived atmospheric parameters and Fe, Ni, Cr, Si, Ca and Ti abundances from 18 OCs in an homogeneous way. The analysed OCs cover a range in Galactocentric radius of $6.8 < R_{GC} < 11$ kpc, and span ages between 0.3 and 10.2 Gyr. All the clusters in the sample have $|z| < 1$ kpc (see Table 2.2).

In Fig. 7.1 we show the [Fe/H] vs R_{GC} distribution of the OCs in 3 bins of age, along with the pure chemical evolution model for the thin disc by Chiappini (2009), and the chemo-dynamical thin-disc model by Minchev, Chiappini, and Martig (2013, 2014, MCM hereafter). In the right of Fig. 7.1 we show the results of [Fe/H] derived using the EW method and the SS method.

Chiappini (2009) assumes an exponentially decreasing infall rate of metal poor gas $f(t)$ and star formation law $\psi(t)$:

$$f(t) = A \exp(-t/\tau) \tag{7.1}$$

$$\psi(t) = B(R)\,\Sigma_g^{1.5} \tag{7.2}$$

where $\tau = 7$ Gyr, compatible with infall rates obtained by cosmological assumptions (Colavitti, Matteucci, and Murante 2008), $B(R)$ is related to the star formation efficiency and the total mass density at each Galactocentric radii R, and Σ_g is the gas surface mass density.

The MCM model is a fusion of the chemical evolution model of Chiappini (2009) and a high-resolution simulation at a cosmological context, which includes dynamical effects such as radial migration and heating. The abundances of both models are scaled such that the Solar abundance matches the model at the age of the Sun (4.5 Gyr) at the most probable birth position of the Sun (2 kpc closer to the Galactic centre than today; see Minchev, Chiappini, and Martig 2013). This calibration agrees very well with the abundance scale set by local disc Cepheids (Genovali et al. 2013). The chemical model is shifted by a fix value (+0.1 dex) to fit the Cepheids gradient.

Our statistics is not large but our uncertainties in iron abundance (up to 0.05 dex excluding NGC 6791, see Table 6.2) and in ages compared with field stars are small, and this makes our conclusion strong. It can be clearly seen that the younger OCs fit perfectly the pure chemical gradient (left panel in Fig. 7.1). As OCs get older they start to deviate from the chemical model, and in the oldest bin of age they fall out of it by more than 3σ. This deviation though, can be explained by the chemodynamical model which includes radial mixing, since in fact there are blue points at the position of the two oldest clusters. Anyhow, the three oldest OCs are still clearly above the bulk of the MCM distribution. Probably a fine tunning of the assumed free parameters of the dynamical effects that the MCM model takes into account can make the distribution fit the position that the OCs are tracing. Of course the higher than expected metallicities of the oldest OCs could also be explained by a model that predicts a gradient that does not decrease with lookback time.

In Fig. 7.2 we show the [Fe/H] vs height above the plane $|z|$ distribution of the 18 OCs in the same bins of age as in Fig. 7.1. In the younger bin it is seen a very strong correlation until $|z| \sim 100$ pc of growing [Fe/H] with $|z|$. In the intermediate bin the OCs show a rather flat distribution with the two clusters at $z > 400$ pc slightly down around 0.1 dex. The distribution of the three older OCs is also compatible with a flat trend, but we suffer from low statistics.

Table 7.1. [Fe/H] determinations by OCCASO-EW and GES of the two OCs in common. The difference Δ in the direction OCCASO-GES is indicated.

OC	$[Fe/H]_{OCCASO}$	$[Fe/H]_{J16}$	Δ
NGC 6633	0.03 ± 0.02	-0.05 ± 0.06	0.08
NGC 6705	0.17 ± 0.04	0.14 ± 0.06	0.03

7.2 GLOBAL TRENDS WITH A SAMPLE OF 40 OCS

To enlarge the statistics of OCCASO we have investigated the [Fe/H] relations traced by the OCCASO OCs in addition to: 12 inner disc OCs from GES (Jacobson et al. 2016, J16 hereafter), and 10 anticentre OCs (Cantat-Gaudin et al. 2016, CG16 hereafter). The three studies are complementary in the age and R_{GC} range. They use similar high-resolution spectra and similar wavelength coverage. The spatial distribution of these OCs is plotted in Fig. 7.3.

In this section we use only the OCCASO-EW results for [Fe/H]. In this way the spectroscopic analysis is done in the three samples in a similar way using: the same line list (Heiter et al. 2015a)[1] and model atmospheres (MARCS; Gustafsson et al. 2008). The analysis of CG16 and OCCASO are even more similar since they use `DOOp` (Cantat-Gaudin et al. 2014a) + `FAMA` (Magrini et al. 2013), and `DOOp` + `GALA` (Mucciarelli et al. 2013), respectively, which are two very similar methods to derive abundances from EW. Both `GALA` and `FAMA` deliver similar results as the final GES adopted values especially in the analysis of red giants (Smiljanic et al. 2014). However, the results from GES are derived using a mixture of different methods, that possibly hides internal systematics.

We have two OCs in common between OCCASO and J16, NGC 6705 and NGC 6633 which allow for a more detailed comparison between the two studies (these OCs are remarked in Fig. 7.4). In Table 7.1 we list the two determinations of the iron abundances. Judging by these two OCs, J16 gives lower abundances than OCCASO. The differences are of the same order as the offset found for the two OCCASO methods in Section 6.1.1. More OCs in common would help in deriving conclusions. For now, when analysing the results of the complete sample, one has to be conscious that probably an offset of the same order as found between the EW and SS methods could exist between OCCASO and GES datasets.

1 Each method/author uses its own line selection.

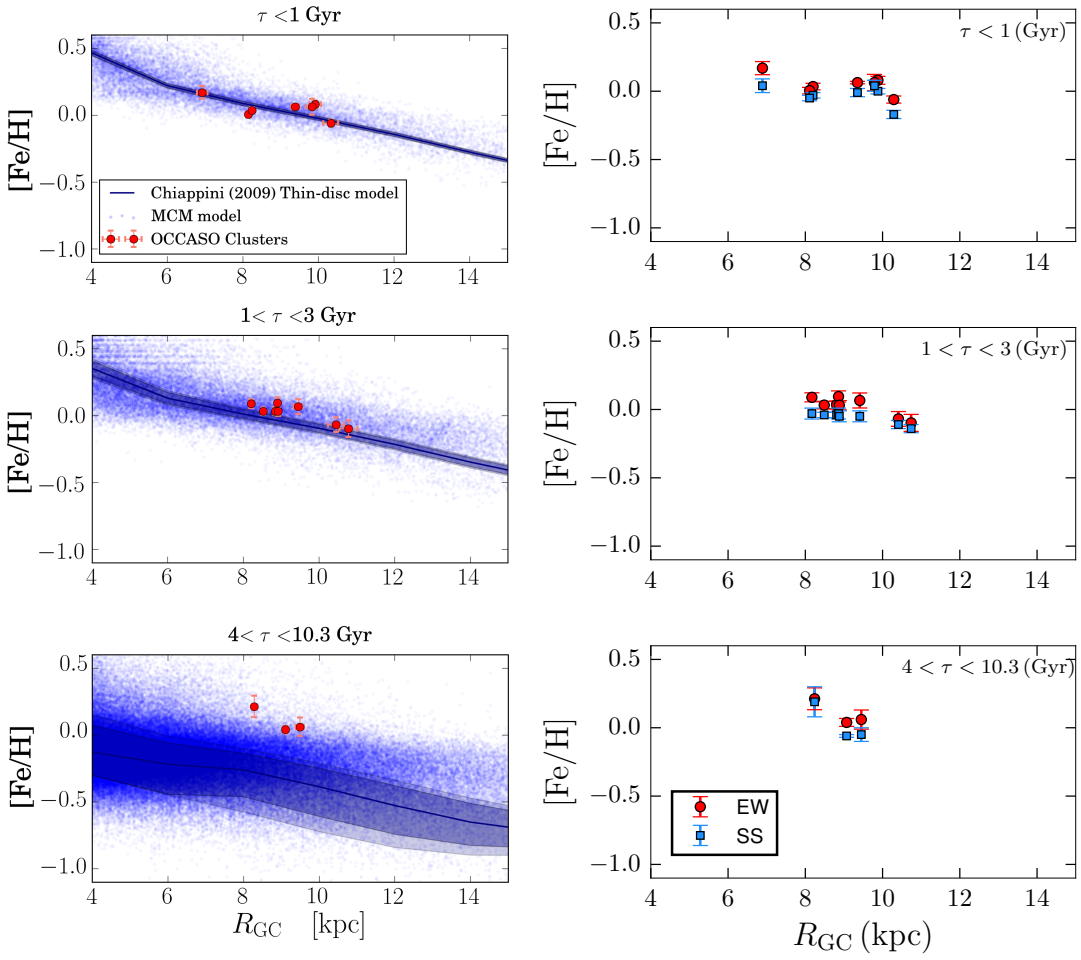

Figure 7.1. In the left [Fe/H] (EW) vs R_{GC} distribution of the 18 OCs in three bins of age. We overplot the pure chemical-evolution model for the thin disc of Chiappini (2009) plotted as dark and light blue bands, and the N-body chemo-dynamical model by Minchev, Chiappini, and Martig (2013, 2014, p. MCM) plotted as individual blue dots. In the right the distributions as deduced by the EW (red) and the SS (green) determinations of [Fe/H], for comparison.

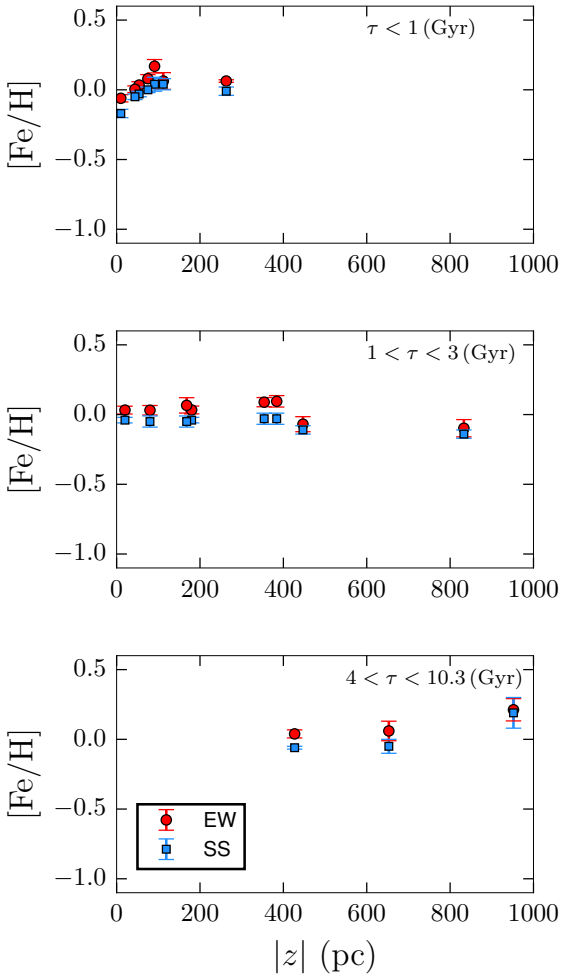

Figure 7.2. [Fe/H] as a function of |z|. The upper plot includes the younger OCs (t < 1 Gyr), the middle plot includes OCs of ages 1 < t < 4 Gyr, the bottom plot shows the older OCs of ages 4 < t < 10 Gyr.

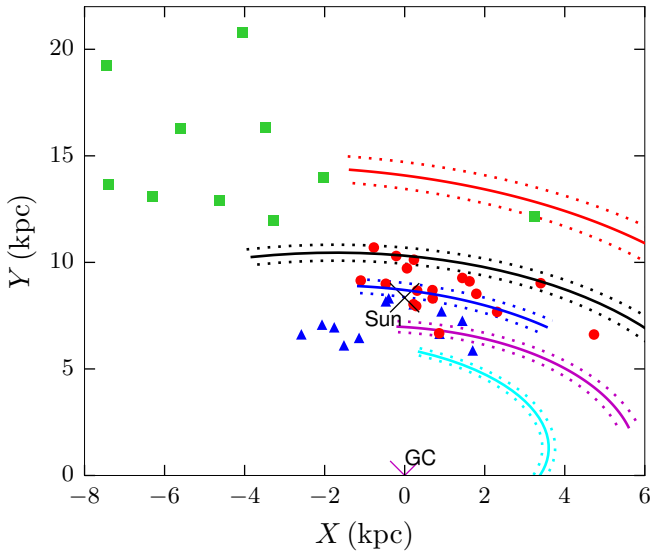

Figure 7.3. Spatial distribution of the 40 OCs: 18 from OCCASO (red dots), 12 from GES (Jacobson et al. 2016, blue triangles) and 10 from Cantat-Gaudin et al. (2016, green squares). Galactic center is at $(0, 0)$ and the Sun is located at $(0, 8.5)$ kpc. Galactic rotation goes from left to right. Spiral arms are plotted with the same parametes as in Fig. 4.5.

Trend with Galactocentric radius

We present in Fig. 7.4 [Fe/H] vs R_{GC} of the complete sample in the same three bins of age as in Fig. 7.1 of the complete sample. Fitting a linear function to the subsamples we find the slopes[2]:

- For the younger age bin $Age < 1$ Gyr, which covers between $6 < R_{GC} < 14$ kpc, we obtain -0.052 ± 0.010 dex kpc^{-1} consistent with the one traced by Cepheids, -0.061 ± 0.019 and -0.060 ± 0.002 dex kpc^{-1}, according to Lemasle et al. (2007); and Genovali et al. (2014), respectively. It is also consistent with previous determination of the gradient traced by OCs, such as -0.053 ± 0.029 dex kpc^{-1} by Magrini et al. (2009).

- For $1 < Age < 4$ Gyr, we can fit a linear function with a slope of -0.053 ± 0.005 dex kpc^{-1}. This region comprises a slightly larger range in Galactocentric radius than the previous one, $6 < R_{GC} < 18$ kpc. Several studies suggest that there is a change in slope at $R_{GC} < 11$ kpc, where the inner gradient is steeper than the outer one. For example, Sestito et al. (2008) found -0.17 ± 0.02 dex kpc^{-1} for the inner region, and a slope consistent with zero for the outer region, using high-resolution results from several sources in the literature (not homogeneous).

2 Uncertainties in the slopes are calculated using standard prescriptions for linear fits: $\sqrt{\frac{\frac{1}{n-2}\Sigma_i (y_i - \hat{y}_i)^2}{\Sigma_i (x_i - \bar{x})^2}}$.

In this age bin we only have 3 OCs in the outer disc, which could show a slope compatible with zero taking into account their errors.

– For the older age bin $4 < Age < 10.3$ Gyr, we only have seven clusters covering a large range in radius: $9 < R_{GC} < 22$ kpc. Its overall shape seems compatible with a linear function for which we obtain a slope of -0.050 ± 0.008 dex kpc^{-1}. A linear fit to the only 4 OCs that we have in this age bin for the outer disc, gives a slope of -0.029 ± 0.012 dex kpc^{-1}, not compatible with zero and slightly steeper than previous values for the outer disc: -0.02 dex kpc^{-1} outside 13 and 12 kpc for both Yong, Carney, and Friel (2012) and Frinchaboy et al. (2013), respectively.

In particular, Frinchaboy et al. (2013) did a similar procedure splitting APOGEE-DR10 OCs into: nine young ($Age < 0.3$ Gyr) clusters, five intermediate ($0.3 < Age < 1$ Gyr) clusters, and fourteen old ($1 < Age < 8.3$ Gyr) clusters. For the two younger bins they find a very similar slope of -0.04 dex kpc^{-1}, and for the old bin they compute a significantly steeper gradient of -0.10 dex kpc^{-1}. The bins in which they divide their sample are quite different than ours, but in any case we do not see any hint of this steeper slope in the older age bin that could point towards an evolution of the radial gradient.

The present day gradients may not be representative of the true gradient at birth moment because of the known dynamical effects that would make the clusters to migrate in Galactocentric distances. Thus the tracer would represent a population original of a different R_{GC} in the disc. A proper way to approach this is to use the birth radius calculated from the integration back in time of the orbit of the OC. However, the uncertainties involved in the orbit reconstruction procedure are very large to do this kind of analysis, coming from: the uncertainties in proper motions, velocities, age and distance; the free parameters of the assumed model; and the assumed model itself (axisymmetric, with spirals and/or bar). A further insight to the errors that we may be doing with this procedure is discussed in Section 7.3.5.

Anyway, we use the results derived in Section 4.3 for the birth position to replot the gradients using the same age bins in Fig. 7.5. We do not plot any errorbar in $R_{GC,birth}$ because it is difficult to estimate the real uncertainty that we have. In any case it is very large, therefore we do not attempt to perform any fit. We replot the gradient obtained in for the current radius (Fig. 7.4). We can perform a qualitative analysis of the significant changes that one could expect.

– There are two OCs out of the plot, Be 75 and Sau 1, that appear to have very eccentric orbits and give a birth radius of 62 and 49 kpc. They are quite distant, currently at 15.5 and 20.7 kpc, so we must consider the possibility that the proper motions, radial velocities or distances are not enough accurate, and therefore the orbit would be wrong. Otherwise, they could be accreted systems because these orbits are not compatible with typical ones from the Galactic disc (Cantat-Gaudin et al. 2016).

– The young and intermediate age bins seem qualitatively compatible with the current observed gradient.

– The Galactocentric radii of the OCs from the older age bin have significantly changed, generally migrating inwards. Therefore, we can deduce that for old ages present-day gradients could be not representative of the gradient at birth time. This seems to affect more the clusters that are at large Galactocentric distances.

Age-Metallicity Relation

We explore the AMR using the sample of 40 OCs. We have split the sample into four bins of Galactocentric radius and we plot [Fe/H] as a function of age in Fig. 7.6.

As can be seen in the figure, the most inner OCs are all clumped in the range $0 < Age < 2$ Gyr quite spread (0.06 dex). If we fit a linear function we obtain a slope of $+0.016$ dex Gyr^{-1}, but we consider that this trend is spurious and therefore we cannot extract any conclusion.

If a linear function is fitted in the range $7.5 < R_{GC} < 10$ kpc we find a positive slope of 0.016 ± 0.004 dex Gyr^{-1} (dotted line in Fig. 7.6). To the eye the positive slope seems driven by the oldest OC (NGC 6791). However, discarding it has little influence and yields a still positive value of 0.010 ± 0.007 dex Gyr^{-1} (dashed line). On the other hand, judging by the comparison in Table 7.1 (discussion in Section 7.2), it can be possible that the three J16 OCs have a systematic lower offset with respect to the OCCASO OCs (in mean $[Fe/H]_{GES} - [Fe/H]_{OCCASO} = -0.055$ dex), and therefore could be forcing the gradient. Discarding them leads to a flat slope 0.001 ± 0.005 dex Gyr^{-1} (solid line), and shifting up the metallicity of the three clusters yields a slope 0.014 ± 0.003 dex Gyr^{-1}.

For $R_{GC} > 10$ kpc the OCs are much more spread in position. We split the range in two bins $10 < R_{GC} < 13$ kpc and $13 < R_{GC} < 22$ kpc obtaining a hint of a dependence of [Fe/H] with Age, where older OCs have lower metallicities. The slopes of the two bins are similar -0.029 ± 0.011 and -0.026 ± 0.014 dex Gyr^{-1}, but with different zeropoints.

The existence of an AMR is not clear, from field stars some authors find it (Bensby, Feltzing, and Lundström 2004; Reid et al. 2007) but others do not (Feltzing, Holmberg, and Hurley 2001; Nordström et al. 2004). In the case of OCs no clear trend has been found. Carrera and Pancino (2011) use a compilation of high-resolution data from literature to investigate this in bins of Galactocentric radius. They find no trend in any of the studied annuli, and a weak but not very significant trend (-0.02 ± 0.02) in the outer region $R > 13$ kpc. This is compatible with the trend found here, though we find a very similar trend in the $10 < R_{GC} < 13$ kpc bin, where they do not find it. In general, the lack of old clusters in all Galactocentric annuli hampers this kind of investigation.

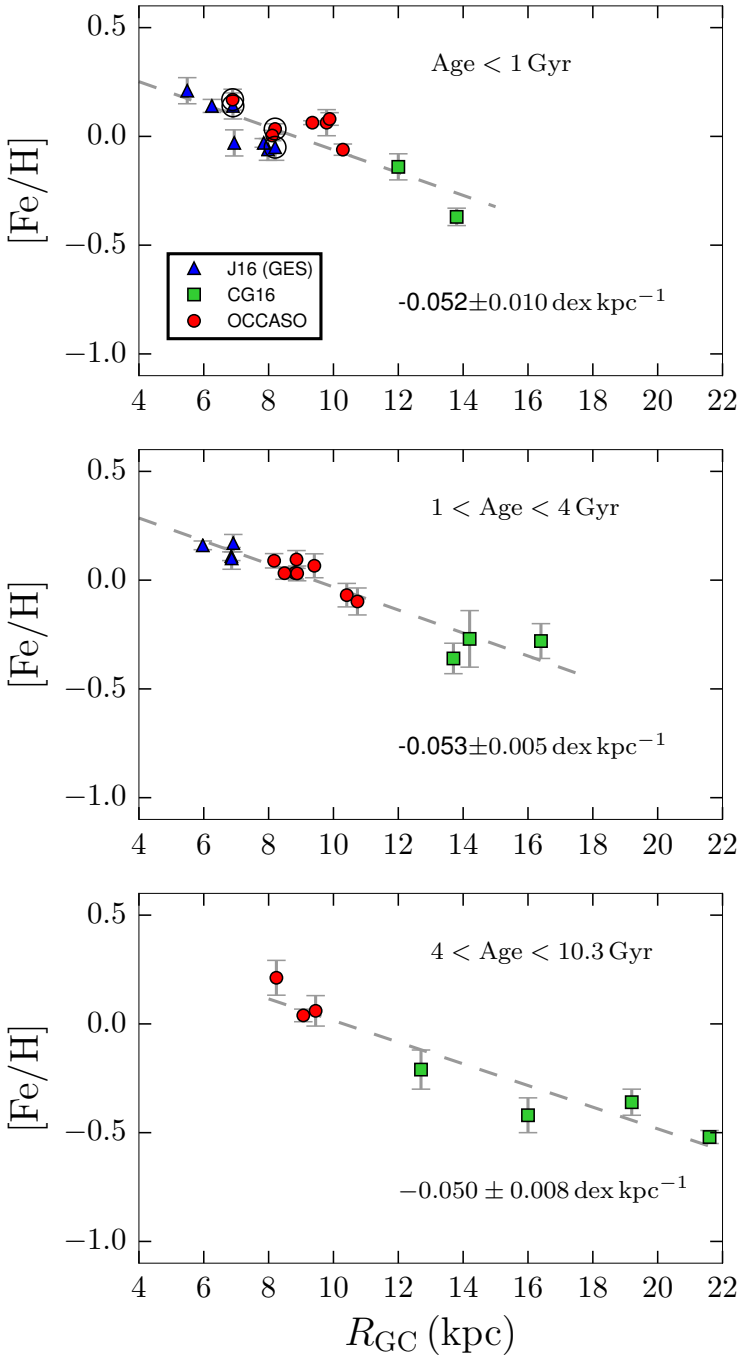

Figure 7.4. [Fe/H] vs R_{GC} distribution of the 40 OCs from OCCASO (red dots), GES (Jacobson et al. 2016, blue triangles) and Cantat-Gaudin et al. (2016, green squares), in three bins of age. Black empty circles indicate the two clusters in common: NGC 6705 and NGC 6633. We overplot the fitted gradient and we indicate the slope.

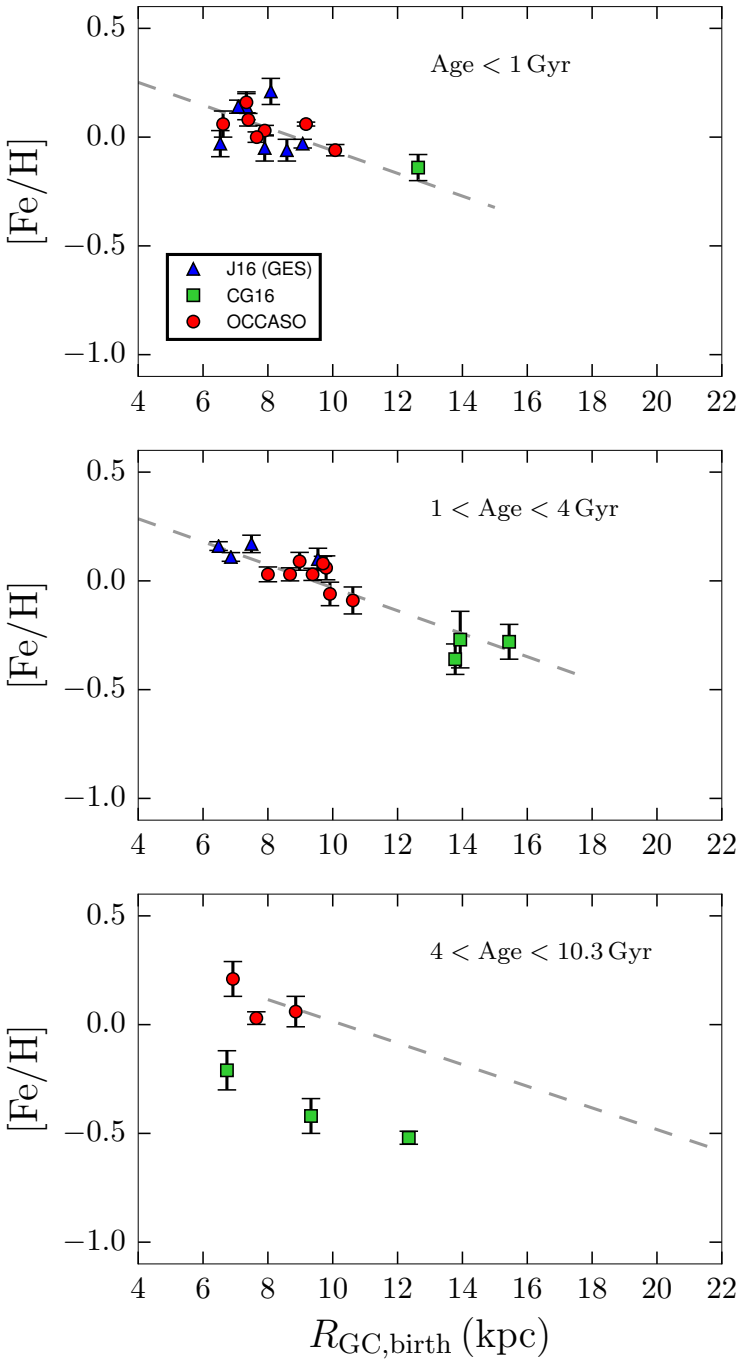

Figure 7.5. [Fe/H] vs $R_{GC,birth}$ distribution of OCs in three bins of age. Symbols are the same as in Fig. 7.4. We overplot the current gradient calculated in Fig. 7.4.

As in the case of the Galactocentric trend in the previous subsection we can see how the [Fe/H] vs age in the different bins of radius, changes when the birth radius is used instead of the current one. This is plotted in Fig. 7.7, together with the fits performed using the current radius. In this case there is no change in the general conclusions, though there are several clusters that change through panels, which are the ones that have more peculiar orbits:

- Be 75 and Sau 1 have birth radius at 62 and 49 kpc (as commented in the previous subsection) and fall out of the outer bin ($13 < R_{GC} < 22$ kpc).
- Be 66 migrated from 12 to 7 kpc, thus falling in the inner bin in Fig. 7.7.
- Be 20 migrated from 16 to 9 kpc, changing from the outer bin to the ($7.5 < R_{GC} < 10$ kpc).
- Be 29 migrated from 21 to 12 kpc, falling now in the ($10 < R_{GC} < 13$ kpc).

7.3 NGC6705: A YOUNG METAL-RICH AND α-ENHANCED OC

As discussed in Section 6.2 NGC 6705 stands out in our sample because it is slightly metal-rich and α-enhanced. It has been targeted by the spectroscopic surveys APOGEE and GES (Cantat-Gaudin et al. 2014b; Magrini et al. 2014; Tautvaišienė et al. 2015; Magrini et al. 2015) with still controversial results about its chemical composition. In particular, Magrini et al. (2015) also found an α-enhancement (see Section 7.3.6 for details).

It is one of the most crowded and populated OCs currently known, containing several thousands of Solar masses (Santos, Bonatto, and Bica 2005), which places it in the near limit between the most massive OCs and the least massive Globular Clusters. Many studies from Johnson and Strömgren photometry determine the age of this OC from isochrone fit to range between $0.25 - 0.32$ Gyr (e.g. Sung et al. 1999b; Santos, Bonatto, and Bica 2005; Beaver et al. 2013; Cantat-Gaudin et al. 2014b). It is located at a Galactocentric distance of 6.89 kpc Table 2.2 and very close to the plane at $z = -90$ pc.

7.3.1 *Abundance ratios of α-elements in the Galactic disc*

The study of abundance ratios to tag stellar populations is one of the pillars of Galactic Archaeology. In particular, [α/Fe] has long been used as an indirect age estimator. As detailed in Section 1.2 short-lived type II supernovae (core-collapse) produce Fe-peak and mainly α-elements, while in a longer timescale supernovae type Ia produce mainly Fe-peak elements (Matteucci 2001). In this picture, [α/Fe] enhancement means

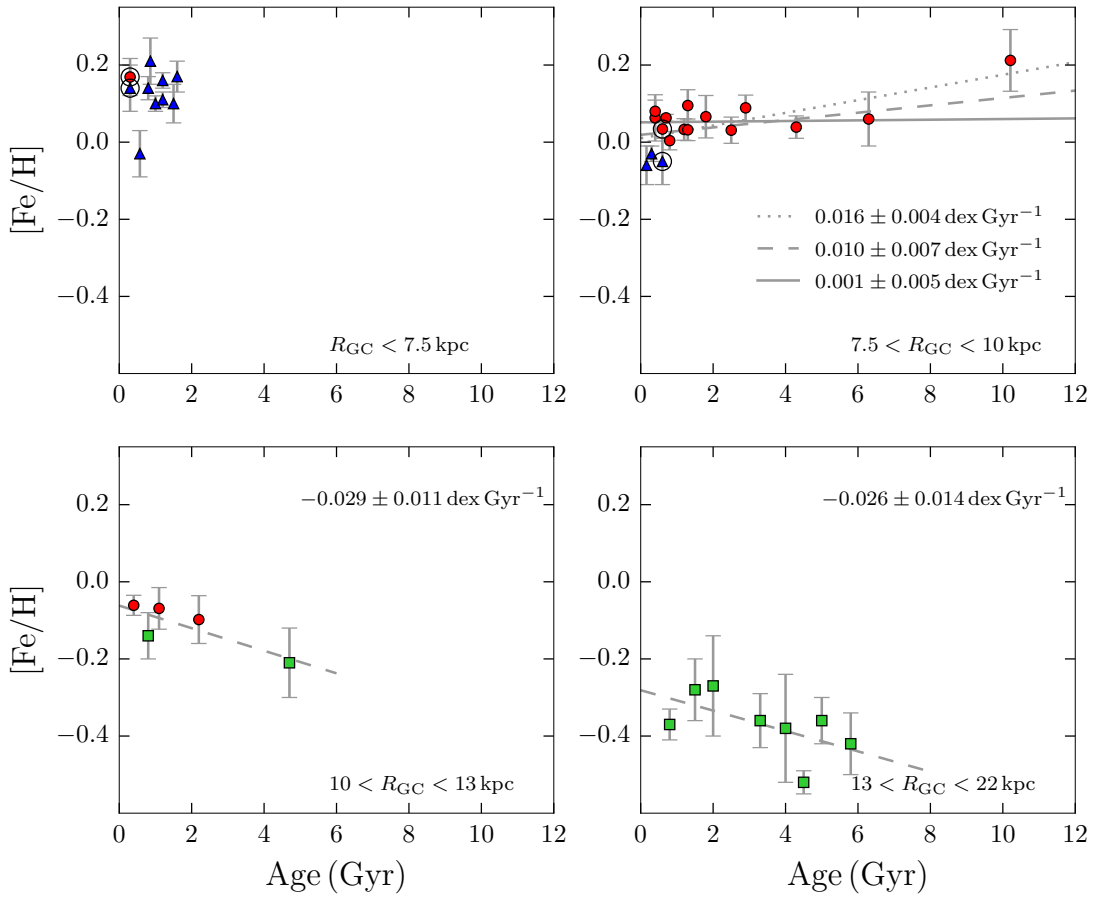

Figure 7.6. [Fe/H] vs Age distribution of the 40 OCs from OCCASO (red dots), GES (Jacobson et al. 2016, blue triangles) and Cantat-Gaudin et al. (2016, green squares), in three bins of R_{GC}. Black empty circles indicate the two clusters in common: NGC 6705 and NGC 6633. Except for the youngest bin we overplot the fitted trend with its slope. For the second bin we overplot three possible trends (see text).

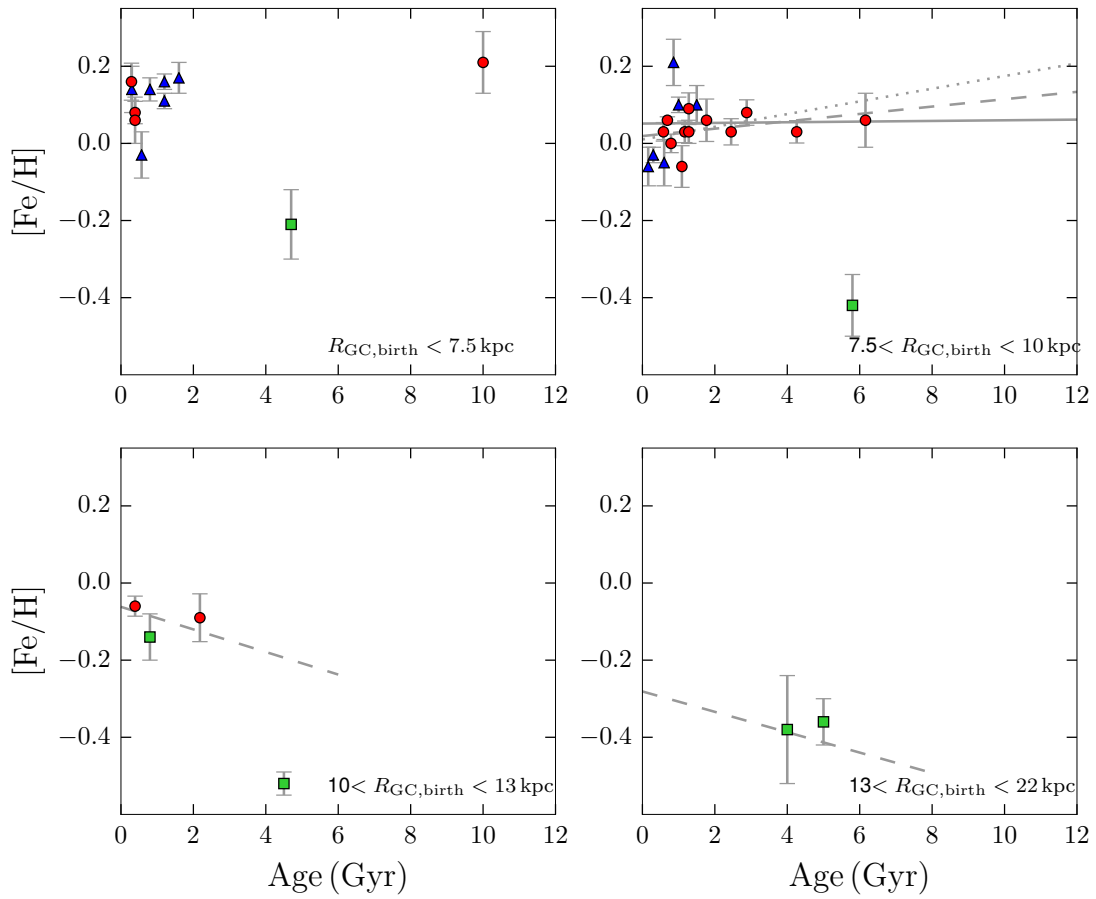

Figure 7.7. [Fe/H] vs Age distribution of the OCs in three bins of R_{GC}. Symbols and lines are the same as in Fig. 7.6.

that the star was born in a gas enriched only by supernovae II, and other polluters did not have time to enrich the gas. This correlation with age has been studied in several works such as Fuhrmann (2011), where ages could be derived from isochrone fit for a very local set ($d < 25$ pc) of HIPPARCOS stars. They identified that [α/Fe] enhanced stars are older than $\sim$ 10 Gyr. In the [α/Fe] vs [Fe/H] plane they show the clear discontinuity thin-thick disc where [α/Fe] enhanced stars are identified as chemical thick disc. Other works with larger samples have confirmed this result (e. g. Adibekyan et al. 2012).

Recently, in other samples of stars outside the local volume it has been seen that [α/Fe] enhancement is not guarantee that a star is old. In Chiappini et al. (2015) a sample of COnvection ROtation et Transits planétaires (CoRoT)-APOGEE stars are analysed. From CoRoT (Miglio et al. 2013) data they obtained masses, ages, distances and extinctions. They use abundances of α-elements from APOGEE high-resolution infrared spectra (Holtzman et al. 2015). They show that yet most of the data follows the standard chemical evolution models plus uncertainties, there are several stars that have high [α/Fe] ratios despite their young ages, and that cannot be explained by the models (see Fig. 7.8). More interestingly the majority of these stars are found towards small Galactocentric distances. Chiappini et al. (2015) also details that young α-enhanced stars are found in other works (Haywood et al. 2013; Bensby, Feltzing, and Oey 2014; Bergemann et al. 2014), where they are always treated as outliers. These stars are also present in other samples such as Martig et al. (APOKASC, 2015), where seismic parameters from *Kepler* and abundances from APOGEE are used. The authors find at least 14 stars that are α-enhanced ([α/Fe]$>$ 0.13) and younger than 6 Gyr. NGC 6705 is then the first identified cluster that shares this characteristic.

7.3.2 *Spectroscopic analysis from OCCASO*

In Fig. 7.9 we plot the position of the target stars in a color-magnitude diagram from Sung et al. (1999a). We overplot a PARSEC isochrone (Bressan et al. 2012) with age, metallicity, extinction and distance calculated by Cantat-Gaudin et al. (2014b): age=316 ± 50 Myr, $Z = 0.019$, $E(B-V) = 0.40 \pm 0.03$ and $V - M_V = 11.45 \pm 0.2$ ($d = 1950 \pm 200$ pc)[3]. We plot the results of the atmospheric parameters in the theoretical HR diagram in Fig. 7.9. The theoretical position of the red clump traced by the isochrone is well reproduced by our values of T_{eff} and $\log g$.

Radial velocities for the observed stars were calculated in Section 4.1.3 showing that all observed stars are compatible with being members within 1σ. We have noticed that the star W1256 has a lower probability of membership from proper motions than the other stars (77%). Looking at the abundance results from Chapter 6 we see that this star has lower abundances than the rest of the members in all the elements. Though it

3 Details of the observed stars of NGC 6705 are in Tables B.1 and B.2.

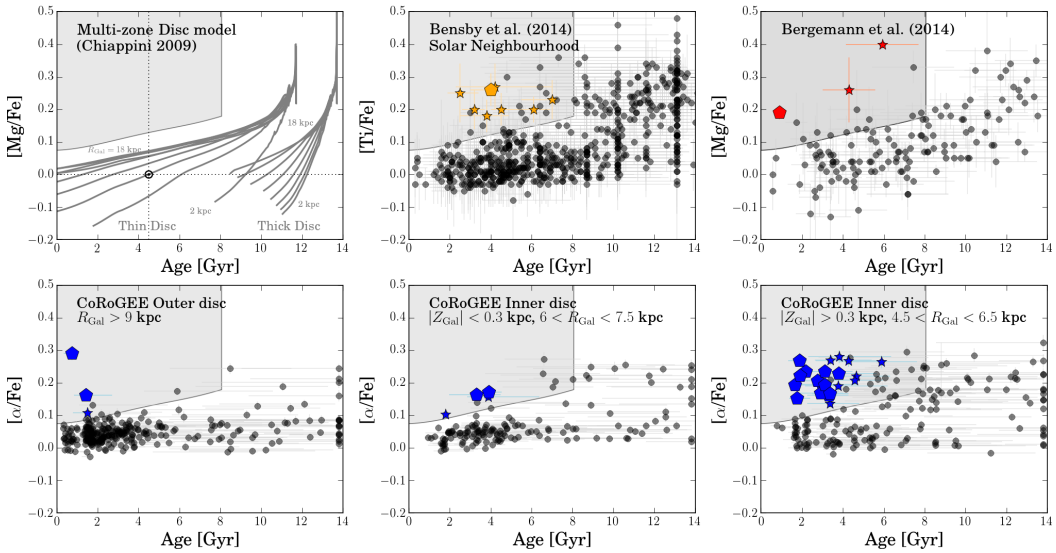

Figure 7.8. Age-[α/Fe] relation in different regions of the Galactic disc. *Upper left panel*: predictions of the Galactic chemical-evolution model of Chiappini (2009) for the thin and thick discs, where different tracks were calculated for different Galactocentric annuli situated between 2 and 18 kpc from the Galactic Centre. The Solar position is indicated in the diagram for the 6 kpc curve, the distance of the most probable birth position of the Sun (Minchev, Chiappini, and Martig 2013). The grey shadings provide a heuristic estimate of the typical uncertainties. The other pannels show different samples for which you [α/Fe] enhanced stars were identified. Figure from Chiappini et al. (2015).

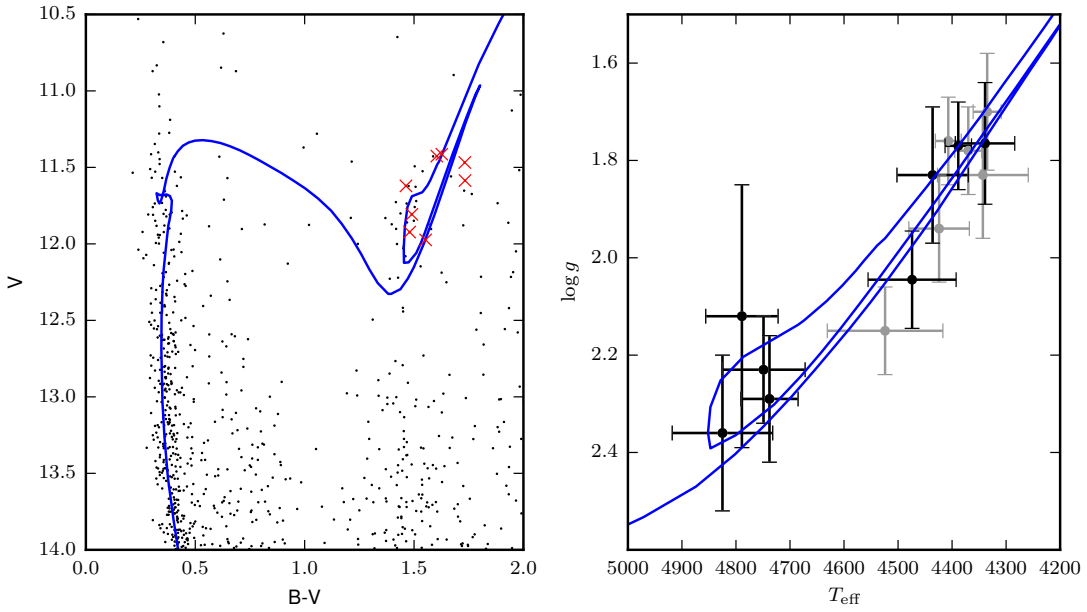

Figure 7.9. Left: Color-magnitude diagram with the photometry from Sung et al. (1999a) (black dots). Target stars are marked with red crosses. A PARSEC isochrone of age 316 Myr and $Z = 0.019$ shifted by $V - M_V = 11.45$ ($d = 1950$ pc) and $E(B-V) = 0.40$ (Cantat-Gaudin et al. 2014b) is overplotted. Right: Derived $T_{\rm eff}$ and $\log g$ from Section 5.4. Grey points are the values of the stars observed with both FIES and HERMES. For these stars we also plot the mean values (in black). The same isochrone as in the left panel is plotted.

is inside 1σ, for the very detailed study done in this chapter we decide to reject it for the analysis.

7.3.2.1 *Mg and O*

Given that α-enhancement is the key property of this OC, in this section we analyse two pure α-elements: Mg and O. We have found three measurable magnesium lines in the HERMES spectra at 5711.088, 7387.701 and 8717.825 Å. Oxygen abundances are calculated measuring the [O I] feature at 6300.304 Å.

Atomic parameters are taken from Vienna Atomic Line Database (VALD) database, $\log gf$'s are updated using Kurucz 2010 database.

Spectral synthesis fits of Mg and O lines are performed with `Salvador` (A. Mucciarelli, priv. comm.). This tool is used to perform fits of individual lines from an observed spectrum, to synthetic spectra created from an assumed model atmosphere. It allows the user to choose parameters like: normalization, window used in the fit, or abundance variations of specific elements with respect to the assumed by the model (used for blended lines). An example of the performed fits in Fig. 7.10.

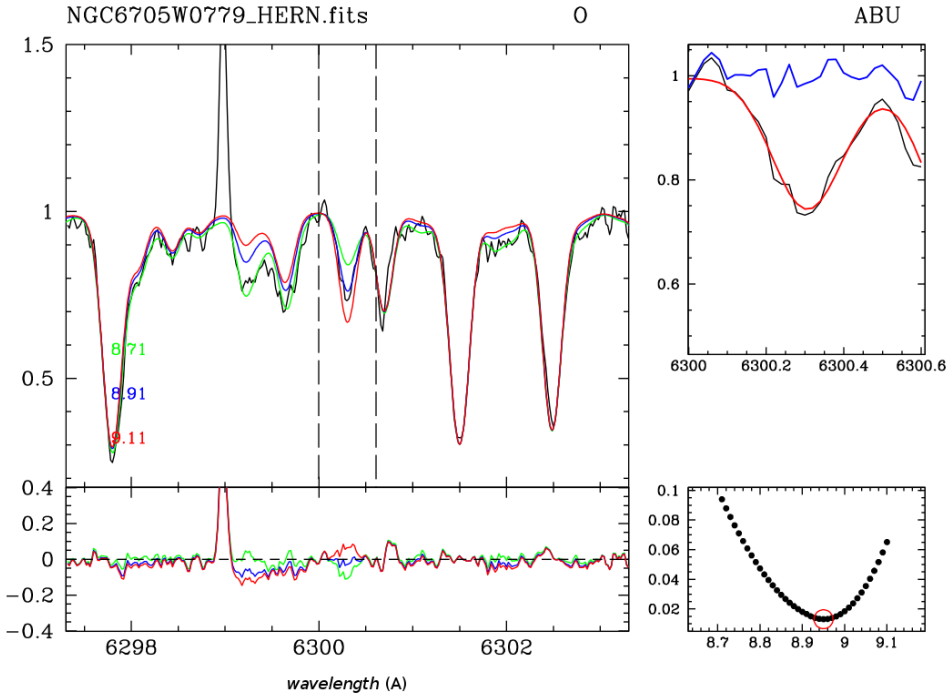

Figure 7.10. Fit performed by `Salvador` to the [O I] line at 6300.304 Å, for the star W0779 (HERMES). The main pannel shows the fitted region (within the vertical dashed lines) of the observed spectrum in black, with three synthetic spectra with possible oxygen abundances. The bottom left pannel shows the residuals. The upper right pannel shows the best fit spectrum in red, and its residuals in blue. The bottom right pannel shows the χ^2 values for the different sampled abundances, and the minimum is indicated with a red circle (which corresponds to the top right pannel).

We assume Solar abundances from Asplund et al. (2009) $A(\mathrm{Mg})_\odot = 7.53 \pm 0.01$, $A(\mathrm{O})_\odot = 8.69 \pm 0.05$.

As in previous chapters the adopted model atmospheres are the MARCS grid (Gustafsson et al. 2008), which assume Solar abundances and α-enhancement at low metalliticies. The spectra are synthesised using the set of Kurucz codes (Kurucz 2005; Sbordone et al. 2004) in a wavelength window of 6 Å around the given spectral line. The region around the line is renormalized by the code using the ratio between the observed and the best-fit spectrum. To perform the fit we feed the code with: the spectrum in fits format, the atmospheric parameters, the radial velocity and the resolution.

It is well known that the oxygen forbidden line at 6300.304 Å is blended with a Ni I line (Allende Prieto, Lambert, and Asplund 2001). To perform an accurate fit we have set the Ni abundance derived from EW analysis (Section 6.2) when synthesising the spectrum for each star.

To compute the errors in the derived abundances we take into account two sources of uncertainty: the errors due to the choice of the atmospheric parameters, and the errors due to the fit.

- The uncertainty from the parameters is calculated altering each atmospheric parameter (T_{eff}, log g and ξ) by $+\sigma_i$ and $-\sigma_i$, and calculating the standard deviation of the obtained values.

- The uncertainty due to the fit can be calculated using a subroutine in `Salvador` that performs N Monte Carlo simulations of one line with a desired SNR. In other words, after the fitting procedure, it takes the best-fit spectrum for that line, adds a Poisson noise in order to simulate the provided SNR and repeat the fit; this process is repeated N times. We took N=100 and the lowest SNR that we have (54). We have taken the standard deviation of the 100 abundances obtained as a measure of the uncertainties due to the fit. This procedure accounts for the error due to the SNR and partially to the continuum placement

We have performed this test for the four lines in a representative star (W0779_HER), and we assume that the variations in abundances will be the same for the other stars.

The results of the absolute abundances for each line and star are detailed in Table 7.2. 7387.701 and 8717.825 Å fall out of the spectral range of the FIES spectra. For the star W0669 the regions around the 5711.088 Å line are very noisy and the continuum is uncertain. The oxygen line could not be measured in: W1256 because there is a skyline on top of it, and W0686 because there is too much noise and the continuum could not be determined.

The abundances respect to the Sun are plotted in Fig. 7.11. We obtain cluster mean abundances of $[\mathrm{Mg/H}] = 0.28 \pm 0.05$, $[\mathrm{O/H}] = 0.33 \pm 0.02$ (excluding W1256).

Table 7.2. Wavelengths, log gf, and absolute abundances of magnesium and oxygen lines. The assumed uncertainties in abundance for each line are: 0.1, 0.06, 0.07, 0.05, for 5711, 7387, 8717 and 6300 Å, respectively. W1256 is considered not member (see text).

λ (Å)	5711.088	7387.701	8717.825	6300.304
Element	12.00	12.00	12.00	8.00
log gf	−1.830	−2.113	−0.941	−9.776
W0660 HER	8.07	7.61	7.71	8.99
W0669 HER	-	7.83	7.75	9.05
W0686 HER	8.06	7.51	-	-
W0779 FIE	7.93	-	-	9.04
W0779 HER	8.02	7.76	7.6	8.95
W0916 HER	7.88	7.81	7.64	9.02
W1184 FIE	7.93	-	-	9.05
W1184 HER	7.95	7.8	7.62	9.01
W1256 HER	7.63	7.63	-	-
W1423 FIE	7.9	-	-	9.02
W1423 HER	8.04	7.71	7.62	9.08

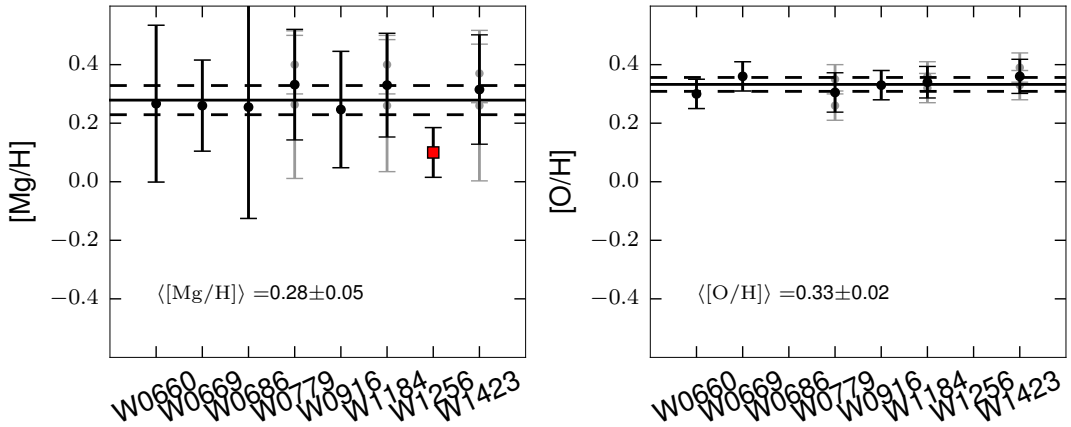

Figure 7.11. Chemical abundances of Mg and O in the analysed stars. In grey, the stars observed with both FIES and HERMES (in black, the mean value). In red W1256 considered as not member (see text). The solid line shows the mean value of the members (in black), and the dashed lines indicate the 1σ level.

7.3.2.2 *Abundance ratios*

Once we have established a reliable membership selection and have calculated the abundances of the stars, we compute abundance ratios respect to Fe. We compute the average abundance as representative of the entire cluster. In Fig. 7.12 we graphically present these results and we overplot the mean values and standard deviations of each element.

We can notice different peculiarities in the abundance patterns. Ni and Cr are Fe-peak elements, so they are expected to follow Fe. Cr does, with a large spread, also noticeable in Fig. 6.13. Ni shows an over abundance respect to Fe of $[Ni/Fe] = 0.07 \pm 0.03$. Regarding the α-elements Si shows a remarkable enhancement of 0.10 ± 0.05 dex. Mg and O show a clear enhancement of 0.12 ± 0.06 and 0.16 ± 0.05, respectively. Ca and Ti are roughly enhanced by 0.03 ± 0.06 and 0.03 ± 0.02 dex, respectively. Ca has the largest spread.

Judging by our analysis of Mg and O it is confirmed that NGC 6705 shows a clear α-enhancement in Ti, Si, Mg, and O. It also has a mild enhancement in Ca. We obtain a mean $[\alpha/Fe]=0.09 \pm 0.05$.

The star W1184 shows quite discrepant values of [Mg/Fe] and [O/Fe], but not of [Mg/H] and [O/H]. It is the most metal poor star in our sample, for which we have FIES and HERMES spectra that yield $[Fe/H]=0.03 \pm 0.11$ and $[Fe/H]=0.13 \pm 0.08$, respectively from EW analysis. This gives 0.08 ± 0.04 in mean, which makes it compatible with the rest of stars. We should further investigate what is causing this difference in the calculated abundance. However, discarding it as a member would yield slightly lower abundance ratios of both elements, but still the whole cluster would exhibit enhancement.

7.3.3 *Abundance ratios from APOGEE DR13*

NGC 6705 has been observed by the APOGEE spectroscopic survey. So, additionally to OCCASO data, we have used the public data from APOGEE (Holtzman et al. 2015) to do a parallel analysis.

We have selected all the stars in a radius of 16 arcmin around the center of the cluster. This returns 28 stars. We do a membership selection based on radial velocities only keeping stars within 3σ around the average radial velocity calculated from the OCCASO sample: $32 < v_r < 38$ km s^{-1}. We also refine the selection taking into account abundances in Fe, Si, Ca, Mg and O. This makes 12 probable members.

We analyse the results of Fe and the α-elements Si, Ca, Mg and O obtained by APOGEE for these 12 stars. We do not study the Ti abundances because it is known that the APOGEE pipeline does not give reliable Ti abundances (Hawkins et al. 2016a). The results are presented in Fig. 7.13. We obtain very similar Fe and Si abundances as in OCCASO: $[Fe/H]= 0.16 \pm 0.03$, $[Si/Fe]= 0.10 \pm 0.04$. For [Ca/Fe] the results

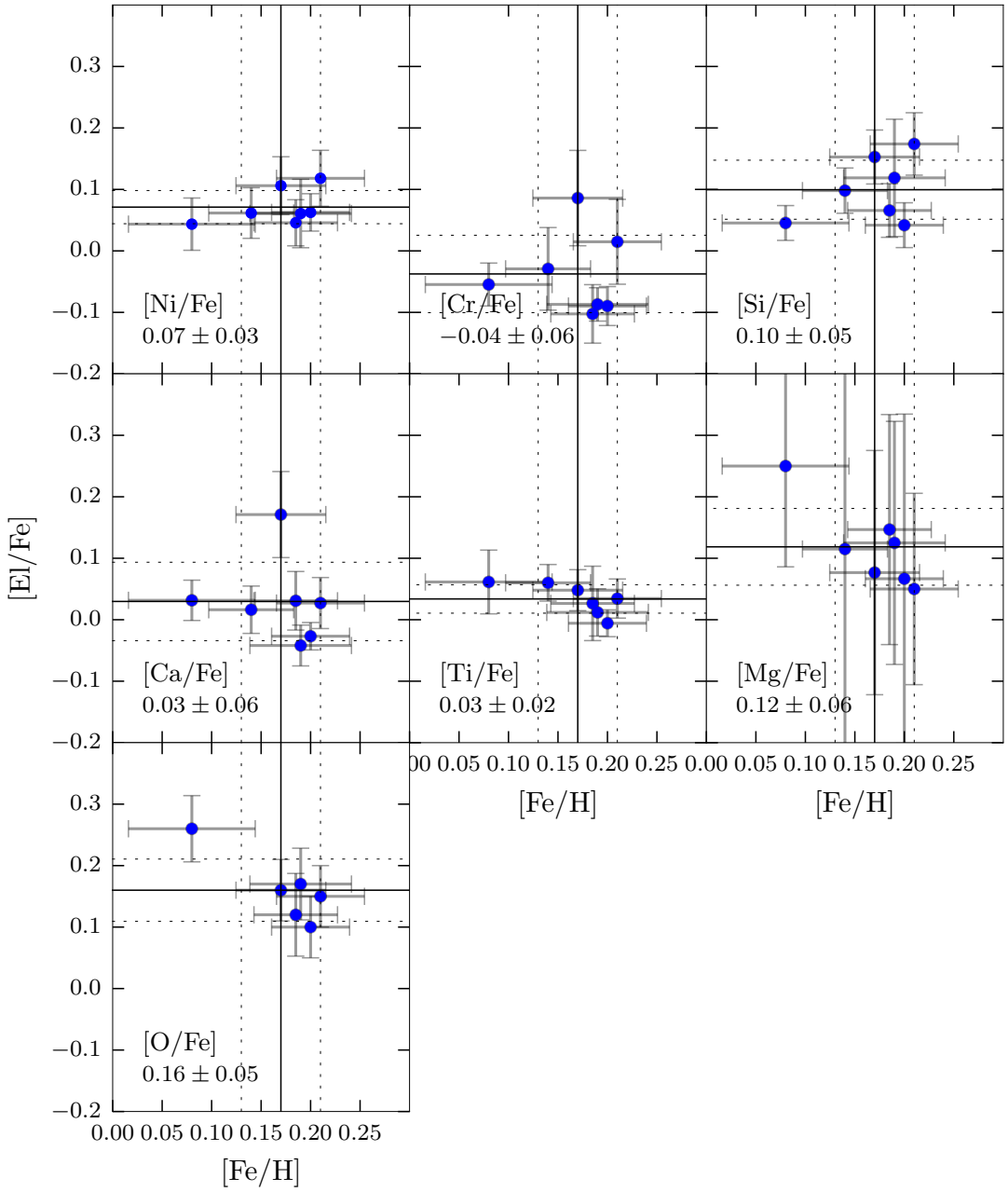

Figure 7.12. Abundance ratios of Ni, Cr, Si, Ca, Ti, Mg and O for the member stars in OCCASO data. Mean abundances and standard deviations are overplotted in each pannel. We have used the 7 member stars except for oxygen, which was calculated with 6 members (see text). The solid line shows the mean value and the dotted lines indicate the 1σ level.

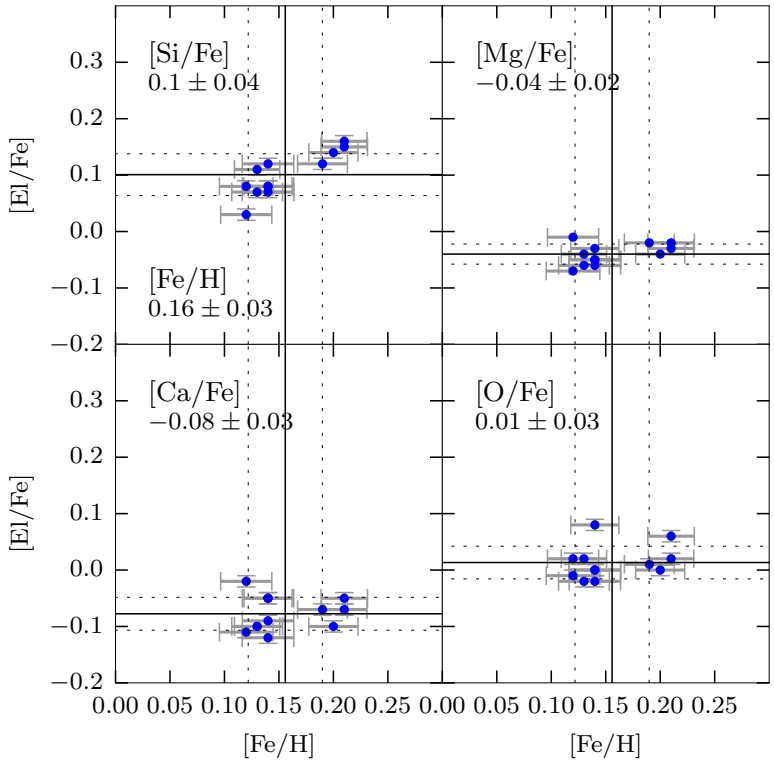

Figure 7.13. Abundance ratios from APOGEE of Si, Ca, Mg and O for 12 member stars. Mean abundances and standard deviations are overplotted in each panel. We also overplot the mean [Fe/H] abundance. The solid line shows the mean value and the dotted lines indicate the 1σ level.

are compatible within 1.6σ, and for [Mg/Fe] and [O/Fe] within 2.5σ. However, O abundances in APOGEE are obtained from molecules, which depend on the assumed C abundances. The mean $[\alpha/Fe]=0.00 \pm 0.07$, so, as a whole, APOGEE does not find the cluster α enhanced. We include a summary in Table 7.4.

7.3.4 *Star-by-star comparison with literature*

In Section 5.4.1 we compare the values of atmospheric parameters derived in OCCASO with the literature values in GESiDR1 (Cantat-Gaudin et al. 2014b). Here we compare more exhaustively with other values, several GES data releases that include a recomputation of atmospheric parameters and abundances: GESiDR2 Tautvaišienė et al. (2015), and the second public version of GES[4] (GESv2). We have 3 stars in common with the sample of 12 members from APOGEE (Holtzman et al. 2015). This OC

4 The second public version of GES (GESv2) corresponds to the internal data release 4 (iDR4)

also has a previous high-resolution spectroscopic study of 10 K-giants by Gonzalez and Wallerstein (2000, GW2000). We have 8 stars in common with them. We present the full comparison in Fig. 7.14. We compute mean offsets and dispersions listed in Table 7.3 for an exhaustive comparison.

From the offsets and dispersions found comparing OCCASO with the different authors in the literature we can draw some conclusions:

- Gonzalez and Wallerstein (2000) have the largest dispersions in the three parameters. They derive errors of ~ 150 K in T_{eff}, ~ 0.4 dex in $\log g$ and ~ 0.14 in [Fe/H], so their results have less precision than the other studies. In particular, we see that for the group of stars at $T_{eff} > 4700$ K Gonzalez and Wallerstein (2000) give systematically lower values than the other authors, and for the coolest stars the systematics is the opposite. A similar behaviour is seen for surface gravity where $\log g > 2.1$ have positive differences, and almost all stars with $\log g < 2.1$ have negative differences.
- In general, T_{eff} shows mild offsets and dispersions, that agree with the observational errors. The largest one is for Tautvaišienė et al. (2015): 45 ± 39 K.
- $\log g$ shows quite good agreement besides Gonzalez and Wallerstein (2000) which shows a very large spread. APOGEE results also show a large difference -0.21 ± 0.16 dex, although it is only from three stars.
- We find a large offset in [Fe/H] of 0.13 ± 0.03 with Tautvaišienė et al. (2015), compared with Magrini et al. (2014) whose results essentially come from the same spectra.
- The [Fe/H] of the three stars in APOGEE agrees with OCCASO results.
- GESv2 results on T_{eff} and $\log g$ are very similar to those in GESiDR2 Tautvaišienė et al. (2015), but [Fe/H] agrees much better with OCCASO with an offset of 0.04 ± 0.01.

7.3.5 *Orbit computation*

In Section 4.3 we have calculated the position of this cluster in the moment of its birth obtaining $R_{GC,birth} - R_{GC} = +0.6$ and $+0.5$ kpc for the axisymmetric, and the non-axisymmetric models, respectively. We wonder if the interesting abundance patterns shown by this OC could be partly explained if it was born in a very different Galactocentric radius (i. e. in the inner Galaxy near the bar, see next section for a discussion).

Since this OC is young, the uncertainties that come from assuming a static potential when integrating back the orbit are small. In this section we examine in detail the propagation of errors in the assumed motions, distance, and age. We also quantify the uncertainties that come from the choice of the model. We do two tests:

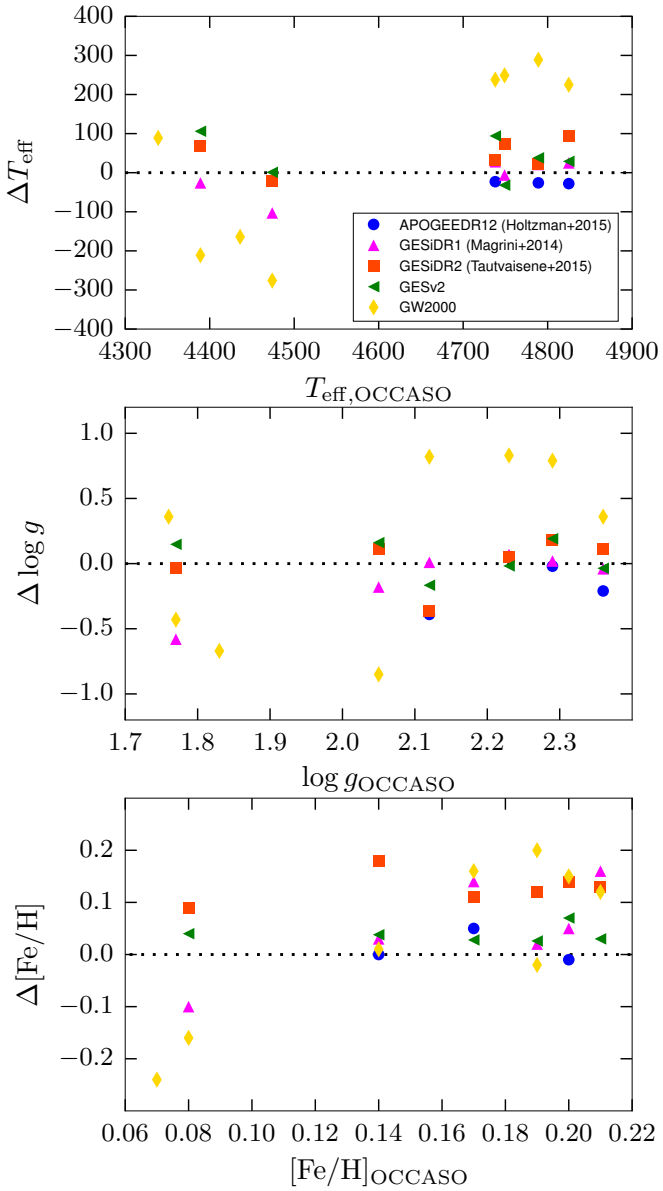

Figure 7.14. Star by star comparison of OCCASO results of $T_{\rm eff}$, log g and [Fe/H] presented in this study with previous high-resolution studies: Holtzman et al. (2015), Magrini et al. (2014), Tautvaišienė et al. (2015), GESv2 and Gonzalez and Wallerstein (2000). Differences are in the direction OCCASO-literature. Mean differences listed in Table 7.3.

Table 7.3. Mean differences and standard deviations in atmospheric parameters and iron abundances between OCCASO (EW) and literature for the five references that have studied this OC with high-resolution spectroscopy. Differences are in the direction OCCASO-literature.

Reference	ΔT_{eff}	$\Delta \log g$	Δ[Fe/H]	Num. stars
APOGEE[1]	-26 ± 2	-0.21 ± 0.16	0.01 ± 0.03	3
GESiDR1[2]	-10 ± 46	-0.12 ± 0.22	0.05 ± 0.09	6
GESiDR2[3]	45 ± 39	0.01 ± 0.18	0.13 ± 0.03	6
GESv2	39 ± 48	0.05 ± 0.13	0.04 ± 0.01	6
GW2000[4]	55 ± 219	0.15 ± 0.65	0.03 ± 0.13	8

[1]Holtzman et al. (2015), [2]Magrini et al. (2014), [3]Tautvaišienė et al. (2015), [4]Gonzalez and Wallerstein (2000)

Table 7.4. Mean iron abundance and abundance ratios calculated in this study: using OCCASO results (using 6 or 7 member stars, depending on the chemical species), and also using APOGEE results from Holtzman et al. (2015) (12 member stars). Comparison with the results obtained in the two GES data releases GESiDR1 (Magrini et al. 2014), and GESiDR2 (Tautvaišienė et al. 2015).

Element	OCCASO	APOGEE	GESiDR1	GESiDR2
[Fe/H]	0.17±0.04	0.16±0.03	0.14±0.06	0.00±0.05
[Ni/Fe]	0.07±0.03	-	0.01±0.03	-
[Cr/Fe]	-0.04±0.06	-	-0.07±0.05	-
[Si/Fe]	0.10±0.05	0.10±0.04	0.03±0.05	-
[Ca/Fe]	0.03±0.06	-0.08±0.03	-0.02±0.05	-
[Ti/Fe]	0.03±0.02	-	-0.05±0.07	-
[Mg/Fe]	0.12±0.06	-0.04±0.02	0.20±0.09	-
[O/Fe]	0.16±0.05	0.01±0.03	-	0.13±0.05

Table 7.5. The three datasets of assumed distances and proper motions in the computation of the birth radius of NGC 6705. We include the mean from the 475 models and its standard deviation of the birth radius $R_{GC,birth}$, maximum and minimumm radius of the orbit.

Reference	d	$\mu_\alpha \cos\delta$	μ_δ	$R_{GC,birth}$	$R_{GC,min}$	$R_{GC,max}$
	kpc	mas yr^{-1}	mas yr^{-1}	kpc	kpc	kpc
data1	1.754 [a]	-1.93 ± 0.39 [i]	-4.88 ± 0.42	7.35 ± 0.52	6.00 ± 0.24	7.80 ± 0.21
data2	1.877 [b]	-1.23 ± 3.85 [iii]	1.31 ± 4.32	7.33 ± 0.27	6.88 ± 0.03	9.21 ± 0.22
data3	1.647 [c]	-1.04 ± 0.25 [iii]	-3.80 ± 0.30	7.81 ± 0.34	6.51 ± 0.28	8.06 ± 0.22

Reference for distances: [a] from TGAS parallaxes, mean of 8 stars (Cantat-Gaudin et al. 2017, in prep), [b] Dias et al. (2002) (photometry), [c] from TGAS parallaxes, mean of 32 stars (Casamiquela et al. 2017, in prep).
Reference for proper motions: [i] from TGAS, mean of 8 stars (Cantat-Gaudin et al. 2017, in prep), [ii] Dias et al. (2002), [iii] from TGAS, mean of 32 stars (Casamiquela et al. 2017, in prep).

i. First we use 3 sets of proper motions, and distances specified in Table 7.5 to compute the orbits. Data1 uses TGAS results as a mean of 8 stars, data2 uses proper motions and distances from Dias et al. (2002), data3 uses TGAS results as a mean of 32 stars. In all cases $v_r = 34.5 \pm 1.7\,\mathrm{km\,s^{-1}}$ (result from Chapter 4), and the age 316 ± 50 Myr (derived by Cantat-Gaudin et al. 2014b). For each dataset we sweep 475 models of a non-axisymmetric gravitational potential with bar and spirals. We have explored values of: spiral arms mass (0, 0.03, 0.05 in units of disc mass, $8.56 \times 10^{10}\,M_\odot$), spiral arms pattern speed (15, 18, 20, 30 km s^{-1} kpc^{-1}) and spiral arms orientation (0,−20, 20 deg, respect to Drimmel and Spergel 2001), mass of the bar (0, 0.6, 0.8 in units of bulge mass, $1.41 \times 10^{10}\,M_\odot$), bar pattern speed (36, 46, 56 km s^{-1} kpc^{-1}) and bar orientation respect to the sun (20, 30, 40 deg)

ii. To evaluate the impact of the errors in the motions, distance and age we do 1000 realizations of the orbit integration assuming Gaussian errors in these five parameters. We have used the data3 set and the model with spiral arms (pattern speed of 21 km s^{-1} kpc^{-1} and 0.04 times the disc mass). We have computed the 1000 realizations with 100 different models of the gravitational potential varying in 10 steps the mass of the arms, and in 10 steps the spiral pattern speed.

The results of the test (i) are plotted in Fig. 7.15. It is seen that the three determinations of proper motions and distance lead to a significant difference in the computed orbits. For instance, in Fig. 7.15 the maximum radius (bottom panel) of the orbits differs about 1 kpc assuming data1 or data3 (both TGAS proper motions and distance) and data2 (Dias et al. 2002). Even with proper motions coming from the same source but using different membership selections (data1 and data3) the minimum radius can be significantly different by 0.5 kpc. The minimum radius for data2 has the particular-

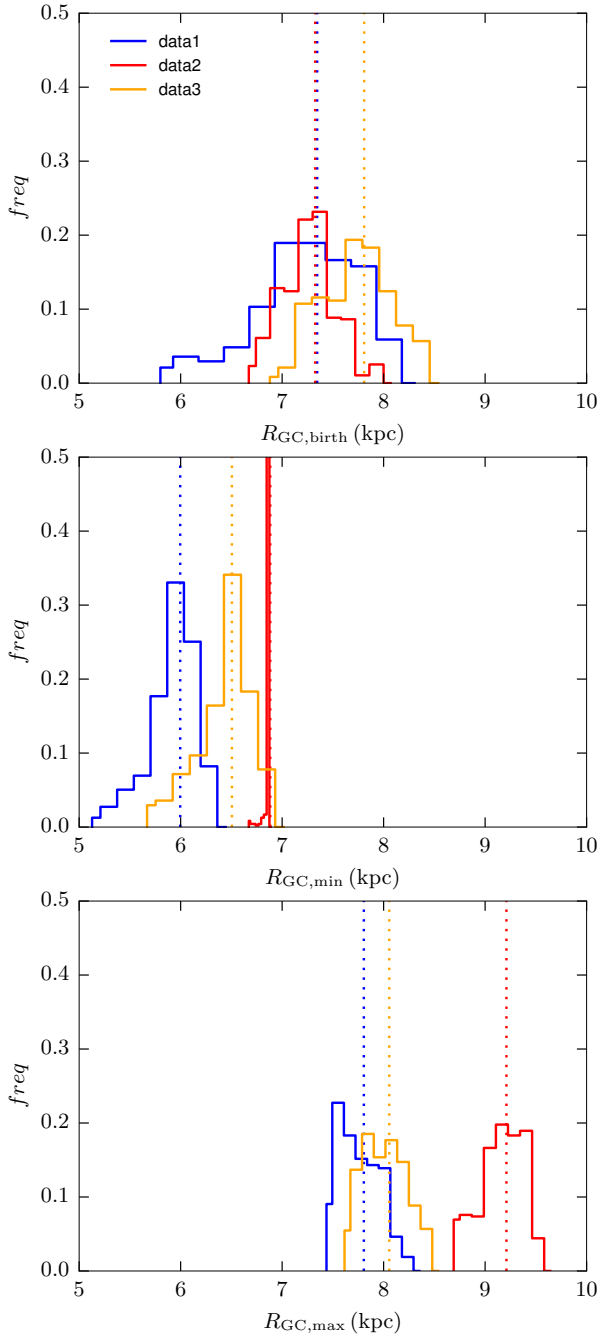

Figure 7.15. Normalized distribution of the birth, minimum and maximum radius of the orbits given by 475 different models of the gravitational potential, and the three datasets of assumed observational parameters in Table 7.5. The mean values are plotted as vertical dashed lines.

ity that is almost the same in all cases. The $R_{GC,birth}$ obtained from data1 and data3 is almost the same ~ 7.3 kpc, though the proper motions are quite different. In the case of data1, in 64% of the models the radius at birth is between $6.8 < R_{GC,birth} < 7.8$ kpc (1σ from the mean). For data2 the distribution is more peaked and 81% of the cases lie within 1σ, $7 < R_{GC,birth} < 7.9$ kpc. In the case of data3 we obtain $7.5 < R_{GC,birth} < 8.2$ kpc in 61% of the cases.

In the case of test (ii) each run of a model has a distribution of possible orbits given the assumed errors. An example for one of the models is plotted in Fig. 7.16, where the most probable birth radius is at 7.36 kpc with a spread of 0.06 kpc. In this case the model predicts that the cluster was born outwards the current radius. The distribution given by all models of the: birth, current, minimum and maximum radius are plot in Fig. 7.17. From this figure, the distribution of spreads (bottom panels) measure the impact of the propagation of the input uncertainties, since they are the widths of the distribution of the 1000 realizations. On the other side, the dispersion given by all the most probable values are a measure of the impact of the choice of the model. We can see that the current Galactocentric radius is rather well defined at 7.07 kpc with a very small spread (0.003 kpc) and the obtained dispersion given by the realizations is also small with a mean value of 0.12 kpc. This is because in the current radius the error in distance is the only one that plays a role. The minimum and maximum orbit radii have means of 5.4 and 8.36 kpc, and spreads 0.5 and 0.09 kpc, respectively. Their σR distributions have similar median values (0.19 and 0.21 kpc) though the minimum radius has a larger tail, so its more affected by errors than the maximum radius. The most probable radius at birth is 7.4 kpc with a spread of 0.5 kpc. The distribution of $\sigma R_{GC,birth}$ has a median value of 0.3 kpc and goes up to 1 kpc.

From these results that take into account different models of the gravitational potential, different sources and errors in the proper motions, radial velocity, distance and age, we can conclude that the Galactocentric radius at birth of NGC 6705 is between $6.5 < R_{GC,birth} < 7.8$ kpc with high probability.

7.3.6 *Discussion*

All indications seem to point towards a young metal rich and α-enhanced OC, at least in some of the α-elements. This is seen in other samples of field stars (Fig. 7.8). There are different explanations possible to this phenomenon, among which is the ambiguity of determining ages from masses in asteroseismology, where higher masses are assigned to younger ages. As stated by Jofré et al. (2016) and Yong et al. (2016) it can be that young α-rich stars appear young because they have accreted mass from a binary companion or because they are a result of a binary merger (blue straggler). In this case the mass would not reflect the real age of the progenitor star. In the case that these stars are indeed young, they could have been formed from a recent gas accretion event. Another interpretation is that they could be born in a region near the

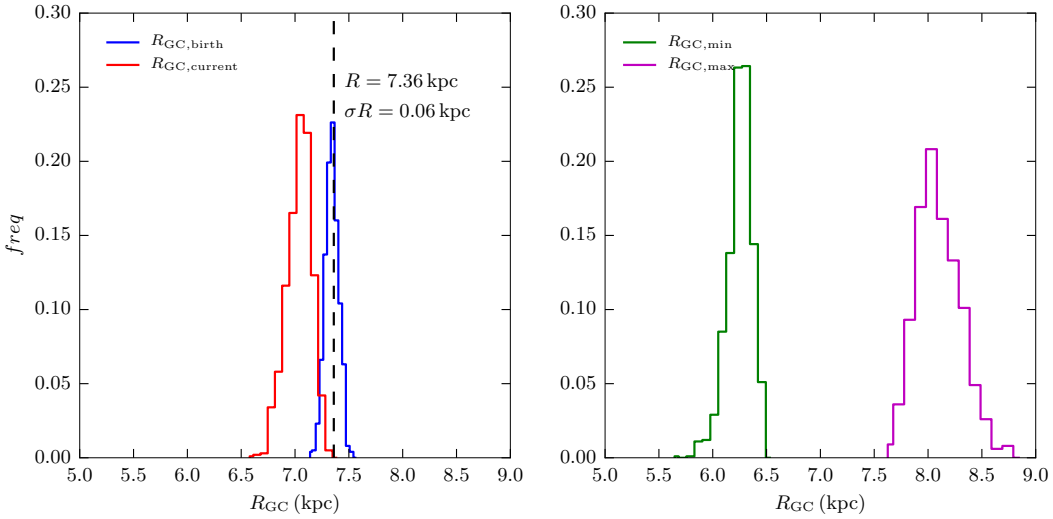

Figure 7.16. Distributions of current radius and birth radius (left), maximum orbit radius and minimum orbit radius (right), given by 1000 realizations of the one of the models of the gravitational potential. The most probable (computed as an average) birth radius of this model is 7.36 kpc (dashed vertical line), with a dispersion of 0.06 kpc.

corrotation of the bar where gas can be kept inert for a long time reflecting only type II supernovae ejecta. Then they could be kicked to their current location.

Unlike the stars analysed by Chiappini et al. (2015), in this work we have an object for which distance, and more importantly age, is determined reliably with an error of 50 Myr. This gives a reliable chance to the hypothesis stated by the authors, that at least some of the analysed stars in the CoRoGEE sample can be indeed young. Also, this object is in the thin disc ($z = -90$ pc), which also supports the idea that these young α-rich stars are thin disc objects, despite the CoRoT field is out of the plane in the inner field. However, in Chiappini et al. (2015) they argue by computing the guiding radii of their analysed stars, that they find a preferential location towards the inner Galaxy, thus giving support to the idea that their stars have a common origin towards the very inner Galaxy. After our analysis this seems that it is not the case for NGC 6705. We have integrated its orbit back to its birth age showing that it was probably born near the current radius or even slightly further from the Galactic center. In any case at most we could say that it comes from a radii of 6.5 kpc.

Magrini et al. (2015) analyses this cluster together with four inner disc OCs, wondering if the α-enhancement they found in three OCs is real, or if it is due to NLTE effects. They conclude that at least for NGC 6705 the α-enhancement is genuine, and they explore the possibility that this cluster has suffered from the effect of a local enrichment by a supernova type II.

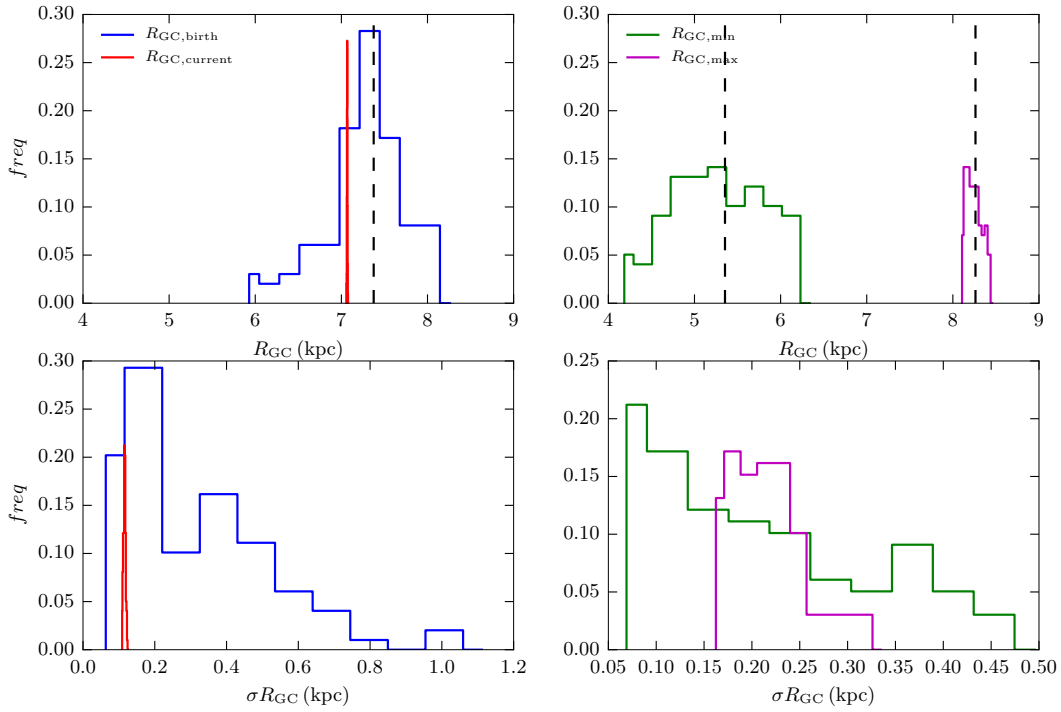

Figure 7.17. Given the 100 different models of the gravitational potential, in the left distribution of the most probable R_{GC} current, birth (top), minimum and maximum (bottom), and in the right their spreads from the 1000 realizations.

7.4 CONCLUSIONS

We have done an analysis of the OCCASO results from Chapters 4, 5 and 6 in the context of the Milky Way disc.

First, we have studied the [Fe/H] vs R_{GC} and vs z in three subsets of age. Taking into account a chemical-evolution model (Chiappini 2009) we see that the predicted dependence is not well reproduced by the oldest clusters. A comparison with the results of the N-body simulation by Minchev, Chiappini, and Martig (2013, 2014) shows a wipe-out of the radial gradient that is consistent with the deviation of the results from the pure chemical model. The three oldest clusters have still higher metallicities than the bulk of the MCM simulation. Probably, a fine tunning of the assumed free parameters in the dynamical model could acount for this difference.

To enlarge OCCASO sample we use two additional samples from the literature that are complementary in age and Galactocentric distance: 12 inner disc OCs (Jacobson et al. 2016) and 10 anticenter OCs (Cantat-Gaudin et al. 2016). Derived [Fe/H] are presumably compatible (same methods, models and linelists used). With two clusters in common between OCCASO and Jacobson et al. (2016) we see that there could be a small offset of around 0.06 dex. With this whole sample of 40 OCs we compute the Galactocentric gradients using three bins of age. The younger age bin is in perfect agreement with previous determinations from OCs and Cepheids. For the intermediate-age and older bins, which range $6 < R_{GC} < 18$ kpc and $9 < R_{GC} < 22$ kpc, respectively, we find basically the same slope as the younger bin. We do not see any difference between inner and outer disc that would point to a change of slope (as previously seen in the literature). From a linear fit to the 4 only outer clusters in the older age bin we find slightly steeper values than previous determinations.

We use the results from the computed orbits in Chapter 4 for this larger sample of OCs to study the same gradients traced by the birth position of the clusters instead of the current ones. The young and intermediate age bin gradients seem compatible with the calculated ones with the current radius, though the individual positions of the clusters have changed. The only case that shows a significant change is for the older clusters, generally migrating inwards the Galaxy. This could be an indication that for old ages, studying gradients using the current position may lead to incorrect conclusions.

We inspect the age-metallicity relation in four bins in Galactocentric radius, using the large sample of OCs. Inside 10 kpc we see [Fe/H] vs Age compatible with a flat function. Outside, in two radius bins $10 < R_{GC} < 13$ kpc and $13 < R_{GC} < 22$ kpc we obtain a steeper trend with slopes -0.029 ± 0.011 and -0.026 ± 0.014 dex Gyr^{-1}, respectively.

We study in detail the cluster NGC 6705 for its interesting α-enhancement computed in Chapter 6. We have performed an abundance analysis of Fe, Ni, Cr, Si, Ca, Ti, Mg and O from high-resolution spectroscopic data. First, we have used OCCASO

spectra of 7 stars. We have complemented our analysis using APOGEE results from Holtzman et al. (2015) of Ca, Si, Mg and O. Finally, we compare the derived cluster mean abundances from both studies with GES results of different data releases.

We have found that according to OCCASO results this OC is metal rich ([Fe/H]=0.17 ± 0.04) and it shows a clear α-enhancement in Ti, Si, Mg and O, and a mild enhancement with large dispersion in Ca. APOGEE finds a very similar metallicity (0.16 ± 0.03) and a very similar enhancement in Si. Ca and Mg show a depletion respect to Fe, and O follows Fe. However, O abundances in APOGEE are obtained from molecules, which depend on the assumed C abundances. Results from GES papers (Magrini et al. 2014; Tautvaišienė et al. 2015) for Fe are quite contradictory, see Table 7.4. They find no significant enhancement in Si nor in Ti. Mg is enhanced in 0.20 ± 0.09 in Magrini et al. (2014), and O is enhanced in 0.13 ± 0.05 in Tautvaišienė et al. (2015).

We have computed the orbit of this cluster to trace its place of birth using different proper motions and distances, and different assumed models for the gravitational potential of the disc (all with bar and spiral arms). We have also tested the effect of the uncertainties in proper motions, distance, radial velocity and age. All cases point towards a Galactocentric radius at birth between $6.5 < R_{GC,birth} < 7.8$ kpc with high probability.

The analysed results from different sources (OCCASO, GES, APOGEE) confirm the α-enhancement of NGC 6705, at least for some α-elements. However, the origin of this is still unclear and seems that cannot be explained by a very different place of birth of this cluster (i. e. the inner Galaxy), which from our calculations would be at most 0.5 kpc inside or outside its current location.

8

CONCLUSIONS AND FUTURE WORK

8.1 GENERAL CONCLUSIONS

This thesis contributes to the understanding of the chemical evolution of the Milky Way by providing new observational material and detailed abundance analysis of Open Clusters. The work developed during this thesis can be separated in several parts described below.

First, we developed OCCASO, an Open Cluster high-resolution spectroscopic survey in the Northern hemisphere. We chose three fiber fed high-resolution ($R > 62,000$, $3700 < \lambda < 9000$ Å) spectrographs in the Spanish ORM and CAHA observatories, to distribute our targets among the three telescopes (Section 2.1). We selected a sample of 33 intermediate-age and old ($Age \gtrsim 0.3$ Gyr) Northern Open Clusters with Red Clump magnitude brighter than $V \sim 15$ (Section 2.3), limited by the observational facilities. We targeted at least 6 RC stars in each cluster to have a representative sample of the cluster stars. We selected them taking into account the position in the CMD, and the membership information based on radial velocities and proper motions from the literature. For some poorly studied clusters this information was not available, so we acquired complementary medium resolution spectra to constrain the membership selection. Until August 2016 we performed 81 nights of observations that let us complete SNR~ 70 (relaxed to SNR~ 50 for the faintest stars) for 115 stars in 18 OCs with a total of 154 spectra, plus two GBS: Arcturus and μ-Leo (Section 3.2). Additionally, 6 clusters have partial observations. Several stars were observed with different instruments to analyse systematics between instruments, if any. For every star we acquire at least 3 individual spectra were combined to obtain the required SNR. To maximize the quality of the spectra for the chemical abundance analysis we designed our own data reduction pipeline, which includes: sky emission lines and telluric features subtraction, heliocentric correction of the radial velocity, combination of individual exposures, normalization and order merge.

The first part of the spectroscopic analysis consists in computing radial velocities for the whole sample of stars (Chapter 4). To calculate them we used `DAOSPEC` through the wrapper `DOOp`, which performs a cross-correlation with a laboratory linelist. We measured epoch radial velocities from the individual spectra of each star, collected to reach the final SNR. With this, we were able to detect two previously unknown spectroscopic binaries in NGC 6819 and NGC 7245, and a possible binary in NGC 6791. From

the mean combined spectra per star we calculated the mean radial velocity using the same code. We checked the consistency of the radial velocities measured by the three instruments with the set of common observed stars, and we found differences of at most 0.6 km s^{-1} (Section 4.1.3). Using the final radial velocities per star we performed a re-analysis of the membership testing their consistency within every cluster. With this analysis we found six non-members or spectroscopic binaries. Using the bona-fide member stars we computed mean radial velocities per cluster obtaining internal dispersions of the order of $0.3 - 1.7$ km s^{-1} (Section 4.1.4). We made an extensive comparison with literature of the mean star radial velocities obtaining an overall offset of 0.2 ± 0.9 km s^{-1} (Section 4.1.5).

We have obtained radial velocities for OCs never studied before with high-resolution spectroscopy: NGC 1907 ($v_r = 2.3 \pm 0.5$ km s^{-1}), NGC 6991 ($v_r = -12.3 \pm 0.6$ km s^{-1}) and NGC 7245 ($v_r = -74.0 \pm 1.4$ km s^{-1}). We used the computed radial velocities per cluster and proper motions available in the literature to perform a kinematic study of the 18 OCs in the context of the Galactic disc. In general, the studied clusters follow the expected rotation of the Milky Way assuming the rotation curve derived by Reid et al. (2014) (Fig. 4.6), with mean spatial velocities respect to the regional standard of rest $\langle U_s \rangle = -7 \pm 20$ km s^{-1}, $\langle V_s \rangle = 14 \pm 18$ km s^{-1}, $\langle W_s \rangle = 13 \pm 18$ km s^{-1}. The clusters with velocities larger than about 30 km s'-1 are the ones with the larger errors. We found that NGC 6633 and IC 4756, which are located closeby in the Local arm, have similar projected radial velocities and similar ages, which could mean a relationship in their formation. We have computed the orbits of the OCs using two gravitational potentials for the Milky Way: an axisymmetric model, and a model featuring the bar and the spiral arms. With this we have recovered the position of the clusters at birth.

The second part of the spectroscopic analysis is the derivation of atmospheric parameters T_{eff}, $\log g$, ξ (Chapter 5). We used two methods, EW (`DAOSPEC+GALA`) and SS (`iSpec`), with the same linelist and model atmospheres. The linelist is the version 5 of the GES linelist, it covers a wavelength range between $4200 \leqslant \lambda \leqslant 9200$ Å and contains atomic information for 35 different chemical species. We extensively investigated the values and errors derived by the two methods. Comparing the whole sample of OCCASO stars, and Arcturus and μ-Leo in particular, we obtained no systematics in T_{eff} and $\log g$ within the quoted errors, though with a quite large dispersion in surface gravity. We also compared the performances of the methods with a set of 23 GBS, for which we obtain very similar offsets and dispersions comparing with the reference values: -1 ± 87, -9 ± 82 K in T_{eff}, -0.05 ± 0.21, -0.05 ± 0.16 in $\log g$, for EW and SS, respectively (Fig. 5.3). As a sanity check we derived atmospheric parameters from BVI photometry for the stars from NGC 2420 and NGC 6791. We found systematic differences between spectroscopic and photometric determinations which change with slight variations of the assumed reddening, distance, age and metallicity to compute photometric parameters. Taking into account all the comparisons we adopted the mean of T_{eff} and $\log g$ values from the two methods to perform the chem-

ical abundance analysis. Mean uncertainties in the final adopted in T_{eff} and log g are around 40 K and 0.1 dex (Section 5.4). The comparison with literature values gives mean offsets of 10 ± 92 K, -0.02 ± 0.27 dex in T_{eff} and log g.

We performed the chemical abundance analysis of Fe, Ni, Cr, Si, Ca and Ti. We derived Fe abundances using the two methods and we obtain an overall offset of 0.07 ± 0.05 dex (Section 6.1.2). We studied the performances of the methods when deriving iron abundances using the set of GBS. We showed that the differences of the methods are intrinsic to each technique, and particularly the treatment of the blends plays an important role. From member stars we derived mean cluster abundances with the two methods. We did an extensive star-by-star comparison with literature, showing good agreement. We also derived mean cluster Fe, Ni, Cr, Si, Ca and Ti abundances using the EW, and its abundance ratios respect to Fe. In particular, we compared the results of these elements with the reference values of Arcturus and μ-Leo in Jofré et al. (2015), where we found the largest differences for the Cr and Si of μ-Leo.

We see that all the clusters present small dispersions in abundance. The larger ones are 0.03 ([Ni/Fe]), 0.06 ([Cr/Fe]), 0.05 ([Si/Fe]), 0.07 ([Ca/Fe]), 0.05 ([Ti/Fe]) dex, excluding NGC 6791 (for which we have larger errors). We analyse the average cluster [α/Fe] abundances respect to [Fe/H], which shows a decreasing trend between [Fe/H] -0.1 and 0.1 dex. NGC 6705 is very well above this trend showing a clear α-enhancement.

We analyzed the results of Fe abundance of the OCs in the context of the Galactic disc:

i. We explored the dependence of [Fe/H] as a function of Galactocentric radius in three different age bins and we compared it with the predictions of a pure chemical evolution model and a chemo-dynamical N-body simulation. We obtained a discrepancy between the radial gradient traced by the older OCs and the predictions of the chemical evolution model. This could be explained by the chemo-dynamical model which includes effects that can have a very high impact in the evolution of the radial gradient, like radial mixing (Section 7.1).

ii. We also analyzed the dependence of [Fe/H] as a function of the height above the plane z. We did not obtain any dependence except for the young OCs $Age < 1$ Gyr where a strong correlation until $|z| \sim 100$ pc was seen.

iii. The sample of OCCASO OCs was enlarged with 12 OCs from GES and 10 anti-center OCs from Cantat-Gaudin et al. (2016) to do a further analysis of the radial gradient and the age-metallicity relation. We obtained very similar slopes in the three different age bins: -0.052 ± 0.010, -0.053 ± 0.005 and -0.050 ± 0.008 dex kpc^{-1}, for $Age < 1$ Gyr, $1 < Age < 4$ Gyr, $4 < Age < 10.3$ Gyr, respectively.

iv. Making use of the birth place computed in Chapter 4 we investigated how a possible change in the radius would change the radial gradient. We obtained no qualitative changes in the younger age bins $Age < 4$ Gyr. For the older clusters the derived current gradient is no longer representative of the distribution at birth.

v. We investigated the age-metallicity relation of the large sample of OCs dividing them in four bins of Galactocentric radius. For the two inner bins ($R_{GC} < 7.5$ kpc, $7.5 < R_{GC} < 10$ kpc) we did not find any significant trend if outliers were discarded. On the other hand, for the outer Galaxy we found steeper gradients of -0.029 ± 0.011 and -0.026 ± 0.014 dex Gyr^{-1} at $10 < R_{GC} < 13$ kpc and $13 < R_{GC} < 22$ kpc, respectively.

We analyze in detail the abundances and orbit of the cluster NGC 6705, for its α-enhancement found in Chapter 6. Additionally, we calculated Mg abundances using three spectral lines, and O abundance from the forbidden line at 6300 Å. We obtained a clear enhancement in Ti, Si, Mg and O using OCCASO data from 7 stars. We also analysed APOGEE results for Si, Ca, Mg and O for 12 member stars. We saw a similar clear enhancement in Si, not in Ca, Mg and O. GES results for this cluster (Magrini et al. 2014; Tautvaišienė et al. 2015) do show a high α-enhancement in Mg and O. All indications seem to point towards an α-enhanced OC, at least in some α-elements, which is completely unexpected for a cluster of its young age ~ 300 Myr. We computed its place of birth to investigate if the cluster could be born in a region close to the Galactic bar, which is an scenario suggested by Chiappini et al. (2015) to explain a similar feature (α enhancement and youth) of field stars. We computed its orbit using different assumptions for the gravitational potential (different masses for the spiral arms, and different pattern speeds), three different determinations of proper motions and distances, and taking into account uncertainties in: proper motions, radial velocity, distance and age. With this we obtain that this cluster was probably born between $6.5 < R_{GC,birth} < 7.8$ kpc from the Galactic center. This results favours the hypothesis that this unexpected α abundance patters might be caused by the effect of the local enrichment of a nearby supernova type II.

8.2 FUTURE WORK

OCCASO observations are still ongoing since there are pending stars to observe in 6 OCs, few selected OCs to start observations (see Table 2.3), and other OCs that can be added to our sample. The majority of these OCs are also the faintest in our sample, and for some stars we need up to 7 hours in the NOT telescope to reach the SNR requirement. So, to advance more steadily we should probably start applying for observing time to a larger telescope. Some of these clusters are also very interesting:

– Be 17 is among the oldest, if not the oldest, OC known.

- Be 32 is a rather old (~ 4 Gyr) OC with has a well-determined metallicity of −0.3 dex. (Heiter et al. 2014), but the most recent high-resolution studies find disagreements in the abundances of Na, Mg, Si, and Ba (Carrera and Pancino 2011).

- NGC 2158 is an intermediate-age OC (~ 1 Gyr) towards the anticenter. High-resolution spectroscopic analyses of one bright giant reported Solar metallicity, significantly higher than earlier medium or low-resolution studies (~ −0.3 dex Heiter et al. 2014).

- NGC 2355 has spectroscopic observations for the determination of physical parameters and metallicity (Soubiran, Odenkirchen, and Le Campion 2000), but it has no detailed abundance studies.

- NGC 6603 is an OC located in an inner Galactocentric distance, and in fact one of the closest known to the Galactic center, and also one of the most metal-rich. It is a young OC (200 Myr) assumed to have Solar abundance from previous studies (Sagar and Griffiths 1998; Kharchenko et al. 2005). However, Carrera et al. (2015) found a mean metallicity of $+0.43 \pm 0.15$ dex, from medium resolution CaT spectroscopy.

- NGC 7142 is a quite old (4-5 Gyr) and loose OC that seems to be on the verge of dissolving into the Galactic disc. It has one of the highest z for its Galactocentric radius.

With the data that we have up to now there is still a lot to do. A more detailed chemical analysis needs to be done for some clusters. For example, NGC 6791 for which we have found slightly lower metallicities than previous determinations in the literature (Carraro et al. 2006b; Geisler et al. 2012; Bragaglia et al. 2014), but that are still very high for such an old cluster in its current location. Our computations of the orbit of this cluster, though unrealistic at high drawback time (e. g. to derive its birth radius), yield very variable Galactocentric radius. This needs a further investigation but shows a hint that it might have come from a very different place in the Galaxy, and therefore its abundances do not agree with chemical evolution expectations for its current location.

Taking advantage of the very high resolution of the OCCASO spectra there are still a lot of chemical groups to analyze: other Fe-peak elements that require a careful analysis (Sc, V, Mn, Co), light and odd-Z elements (Li, C, N, Al, Na), s- (e. g. Rb, Ba, La) and r- (e. g. Eu, Mo) process elements, p-process (Cu and Zn) elements. Mg and O need to be analyzed for the other clusters to have a more complete α abundance determination. Comparison of the expected abundances of these elements at the ages and positions of the studied clusters will for sure provide more constrains on the chemical evolution models and the nucleosynthesis processes.

The publication of *Gaia* Data Release 2 (foreseen by April 2018) will provide proper motions and parallaxes for more than one billion sources. This will allow us to redetermine mean distances and proper motions of our clusters. This accurate data combined with our radial velocities will allow a reanalysis of the 3D kinematics, orbits and birth locations.

We would like to finish remarking the legacy value of the OCCASO survey for other studies like: stellar evolution, for the detailed chemical abundances in combination with absolute luminosities from *Gaia* parallaxes; diffuse interstellar bands, since our high resolution and wide wavelength coverage are excellent material to investigate correlations among these bands and interstellar medium; among others.

Part IV

APPENDIX

A

EFFECTS ON ABUNDANCE DETERMINATIONS USING THE GAIA BENCHMARK STARS

In this study we have seen that different methods may derive abundances even when using high-resolution, precise atmospheric parameters and carefully selected linelists. This has been seen in the literature, for example from the GES analysis strategy (Smiljanic et al. 2014). The comparison of the results from different methods is not trivial as discrepancies between results can be large and difficult to improve.

In particular, Jofré et al. (2015) found that differences in spectral analyses methods can lead to differences in abundances of more than 0.3 dex, even when using the same high quality spectra and the stellar parameters and atomic data were kept fixed. These disagreements between methods cannot be justified given the same material and input parameters used for the analysis. Thus, we investigated what might cause these differences during the workshop "Opening the black box of stellar spectroscopy". The aim was to investigate through different tests, which of the many assumptions in each pipeline can lead to large abundance differences. Since for many of the technical assumptions in such analyses there is no consensus on the correct approach, this study also aims to provide guidelines for a realistic error estimation. This appendix presents the results we obtained. More details can be found in Jofre et al. (2016).

The GBS have become a crucial resource in the cross-calibration of stellar parametrisation methods and stellar population surveys. Provided as a spectral library (Blanco-Cuaresma et al. 2014b) with which different instruments and resolutions can be simulated, key studies have extended the GBS known characteristics from stellar parameters (T_{eff} and $\log g$) to metallicity (Jofré et al. 2014; Heiter et al. 2015b), α and Fe-peak element abundances (Jofré et al. 2015) and extensions of the sample towards low metallicities (Hawkins et al. 2016b).

In this study we used four of the GBS and six analysis methods: three methods are based on SS and three on EW, which are summarised in Table A.1 and described more in detail in Jofre et al. (2016). All methods use the MARCS models (Gustafsson et al. 2008), which are computed under the 1D-LTE assumption and assume the standard composition for α-enhancement with respect to iron abundance. The results were ob-

tained fixing the stellar parameters (T_{eff} , log g, [Fe/H], ξ, $v \sin i$[1]) to the recommended values[2] (see Table A.2).

Table A.1. Summary of spectroscopic methods employed in this work. The name of the method, the approach, the radiative transfer code employed and the wrapper code that uses the radiative transfer code (if applicable) are indicated. From Jofre et al. (2016).

name	approach	radiative transfer code	wrapper
iSpec	SS	SPECTRUM	iSpec
ULB	SS	Turbospectrum	BACCHUS
SME	SS	sme_synth	SME
Porto	EW	MOOG	
BOL	EW	SYNTHE	GALA
UCM	EW	MOOG	StePar

A.1 INPUT DATA

Four GBS were chosen as representative of the groups FG-Dwarfs, K-dwarfs, FGK-giants and metal-poor stars: Sun, 61CygA, Arcturus, HD22879. Table A.2 summarises their fundamental T_{eff} and log g from Heiter et al. (2015b) and recommended NLTE [FeH] determined in Jofré et al. (2014) as well as the adopted ξ, and $v \sin i$. The four spectra are convolved to a common resolution of 70,000, corrected by radial velocity and normalized using iSpec.

Four lines, of Ca I, Cr I, Co I and Mn I, were chosen to make the tests. The atomic data were taken from the fifth version of the line list created for the GES (Heiter et al. 2015a). All have log gf values which have been evaluated to be of good quality (for details see Heiter et al. 2015a). Their atomic data are listed in Table A.4. The two elements, Co I and Mn I have HFS. Those components are also listed.

Their profiles are plotted for each star in Fig. A.1. One can see that the lines are mostly clean, and of weak to moderate strength. Note that the Cr line in the metal-poor star HD22789 is very weak and could not be measured by all methods. We consider a reference value for comparison indicated in Table A.3, which is the average of the abundances obtained by all methods for each star in Jofré et al. (2015).

1 $v \sin i$ is the component of the radial velocity projected to the inclination of the star's pole with respect to the line of sight

2 $v_{mac}$is defined as a scale of turbulence in the stellar atmosphere in which the size of the turbulent cell is greater than the mean-free path of the photon

Table A.2. Atmospheric parameters of the four GBS from Heiter et al. (2015b) and Jofré et al. (2014). $v_{mac}$was used only as input parameter by `SME` and `iSpec`. From Jofre et al. (2016).

Star	T_{eff}	log g	[Fe/H]	ξ	$v \sin i$	v_{mac}
	K	dex	dex	km s^{-1}	km s^{-1}	km s^{-1}
Sun	5771 ± 01	4.44 ± 0.00	0.03 ± 0.05	1.06 ± 0.18	1.6	4.2
Arcturus	4286 ± 35	1.64 ± 0.09	-0.52 ± 0.08	1.58 ± 0.12	3.8	5.0
61CygA	4374 ± 22	4.63 ± 0.04	-0.33 ± 0.38	1.07 ± 0.04	0.0	4.2
HD22879	5868 ± 89	4.27 ± 0.03	-0.86 ± 0.05	1.05 ± 0.19	4.4	5.4

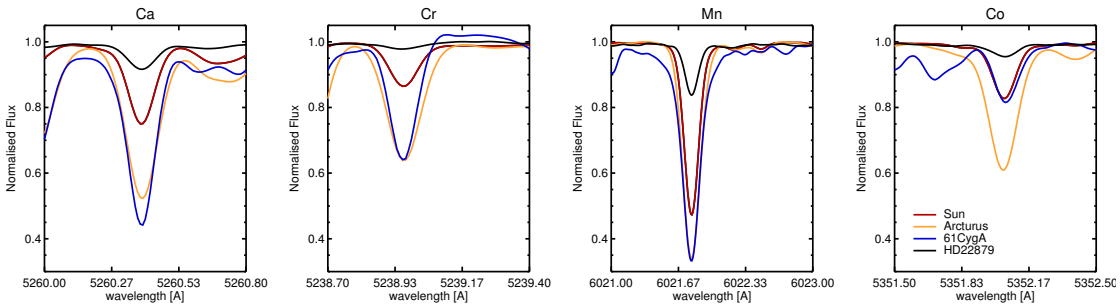

Figure A.1. Observed profiles of the four different lines that were selected and analysed, for each of the four GBS. From Jofre et al. (2016).

A.2 RESULTS

We aimed at making a systematic study of the effects listed below, which are commonly not discussed in the literature because they are believed to have a small impact in the final abundances. To do so, we determined abundances for each of these tests letting the rest of input parameters fixed. In Jofré et al. (2016) we include the details of the design and performance of each test. Here we describe the main results obtained.

Linelist test

We found that the wavelength of the selected Mn feature was incorrect in the GES linelist version 5.0. This was realised because no extra local radial velocity correction was applied to the synthesis methods and therefore the core of the Mn line in the synthesis of each star was slightly shifted (by the same amount) with respect to the observation. In automatic determination of elemental abundances of large high resolution spectroscopic surveys, it is highly probable that some atomic transitions will have laboratory wavelengths that do not perfectly agree with the observations (due to wavelength calibration problems, for example).

Table A.3. Reference absolute abundances of the four chosen lines for each GBS. From Jofre et al. (2016).

	A(Ca)	A(Cr)	A(Mn)	A(Co)
Sun	6.28	5.51	5.34	4.83
Arcturus	5.82	4.97	4.41	4.45
61CygA	5.87	5.11	4.83	4.10
HD22879	5.75	4.77	4.08	4.11

As a result of this test we concluded that EW methods are robust for shifts in wavelength in the linelist, but SS methods can be significantly affected and easily produce differences of 0.2 dex. To overcome this issue, SS methods should always perform an extra local wavelength correction to ensure proper alignment of model and observation, on top of using a well-tested line list.

Continuum normalization

The vast majority of the spectral analyses methods to determine atmospheric parameters and chemical abundances need to perform a normalisation of the continuum flux. This fundamental step is done in several different ways, such as by fitting global polynomials to the pseudo-continuum, to more local functions using synthetic spectra or linear fits. Since there is still no consensus on the best way to treat the continuum flux of the data, it is well known that the measured abundances carry an error due to normalisation.

In general, the agreement between methods is improved if the continuum of a spectrum is fixed, although the final absolute values highly depend on which continuum is applied to the data. Therefore, a careful continuum normalisation should be performed which then should be kept fixed for abundance determination. We warn that this conclusion is only applicable when analysing abundances provided by a single unblended line. When blended lines are included, EW methods cannot reproduce blends, so they usually use the so called effective continuum placement technique (see Stetson and Pancino 2008, Sect. 3.2) that places a depressed continuum which tries to take into account, in a statistical way, the unrecognised flux deficits and excesses due to contamination effects. In this case, not letting the continuum free would lead to overestimated abundances.

Hyperfine structure splitting

Current high-resolution spectrographs like APOGEE or HERMES can fully resolve many features in absorption lines. On top of the basic atomic data of wavelength and

oscillator strength, information on line broadening due to quantum effects such as HFS can be disentangled. Since HFS causes the line profile to increase in width and the peak intensity of the line to decrease, the line appears asymmetric and can no longer be described by a simple Voigt profile (Blackwell-Whitehead et al. 2005). Neglecting this results in the incorrect measurement of the wavelength and a miscalculation of the EW or synthetic spectrum, leading to an incorrect calculation of the abundance of this given element.

We tested the results of Mn and Co when methods consider or do not consider HFS. Overabundances of the order of 0.4 dex can appear in strong Mn lines in giants if HFS is neglected, but even for weak lines, overabundances of 0.15 dex can be obtained. The HFS effect of Co is less significant but still for giants it can be of 0.2 dex. These differences are much larger than expected accuracies of 0.05 dex in Fe-peak elements needed for disentangling different stellar populations, star formation histories and constraining chemical evolution models as well as nucleosynthesis yields (e.g. Feltzing, Fohlman, and Bensby 2007).

Microturbulence

When deriving atmospheric parameters and chemical abundances using 1D model atmospheres, the microturbulence (ξ) parameter also needs to be determined. In 1D models, this parameter is meant to account for some of the turbulent motions in the atmosphere which cause the spectral lines to be broadened. A realistic description of this physical mechanism leading to an accurate modelling of the line profiles can only be done in 3D. This is computationally expensive and currently only few of these accurate models are available to the community (e. g. Magic et al. 2013). The stronger the line, the more it is affected by this broadening and thus by ξ. Because in spectral synthesis calculations under 1D ξ is not physical, each code can employ slightly different values for ξ given an otherwise defined set of stellar parameters.

To perform this test all methods derived abundances for all lines fixing the ξ to six different values. A strong dependency of derived abundance on ξ can be seen for almost every star, element and method. Exceptions are Cr and Ca for HD 22879 and Co for all stars except Arcturus. When there is a dependency, it behaves for every method in the same way, in which the larger the ξ value, the smaller the obtained abundance. This is because a large ξ value will imply a stronger line and therefore less abundance is needed to model a line of a given strength. Differences in 0.2 km s^{-1}correspond to differences of 0.1 dex in abundance for strong lines like those of Arcturus but of 0.05 dex or less for weaker lines.

Therefore, the absolute value of the abundance depends on the adopted value of ξ, but since this parameter is not a physical parameter per se, it is difficult to find an absolute value for ξ that would account for the correct line broadening in every

method. We also found that if HFS is taken into account, strong lines become less dependent on ξ.

Enhancement of α-elements and continuum opacities

When solving the radiative transfer equations to derive chemical abundances of a star, there are three main inputs. The model atmosphere, providing the pressure and temperature of the gas at different depths in the atmosphere; the line list, providing the atomic (and molecular) data regarding the interactions between radiation and matter in the atmosphere; and the chemical composition, providing the distribution of the different elements in the gas and hence the ionisation equilibrium of atoms and the dissociation equilibrium of molecules. Moreover, chemical composition is key for calculating continuous absorption, scattering coefficients and partition functions.

Usually, the chemical composition of the Sun is adopted. This composition can then be scaled appropriately to different stellar metallicities because non-Solar abundance patterns can change the overall opacities and therefore the radiative transfer equations can lead to different solutions for the continuum flux. In principle, this applies every element, but beyond C, N, $\alpha-$ and Fe-peak elements, the number of other elements in a stellar atmosphere are too small to significantly affect the overall opacities and radiative transfer equation solutions.

When $\alpha-$abundances are different of Solar, it is important that the abundances are consistent with the model-atmosphere. While MOOG does it automatically, this is not the case in most of the classical methods to determine abundances. If the abundances are not accordingly scaled, differences of up to 0.1 dex can arise in retrieved abundances of cool stars. This uncertainty is larger than aimed for current pipelines to determine abundances in large spectroscopic surveys.

Atmospheric model interpolation

When deriving stellar parameters and abundances methods require an appropriate model atmosphere, which usually is taken from a grid of models, like the MARCS one in this case. These grids cover the parameter space at fixed steps in T_{eff}, $\log g$ and [Fe/H]. It is very common that when deriving abundances the model atmosphere computed for the exact parameters of the star is not available, so the radiative transfer code operates considering an interpolated model atmosphere of the exact stellar parameters. How this interpolation is done is rarely documented in spectroscopic methods, and may have an impact in abundance determination.

The considered methods follow very similar approaches. As a result of the test subtle differences of about 1% in the temperature and of 5% in gas profiles are found. This is translated to differences of the order of 0.02 dex in the derived abundances, although this number depends on the method considered. Such differences are of the

order of magnitude of uncertainties accepted by big surveys, but are larger than those aimed for very high precision abundance studies (~ 0.01 dex).

Blends

Although abundance determination from spectral lines aims at analysing lines that are free of blends and isolated enough to identify robust continuum points, it is difficult to find perfect clean lines for all type of stars. Indeed, even in our careful choice of optical lines for this work, it was not possible to find perfectly clean and unblended lines for all 4 different GBS. The example of the Ca line is seen in the upper panel of Fig. A.2, which shows the region around the Ca I λ5260 Å line. One can see that the right wing of the line is blended, even in the metal-poor star HD22879. This blend corresponds to a blend of Si I and Mn I. The lower panel of Fig. A.2 shows another Ca I line (λ6455 Å), which is placed at a less crowded region and does not show strong blends on its wings, except for the left wing of 61CygA.

Although synthesis methods can cope better with blends by disregarding the blended regions and synthesising only part of the lines, this is not always done as these blends need to be previously identified, with the amount of blend varying from star to star. The EW methods suffer more evidently from this effect as the total area covered by the line is larger than the actual area filled by the corresponding element, yielding larger abundances (Stetson and Pancino 2008).

The differences obtained between both lines are in general very small for all methods and stars except for the three EW methods for 61CygA with a difference of the order of 0.15 dex. This suggests that abundances derived from EW are only affected in the most extreme case of blending (see Fig. A.2), while SS methods are robust with respect to blends in all cases. It is worth to comment that this conclusion is obtained from this test only, applied to these two lines in these 4 stars.

Radiative transfer codes

If all the studied quantities are fixed, then one can explore the differences obtained in abundances due to the radiative transfer codes. For that, we explore differences between the EW and SS codes.

When all EW codes used the same EW and all input parameters fixed, differences of up to 0.05 dex can be obtained when different radiative transfer codes are used. For lines affected by HFS, differences are more notable, even if the same radiative transfer code is employed. We conclude that the treatment of HFS is an important driver of differences between same radiative transfer codes, which can reach 0.18 dex for Mn.

In the case of the SS methods we studied the effect of the choice of the region where the fitting is performed (mask), and the broadening parameters (macroturbulence, stellar rotation and instrumental profile). The choice of mask had in most of the

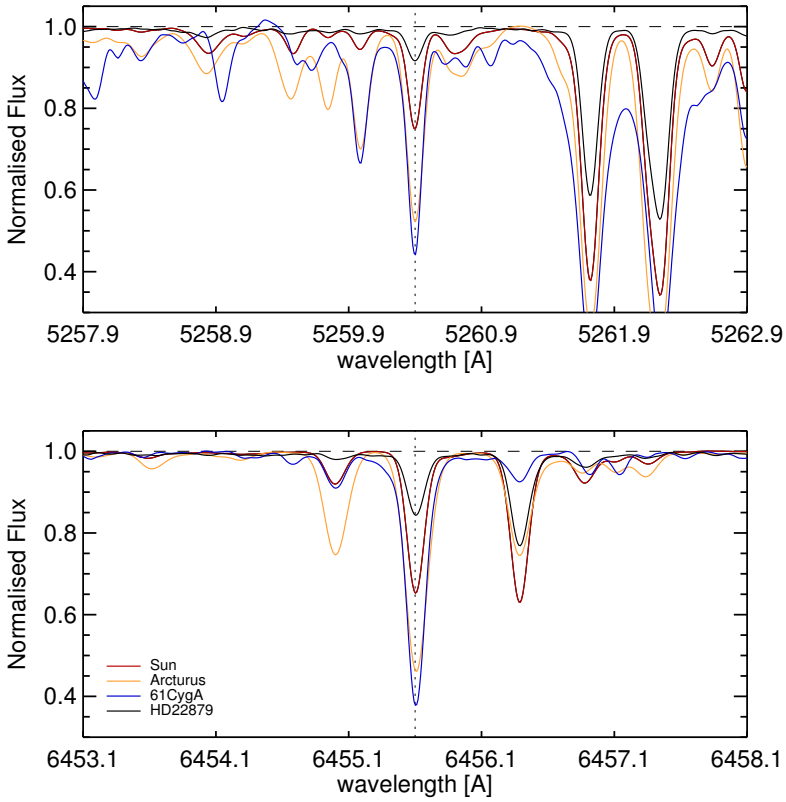

Figure A.2. Observed profiles of two Ca lines in the four GBS. The upper panel shows the profiles for the Ca line analysed throughout this work, while the lower panel shows the profiles for a cleaner Ca line. From Jofre et al. (2016).

cases very little impact in the determination of abundances, even if the masks differed significantly. On the other hand, the broadening parameters (convolved) can produce differences of up to 0.1 dex.

Table A.4. Atomic line data of the four chosen lines and the additional Ca line used for the blending test published in Jofré et al. (2015) as well as the HFS for Co I and Mn I. From Jofre et al. (2016).

Element	Ion	λ (Å)	χ (eV)	log gf
Ca	1	5260.3870	2.521	−1.719
Ca	1	6455.598	2.523	−1.290
Cr	1	5238.9610	2.709	−1.270
Mn	1	6021.7933	3.075	−0.054
Co	1	5352.0397	3.576	0.060
HFS:				
Mn	1	6021.7210	3.075	−2.756
Mn	1	6021.7470	3.075	−1.539
Mn	1	6021.7490	3.075	−2.404
Mn	1	6021.7690	3.075	−1.363
Mn	1	6021.7720	3.075	−2.279
Mn	1	6021.7780	3.075	−0.621
Mn	1	6021.7880	3.075	−1.337
Mn	1	6021.7910	3.075	−2.358
Mn	1	6021.7950	3.075	−0.761
Mn	1	6021.8020	3.075	−1.404
Mn	1	6021.8080	3.075	−0.919
Mn	1	6021.8110	3.075	−1.580
Mn	1	6021.8170	3.075	−1.103
Mn	1	6021.8210	3.075	−1.325
Mn	1	6021.8210	3.075	−1.610
Co	1	5351.8931	3.576	−3.244
Co	1	5351.9244	3.576	−2.855
Co	1	5351.9526	3.576	−1.736
Co	1	5351.9770	3.576	−1.532
Co	1	5351.9985	3.576	−1.459
Co	1	5352.0191	3.576	−0.581
Co	1	5352.0321	3.576	−0.662
Co	1	5352.0509	3.576	−0.503
Co	1	5352.0696	3.576	−0.569

B

TABLES

In this appendix we include long tables that are cited in the text.

Table B.1 includes details of the target stars: equatorial coordinates, V magnitude, probability of membership from proper motions, probability of membership from radial velocity previous to OCCASO and classification provided in the literature (M: member, NM: non-member, SM: single member, BM: binary member, SB: spectroscopic binary). We also include the radial velocity derived in OCCASO, both with each instrument and the mean final value, and previous determinations of the radial velocity with its reference.

Table B.2 includes the results of atmospheric parameters T_{eff}, $\log g$ and ξ, obtained from the spectroscopic analysis with `GALA` and `iSpec` for the OCCASO target stars. We list the mean values and errors of T_{eff}, $\log g$ which are those used for the calculation of [Fe/H] which is also included.

Table B.3 lists the reference values of T_{eff}, $\log g$ and [Fe/H] of the sample of GBS used in this work. We list the values obtained from the spectroscopic analysis with `GALA` and `iSpec` (Chapter 5).

Table B.4 lists the abundances star by star derived in Chapter 6 from EW: [Ni/H], [Cr/H], [Si/H], [Ca/H], [Ti/H], and its abundance ratios [X/Fe].

Table B.1. Radial velocities obtained with FIES, HERMES and CAFE, and the combination of all instruments $v_{r,OCCASO}$. Values from literature are $v_{r,ref}$, and differences with literature are computed as $\Delta v_r = v_{r,OCCASO} - v_{r,ref}$. Information on membership in the literature is shown: probability from proper motion (P_μ), from radial velocity P_{v_r}, and membership classification (Class). Last column points out a remark for special cases discussed in the text. Star IDs are from WEBDA.

Membership probabilities: P_μ: [1]Herzog, Sanders, and Seggewiss (1975), [2]Platais (1991),[3]Zhao et al. (1985), [4]Sanders (1977), [5]Sanders (1973), [6]McNamara, Pratt, and Sanders (1977), [7]Sanders (1972),[8]Kharchenko et al. (2005), [9]McNamara and Solomon (1981), [10]Dias et al. (2014),[11]Platais et al. (2003),[12]Balaguer-Núñez et al. (2004),[13]van Altena and Jones (1970),[14]Zhao et al. (1985); P_{v_r}: [i]Geller, Latham, and Mathieu (2015), [ii]Milliman et al. (2014)

Membership classification provided by literature from: [a]Böcek Topcu et al. (2015), [b]Geller, Latham, and Mathieu (2015), [c]Cantat-Gaudin et al. (2014b), [d]Mathieu et al. (1986),[e]Milliman et al. (2014), [f]Jacobson, Pilachowski, and Friel (2011), [g]Geller et al. (2008), [h]Carrera et al. (2015)

Cluster	Star	RA	DEC	V	P_μ	P_{v_r}	Class	$v_{r,FIES}$	$v_{r,HERMES}$	$v_{r,CAFE}$	$v_{r,OCCASO}$	$v_{r,ref}$	Δv_r	Reference	Remark
	Arcturus	14 : 15 : 39.672	+19 : 10 : 56.67	−0.05				-5.1 ± 0.5	-5.0 ± 0.6	-4.9 ± 0.8	-5.0 ± 0.9	-5.19 ± 0.03	0.19	Blanco-Cuaresma et al. (2014b)	
	μ-Leo	09 : 52 : 45.817	+26 : 00 : 25.03	3.88				13.7 ± 0.6	13.8 ± 0.7	14.5 ± 1.0	13.9 ± 1.2	13.53 ± 0.03	0.37	Blanco-Cuaresma et al. (2014b)	
IC 4756	W0042	18 : 37 : 20.77	+05 : 53 : 43.1	9.46					-24.7 ± 0.6		-24.7 ± 0.6	-24.9 ± 0.2	0.2	Mermilliod, Mayor, and Udry (2008)	
												-25.2 ± 0.7	0.5	Valitova et al. (1990)	
	W0044	18 : 37 : 29.72	+05 : 12 : 15.5	9.79	0.96[1]				-25.8 ± 0.7		-25.8 ± 0.7	-26.0 ± 0.1	0.2	Mermilliod, Mayor, and Udry (2008)	
												-26.6 ± 0.2	0.8	Valitova et al. (1990)	
	W0049	18 : 37 : 34.22	+05 : 28 : 33.5	9.43	0.96[1]				-25.2 ± 0.6		-25.2 ± 0.6	-25.4 ± 0.1	0.2	Mermilliod, Mayor, and Udry (2008)	
												-26.0 ± 0.4	0.8	Valitova et al. (1990)	
	W0081	18 : 38 : 20.76	+05 : 26 : 02.3	9.38	0.91[1],0.99[10]				-23.1 ± 0.7		-23.1 ± 0.7	-23.2 ± 0.1	0.1	Mermilliod, Mayor, and Udry (2008)	
												-27.9 ± 0.5	4.8	Valitova et al. (1990)	
	W0101	18 : 38 : 43.79	+05 : 14 : 20.0	9.38	0.94[1],0.99[10]				-25.5 ± 0.7		-25.5 ± 0.7	-25.7 ± 0.1	0.2	Mermilliod, Mayor, and Udry (2008)	
												-25.6 ± 0.2	0.1	Valitova et al. (1990)	
	W0109	18 : 38 : 52.93	+05 : 20 : 16.5	9.02	0.96[1],0.99[10]			-24.5 ± 0.5	-24.8 ± 0.6	-24.0 ± 0.9	-24.5 ± 0.6	-25.2 ± 0.1	0.7	Mermilliod, Mayor, and Udry (2008)	
												-24.4 ± 0.4	−0.1	Valitova et al. (1990)	
	W0125	18 : 39 : 17.88	+05 : 13 : 48.8	9.29	0.92[1],0.99[10]			-24.5 ± 0.4	-24.7 ± 0.5	-24.0 ± 0.9	-24.5 ± 0.6	-24.9 ± 0.1	0.4	Mermilliod, Mayor, and Udry (2008)	
												-24.4 ± 0.4	−0.1	Valitova et al. (1990)	
NGC 188	W1105	00:46:59.616	+85:13:15.80	12.36	0.98[11]	0.98[i]	M[f],SM[g]		-41.1 ± 1.0		-41.1 ± 1.0	$-41.2\pm$	0.1	Jacobson, Pilachowski, and Friel (2011)	
												$-42.09\pm$	0.89	Geller et al. (2008)	
	W2051	00:42:25.551	+85:16:22.03	12.95	0.96[11]	0.98[i]	SM[g]		-39.7 ± 0.9		-39.7 ± 0.9	$-41.1\pm$	1.4	Friel, Jacobson, and Pilachowski (2010)	X
												$-42.57\pm$	2.87	Geller et al. (2008)	
	W2088	00:47:18.420	+85:19:45.78	13.01	0.96[11]	0.98[i]	M[f],SM[g]		-42.5 ± 0.8		-42.5 ± 0.8	$-42.4\pm$	−0.1	Friel, Jacobson, and Pilachowski (2010)	
												$-42.95\pm$	0.45	Geller et al. (2008)	
	W5217	00:54:11.476	+85:15:23.19	12.40	0.74[11]	0.98[i]	M[f],SM[g]		-41.7 ± 0.8		-41.7 ± 0.8	$-41.6\pm$	−0.1	Jacobson, Pilachowski, and Friel (2011)	
												$-42.14\pm$	0.44	Geller et al. (2008)	
	W5224	00:54:36.603	+85:01:15.31	12.45	0.88[11]	0.98[i]	M[f],SM[g]		-42.0 ± 0.8		-42.0 ± 0.8	$-42.0\pm$	0	Jacobson, Pilachowski, and Friel (2011)	
												$-42.83\pm$	0.83	Geller et al. (2008)	

Table B.1 Continued from previous page

Cluster	Star	RA	DEC	V	P_μ	P_{v_r}	Class	$v_{r,FIES}$	$v_{r,HERMES}$	$v_{r,CAFE}$	$v_{r,OCCASO}$	$v_{r,ref}$	Δv_r	Reference	Remark
	W7323	00:49:05.596	+85:26:07.78	12.72	0.94[11]	0.98[i]	M[f],SM[g]	-42.3 ± 0.9			-42.3 ± 0.9	$-42.3\pm$	0	Jacobson, Pilachowski, and Friel (2011)	
												$-42.66\pm$	0.36	Geller et al. (2008)	
NGC 752	W0001	01 : 55 : 12.60	+37 : 50 : 14.60	9.48	0.93[2],0.93[10]		M[a]	5.3 ± 0.4			5.3 ± 0.4	5.2 ± 0.1	0.1	Mermilliod, Mayor, and Udry (2008)	
												4.73 ± 0.20	0.57	Böcek Topcu et al. (2015)	
	W0024	01 : 55 : 39.35	+37 : 52 : 52.69	8.91	0.99[2],0.93[10]		M[a]	5.6 ± 0.4	5.7 ± 0.5		5.6 ± 0.5	5.4 ± 0.1	0.2	Mermilliod, Mayor, and Udry (2008)	
												4.86 ± 0.19	0.74	Böcek Topcu et al. (2015)	
	W0027	01 : 55 : 42.39	+37 : 37 : 54.66	9.17	0.99[2],0.93[10]		M[a]	4.9 ± 0.5	4.8 ± 0.5		4.9 ± 0.5	4.6 ± 0.1	0.3	Mermilliod, Mayor, and Udry (2008)	
												4.39 ± 0.19	0.51	Böcek Topcu et al. (2015)	
	W0077	01 : 56 : 21.63	+37 : 36 : 08.53	9.38	0.98[2],0.91[10]		M[a]		5.2 ± 0.5		5.2 ± 0.5	5.0 ± 0.1	0.2	Mermilliod, Mayor, and Udry (2008)	
												4.58 ± 0.20	0.62	Böcek Topcu et al. (2015)	
	W0137	01 : 57 : 03.12	+38 : 08 : 02.73	8.90	0.99[2],0.93[10]		M[a]	5.7 ± 0.5	5.5 ± 0.6		5.6 ± 0.5	5.2 ± 0.1	0.4	Mermilliod, Mayor, and Udry (2008)	
												5.59 ± 0.20	0.01	Böcek Topcu et al. (2015)	
	W0295	01 : 58 : 29.81	+37 : 51 : 37.68	9.30	0.99[2],0.93[10]		M[a]	5.6 ± 0.5			5.6 ± 0.5	5.2 ± 0.1	0.4	Mermilliod, Mayor, and Udry (2008)	
												6.32 ± 0.23	-0.72	Böcek Topcu et al. (2015)	
	W0311	01 : 58 : 52.90	+37 : 48 : 57.30	9.06	0.99[2],0.92[10]		M[a]		6.0 ± 0.6		6.0 ± 0.6	5.8 ± 0.1	0.2	Mermilliod, Mayor, and Udry (2008)	
												5.19 ± 0.19	0.81	Böcek Topcu et al. (2015)	
NGC 1817	W0008	5:12:19.388	+16:40:48.6	12.12	0.65[12]		M[f]	65.6 ± 0.4			65.6 ± 0.4	64.92 ± 0.36	0.68	Mermilliod, Mayor, and Udry (2008)	
												$64.8\pm$	0.8	Jacobson, Pilachowski, and Friel (2011)	
												66.1 ± 0.2	-0.5	Reddy, Giridhar, and Lambert (2012)	
	W0030	5:12:32.559	+16:39:57.7	12.46	0.63[12]		M[f]	65.4 ± 0.8			65.4 ± 0.8	65.00 ± 0.44	0.4	Mermilliod, Mayor, and Udry (2008)	
												$65.0\pm$	0.4	Jacobson, Pilachowski, and Friel (2011)	
	W0073	5:12:24.649	+16:35:48.8	12.04	0.81[12]		M[f]	65.4 ± 0.6			65.4 ± 0.6	65.44 ± 0.36	-0.04	Mermilliod, Mayor, and Udry (2008)	
												$65.1\pm$	0.3	Jacobson, Pilachowski, and Friel (2011)	
												66.5 ± 0.2	-1.1	Reddy, Giridhar, and Lambert (2012)	
	W0079	5:12:10.675	+16:38:31.2	12.49	0.77[12]		M[f]	66.1 ± 0.6			66.1 ± 0.6	64.87 ± 0.36	1.23	Mermilliod, Mayor, and Udry (2008)	
												$65.8\pm$	0.3	Jacobson, Pilachowski, and Friel (2011)	
	W0127	5:12:50.097	+16:40:49.7	12.25	0.82[12]		M[f]	65.6 ± 0.6			65.6 ± 0.6	65.27 ± 0.30	0.33	Mermilliod, Mayor, and Udry (2008)	
												$65.1\pm$	0.5	Jacobson, Pilachowski, and Friel (2011)	
NGC 1907	W0062	05:27:49.053	+35:20:10.13	12.41	0.98[10]		M[b]		2.6 ± 1.6		2.6 ± 1.6	-2.08 ± 1.4	4.68	Glushkova and Rastorguev (1991)	
	W0113	05:28:04.207	+35:19:16.32	11.81	0.61[10]		M[b]		2.2 ± 0.6		2.2 ± 0.6	1.67 ± 0.9	0.53	Glushkova and Rastorguev (1991)	
	W0131	05:28:05.276	+35:19:49.64	12.30	0.98[10]		M[b]		2.3 ± 1.2		2.3 ± 1.2	-0.68 ± 2	2.98	Glushkova and Rastorguev (1991)	
	W0133	05:28:05.863	+35:19:38.87	12.74	0.98[10]				-0.2 ± 1.7		-0.2 ± 1.7				
	W0256	05:28:01.783	+35:21:14.89	11.23	0.98[10]		M[b]		2.8 ± 0.8		2.8 ± 0.8	1.45 ± 0.69	1.35	Glushkova and Rastorguev (1991)	
	W2087	05:27:38.899	+35:17:18.04	13.09					63.4 ± 1.0		63.4 ± 1.0				X
NGC 2099	W007	05:52:20.31	+32:33:49.3	11.42	0.85[3],1.00[10]		M[g]		8.9 ± 0.9		8.9 ± 0.9	8.7 ± 0.2	0.2	Mermilliod, Mayor, and Udry (2008)	
	W016	05:52:17.26	+32:32:56.5	11.26	0.89[3],0.98[10]		M[g]		7.5 ± 0.9		7.5 ± 0.9	7.2 ± 0.2	0.3	Mermilliod, Mayor, and Udry (2008)	
	W031	05:52:16.68	+32:31:39.3	11.52	0.87[3],0.98[10]		M[g]		7.4 ± 1.3		7.4 ± 1.3	7.1 ± 0.2	0.3	Mermilliod, Mayor, and Udry (2008)	
	W148	05:52:08.10	+32:30:33.1	11.09	0.86[3],0.93[10]		M[g]		8.6 ± 0.9		8.6 ± 0.9	8.7 ± 0.2	-0.1	Mermilliod, Mayor, and Udry (2008)	

Table B.1 Continued from previous page

Cluster	Star	RA	DEC	V	P_μ	P_{v_r}	Class	$v_{r,FIES}$	$v_{r,HERMES}$	$v_{r,CAFE}$	$v_{r,OCCASO}$	$v_{r,ref}$	Δv_r	Reference	Remark
												9.1 ± 0.4	-0.5	Pancino et al. (2010)	
NGC 2420	W041	07:38:06.27	+21:36:54.6	12.67	0.89[13]		M[f]	73.8 ± 0.6			73.8 ± 0.6	73.66 ± 0.33	0.14	Mermilliod, Mayor, and Udry (2008)	
												74.23 ± 0.87	-0.43	Pancino et al. (2010)	
												73.9±	-0.1	Jacobson, Pilachowski, and Friel (2011)	
	W076	07:38:15.5	+21:38:01.8	12.66	0.87[13]		M,SB?[f]	74.3 ± 0.6			74.3 ± 0.6	74.13 ± 0.34	0.17	Mermilliod, Mayor, and Udry (2008)	
												75.49 ± 0.41	-1.19	Pancino et al. (2010)	
												74.3±	0	Jacobson, Pilachowski, and Friel (2011)	
	W091	07:38:18.17	+21:32:06.8	12.61	0.84[13]		M[f]	73.7 ± 0.6			73.7 ± 0.6	73.85 ± 0.37	-0.15	Mermilliod, Mayor, and Udry (2008)	
												73.5±	0.2	Jacobson, Pilachowski, and Friel (2011)	
	W111	07:38:21.43	+21:35:05.6	12.60	0.77[13]		M,SB?[f]	74.0 ± 0.5			74.0 ± 0.5	73.44 ± 0.30	0.56	Mermilliod, Mayor, and Udry (2008)	
												73.5±	0.5	Jacobson, Pilachowski, and Friel (2011)	
	W118	07:38:21.90	+21:35:50.9	12.57	0.91[13]		M[f]	73.5 ± 0.5			73.5 ± 0.5	73.53 ± 0.35	-0.03	Mermilliod, Mayor, and Udry (2008)	
												73.2±	0.3	Jacobson, Pilachowski, and Friel (2011)	
	W174	07:38:26.93	+21:38:24.8	12.40	0.89[13]		M,SB?[f]	73.8 ± 0.5			73.8 ± 0.5	73.18 ± 0.31	0.62	Mermilliod, Mayor, and Udry (2008)	
												73.66 ± 1.17	0.14	Pancino et al. (2010)	
												73.8±	0	Jacobson, Pilachowski, and Friel (2011)	
	W236	07:38:37.59	+21:34:12.4	12.58	0.80[13]		M[f]	73.6 ± 0.6			73.6 ± 0.6	73.24 ± 0.50	0.36	Mermilliod, Mayor, and Udry (2008)	
												73.4±	0.2	Jacobson, Pilachowski, and Friel (2011)	
NGC 2539	W229	08:10:33.80	-12:51:48.9	11.20	0.99[10]				29.8 ± 0.7		29.8 ± 0.7				
	W233	08:10:34.35	-12:49:55.2	10.89	0.99[10]		SB1[g]		34.8 ± 1.1		34.8 ± 1.1	26.7 ± 0.2	8.1	Mermilliod, Mayor, and Udry (2008)	X
	W251	08:10:38.99	-12:44:44.7	11.23	0.98[10]		M[g]		29.4 ± 1.0		29.4 ± 1.0	29.4 ± 0.2	0	Mermilliod, Mayor, and Udry (2008)	
	W346	08:10:23.02	-12:50:43.3	10.92	0.97[10]		M[g]		30.0 ± 0.6		30.0 ± 0.6	29.7 ± 0.1	0.3	Mermilliod, Mayor, and Udry (2008)	
												29.7 ± 0.2	0.3	Reddy, Giridhar, and Lambert (2013)	
	W463	08:10:42.87	-12:40:11.8	10.69			M[g]		29.0 ± 0.7		29.0 ± 0.7	28.8 ± 0.1	0.2	Mermilliod, Mayor, and Udry (2008)	
												28.7 ± 0.2	0.3	Reddy, Giridhar, and Lambert (2013)	
	W502	08:11:27.67	-12:41:06.8	11.03			M[g]		28.9 ± 0.8		28.9 ± 0.8	28.9 ± 0.2	0	Mermilliod, Mayor, and Udry (2008)	
NGC 2682	W084	08:51:12.73	+11:52:42.7	10.52	0.91[4],0.98[10]	0.98[i]	SM[b],M[g]		34.2 ± 0.6		34.2 ± 0.6	34.0 ± 0.2	0.2	Mermilliod, Mayor, and Udry (2008)	
												33.94 ± 0.3	0.26	Pasquini et al. (2011)	
												33.8	0.4	Jacobson, Pilachowski, and Friel (2011)	
												34.141 ± 0.008	0.06	Pasquini et al. (2012)	
												34.1 ± 0.4	0.1	Mathieu et al. (1986)	
												34.09 ± 0.03	0.11	Geller, Latham, and Mathieu (2015)	
	W141	08:51:22.83	+11:48:02.0	10.48	0.96[4],0.98[10]	0.98[i]	SM[b],M[g]		33.9 ± 0.5		33.9 ± 0.5	33.8 ± 0.4	0.1	Mermilliod, Mayor, and Udry (2008)	
												35.2 ± 0.1	-1.3	Pancino et al. (2010)	
												33.95 ± 0.3	-0.05	Pasquini et al. (2011)	
												33.3	0.6	Jacobson, Pilachowski, and Friel (2011)	
												33.9 ± 1.0	0	Sakari et al. (2011)	
												33.723 ± 0.023	0.177	Pasquini et al. (2012)	

Table B.1 Continued from previous page

Cluster	Star	RA	DEC	V	P_μ	P_{v_r}	Class	$v_{r,FIES}$	$v_{r,HERMES}$	$v_{r,CAFE}$	$v_{r,OCCASO}$	$v_{r,ref}$	Δv_r	Reference	Remark
												33.6 ± 0.4	0.3	Mathieu et al. (1986)	
												33.68 ± 0.06	0.22	Geller, Latham, and Mathieu (2015)	
												33.900 ± 0.008	0	Yadav et al. (2008)	
	W151	08:51:26.22	+11:53:52.2	10.48	0.92^4,0.90^{10}	0.98^i	SM[b],M[g]		33.9 ± 0.6		33.9 ± 0.6	34.0 ± 0.3	-0.1	Mermilliod, Mayor, and Udry (2008)	
												33.87 ± 0.3	0.03	Pasquini et al. (2011)	
												33.2	0.7	Jacobson, Pilachowski, and Friel (2011)	
												33.901 ± 0.024	-0.001	Pasquini et al. (2012)	
												34.2 ± 0.1	-0.3	Alam et al. (2015)	
												34.51	-0.61	Mészáros et al. (2013)	
												33.9 ± 0.5	0	Mathieu et al. (1986)	
												33.85 ± 0.04	0.05	Geller, Latham, and Mathieu (2015)	
	W164	08:51:29.03	+11:50:33.4	10.52	0.92^4,0.96^{10}		M[g]		33.5 ± 0.6		33.5 ± 0.6	33.2 ± 0.2	0.3	Mermilliod, Mayor, and Udry (2008)	
												33.4 ± 0.3	0.1	Pasquini et al. (2011)	
												33.385 ± 0.019	0.115	Pasquini et al. (2012)	
												33.45 ± 0.08	0.05	Alam et al. (2015)	
												33.84	-0.34	Mészáros et al. (2013)	
												33.3 ± 0.4	0.2	Mathieu et al. (1986)	
												33.650 ± 0.008	-0.15	Yadav et al. (2008)	
	W223	08:51:43.91	+11:56:42.9	10.58	0.95^4,0.95^{10}	0.98^i	SM[b],M[g]		33.0 ± 0.6		33.0 ± 0.6	32.9 ± 0.2	0.1	Mermilliod, Mayor, and Udry (2008)	
												34.9 ± 0.3	-1.9	Pancino et al. (2010)	
												32.81 ± 0.3	0.19	Pasquini et al. (2011)	
												32.3	0.89	Jacobson, Pilachowski, and Friel (2011)	
												32.844 ± 0.023	0.35	Pasquini et al. (2012)	
												33.33	-0.14	Mészáros et al. (2013)	
												32.8 ± 0.4	0.39	Mathieu et al. (1986)	
												32.85 ± 0.06	0.15	Geller, Latham, and Mathieu (2015)	
												32.955 ± 0.006	0.04	Yadav et al. (2008)	
	W224	08:51:43.55	+11:44:26.8	10.76	0.90^4,0.91^{10}	0.98^i	BM,SB1[b],SB1[g]		27.5 ± 0.6		27.5 ± 0.6	32.5 ± 0.1	-5	Mermilliod, Mayor, and Udry (2008)	X
												30.37 ± 0.3	-2.87	Pasquini et al. (2011)	
												35.6	-8.1	Jacobson, Pilachowski, and Friel (2011)	
												28.33	-0.83	Mészáros et al. (2013)	
												34.1 ± 3.1	-6.6	Mathieu et al. (1986)	
												32.83 ± 0.06	-5.33	Geller, Latham, and Mathieu (2015)	
	W266	08:51:59.56	+11:55:05.2	10.55	0.95^4,0.98^{10}	0.98^i	SM[b],M[g]		34.5 ± 0.5		34.5 ± 0.5	34.5 ± 0.2	0	Mermilliod, Mayor, and Udry (2008)	
												33.4 ± 0.3	1.1	Pasquini et al. (2011)	
												33.8	0.7	Jacobson, Pilachowski, and Friel (2011)	
												34.327 ± 0.021	0.173	Pasquini et al. (2012)	
												34.426 ± 0.004	0.07	Alam et al. (2015)	

Table B.1 Continued from previous page

Cluster	Star	RA	DEC	V	P_μ	P_{v_r}	Class	$v_{r,FIES}$	$v_{r,HERMES}$	$v_{r,CAFE}$	$v_{r,OCCASO}$	$v_{r,ref}$	Δv_r	Reference	Remark
												34.71	-0.21	Mészáros et al. (2013)	
												34.3 ± 0.4	0.2	Mathieu et al. (1986)	
												34.40 ± 0.05	0.1	Geller, Latham, and Mathieu (2015)	
	W286	08:52:18.61	+11:44:26.5	10.47	0.92[4]		NM[g]		33.8 ± 0.6		33.8 ± 0.6	25.7 ± 7.5	8.1	Mermilliod, Mayor, and Udry (2008)	
												38.9 ± 0.5	-5.1	Pancino et al. (2010)	
												33.64 ± 0.3	0.16	Pasquini et al. (2011)	
												33.0	0.8	Jacobson, Pilachowski, and Friel (2011)	
												33.646 ± 0.002	0.154	Pasquini et al. (2012)	
												33.02 ± 0.02	0.78	Alam et al. (2015)	
												34.05	-0.25	Mészáros et al. (2013)	
												33.6 ± 0.5	0.2	Mathieu et al. (1986)	
NGC 6633	W100	18:27:54.73	+06:36:00.3	8.30	0.92[5]		M[g]	-28.6 ± 0.6	-28.7 ± 0.6	-27.9 ± 1.0	-28.5 ± 1.1	-29.1 ± 0.1	0.6	Mermilliod, Mayor, and Udry (2008)	
	W106	18:28:00.18	+06:54:51.5	8.67			M[g]	-28.2 ± 0.7	-28.3 ± 0.8		-28.2 ± 0.7	-28.5 ± 0.1	0.3	Mermilliod, Mayor, and Udry (2008)	
	W119	18:28:17.64	+06:46:00.1	8.95	0.43[5]		M[g]	-28.6 ± 0.8	-28.7 ± 0.7		-28.7 ± 0.8	-29.0 ± 0.1	0.3	Mermilliod, Mayor, and Udry (2008)	
	W126	18:28:22.97	+06:42:29.3	8.77	0.16[5]		M[g]	-28.8 ± 0.5	-29.0 ± 0.7		-28.9 ± 0.6	-29.3 ± 0.1	0.4	Mermilliod, Mayor, and Udry (2008)	
NGC 6705	W0660	18:51:15.691	-06:18:14.47	11.81	0.99[6],0.83[10]		SM[c],SM[d],M[g]		35.6 ± 0.9		35.6 ± 0.9	35.5 ± 0.5	0.1	Mermilliod, Mayor, and Udry (2008)	
												35.0 ± 0.6	0.6	Cantat-Gaudin et al. (2014b)	
												35.5 ± 0.5	0.1	Mathieu et al. (1986)	
	W0669	18:51:15.318	-06:18:35.51	11.97	0.98[6],0[10]		SM[c],SM[d],M[g]		34.5 ± 1.5		34.5 ± 1.5	34.2 ± 0.7	0.3	Mermilliod, Mayor, and Udry (2008)	
												33.7 ± 0.6	0.8	Cantat-Gaudin et al. (2014b)	
												33.9 ± 0.4	0.6	Mathieu et al. (1986)	
	W0686	18:51:14.507	-06:16:54.74	11.92	0.99[6],0.84[10]		SM[c],SM[d],M[g]		36.2 ± 1.5		36.2 ± 1.5	36.8 ± 0.6	-0.6	Mermilliod, Mayor, and Udry (2008)	
												35.1 ± 0.6	1.1	Cantat-Gaudin et al. (2014b)	
												35.7 ± 0.6	0.5	Mathieu et al. (1986)	
	W0779	18:51:11.141	-06:14:33.76	11.47	0.98[6],0[10]		SM[d],M[g]	34.4 ± 0.8	34.3 ± 1.0		34.3 ± 0.9	33.7 ± 0.5	0.6	Mermilliod, Mayor, and Udry (2008)	
												34.3 ± 0.5	0	Mathieu et al. (1986)	
	W0916	18:51:07.847	-06:17:11.89	11.62	0.99[6],0[10]		SM[c],SM[d]		34.5 ± 1.5		34.5 ± 1.5	34.0 ± 0.7	0.5	Mathieu et al. (1986)	
												33.6 ± 0.6	0.9	Cantat-Gaudin et al. (2014b)	
	W1184	18:51:01.989	-06:17:26.50	11.43	0.99[6],0.87[10]		SM[c],SM[d]	33.1 ± 0.7	33.0 ± 0.8		33.1 ± 0.8	32.9 ± 0.6	0.2	Mathieu et al. (1986)	
												32.0 ± 0.6	1.1	Cantat-Gaudin et al. (2014b)	
	W1256	18:51:00.194	-06:16:59.06	11.6	0.77[6]		M[c],SM[d]		35.7 ± 0.9		35.7 ± 0.9				
	W1423	18:50:55.789	-06:18:14.26	11.41	0.99[6],0.85[10]		SM[c],SM[d],M[g]	36.4 ± 0.8	36.2 ± 1.0		36.3 ± 0.9	36.1 ± 0.3	0.2	Mermilliod, Mayor, and Udry (2008)	
												35.1 ± 0.6	1.2	Cantat-Gaudin et al. (2014b)	
												36.1 ± 0.4	0.2	Mathieu et al. (1986)	
NGC 6791	W1794	19:21:06.31	+37:44:59.9	14.48				-45.1 ± 1.3			-45.1 ± 1.3	-45.8 ± 0.4	0.7	Smolinski et al. (2011)	
												-45.4 ± 0.2	0.3	Alam et al. (2015)	
												−45.1	0	Mészáros et al. (2013)	
												−44.97	−0.13	Tofflemire et al. (2014)	

Table B.1 Continued from previous page

Cluster	Star	RA	DEC	V	P_μ	P_{v_r}	Class	$v_{r,FIES}$	$v_{r,HERMES}$	$v_{r,CAFE}$	$v_{r,OCCASO}$	$v_{r,ref}$	Δv_r	Reference	Remark
	W2562	19:21:00.87	+37:46:39.9	14.58				-48.3 ± 0.9			-48.3 ± 0.9	-45.5 ± 0.6	-2.8	Smolinski et al. (2011)	
												-48.91	0.61	Tofflemire et al. (2014)	
	W2579	19:21:00.87	+37:45:34.1	14.55				-45.8 ± 1.4			-45.8 ± 1.4	-46.8 ± 0.5	1	Smolinski et al. (2011)	
												-45.75	-0.05	Mészáros et al. (2013)	
												-45.79	-0.01	Tofflemire et al. (2014)	
	W3363	19:20:56.31	+37:44:33.7	14.65				-48.5 ± 1.1			-48.5 ± 1.1	-48.7	0.2	Tofflemire et al. (2014)	
												-48.55	0.05	Mészáros et al. (2013)	
												-48.99 ± 0.06	0.49	Alam et al. (2015)	
	W3899	19:20:52.47	+37:50:15.8	14.48				-48.1 ± 3.2			-48.1 ± 3.2	-48.3 ± 0.1	0.2	Carraro et al. (2006b)	X
												-48.47	0.37	Tofflemire et al. (2014)	
	W3926	19:20:52.89	+37:45:33.4	14.55				-45.8 ± 1.3			-45.8 ± 1.3	-45.6 ± 0.6	-0.2	Smolinski et al. (2011)	
												-46.2 ± 0.1	0.4	Carraro et al. (2006b)	
												-46.1 ± 0.03	0.3	Alam et al. (2015)	
												-45.68	-0.12	Mészáros et al. (2013)	
												-46.02	0.22	Tofflemire et al. (2014)	
NGC 6819	W0333	19:41:13.55	+40:12:20.5	13.069	0.92[7],0[10]	0.94[ii]	SM[e]		2.8 ± 0.6		2.8 ± 0.6	5.31	-2.51	Bragaglia et al. (2001)	
												-5.6 ± 0.6	8.4	Alam et al. (2015)	
												2.53	0.3	Mészáros et al. (2013)	
												2.37 ± 0.23	0.43	Milliman et al. (2014)	
	W0386	19:41:22.45	+40:12:05.3	13.016	0.89[7]	0.91[ii]	SM[e]		2.6 ± 0.7		2.6 ± 0.7				
	W0398	19:41:13.45	+40:11:57.9	13.119	0.90[7]	0.93[ii]	SM[e]		3.3 ± 0.7		3.3 ± 0.7				
	W0978	19:41:14.76	+40:11:00.8	12.869	0.90[7],0.76[10]	0.80[ii]	SM[e]		1.2 ± 0.8		1.2 ± 0.8	5.96	-4.76	Bragaglia et al. (2001)	
												1.3 ± 0.2	-0.1	Alam et al. (2015)	
												1.6	-0.4	Mészáros et al. (2013)	
												0.79 ± 0.21	0.41	Milliman et al. (2014)	
	W0979	19:41:15.93	+40:11:11.5	12.956	0.91[7],0.99[10]	0.94[ii]	BM,SB1[e]		3.0 ± 0.8		3.0 ± 0.8	1.44	1.56	Bragaglia et al. (2001)	
												1.46 ± 0.69	1.54	Milliman et al. (2014)	
NGC 6939	W145	20:31:28.55	+60:40:07.82	12.98	0.98[14]				-18.2 ± 0.9		-18.2 ± 0.9	-18.4 ± 0.5	0.2	Milone (1994)	
	W170	20:31:32.03	+60:39:27.37	12.99	0.97[14]				-17.9 ± 0.8		-17.9 ± 0.8	-17.7 ± 0.8	-0.2	Milone (1994)	
	W214	20:31:40.18	+60:41:31.69	13.08	0.98[14]				-18.5 ± 0.9		-18.5 ± 0.9	-18.5 ± 0.7	0	Milone (1994)	
	W230	20:31:43.42	+60:40:38.82	12.99	0.95[14]				-19.3 ± 0.8		-19.3 ± 0.8	-19.2 ± 0.5	-0.1	Milone (1994)	
	W292	20:31:59.11	+60:42:04.76	13.11	0.98[14]				-18.8 ± 0.9		-18.8 ± 0.9	-19.2 ± 0.5	0.4	Milone (1994)	
NGC 6991	W034	20:53:37.68	+47:12:23.66	10.30	0.64[8]			-13.9 ± 0.5		-13.7 ± 0.9	-13.8 ± 0.7				
	W043	20:53:50.82	+47:05:06.75	10.08	0.66[8]					-11.9 ± 0.9	-11.9 ± 0.9				
	W049	20:54:01.74	+47:25:49.16	10.17	0.59[8],0.89[10]			-12.3 ± 0.4		-12.2 ± 0.9	-12.3 ± 0.6				
	W067	20:54:29.81	+47:28:03.15	9.43	0.91[8],0.91[10]			-12.7 ± 0.5		-12.5 ± 0.9	-12.7 ± 0.7				
	W100	20:55.03.98	+47:19:20.03	9.87	0.88[8],0.90[10]					-11.7 ± 1.0	-11.7 ± 1.0				
	W131	20:55:42.69	+47:22:32.60	9.66	0.87[8],0.90[10]			-12.4 ± 0.4		-12.0 ± 0.9	-12.3 ± 0.7				

Table B.1 Continued from previous page

Cluster	Star	RA	DEC	V	P_μ	P_{v_r}	Class	$v_{r,FIES}$	$v_{r,HERMES}$	$v_{r,CAFE}$	$v_{r,OCCASO}$	$v_{r,ref}$	Δv_r	Reference	Remark
NGC 7245	W055	22:15:17.5	+54 18 12.6	13.11			M[h]	-70.8 ± 0.8			-70.8 ± 0.8				
	W095	22:15:12.0	+54 21 11.4	13.37			M[h]	-74.0 ± 0.8			-74.0 ± 0.8				
	W178	22:15:05.4	+54 22 43.6	13.76			M[h]	-78.5 ± 1.5			-78.5 ± 1.5				
	W179	22:15:05.4	+54 22 49.4	12.97			M[h]	-73.1 ± 0.8			-73.1 ± 0.8				
	W205	22:15:14.9	+54 20 04.1	13.87			M[h]	-74.6 ± 1.7			-74.6 ± 1.7				
NGC 7762	W0002	23:49:48.40	+68:01:35.14	12.56					-45.7 ± 0.7		-45.7 ± 0.7				
	W0003	23:49:49.26	+68:01:07.35	12.88					-47.0 ± 0.7		-47.0 ± 0.7				
	W0084	23:50:13.52	+68:03:02.57	12.24					-5.8 ± 0.7		-5.8 ± 0.7				X
	W0110	23:49:06.13	+67:59:08.58	12.56					-45.9 ± 0.6		-45.9 ± 0.6				
	W0125	23:49:15.74	+68:05:32.14	12.57					-45.5 ± 0.6		-45.5 ± 0.6				
	W0139	23:50:59.35	+68:00:36.61	12.80					-45.6 ± 0.6		-45.6 ± 0.6				
NGC 7789	W05862	23:56:57.38	+56:36:54.69	12.98	0.94[9],0.98[10]		SM[f]		-53.8 ± 0.7		-53.8 ± 0.7	-53.4 ± 0.3	-0.4	Gim et al. (1998)	
												-54.1	0.3	Jacobson, Pilachowski, and Friel (2011)	
	W07176	23:57:12.50	+56:50:00.41	12.84	0.98[10]		SM[f]		-52.2 ± 0.7		-52.2 ± 0.7	-52.5 ± 0.4	0.3	Gim et al. (1998)	
												-53.7	1.5	Jacobson, Pilachowski, and Friel (2011)	
	W07714	23:57:18.57	+56:50:26.72	13.01	0.94[9],0.95[10]		SM[f]		-55.9 ± 0.7		-55.9 ± 0.7	-56.3 ± 0.4	0.4	Gim et al. (1998)	
												-56.0	0.1	Jacobson, Pilachowski, and Friel (2011)	
	W08260	23:57:24.05	+56:45:33.53	12.84	0.98[9],0.88[10]		SM[f]		-57.7 ± 0.7		-57.7 ± 0.7	-58.4	0.7	Jacobson, Pilachowski, and Friel (2011)	
	W08556	23:57:27.60	+56:45:39.20	12.97	0.98[9],0.98[10]			-53.2 ± 0.5			-53.2 ± 0.5	-54.1 ± 0.3	0.9	Gim et al. (1998)	
												-53.4 ± 0.8	0.2	Pancino et al. (2010)	
	W08734	23:57:29.65	+56:42:23.23	12.69	0.98[9],0.83[10]		SM[f]	-53.3 ± 0.4			-53.3 ± 0.4	-53.5 ± 0.2	0.2	Gim et al. (1998)	
												-53.6	0.3	Jacobson, Pilachowski, and Friel (2011)	
												-53.44	0.1	Overbeek et al. (2015)	
	W10915	23:57:54.51	+56:47:43.46	12.82	0.97[9],0.97[10]		SM[f]	-53.6 ± 0.5	-53.6 ± 0.7		-53.6 ± 0.6	-54.7 ± 0.4	1.1	Gim et al. (1998)	
												-53.7	0.1	Jacobson, Pilachowski, and Friel (2011)	

Table B.2. Atmospheric parameters and iron abundances obtained for the stars analysed in OCCASO. Basic data of each star, SNR and the instrument used, is listed in the first 7 columns. T_{eff}, log g and ξ, derived with each method are indicated. We list the mean effective temperature T_{eff} and surface gravity log g, and we give two errors: the mean of the errors quoted by both methods δ_1, and the standard deviation between the two values δ_2. Also [Fe/H] derived with each method (using mean atmospheric parameters) is listed, with the errors (spread) quoted by each method and the number of lines used, and σ[Fe/H] stands for the standard deviation of the two values.

Cluster	Star	RA	DEC	V	SNR	Instr	T_{eff}	log g	ξ	T_{eff}	log g	ξ	T_{eff}	δ_1 T	δ_2 T	log g	δ_1 log g	δ_2 log g	[Fe/H]$_{EW}$	[Fe/H]$_{SS}$	σ[Fe/H]
							EW			SS											
-	Arcturus	14:15:39.672	+19:10:56.67	-0.05	715	CAFE	4359 ± 56	1.90 ± 0.18	1.38 ± 0.05	4228 ± 6	1.45 ± 0.03	1.67 ± 0.01	4293	31	92	1.68	0.10	0.32	-0.56 ± 0.08 (271)	-0.51 ± 0.20 (150)	0.03
					399	FIES	4345 ± 53	1.79 ± 0.14	1.49 ± 0.06	4230 ± 4	1.48 ± 0.02	1.68 ± 0.01	4287	28	80	1.64	0.08	0.22	-0.55 ± 0.09 (193)	-0.55 ± 0.13 (145)	0.00
					414	HERMES	4271 ± 55	1.74 ± 0.10	1.35 ± 0.06	4243 ± 3	1.46 ± 0.01	1.66 ± 0.01	4257	29	19	1.60	0.06	0.20	-0.51 ± 0.10 (245)	-0.58 ± 0.11 (152)	0.03
-	μ-Leo	09:52:45.817	+26:00:25.03	3.88	149	CAFE	4499 ± 93	2.54 ± 0.24	1.46 ± 0.18	4453 ± 8	2.37 ± 0.03	1.48 ± 0.02	4476	50	31	2.46	0.14	0.12	0.21 ± 0.10 (266)	0.07 ± 0.28 (114)	0.07
					396	FIES	4532 ± 112	2.27 ± 0.21	1.15 ± 0.16	4442 ± 3	2.35 ± 0.01	1.47 ± 0.01	4487	57	63	2.31	0.11	0.06	0.31 ± 0.14 (154)	0.17 ± 0.21 (119)	0.07
					161	HERMES	4494 ± 88	2.26 ± 0.15	1.14 ± 0.09	4449 ± 4	2.31 ± 0.02	1.46 ± 0.01	4471	46	31	2.28	0.08	0.04	0.30 ± 0.09 (196)	0.14 ± 0.16 (121)	0.08
IC4756	W0038	18:37:05.22	+05:17:31.6	9.77	81	FIES	5136 ± 52	3.10 ± 0.07	1.43 ± 0.13	5069 ± 12	2.85 ± 0.04	1.45 ± 0.02	5102	32	46	2.98	0.06	0.18	-0.04 ± 0.09 (211)	-0.04 ± 0.08 (166)	0.00
	W0042	18:37:20.77	+05:53:43.1	9.46	106	HERMES	5200 ± 33	3.06 ± 0.06	1.06 ± 0.04	5232 ± 14	3.10 ± 0.03	1.31 ± 0.02	5216	23	23	3.08	0.04	0.03	0.03 ± 0.04 (273)	-0.01 ± 0.11 (173)	0.02
	W0044	18:37:29.72	+05:12:15.5	9.79	68	HERMES	5222 ± 60	3.29 ± 0.07	1.16 ± 0.04	5147 ± 17	3.06 ± 0.03	1.41 ± 0.02	5184	38	52	3.18	0.05	0.16	0.04 ± 0.04 (266)	-0.03 ± 0.09 (171)	0.04
	W0049	18:37:34.22	+05:28:33.5	9.43	68	HERMES	5126 ± 45	2.89 ± 0.06	1.28 ± 0.05	5093 ± 13	2.76 ± 0.04	1.46 ± 0.02	5109	29	22	2.82	0.05	0.09	-0.02 ± 0.05 (259)	-0.07 ± 0.09 (170)	0.02
	W0081	18:38:20.76	+05:26:02.3	9.38	72	HERMES	5220 ± 44	3.12 ± 0.07	1.11 ± 0.05	5200 ± 18	3.03 ± 0.03	1.27 ± 0.02	5210	31	14	3.08	0.05	0.06	0.02 ± 0.05 (274)	-0.05 ± 0.09 (170)	0.04
	W0101	18:38:43.79	+05:14:20.0	9.38	78	HERMES	5136 ± 36	3.07 ± 0.07	1.26 ± 0.05	5141 ± 11	2.88 ± 0.04	1.45 ± 0.02	5138	23	3	2.98	0.06	0.13	0.02 ± 0.05 (264)	-0.04 ± 0.08 (172)	0.03
	W0109	18:38:52.93	+05:20:16.5	9.02	87	CAFE	4973 ± 43	2.55 ± 0.12	1.34 ± 0.06	4919 ± 10	2.41 ± 0.04	1.59 ± 0.02	4946	26	38	2.48	0.08	0.10	-0.07 ± 0.05 (289)	-0.07 ± 0.10 (145)	0.00
					114	FIES	4917 ± 49	2.52 ± 0.08	1.23 ± 0.11	4975 ± 12	2.64 ± 0.03	1.57 ± 0.02	4946	30	41	2.58	0.06	0.08	0.02 ± 0.10 (197)	-0.05 ± 0.10 (155)	0.04
					87	HERMES	4969 ± 45	2.64 ± 0.05	1.33 ± 0.05	4984 ± 12	2.67 ± 0.03	1.50 ± 0.02	4976	28	10	2.66	0.04	0.02	-0.02 ± 0.05 (246)	-0.07 ± 0.08 (167)	0.02
	W0125	18:39:17.88	+05:13:48.8	9.29	75	CAFE	5123 ± 56	2.80 ± 0.09	1.30 ± 0.07	5109 ± 13	2.76 ± 0.04	1.54 ± 0.02	5116	34	9	2.78	0.06	0.03	-0.02 ± 0.04 (288)	-0.06 ± 0.10 (150)	0.02
					82	FIES	5108 ± 46	2.88 ± 0.05	1.22 ± 0.07	5110 ± 13	2.77 ± 0.04	1.51 ± 0.02	5109	29	2	2.82	0.04	0.08	0.02 ± 0.10 (206)	-0.03 ± 0.09 (162)	0.02
					75	HERMES	5121 ± 41	2.87 ± 0.05	1.32 ± 0.05	5125 ± 11	2.86 ± 0.04	1.47 ± 0.02	5123	26	3	2.86	0.04	0.01	-0.04 ± 0.05 (264)	-0.09 ± 0.08 (171)	0.02
NGC188	W1105	0:46:59.62	85:13:15.80	12.36	64	HERMES	4530 ± 114	2.29 ± 0.14	1.25 ± 0.07	4589 ± 10	2.24 ± 0.04	1.36 ± 0.02	4559	62	42	2.26	0.09	0.04	-0.01 ± 0.07 (216)	-0.10 ± 0.20 (128)	0.04
	W2051	0:42:25.55	85:16:22.03	12.95	50	HERMES	4668 ± 63	2.92 ± 0.16	0.87 ± 0.10	4548 ± 15	2.55 ± 0.04	1.14 ± 0.02	4608	39	84	2.74	0.10	0.26	0.22 ± 0.10 (227)	-0.01 ± 0.20 (130)	0.12
	W2088	0:47:18.42	85:19:45.78	13.01	49	HERMES	4516 ± 60	2.44 ± 0.15	1.14 ± 0.07	4538 ± 10	2.38 ± 0.04	1.22 ± 0.02	4527	35	15	2.41	0.10	0.04	0.04 ± 0.07 (227)	-0.08 ± 0.18 (136)	0.06
	W5217	0:54:11.48	85:15:23.19	12.40	56	HERMES	4639 ± 65	2.30 ± 0.13	1.30 ± 0.07	4626 ± 10	2.32 ± 0.05	1.47 ± 0.02	4632	37	9	2.31	0.09	0.01	0.03 ± 0.07 (211)	-0.08 ± 0.19 (139)	0.06
	W5224	0:54:36.60	85:1:15.31	12.45	60	HERMES	4695 ± 48	2.31 ± 0.42	1.33 ± 0.07	4643 ± 11	2.46 ± 0.04	1.40 ± 0.02	4669	29	36	2.38	0.23	0.11	0.04 ± 0.07 (221)	0.01 ± 0.16 (143)	0.02
	W7323	0:49:5.60	85:26:7.78	12.72	71	FIES	4519 ± 103	2.74 ± 0.21	1.53 ± 0.11	4474 ± 8	2.41 ± 0.03	1.34 ± 0.02	4496	55	31	2.58	0.12	0.23	0.01 ± 0.16 (167)	0.02 ± 0.18 (120)	0.00
NGC752	W0001	01:55:12.60	+37:50:14.60	9.48	71	FIES	5044 ± 49	3.24 ± 0.07	1.22 ± 0.10	5033 ± 17	3.06 ± 0.03	1.37 ± 0.02	5038	33	7	3.15	0.05	0.13	-0.01 ± 0.11 (220)	-0.03 ± 0.17 (166)	0.01
	W0024	01:55:39.35	+37:52:52.69	8.91	89	FIES	5044 ± 67	3.03 ± 0.06	1.35 ± 0.11	4950 ± 11	2.75 ± 0.03	1.47 ± 0.02	4997	39	66	2.89	0.04	0.20	0.03 ± 0.10 (206)	0.01 ± 0.11 (163)	0.01
					72	HERMES	4964 ± 31	2.79 ± 0.07	1.19 ± 0.05	4954 ± 13	2.69 ± 0.04	1.43 ± 0.02	4959	22	6	2.74	0.06	0.07	0.02 ± 0.05 (253)	-0.05 ± 0.09 (164)	0.04
	W0027	01:55:42.39	+37:37:54.66	9.17	71	FIES	4920 ± 49	2.77 ± 0.05	1.32 ± 0.07	4945 ± 11	2.81 ± 0.04	1.45 ± 0.02	4932	30	17	2.79	0.04	0.03	0.00 ± 0.10 (200)	-0.04 ± 0.15 (158)	0.02

Table B.2 Continued from previous page

Cluster	Star	RA	DEC	V	SNR	Instr	T_{eff}	log g	ξ	T_{eff}	log g	ξ	T_{eff}	δ_1 T	δ_2 T	log g	δ_1 g	δ_2 g	[Fe/H]$_{EW}$	[Fe/H]$_{SS}$	σ[Fe/H]
								EW			SS										
					67	HERMES	4956 ± 32	2.98 ± 0.05	1.15 ± 0.04	4957 ± 13	2.76 ± 0.04	1.36 ± 0.02	4956	22	0	2.87	0.04	0.16	0.04 ± 0.04 (257)	-0.04 ± 0.09 (165)	0.04
	W0077	01:56:21.63	+37:36:08.53	9.38	69	HERMES	4837 ± 40	2.92 ± 0.05	1.04 ± 0.05	4863 ± 11	2.79 ± 0.04	1.30 ± 0.02	4850	25	18	2.86	0.04	0.09	0.04 ± 0.05 (264)	-0.06 ± 0.10 (163)	0.05
	W0137	01:57:03.12	+38:08:02.73	8.90	75	FIES	4909 ± 63	2.79 ± 0.10	1.36 ± 0.12	4918 ± 13	2.68 ± 0.04	1.47 ± 0.02	4913	38	6	2.74	0.07	0.08	0.01 ± 0.12 (201)	-0.03 ± 0.13 (159)	0.02
					72	HERMES	4848 ± 63	2.57 ± 0.06	1.17 ± 0.04	4931 ± 13	2.67 ± 0.04	1.41 ± 0.02	4889	38	59	2.62	0.05	0.07	-0.03 ± 0.04 (248)	-0.09 ± 0.09 (167)	0.03
	W0295	01:58:29.81	+37:51:37.68	9.30	69	FIES	5074 ± 65	2.94 ± 0.11	1.15 ± 0.09	5030 ± 12	2.89 ± 0.04	1.41 ± 0.02	5052	38	30	2.92	0.08	0.04	0.06 ± 0.12 (210)	-0.01 ± 0.16 (166)	0.03
	W0311	01:58:52.90	+37:48:57.30	9.06	74	HERMES	4851 ± 36	2.78 ± 0.05	1.18 ± 0.06	4900 ± 12	2.69 ± 0.04	1.38 ± 0.02	4875	24	34	2.74	0.04	0.06	0.01 ± 0.06 (257)	-0.04 ± 0.09 (161)	0.02
NGC1817	W0008	5:12:19.39	16:40:48.64	12.12	92	FIES	5016 ± 54	2.60 ± 0.05	1.28 ± 0.05	5087 ± 15	2.68 ± 0.04	1.57 ± 0.02	5051	34	50	2.64	0.04	0.06	-0.12 ± 0.10 (219)	-0.16 ± 0.10 (166)	0.02
	W0022	5:12:38.44	16:42:23.12	12.34	66	FIES	5094 ± 45	2.59 ± 0.09	1.31 ± 0.10	5133 ± 16	2.74 ± 0.04	1.55 ± 0.02	5113	30	27	2.66	0.06	0.11	-0.07 ± 0.12 (211)	-0.13 ± 0.15 (168)	0.03
	W0073	5:12:24.65	16:35:48.84	12.04	66	FIES	4863 ± 53	2.74 ± 0.05	1.22 ± 0.08	4854 ± 15	2.61 ± 0.04	1.46 ± 0.02	4858	34	5	2.68	0.04	0.09	-0.07 ± 0.10 (199)	-0.08 ± 0.12 (148)	0.00
	W0079	5:12:10.68	16:38:31.15	12.49	57	FIES	5117 ± 43	2.94 ± 0.09	1.27 ± 0.12	5163 ± 15	2.85 ± 0.05	1.50 ± 0.03	5140	29	32	2.90	0.07	0.06	-0.06 ± 0.12 (216)	-0.08 ± 0.12 (164)	0.01
	W0127	5:12:50.10	16:40:49.73	12.25	52	FIES	5200 ± 75	3.07 ± 0.06	1.48 ± 0.10	5060 ± 21	2.67 ± 0.05	1.49 ± 0.03	5130	48	98	2.87	0.06	0.28	-0.09 ± 0.12 (212)	-0.08 ± 0.12 (160)	0.00
NGC1907	W0062	05:27:49.053	+35:20:10.13	12.41	54	HERMES	5066 ± 66	2.33 ± 0.16	1.39 ± 0.08	5179 ± 19	2.79 ± 0.06	1.48 ± 0.03	5122	42	79	2.56	0.11	0.33	-0.04 ± 0.08 (223)	-0.11 ± 0.18 (156)	0.03
	W0113	05:28:04.207	+35:19:16.32	11.81	88	HERMES	4919 ± 37	2.50 ± 0.04	1.27 ± 0.05	4942 ± 9	2.40 ± 0.04	1.56 ± 0.02	4930	23	16	2.45	0.04	0.07	-0.03 ± 0.05 (255)	-0.17 ± 0.10 (168)	0.07
	W0131	05:28:05.276	+35:19:49.64	12.30	63	HERMES	5108 ± 30	2.36 ± 0.09	1.37 ± 0.06	5150 ± 19	2.67 ± 0.05	1.60 ± 0.02	5129	24	29	2.52	0.07	0.22	-0.10 ± 0.06 (243)	-0.18 ± 0.13 (162)	0.04
	W0133	05:28:05.863	+35:19:38.87	12.74	91	HERMES	5141 ± 48	2.84 ± 0.12	0.69 ± 0.06	5145 ± 16	2.84 ± 0.04	1.03 ± 0.03	5143	32	3	2.84	0.08	0.00	-0.06 ± 0.06 (277)	-0.20 ± 0.17 (158)	0.07
	W0256	05:28:01.783	+35:21:14.89	11.23	92	HERMES	4539 ± 58	2.18 ± 0.08	1.42 ± 0.10	4491 ± 8	1.74 ± 0.04	1.69 ± 0.01	4515	33	33	1.96	0.06	0.31	-0.08 ± 0.10 (201)	-0.18 ± 0.15 (146)	0.05
	W2087	05:27:38.899	+35:17:18.04	13.09	52	HERMES	4694 ± 61	2.51 ± 0.13	0.95 ± 0.06	4619 ± 16	2.47 ± 0.05	1.13 ± 0.03	4656	38	52	2.49	0.09	0.03	-0.53 ± 0.06 (268)	-0.62 ± 0.20 (147)	0.04
NGC2099	W007	05:52:20.31	+32:33:49.3	11.42	59	HERMES	5025 ± 50	2.57 ± 0.09	1.36 ± 0.06	5075 ± 16	2.76 ± 0.05	1.54 ± 0.03	5050	33	35	2.66	0.07	0.13	0.04 ± 0.06 (226)	-0.02 ± 0.11 (156)	0.03
	W016	05:52:17.26	+32:32:56.5	11.26	60	HERMES	5019 ± 72	2.54 ± 0.07	1.43 ± 0.08	5053 ± 17	2.67 ± 0.05	1.62 ± 0.02	5036	44	24	2.60	0.06	0.09	0.09 ± 0.08 (212)	0.03 ± 0.09 (156)	0.03
	W031	05:52:16.68	+32:31:39.3	11.52	62	HERMES	5125 ± 47	2.88 ± 0.07	1.30 ± 0.06	5093 ± 15	2.84 ± 0.05	1.54 ± 0.03	5109	31	22	2.86	0.06	0.03	0.14 ± 0.06 (205)	0.03 ± 0.12 (147)	0.06
	W148	05:52:08.10	+32:30:33.1	11.09	64	HERMES	4970 ± 48	2.54 ± 0.08	1.53 ± 0.08	4971 ± 17	2.54 ± 0.04	1.69 ± 0.02	4970	32	1	2.54	0.06	0.00	0.08 ± 0.08 (213)	-0.01 ± 0.10 (151)	0.04
	W172	05:52:04.89	+32:33:18.3	11.45	61	HERMES	5078 ± 51	2.62 ± 0.09	1.36 ± 0.06	5080 ± 17	2.71 ± 0.05	1.59 ± 0.03	5079	34	2	2.66	0.07	0.06	0.06 ± 0.06 (231)	-0.04 ± 0.11 (158)	0.05
	W401	05:51:55.14	+32:30:03.0	11.36	65	HERMES	4994 ± 42	2.68 ± 0.04	1.46 ± 0.05	5035 ± 15	2.68 ± 0.04	1.57 ± 0.02	5014	28	29	2.68	0.04	0.00	0.08 ± 0.05 (222)	0.02 ± 0.09 (162)	0.03
	W488	05:52:46.97	+32:33:19.4	11.17	62	HERMES	4998 ± 44	2.72 ± 0.09	1.40 ± 0.06	4990 ± 17	2.61 ± 0.04	1.57 ± 0.02	4994	30	5	2.66	0.06	0.08	0.07 ± 0.06 (221)	0.01 ± 0.12 (161)	0.03
NGC2420	W041	7:38:6.27	21:36:54.60	12.67	58	FIES	4732 ± 65	2.41 ± 0.11	1.34 ± 0.07	4806 ± 16	2.60 ± 0.04	1.50 ± 0.02	4769	40	52	2.50	0.08	0.13	-0.18 ± 0.12 (203)	-0.21 ± 0.15 (161)	0.02
	W076	7:38:15.50	21:38:1.80	12.66	78	FIES	5002 ± 63	3.04 ± 0.06	1.32 ± 0.10	4964 ± 16	2.59 ± 0.04	1.51 ± 0.02	4983	39	26	2.82	0.05	0.32	-0.07 ± 0.11 (211)	-0.11 ± 0.12 (161)	0.02
	W091	7:38:18.17	21:32:6.80	12.61	74	FIES	4922 ± 56	2.50 ± 0.12	1.37 ± 0.09	4969 ± 15	2.64 ± 0.04	1.55 ± 0.02	4945	35	33	2.57	0.08	0.10	-0.08 ± 0.15 (205)	-0.12 ± 0.19 (155)	0.02
	W111	7:38:21.43	21:35:5.60	12.60	72	FIES	4888 ± 63	2.78 ± 0.08	1.08 ± 0.11	4951 ± 12	2.92 ± 0.04	1.41 ± 0.02	4919	37	44	2.85	0.06	0.10	-0.05 ± 0.14 (207)	-0.12 ± 0.18 (157)	0.03
	W118	7:38:21.90	21:35:50.90	12.57	60	FIES	4863 ± 55	2.47 ± 0.10	1.33 ± 0.06	4890 ± 17	2.52 ± 0.03	1.49 ± 0.02	4876	36	19	2.50	0.06	0.04	-0.13 ± 0.10 (204)	-0.17 ± 0.12 (166)	0.02
	W174	7:38:26.93	21:38:24.80	12.40	65	FIES	4872 ± 50	2.63 ± 0.06	1.24 ± 0.07	4892 ± 15	2.57 ± 0.04	1.59 ± 0.02	4882	32	14	2.60	0.05	0.04	-0.05 ± 0.09 (195)	-0.15 ± 0.11 (161)	0.05
	W236	7:38:37.59	21:34:12.40	12.58	71	FIES	4978 ± 49	2.75 ± 0.11	1.41 ± 0.09	5001 ± 16	2.66 ± 0.04	1.57 ± 0.02	4989	32	16	2.70	0.08	0.06	-0.10 ± 0.14 (211)	-0.13 ± 0.16 (160)	0.02
NGC2539	W229	08:10:33.80	-12:51:48.9	11.20	73	HERMES	5050 ± 68	2.98 ± 0.12	1.26 ± 0.05	5048 ± 12	2.75 ± 0.04	1.41 ± 0.02	5049	40	0	2.86	0.08	0.16	0.06 ± 0.05 (242)	0.01 ± 0.11 (163)	0.02
	W251	08:10:38.99	-12:44:44.7	11.23	70	HERMES	5106 ± 49	2.61 ± 0.08	1.31 ± 0.08	5086 ± 13	2.86 ± 0.04	1.43 ± 0.03	5096	31	13	2.74	0.06	0.18	0.05 ± 0.08 (219)	-0.06 ± 0.14 (156)	0.06

Table B.2 Continued from previous page

Cluster	Star	RA	DEC	V	SNR	Instr	T_{eff}	log g	ξ	T_{eff}	log g	ξ	T_{eff}	δ_1 T	δ_2 T	log g	δ_1 g	δ_2 g	[Fe/H]$_{EW}$	[Fe/H]$_{SS}$	σ[Fe/H]
								EW			SS										
	W346	08:10:23.02	-12:50:43.3	10.92	101	HERMES	5094 ± 39	2.91 ± 0.07	1.23 ± 0.05	5051 ± 10	2.77 ± 0.03	1.48 ± 0.02	5072	24	30	2.84	0.05	0.10	0.07 ± 0.05 (249)	-0.02 ± 0.12 (169)	0.04
	W463	08:10:42.87	-12:40:11.8	10.69	99	HERMES	4979 ± 38	2.58 ± 0.06	1.32 ± 0.06	4954 ± 13	2.57 ± 0.03	1.56 ± 0.02	4966	25	17	2.58	0.04	0.01	0.07 ± 0.06 (228)	-0.01 ± 0.10 (165)	0.04
	W502	08:11:27.67	-12:41:06.8	11.03	76	HERMES	5147 ± 50	3.14 ± 0.10	1.36 ± 0.07	5057 ± 13	2.73 ± 0.04	1.46 ± 0.02	5102	31	63	2.94	0.07	0.29	0.08 ± 0.07 (233)	0.02 ± 0.11 (169)	0.03
NGC2682	W084	08:51:12.73	+11:52:42.7	10.52	64	HERMES	4728 ± 45	2.52 ± 0.12	1.11 ± 0.06	4731 ± 12	2.46 ± 0.04	1.44 ± 0.02	4729	28	2	2.49	0.08	0.04	0.08 ± 0.06 (205)	-0.08 ± 0.18 (142)	0.08
	W141	08:51:22.83	+11:48:02.0	10.48	70	HERMES	4691 ± 34	2.58 ± 0.13	1.26 ± 0.09	4724 ± 13	2.53 ± 0.03	1.45 ± 0.02	4707	23	23	2.56	0.08	0.04	0.05 ± 0.09 (217)	-0.05 ± 0.15 (153)	0.05
	W151	08:51:26.22	+11:53:52.2	10.48	65	HERMES	4745 ± 58	2.59 ± 0.09	1.19 ± 0.07	4771 ± 13	2.55 ± 0.03	1.43 ± 0.02	4758	35	19	2.57	0.06	0.03	0.04 ± 0.07 (238)	-0.04 ± 0.13 (159)	0.04
	W164	08:51:29.03	+11:50:33.4	10.52	63	HERMES	4686 ± 48	2.50 ± 0.08	1.20 ± 0.06	4704 ± 11	2.45 ± 0.04	1.43 ± 0.02	4695	29	12	2.48	0.06	0.04	0.01 ± 0.06 (235)	-0.07 ± 0.14 (157)	0.04
	W223	08:51:43.91	+11:56:42.9	10.58	55	HERMES	4651 ± 52	2.43 ± 0.16	1.16 ± 0.08	4742 ± 13	2.46 ± 0.04	1.45 ± 0.02	4696	32	64	2.44	0.10	0.02	0.00 ± 0.08 (236)	-0.08 ± 0.14 (154)	0.04
	W224	08:51:43.55	+11:44:26.8	10.76	61	HERMES	4557 ± 89	2.42 ± 0.09	0.99 ± 0.07	4658 ± 13	2.55 ± 0.03	1.29 ± 0.02	4607	51	72	2.48	0.06	0.09	0.09 ± 0.07 (230)	-0.05 ± 0.15 (141)	0.07
	W266	08:51:59.56	+11:55:05.2	10.55	67	HERMES	4762 ± 37	2.63 ± 0.07	1.20 ± 0.05	4776 ± 13	2.54 ± 0.03	1.45 ± 0.02	4769	25	10	2.58	0.05	0.06	0.03 ± 0.05 (237)	-0.06 ± 0.12 (164)	0.04
	W286	08:52:18.61	+11:44:26.5	10.47	94	HERMES	4672 ± 116	2.34 ± 0.10	1.08 ± 0.07	4719 ± 7	2.39 ± 0.03	1.45 ± 0.01	4695	61	33	2.37	0.06	0.04	0.04 ± 0.07 (234)	-0.08 ± 0.14 (152)	0.06
NGC6633	W100	18:27:54.73	+06:36:00.3	8.30	86	CAFE	4976 ± 61	2.57 ± 0.07	1.39 ± 0.07	5011 ± 15	2.60 ± 0.04	1.64 ± 0.02	4993	38	24	2.58	0.06	0.02	-0.05 ± 0.05 (284)	-0.03 ± 0.10 (143)	0.01
					72	FIES	4968 ± 78	2.61 ± 0.06	1.49 ± 0.12	5012 ± 15	2.64 ± 0.04	1.69 ± 0.02	4990	46	31	2.62	0.05	0.02	0.07 ± 0.17 (176)	-0.03 ± 0.17 (155)	0.05
					74	HERMES	5034 ± 38	2.85 ± 0.07	1.33 ± 0.05	5030 ± 13	2.65 ± 0.03	1.56 ± 0.02	5032	25	2	2.75	0.05	0.14	0.04 ± 0.05 (242)	-0.04 ± 0.09 (168)	0.04
	W106	18:28:00.18	+06:54:51.5	8.67	102	FIES	5113 ± 41	2.82 ± 0.05	1.22 ± 0.07	5115 ± 11	2.84 ± 0.04	1.52 ± 0.02	5114	26	1	2.83	0.04	0.01	0.07 ± 0.11 (209)	0.02 ± 0.11 (158)	0.02
					65	HERMES	5147 ± 46	2.98 ± 0.07	1.15 ± 0.06	5106 ± 12	2.85 ± 0.04	1.43 ± 0.02	5126	29	28	2.92	0.06	0.09	0.08 ± 0.06 (250)	-0.02 ± 0.10 (163)	0.05
	W119	18:28:17.64	+06:46:00.1	8.95	67	FIES	5138 ± 42	2.84 ± 0.06	1.28 ± 0.06	5203 ± 21	3.02 ± 0.04	1.47 ± 0.03	5170	31	46	2.93	0.05	0.13	0.03 ± 0.10 (196)	-0.02 ± 0.11 (162)	0.02
					70	HERMES	5192 ± 56	3.03 ± 0.07	1.09 ± 0.05	5218 ± 18	3.08 ± 0.04	1.44 ± 0.02	5205	37	18	3.06	0.06	0.04	0.03 ± 0.05 (271)	-0.07 ± 0.08 (167)	0.05
	W126	18:28:22.97	+06:42:29.3	8.77	95	FIES	5054 ± 50	2.55 ± 0.06	1.28 ± 0.09	5131 ± 12	2.80 ± 0.04	1.53 ± 0.02	5092	31	54	2.68	0.05	0.18	-0.01 ± 0.11 (201)	-0.04 ± 0.11 (159)	0.02
					78	HERMES	5190 ± 37	3.07 ± 0.09	1.23 ± 0.05	5174 ± 12	2.92 ± 0.03	1.44 ± 0.02	5182	24	10	3.00	0.06	0.11	0.04 ± 0.05 (258)	-0.02 ± 0.09 (168)	0.03
NGC6705	W0660	18:51:15.691	-06:18:14.47	11.81	56	HERMES	4756 ± 79	2.36 ± 0.10	1.60 ± 0.09	4719 ± 13	2.22 ± 0.05	1.80 ± 0.02	4737	46	26	2.29	0.08	0.10	0.20 ± 0.09 (163)	0.05 ± 0.20 (137)	0.08
	W0669	18:51:15.318	-06:18:35.51	11.97	54	HERMES	4791 ± 79	2.26 ± 0.15	1.72 ± 0.13	4706 ± 16	2.20 ± 0.06	1.77 ± 0.03	4748	47	59	2.23	0.10	0.04	0.21 ± 0.13 (138)	0.08 ± 0.21 (115)	0.06
	W0686	18:51:14.507	-06:16:54.74	11.92	59	HERMES	4884 ± 69	2.44 ± 0.14	1.85 ± 0.12	4766 ± 16	2.27 ± 0.06	1.73 ± 0.03	4825	42	83	2.36	0.10	0.12	0.14 ± 0.12 (153)	0.09 ± 0.22 (119)	0.03
	W0779	18:51:11.141	-06:14:33.76	11.47	92	FIES	4330 ± 162	1.83 ± 0.23	1.47 ± 0.15	4355 ± 6	1.82 ± 0.04	1.86 ± 0.01	4342	84	18	1.82	0.14	0.01	0.18 ± 0.13 (117)	0.05 ± 0.19 (97)	0.06
					64	HERMES	4317 ± 77	1.63 ± 0.20	1.45 ± 0.17	4354 ± 9	1.74 ± 0.05	1.78 ± 0.02	4335	43	26	1.68	0.12	0.08	0.19 ± 0.17 (140)	-0.03 ± 0.22 (105)	0.11
	W0916	18:51:07.847	-06:17:11.89	11.62	73	HERMES	4810 ± 73	1.95 ± 0.20	1.76 ± 0.13	4768 ± 13	2.29 ± 0.05	1.81 ± 0.02	4789	43	29	2.12	0.12	0.24	0.17 ± 0.13 (137)	0.04 ± 0.18 (115)	0.06
	W1184	18:51:01.989	-06:17:26.50	11.43	74	FIES	4352 ± 125	1.74 ± 0.15	1.66 ± 0.10	4388 ± 7	1.81 ± 0.04	1.83 ± 0.02	4370	66	25	1.78	0.10	0.05	0.03 ± 0.11 (125)	-0.02 ± 0.18 (102)	0.02
					69	HERMES	4425 ± 85	1.79 ± 0.15	1.34 ± 0.08	4390 ± 8	1.72 ± 0.04	1.71 ± 0.02	4407	46	24	1.76	0.10	0.05	0.13 ± 0.08 (161)	-0.09 ± 0.19 (130)	0.11
	W1256	18:51:00.194	-06:16:59.06	11.59	84	HERMES	4467 ± 92	1.90 ± 0.15	1.59 ± 0.12	4405 ± 7	1.76 ± 0.04	1.76 ± 0.01	4436	49	43	1.83	0.10	0.10	0.07 ± 0.12 (151)	-0.05 ± 0.19 (123)	0.06
	W1423	18:50:55.789	-06:18:14.26	11.41	78	FIES	4555 ± 202	2.22 ± 0.15	1.47 ± 0.11	4493 ± 12	2.08 ± 0.03	1.88 ± 0.02	4524	107	43	2.15	0.09	0.10	0.22 ± 0.13 (127)	0.12 ± 0.19 (108)	0.05
					65	HERMES	4384 ± 63	1.93 ± 0.19	1.54 ± 0.10	4464 ± 9	1.95 ± 0.04	1.81 ± 0.02	4424	36	56	1.94	0.12	0.01	0.16 ± 0.10 (143)	0.00 ± 0.18 (110)	0.08
NGC6791	W1794	19:21:6.31	37:44:59.90	14.48	56	FIES	4421 ± 68	1.73 ± 0.14	1.48 ± 0.16	4477 ± 14	2.18 ± 0.05	1.40 ± 0.02	4449	41	39	1.96	0.10	0.32	0.04 ± 0.21 (139)	0.01 ± 0.29 (94)	0.02
	W2562	19:21:0.87	37:46:39.90	14.58	62	FIES	4610 ± 167	2.30 ± 0.18	1.85 ± 0.24	4508 ± 17	2.49 ± 0.03	1.46 ± 0.02	4559	92	71	2.40	0.10	0.13	0.24 ± 0.20 (105)	0.28 ± 0.37 (86)	0.02

Table B.2 Continued from previous page

Cluster	Star	RA	DEC	V	SNR	Instr	T_{eff}	log g	ξ	T_{eff}	log g	ξ	T_{eff}	δ_1 T	δ_2 T	log g	δ_1 g	δ_2 g	[Fe/H]$_{EW}$	[Fe/H]$_{SS}$	σ[Fe/H]
							EW			SS											
	W2579	19:21:0.87	37:45:34.10	14.55	64	FIES	4403 ± 158	1.83 ± 0.21	1.55 ± 0.25	4410 ± 12	2.20 ± 0.04	1.44 ± 0.02	4406	85	5	2.02	0.12	0.26	0.17 ± 0.28 (131)	0.02 ± 0.32 (92)	0.08
	W3363	19:20:56.31	37:44:33.70	14.65	53	FIES	4561 ± 142	2.73 ± 0.25	1.67 ± 0.17	4453 ± 11	2.36 ± 0.04	1.40 ± 0.02	4507	76	75	2.54	0.14	0.26	0.27 ± 0.23 (132)	0.22 ± 0.28 (100)	0.03
	W3926	19:20:52.89	37:45:33.40	14.55	53	FIES	4420 ± 99	1.99 ± 0.25	1.49 ± 0.14	4490 ± 15	2.48 ± 0.04	1.50 ± 0.02	4455	57	49	2.24	0.14	0.35	0.22 ± 0.18 (112)	0.13 ± 0.25 (91)	0.04
NGC6819	W333	19:41:13.55	+40:12:20.5	13.069	66	HERMES	4740 ± 92	2.63 ± 0.08	1.22 ± 0.06	4828 ± 13	2.63 ± 0.04	1.39 ± 0.02	4784	52	62	2.63	0.06	0.00	0.05 ± 0.06 (236)	-0.06 ± 0.14 (159)	0.06
	W386	19:41:22.45	+40:12:05.3	13.016	57	HERMES	4927 ± 52	2.99 ± 0.07	0.88 ± 0.08	4956 ± 14	2.93 ± 0.04	1.34 ± 0.02	4941	33	20	2.96	0.06	0.04	0.09 ± 0.08 (257)	-0.07 ± 0.15 (163)	0.08
	W398	19:41:13.45	+40:11:57.9	13.119	51	HERMES	4767 ± 52	2.61 ± 0.08	1.24 ± 0.07	4745 ± 16	2.55 ± 0.04	1.41 ± 0.02	4756	34	15	2.58	0.06	0.04	0.07 ± 0.07 (229)	-0.06 ± 0.14 (155)	0.06
	W978	19:41:14.76	+40:11:00.8	12.869	62	HERMES	4852 ± 51	2.65 ± 0.09	1.32 ± 0.07	4877 ± 13	2.65 ± 0.04	1.43 ± 0.02	4864	32	18	2.65	0.06	0.00	0.06 ± 0.07 (237)	-0.01 ± 0.13 (160)	0.03
	W979	19:41:15.93	+40:11:11.5	12.956	61	HERMES	5027 ± 59	2.95 ± 0.06	1.18 ± 0.08	5032 ± 12	2.88 ± 0.04	1.30 ± 0.02	5029	35	4	2.92	0.05	0.05	0.14 ± 0.08 (248)	0.04 ± 0.14 (165)	0.05
	W983	19:41:09.91	+40:15:49.5	12.928	57	HERMES	4806 ± 48	2.75 ± 0.09	1.24 ± 0.06	4747 ± 15	2.52 ± 0.03	1.44 ± 0.02	4776	31	41	2.64	0.06	0.16	0.13 ± 0.06 (237)	-0.03 ± 0.14 (158)	0.08
NGC6939	W130	20:31:25.43	60:41:16.67	13.07	42	HERMES	5142 ± 125	2.77 ± 0.19	1.28 ± 0.13	5140 ± 25	3.15 ± 0.06	1.21 ± 0.03	5141	75	1	2.96	0.12	0.27	0.22 ± 0.13 (144)	0.11 ± 0.28 (122)	0.06
	W145	20:31:28.55	60:40:7.82	12.97	56	HERMES	4865 ± 53	2.67 ± 0.10	1.03 ± 0.06	4895 ± 16	2.60 ± 0.04	1.33 ± 0.02	4880	34	21	2.64	0.07	0.05	0.11 ± 0.06 (228)	-0.06 ± 0.19 (154)	0.08
	W170	20:31:32.04	60:39:27.37	12.99	60	HERMES	4924 ± 48	2.76 ± 0.10	1.13 ± 0.06	4897 ± 14	2.64 ± 0.04	1.26 ± 0.02	4910	31	18	2.70	0.07	0.08	0.10 ± 0.06 (232)	0.01 ± 0.15 (161)	0.04
	W214	20:31:40.18	60:41:31.69	13.08	57	HERMES	5039 ± 71	2.99 ± 0.07	1.14 ± 0.08	4993 ± 12	2.85 ± 0.04	1.36 ± 0.02	5016	41	32	2.92	0.06	0.10	0.17 ± 0.08 (245)	0.01 ± 0.17 (167)	0.08
	W230	20:31:43.42	60:40:38.82	12.99	59	HERMES	4893 ± 53	2.82 ± 0.07	1.12 ± 0.06	4890 ± 15	2.63 ± 0.04	1.31 ± 0.02	4891	34	1	2.72	0.06	0.13	0.09 ± 0.06 (242)	-0.03 ± 0.15 (156)	0.06
	W292	20:31:59.11	60:42:4.76	13.11	59	HERMES	4916 ± 43	2.75 ± 0.11	1.18 ± 0.06	4918 ± 15	2.61 ± 0.04	1.43 ± 0.02	4917	29	1	2.68	0.08	0.10	0.04 ± 0.06 (236)	-0.08 ± 0.15 (159)	0.06
NGC6991	W034	20:53:37.68	+47:12:23.66	10.30	80	CAFE	5076 ± 47	3.14 ± 0.09	1.15 ± 0.06	5032 ± 15	2.98 ± 0.03	1.44 ± 0.02	5054	31	30	3.06	0.06	0.11	-0.07 ± 0.05 (280)	-0.09 ± 0.10 (156)	0.01
					73	FIES	5128 ± 63	3.17 ± 0.09	1.09 ± 0.08	5042 ± 16	3.10 ± 0.04	1.33 ± 0.02	5085	39	60	3.14	0.06	0.05	0.05 ± 0.13 (218)	-0.02 ± 0.13 (168)	0.04
	W043	20:53:50.82	+47:05:06.75	10.08	71	CAFE	5068 ± 45	2.85 ± 0.09	1.35 ± 0.07	5059 ± 15	2.94 ± 0.04	1.54 ± 0.02	5063	30	5	2.90	0.06	0.06	-0.02 ± 0.05 (277)	-0.05 ± 0.11 (143)	0.02
	W049	20:54:01.74	+47:25:49.16	10.17	95	CAFE	5118 ± 58	3.23 ± 0.05	1.04 ± 0.07	5021 ± 14	2.96 ± 0.03	1.54 ± 0.02	5069	36	67	3.10	0.04	0.19	-0.04 ± 0.05 (281)	-0.08 ± 0.10 (150)	0.02
					90	FIES	5177 ± 49	3.39 ± 0.04	1.15 ± 0.08	5056 ± 15	3.08 ± 0.03	1.34 ± 0.02	5116	32	85	3.24	0.04	0.22	0.04 ± 0.10 (222)	0.01 ± 0.09 (171)	0.02
	W067	20:54:29.81	+47:28:03.15	9.43	70	CAFE	4917 ± 47	2.54 ± 0.13	1.31 ± 0.07	4907 ± 15	2.61 ± 0.04	1.63 ± 0.02	4912	31	6	2.58	0.08	0.05	-0.06 ± 0.07 (281)	-0.11 ± 0.13 (142)	0.02
					70	FIES	4930 ± 64	2.78 ± 0.12	1.27 ± 0.14	4900 ± 13	2.66 ± 0.04	1.51 ± 0.02	4915	38	20	2.72	0.08	0.08	0.00 ± 0.13 (197)	-0.04 ± 0.13 (157)	0.02
	W100	20:55.03.98	+47:19:20.03	9.87	77	CAFE	5095 ± 58	3.01 ± 0.10	1.20 ± 0.09	5064 ± 14	2.93 ± 0.04	1.48 ± 0.02	5079	36	21	2.97	0.07	0.06	0.02 ± 0.07 (281)	-0.03 ± 0.11 (148)	0.02
	W131	20:55:42.69	+47:22:32.60	9.66	71	CAFE	5118 ± 47	3.15 ± 0.05	1.21 ± 0.08	5032 ± 12	2.80 ± 0.04	1.49 ± 0.02	5075	29	60	2.98	0.04	0.25	0.01 ± 0.06 (285)	0.00 ± 0.09 (147)	0.00
					81	FIES	5057 ± 48	2.99 ± 0.05	1.21 ± 0.06	4993 ± 13	2.76 ± 0.04	1.45 ± 0.02	5025	30	44	2.88	0.04	0.16	0.03 ± 0.09 (197)	-0.03 ± 0.09 (169)	0.03
NGC7245	W0205	22:15:14.90	54:20:4.10	13.87	64	FIES	4893 ± 101	2.14 ± 0.16	1.44 ± 0.17	5071 ± 14	2.86 ± 0.04	1.61 ± 0.02	4982	57	125	2.50	0.10	0.51	0.12 ± 0.24 (167)	0.01 ± 0.28 (126)	0.06
	W045	22:15:7.80	54:18:26.90	14.16	66	FIES	4963 ± 110	2.60 ± 0.12	1.33 ± 0.14	5100 ± 16	3.22 ± 0.04	1.43 ± 0.02	5031	63	97	2.91	0.08	0.44	0.23 ± 0.20 (179)	0.27 ± 0.30 (134)	0.02
	W055	22:15:17.50	54:18:12.60	13.11	75	FIES	5005 ± 71	2.45 ± 0.09	1.21 ± 0.07	4933 ± 16	2.54 ± 0.04	1.47 ± 0.02	4969	43	50	2.50	0.06	0.06	0.09 ± 0.13 (195)	0.01 ± 0.13 (155)	0.04
	W095	22:15:12.00	54:21:11.40	13.37	74	FIES	5023 ± 58	2.69 ± 0.08	1.62 ± 0.13	5017 ± 16	2.57 ± 0.04	1.61 ± 0.02	5020	37	3	2.63	0.06	0.08	-0.02 ± 0.12 (192)	0.01 ± 0.13 (159)	0.02
	W178	22:15:5.40	54:22:43.60	13.76	72	FIES	5166 ± 75	2.75 ± 0.12	1.26 ± 0.08	5105 ± 16	2.77 ± 0.05	1.26 ± 0.03	5135	45	42	2.76	0.08	0.01	0.04 ± 0.17 (202)	0.06 ± 0.21 (144)	0.01
	W179	22:15:5.40	54:22:49.40	12.97	78	FIES	5045 ± 51	2.76 ± 0.08	1.68 ± 0.13	4928 ± 13	2.45 ± 0.04	1.66 ± 0.02	4986	32	82	2.60	0.06	0.22	0.08 ± 0.12 (176)	0.10 ± 0.15 (151)	0.01
NGC7762	W0002	23:49:48.40	+68:01:35.14	12.56	66	HERMES	4798 ± 67	2.69 ± 0.08	1.23 ± 0.07	4820 ± 14	2.54 ± 0.03	1.40 ± 0.02	4809	40	15	2.62	0.06	0.11	0.04 ± 0.07 (239)	-0.02 ± 0.13 (158)	0.03
	W0003	23:49:49.26	+68:01:07.35	12.88	58	HERMES	4700 ± 48	2.53 ± 0.14	1.19 ± 0.08	4681 ± 13	2.47 ± 0.04	1.33 ± 0.02	4690	30	13	2.50	0.09	0.04	-0.01 ± 0.08 (231)	-0.07 ± 0.14 (151)	0.03

Table B.2 Continued from previous page

Cluster	Star	RA	DEC	V	SNR	Instr	T_{eff}	log g	ξ	T_{eff}	log g	ξ	T_{eff}	δ_1 T	δ_2 T	log g	δ_1 g	δ_2 g	[Fe/H]$_{EW}$	[Fe/H]$_{SS}$	σ[Fe/H]
							EW			SS											
	W0084	23:50:13.52	+68:03:02.57	12.24	67	HERMES	5052 ± 56	2.88 ± 0.07	1.27 ± 0.06	5042 ± 12	2.79 ± 0.04	1.42 ± 0.02	5047	34	6	2.84	0.06	0.06	0.06 ± 0.06 (240)	0.02 ± 0.11 (168)	0.02
	W0110	23:49:06.13	+67:59:08.58	12.56	63	HERMES	4859 ± 46	2.94 ± 0.07	1.15 ± 0.06	4850 ± 13	2.62 ± 0.04	1.38 ± 0.02	4854	29	6	2.78	0.06	0.23	0.09 ± 0.06 (240)	0.01 ± 0.13 (157)	0.04
	W0125	23:49:15.74	+68:05:32.14	12.57	68	HERMES	4838 ± 34	2.63 ± 0.10	1.16 ± 0.06	4871 ± 13	2.59 ± 0.03	1.32 ± 0.02	4854	23	24	2.61	0.06	0.03	0.01 ± 0.06 (245)	-0.04 ± 0.13 (158)	0.02
	W0139	23:50:59.35	+68:00:36.61	12.80	56	HERMES	4784 ± 35	2.34 ± 0.09	1.17 ± 0.04	4856 ± 16	2.60 ± 0.04	1.39 ± 0.02	4820	25	50	2.47	0.06	0.18	0.01 ± 0.04 (228)	-0.11 ± 0.17 (153)	0.06
NGC7789	W05862	23:56:57.38	+56:36:54.69	12.98	46	HERMES	4988 ± 49	2.75 ± 0.08	1.27 ± 0.05	4990 ± 17	2.76 ± 0.05	1.37 ± 0.03	4989	33	1	2.76	0.06	0.01	-0.01 ± 0.05 (265)	-0.11 ± 0.17 (158)	0.05
	W07176	23:57:12.50	+56:50:00.41	12.84	50	HERMES	4935 ± 60	2.90 ± 0.09	1.15 ± 0.06	4928 ± 16	2.65 ± 0.05	1.42 ± 0.02	4931	38	4	2.78	0.07	0.18	0.08 ± 0.06 (240)	-0.03 ± 0.13 (154)	0.06
	W07714	23:57:18.57	+56:50:26.72	13.01	46	HERMES	4903 ± 63	2.75 ± 0.08	1.05 ± 0.07	4879 ± 17	2.62 ± 0.05	1.39 ± 0.03	4891	40	16	2.68	0.06	0.09	0.05 ± 0.07 (248)	-0.07 ± 0.15 (156)	0.06
	W08260	23:57:24.05	+56:45:33.53	12.84	48	HERMES	4867 ± 71	2.63 ± 0.10	0.99 ± 0.09	4915 ± 18	2.65 ± 0.05	1.15 ± 0.03	4891	44	34	2.64	0.08	0.01	0.03 ± 0.09 (260)	-0.09 ± 0.14 (156)	0.06
	W08556	23:57:27.60	+56:45:39.20	12.97	88	FIES	5012 ± 68	2.98 ± 0.08	1.33 ± 0.09	4978 ± 11	2.82 ± 0.03	1.46 ± 0.02	4995	39	23	2.90	0.06	0.11	0.02 ± 0.10 (205)	0.00 ± 0.11 (164)	0.01
	W08734	23:57:29.65	+56:42:23.23	12.69	90	FIES	5015 ± 56	2.91 ± 0.09	1.05 ± 0.10	4925 ± 12	2.69 ± 0.03	1.39 ± 0.02	4970	34	63	2.80	0.06	0.16	0.15 ± 0.11 (195)	0.04 ± 0.13 (155)	0.06
	W10915	23:57:54.51	+56:47:43.46	12.82	75	FIES	4985 ± 74	2.89 ± 0.10	1.07 ± 0.12	5005 ± 14	2.82 ± 0.04	1.38 ± 0.02	4995	44	14	2.86	0.07	0.05	0.08 ± 0.15 (208)	-0.01 ± 0.17 (147)	0.04
					49	HERMES	4975 ± 38	2.75 ± 0.08	1.04 ± 0.05	5010 ± 17	2.77 ± 0.05	1.13 ± 0.03	4992	27	24	2.76	0.06	0.01	0.07 ± 0.05 (251)	-0.02 ± 0.17 (156)	0.04

Table B.3. Effective temperature, surface gravity and [Fe/H] for the set of GBS calculated by EW (GALA) and SS (iSpec). The reference values are from Heiter et al. (2015b) and Jofré et al. (2014).

Star ID	$T_{eff,ref}$	$\log g_{ref}$	$[Fe/H]_{ref}$	$T_{eff,EW}$	$\log g_{EW}$	$[Fe/H]_{EW}$	$T_{eff,SS}$	$\log g_{SS}$	$[Fe/H]_{SS}$
HARPS_GBOG_HD22879	5868	4.27	−0.88	5669 ± 23	3.84 ± 0.06	−0.960 ± 0.045	5861 ± 15	4.21 ± 0.02	−0.850 ± 0.045
NARVAL_HD22879	5868	4.27	−0.88	5698 ± 26	3.91 ± 0.04	−0.940 ± 0.046	5895 ± 16	4.28 ± 0.03	−0.830 ± 0.044
NARVAL_muCas	5308	4.41	−0.82	5241 ± 40	4.19 ± 0.05	−0.840 ± 0.047	5334 ± 15	4.47 ± 0.02	−0.810 ± 0.044
HARPS_GBOG_HD220009	4217	1.43	−0.75	4338 ± 29	1.91 ± 0.05	−0.640 ± 0.046	4288 ± 5	1.58 ± 0.02	−0.710 ± 0.048
NARVAL_HD220009	4217	1.43	−0.75	4360 ± 38	1.80 ± 0.06	−0.610 ± 0.047	4274 ± 6	1.54 ± 0.02	−0.720 ± 0.047
HARPS_GBOG_epsFor	5123	3.52	−0.62	5124 ± 26	3.47 ± 0.06	−0.540 ± 0.045	5001 ± 8	3.45 ± 0.02	−0.650 ± 0.044
ATLAS_Arcturus	4286	1.64	−0.53	4354 ± 43	1.90 ± 0.06	−0.430 ± 0.047	4240 ± 7	1.50 ± 0.02	−0.550 ± 0.051
HARPS_Archive_Arcturus	4286	1.64	−0.53	4345 ± 41	1.89 ± 0.07	−0.440 ± 0.047	4234 ± 3	1.42 ± 0.02	−0.570 ± 0.049
NARVAL_Arcturus	4286	1.64	−0.53	4373 ± 42	1.79 ± 0.09	−0.500 ± 0.047	4248 ± 5	1.45 ± 0.02	−0.590 ± 0.050
UVES_Arcturus-1	4286	1.64	−0.53	4387 ± 52	1.84 ± 0.07	−0.500 ± 0.047	4245 ± 6	1.52 ± 0.02	−0.590 ± 0.049
UVES_POP_Arcturus	4286	1.64	−0.53	4358 ± 52	1.88 ± 0.08	−0.490 ± 0.047	4240 ± 3	1.50 ± 0.01	−0.590 ± 0.049
ESPaDOnS_tauCet-1	5414	4.49	−0.50	5380 ± 40	4.43 ± 0.04	−0.460 ± 0.047	5307 ± 5	4.46 ± 0.01	−0.490 ± 0.044
HARPS_Archive_tauCet	5414	4.49	−0.50	5401 ± 39	4.48 ± 0.05	−0.440 ± 0.047	5307 ± 10	4.45 ± 0.02	−0.500 ± 0.044
NARVAL_tauCet	5414	4.49	−0.50	5401 ± 47	4.36 ± 0.06	−0.450 ± 0.047	5314 ± 10	4.45 ± 0.02	−0.490 ± 0.044
ESPaDOnS_HD49933-1	6635	4.20	−0.46	6551 ± 48	3.83 ± 0.08	−0.450 ± 0.046	6589 ± 10	3.97 ± 0.02	−0.440 ± 0.045
HARPS_Archive_HD49933	6635	4.20	−0.46	6495 ± 77	3.79 ± 0.09	−0.460 ± 0.048	6573 ± 15	3.93 ± 0.04	−0.470 ± 0.045
HARPS_GBOG_HD107328	4496	2.09	−0.34	4417 ± 41	1.85 ± 0.07	−0.410 ± 0.046	4377 ± 3	1.69 ± 0.02	−0.490 ± 0.050
NARVAL_HD107328	4496	2.09	−0.34	4430 ± 36	1.90 ± 0.08	−0.410 ± 0.047	4385 ± 4	1.70 ± 0.02	−0.490 ± 0.050
HARPS_Archive_betHyi-w	5873	3.98	−0.07	5730 ± 41	3.67 ± 0.06	−0.120 ± 0.046	5902 ± 10	4.00 ± 0.02	−0.050 ± 0.043
UVES_betHyi-1	5873	3.98	−0.07	5892 ± 42	4.06 ± 0.05	−0.090 ± 0.047	5915 ± 11	4.02 ± 0.02	−0.050 ± 0.044
UVES_betHyi-2	5873	3.98	−0.07	5886 ± 43	4.06 ± 0.04	−0.080 ± 0.047	5886 ± 18	4.01 ± 0.02	−0.070 ± 0.043
UVES_POP_betHyi	5873	3.98	−0.07	5854 ± 37	3.94 ± 0.04	−0.090 ± 0.047	5931 ± 8	4.05 ± 0.01	−0.040 ± 0.044
HARPS_GBOG_betAra	4197	1.05	−0.05	4471 ± 145	1.63 ± 0.26	0.040 ± 0.050	4419 ± 4	1.13 ± 0.02	−0.110 ± 0.056
ESPaDOnS_Procyon-1	6554	4.00	−0.04	6626 ± 55	3.80 ± 0.06	0.000 ± 0.046	6439 ± 4	3.67 ± 0.02	−0.110 ± 0.044
HARPS_GBOG_Procyon	6554	4.00	−0.04	6632 ± 66	3.82 ± 0.06	0.030 ± 0.046	6404 ± 7	3.60 ± 0.02	−0.130 ± 0.045
NARVAL_Procyon	6554	4.00	−0.04	6640 ± 61	3.74 ± 0.10	0.050 ± 0.047	6441 ± 5	3.68 ± 0.02	−0.100 ± 0.045
UVES_POP_Procyon	6554	4.00	−0.04	6572 ± 56	3.76 ± 0.06	−0.010 ± 0.046	6399 ± 3	3.61 ± 0.01	−0.130 ± 0.045
UVES_Procyon-1	6554	4.00	−0.04	6608 ± 50	3.81 ± 0.05	−0.030 ± 0.046	6389 ± 5	3.57 ± 0.02	−0.140 ± 0.045
UVES_Procyon-2	6554	4.00	−0.04	6513 ± 56	3.61 ± 0.08	−0.040 ± 0.047	6372 ± 7	3.55 ± 0.03	−0.150 ± 0.045
ESPaDOnS_18Sco-1	5810	4.44	0.01	5858 ± 44	4.57 ± 0.05	0.080 ± 0.047	5814 ± 12	4.48 ± 0.02	0.080 ± 0.043
HARPS_Archive_18Sco	5810	4.44	0.01	5812 ± 37	4.45 ± 0.05	0.050 ± 0.046	5805 ± 16	4.45 ± 0.02	0.060 ± 0.043
NARVAL_18Sco	5810	4.44	0.01	5810 ± 43	4.43 ± 0.05	0.060 ± 0.047	5807 ± 12	4.47 ± 0.02	0.080 ± 0.042
ATLAS_Sun	5771	4.44	0.02	5826 ± 41	4.51 ± 0.04	0.010 ± 0.047	5793 ± 8	4.48 ± 0.01	0.050 ± 0.043
HARPS_Archive_Sun-1	5771	4.44	0.02	5766 ± 45	4.42 ± 0.05	0.000 ± 0.046	5778 ± 11	4.43 ± 0.02	0.020 ± 0.043
HARPS_Archive_Sun-2	5771	4.44	0.02	5740 ± 45	4.45 ± 0.04	0.000 ± 0.046	5786 ± 10	4.45 ± 0.02	0.020 ± 0.043
HARPS_Archive_Sun-3	5771	4.44	0.02	5767 ± 41	4.40 ± 0.06	0.010 ± 0.046	5781 ± 13	4.43 ± 0.02	0.020 ± 0.044
HARPS_Archive_Sun-4	5771	4.44	0.02	5759 ± 44	4.43 ± 0.05	0.000 ± 0.046	5776 ± 8	4.43 ± 0.01	0.020 ± 0.043
NARVAL_Sun-1	5771	4.44	0.02	5788 ± 43	4.50 ± 0.05	0.030 ± 0.047	5783 ± 8	4.46 ± 0.01	0.030 ± 0.042
NARVAL_Sun_Metis	5771	4.44	0.02	5757 ± 51	4.44 ± 0.06	−0.020 ± 0.047	5787 ± 32	4.45 ± 0.05	0.010 ± 0.044
UVES_Sun-1	5771	4.44	0.02	5770 ± 84	4.47 ± 0.05	0.010 ± 0.047	5774 ± 9	4.45 ± 0.01	0.020 ± 0.043
UVES_Sun-2	5771	4.44	0.02	5773 ± 84	4.39 ± 0.05	−0.010 ± 0.047	5774 ± 20	4.46 ± 0.03	0.020 ± 0.043
HARPS_Archive_delEri-w	4954	3.76	0.06	4966 ± 75	3.73 ± 0.04	0.130 ± 0.047	5018 ± 5	3.70 ± 0.01	0.100 ± 0.047
NARVAL_delEri	4954	3.76	0.06	4989 ± 46	3.74 ± 0.07	0.100 ± 0.047	5019 ± 7	3.71 ± 0.02	0.110 ± 0.045
UVES_delEri-1	4954	3.76	0.06	4983 ± 51	3.76 ± 0.05	0.090 ± 0.048	5004 ± 10	3.70 ± 0.02	0.090 ± 0.046
UVES_delEri-2	4954	3.76	0.06	4959 ± 54	3.72 ± 0.04	0.110 ± 0.049	5005 ± 17	3.70 ± 0.03	0.090 ± 0.045
UVES_POP_delEri	4954	3.76	0.06	5008 ± 48	3.63 ± 0.05	0.120 ± 0.048	5016 ± 6	3.71 ± 0.01	0.100 ± 0.047
HARPS_GBOG_betGem	4858	2.90	0.12	4878 ± 37	2.82 ± 0.05	0.140 ± 0.047	4878 ± 5	2.89 ± 0.02	0.070 ± 0.047
UVES_betGem	4858	2.90	0.12	4866 ± 55	2.93 ± 0.07	0.050 ± 0.047	4869 ± 11	2.98 ± 0.02	0.070 ± 0.047
ESPaDOnS_epsVir	4983	2.77	0.13	5096 ± 51	2.90 ± 0.06	0.200 ± 0.047	5113 ± 7	2.93 ± 0.02	0.160 ± 0.046
HARPS_GBOG_epsVir	4983	2.77	0.13	5099 ± 44	2.91 ± 0.05	0.230 ± 0.047	5094 ± 5	2.85 ± 0.02	0.130 ± 0.046
NARVAL_epsVir	4983	2.77	0.13	5076 ± 54	2.91 ± 0.07	0.210 ± 0.047	5109 ± 7	2.93 ± 0.02	0.150 ± 0.045
ESPaDOnS_ksiHya-1	5044	2.87	0.14	5005 ± 39	2.84 ± 0.07	0.090 ± 0.047	5088 ± 8	3.06 ± 0.01	0.120 ± 0.046
HARPS_GBOG_ksiHya	5044	2.87	0.14	5055 ± 38	2.88 ± 0.05	0.140 ± 0.047	5081 ± 8	3.03 ± 0.02	0.110 ± 0.046
ESPaDOnS_betVir-1	6083	4.10	0.21	6187 ± 85	4.15 ± 0.05	0.210 ± 0.047	6199 ± 9	4.17 ± 0.01	0.200 ± 0.043
HARPS_Archive_betVir	6083	4.10	0.21	6067 ± 109	3.86 ± 0.06	0.150 ± 0.047	6144 ± 12	4.11 ± 0.02	0.160 ± 0.044
NARVAL_betVir	6083	4.10	0.21	6183 ± 98	4.09 ± 0.05	0.230 ± 0.047	6186 ± 11	4.17 ± 0.02	0.200 ± 0.043

Table B.3 Continued from previous page

Star ID	$T_{eff,ref}$	$\log g_{ref}$	$[Fe/H]_{ref}$	$T_{eff,EW}$	$\log g_{EW}$	$[Fe/H]_{EW}$	$T_{eff,SS}$	$\log g_{SS}$	$[Fe/H]_{SS}$
HARPS_Archive_alfCenB-w	5231	4.53	0.22	5211 ± 109	4.49 ± 0.05	0.210 ± 0.047	5172 ± 7	4.50 ± 0.01	0.240 ± 0.045
HARPS_Archive_alfCenA	5792	4.31	0.24	5811 ± 48	4.44 ± 0.05	0.230 ± 0.047	5804 ± 8	4.32 ± 0.01	0.260 ± 0.044
HARPS_Archive_alfCenA-w	5792	4.31	0.24	5721 ± 48	3.86 ± 0.06	0.150 ± 0.047	5800 ± 9	4.31 ± 0.01	0.260 ± 0.044
UVES_alfCenA-1	5792	4.31	0.24	5721 ± 90	4.08 ± 0.08	0.180 ± 0.049	5773 ± 10	4.30 ± 0.02	0.230 ± 0.044
ESPaDOnS_muLeo-1	4474	2.51	0.26	4426 ± 58	2.41 ± 0.13	0.300 ± 0.050	4488 ± 4	2.52 ± 0.01	0.200 ± 0.053
NARVAL_muLeo	4474	2.51	0.26	4486 ± 98	2.35 ± 0.16	0.320 ± 0.050	4496 ± 7	2.54 ± 0.01	0.220 ± 0.053
HARPS_GBOG_etaBoo	6099	3.79	0.30	5926 ± 119	3.23 ± 0.09	0.220 ± 0.047	6114 ± 9	3.89 ± 0.02	0.340 ± 0.047
NARVAL_etaBoo	6099	3.79	0.30	5946 ± 87	3.42 ± 0.09	0.260 ± 0.047	6104 ± 14	3.97 ± 0.02	0.250 ± 0.047
HARPS_Archive_muAra	5902	4.30	0.33	5718 ± 44	4.23 ± 0.04	0.260 ± 0.047	5748 ± 12	4.21 ± 0.02	0.300 ± 0.044
UVES_muAra-1	5902	4.30	0.33	5718 ± 79	4.14 ± 0.06	0.260 ± 0.048	5744 ± 11	4.25 ± 0.02	0.300 ± 0.044
UVES_muAra-2	5902	4.30	0.33	5804 ± 60	4.12 ± 0.04	0.300 ± 0.048	5737 ± 12	4.24 ± 0.02	0.300 ± 0.044

Table B.4. Ni, Cr, Si, Ca and Ti abundances, and abundance ratios respect to Fe for the stars analyzed in OCCASO. Errors of [X/H] are the line by line abundance spread, in parentheses we indicate the number of lines used. Errors in [X/Fe] are the squared sum of the error in [X/H] (following the prescription indicated in the text, see Section 6.2) and the error in [Fe/H].

Cluster	Star	Instr	[Ni/H]	[Cr/H]	[Si/H]	[Ca/H]	[Ti/H]	[Ni/Fe]	[Cr/Fe]	[Si/Fe]	[Ca/Fe]	[Ti/Fe]
	Arcturus	HERMES	-0.48 ± 0.09 (27)	-0.65 ± 0.11 (23)	-0.27 ± 0.06 (16)	-0.41 ± 0.06 (14)	-0.25 ± 0.15 (47)	0.03 ± 0.09	-0.14 ± 0.11	0.25 ± 0.06	0.11 ± 0.06	0.26 ± 0.15
	Arcturus	FIES	-0.51 ± 0.09 (26)	-0.67 ± 0.08 (20)	-0.31 ± 0.12 (15)	-0.43 ± 0.07 (14)	-0.30 ± 0.16 (42)	0.04 ± 0.09	-0.12 ± 0.08	0.24 ± 0.12	0.12 ± 0.07	0.25 ± 0.16
	Arcturus	CAFE	-0.52 ± 0.08 (25)	-0.73 ± 0.08 (18)	-0.30 ± 0.05 (14)	-0.45 ± 0.07 (14)	-0.29 ± 0.12 (46)	0.04 ± 0.08	-0.17 ± 0.08	0.26 ± 0.05	0.11 ± 0.07	0.27 ± 0.12
	μ-Leo	HERMES	0.42 ± 0.11 (27)	0.23 ± 0.13 (23)	0.34 ± 0.10 (17)	0.30 ± 0.14 (14)	0.42 ± 0.17 (48)	0.12 ± 0.11	-0.08 ± 0.13	0.04 ± 0.10	0.00 ± 0.14	0.11 ± 0.17
	μ-Leo	FIES	0.42 ± 0.11 (24)	0.22 ± 0.17 (21)	0.33 ± 0.12 (15)	0.31 ± 0.15 (14)	0.39 ± 0.20 (42)	0.11 ± 0.11	-0.09 ± 0.17	0.03 ± 0.12	0.00 ± 0.15	0.09 ± 0.20
	μ-Leo	CAFE	0.34 ± 0.14 (25)	0.07 ± 0.16 (20)	0.37 ± 0.11 (14)	0.13 ± 0.12 (14)	0.24 ± 0.19 (45)	0.13 ± 0.14	-0.14 ± 0.16	0.15 ± 0.11	-0.08 ± 0.12	0.03 ± 0.19
IC4756	W0038	FIES	-0.09 ± 0.12 (25)	-0.11 ± 0.09 (23)	-0.07 ± 0.07 (15)	-0.03 ± 0.06 (13)	-0.05 ± 0.11 (37)	-0.04 ± 0.13	-0.07 ± 0.10	-0.03 ± 0.09	0.01 ± 0.07	-0.01 ± 0.12
	W0042	HERMES	-0.03 ± 0.08 (26)	-0.03 ± 0.10 (22)	-0.08 ± 0.08 (17)	0.05 ± 0.07 (14)	0.04 ± 0.08 (45)	-0.06 ± 0.09	-0.06 ± 0.11	-0.11 ± 0.09	0.02 ± 0.08	0.01 ± 0.09
	W0044	HERMES	-0.02 ± 0.12 (26)	0.04 ± 0.13 (23)	-0.09 ± 0.07 (17)	0.07 ± 0.07 (14)	0.10 ± 0.09 (44)	-0.06 ± 0.13	-0.00 ± 0.14	-0.14 ± 0.08	0.02 ± 0.08	0.05 ± 0.10
	W0049	HERMES	-0.10 ± 0.07 (27)	-0.09 ± 0.09 (22)	-0.09 ± 0.05 (17)	-0.00 ± 0.06 (14)	-0.00 ± 0.09 (43)	-0.08 ± 0.08	-0.08 ± 0.10	-0.07 ± 0.07	0.02 ± 0.08	0.02 ± 0.10
	W0081	HERMES	-0.05 ± 0.11 (26)	-0.05 ± 0.15 (23)	-0.10 ± 0.07 (17)	0.04 ± 0.06 (14)	0.07 ± 0.11 (42)	-0.06 ± 0.11	-0.06 ± 0.16	-0.11 ± 0.08	0.03 ± 0.08	0.05 ± 0.12
	W0101	HERMES	-0.05 ± 0.08 (27)	-0.07 ± 0.08 (23)	-0.06 ± 0.12 (17)	0.04 ± 0.06 (14)	-0.00 ± 0.08 (44)	-0.07 ± 0.09	-0.09 ± 0.10	-0.08 ± 0.13	0.02 ± 0.08	-0.02 ± 0.09
	W0109	HERMES	-0.10 ± 0.09 (27)	-0.08 ± 0.07 (23)	-0.09 ± 0.09 (17)	0.01 ± 0.06 (14)	-0.01 ± 0.08 (44)	-0.08 ± 0.10	-0.06 ± 0.08	-0.07 ± 0.10	0.03 ± 0.07	0.01 ± 0.09
		FIES	-0.06 ± 0.09 (24)	-0.05 ± 0.10 (23)	-0.04 ± 0.14 (15)	0.06 ± 0.06 (13)	-0.03 ± 0.19 (37)	-0.08 ± 0.10	-0.07 ± 0.11	-0.06 ± 0.15	0.04 ± 0.08	-0.05 ± 0.20
	W0109	CAFE	-0.15 ± 0.09 (25)	-0.10 ± 0.12 (16)	-0.07 ± 0.06 (15)	0.02 ± 0.10 (13)	-0.05 ± 0.10 (39)	-0.09 ± 0.10	-0.03 ± 0.13	-0.01 ± 0.07	0.09 ± 0.11	0.02 ± 0.11
	W0125	HERMES	-0.11 ± 0.08 (26)	-0.12 ± 0.07 (23)	-0.12 ± 0.10 (17)	0.01 ± 0.05 (14)	-0.01 ± 0.09 (44)	-0.07 ± 0.09	-0.08 ± 0.08	-0.08 ± 0.11	0.04 ± 0.07	0.03 ± 0.10
		FIES	-0.04 ± 0.08 (25)	-0.09 ± 0.16 (23)	-0.03 ± 0.14 (15)	0.05 ± 0.08 (14)	0.03 ± 0.21 (42)	-0.06 ± 0.09	-0.10 ± 0.16	-0.05 ± 0.15	0.03 ± 0.10	0.01 ± 0.22
	W0125	CAFE	-0.13 ± 0.12 (25)	-0.05 ± 0.17 (18)	-0.09 ± 0.05 (16)	0.04 ± 0.11 (13)	0.01 ± 0.12 (36)	-0.11 ± 0.12	-0.03 ± 0.18	-0.07 ± 0.07	0.06 ± 0.12	0.03 ± 0.13
NGC188	W1105	HERMES	0.06 ± 0.13 (26)	-0.09 ± 0.13 (22)	0.05 ± 0.07 (17)	-0.09 ± 0.17 (14)	-0.05 ± 0.13 (48)	0.07 ± 0.14	-0.08 ± 0.14	0.06 ± 0.09	-0.08 ± 0.18	-0.04 ± 0.14
	W2051	HERMES	0.21 ± 0.18 (27)	0.05 ± 0.32 (23)	0.12 ± 0.13 (17)	0.07 ± 0.20 (14)	0.24 ± 0.19 (47)	-0.01 ± 0.18	-0.17 ± 0.32	-0.10 ± 0.14	-0.15 ± 0.20	0.02 ± 0.20
	W2088	HERMES	0.04 ± 0.20 (27)	-0.09 ± 0.12 (23)	0.04 ± 0.07 (17)	-0.06 ± 0.12 (14)	0.04 ± 0.18 (48)	-0.00 ± 0.21	-0.13 ± 0.13	0.00 ± 0.08	-0.09 ± 0.13	0.00 ± 0.18
	W5217	HERMES	0.02 ± 0.16 (26)	-0.04 ± 0.14 (23)	0.03 ± 0.10 (17)	0.02 ± 0.15 (14)	0.09 ± 0.16 (48)	-0.01 ± 0.17	-0.08 ± 0.15	0.00 ± 0.11	-0.01 ± 0.16	0.06 ± 0.17
	W5224	HERMES	0.04 ± 0.09 (27)	0.00 ± 0.09 (22)	0.05 ± 0.10 (17)	0.02 ± 0.13 (14)	0.11 ± 0.12 (47)	0.00 ± 0.10	-0.04 ± 0.10	0.01 ± 0.11	-0.02 ± 0.14	0.07 ± 0.13
	W7323	FIES	0.04 ± 0.19 (25)	-0.08 ± 0.17 (22)	0.09 ± 0.15 (15)	-0.19 ± 0.24 (14)	0.04 ± 0.21 (42)	0.03 ± 0.19	-0.08 ± 0.18	0.08 ± 0.16	-0.20 ± 0.24	0.03 ± 0.22
NGC752	W0001	FIES	-0.01 ± 0.12 (26)	-0.05 ± 0.08 (22)	-0.05 ± 0.13 (14)	-0.00 ± 0.09 (13)	0.03 ± 0.16 (38)	-0.00 ± 0.13	-0.04 ± 0.09	-0.04 ± 0.14	0.00 ± 0.10	0.04 ± 0.17
	W0024	FIES	-0.03 ± 0.10 (24)	-0.05 ± 0.10 (21)	-0.03 ± 0.11 (15)	-0.04 ± 0.05 (13)	0.06 ± 0.15 (37)	-0.06 ± 0.11	-0.08 ± 0.11	-0.06 ± 0.12	-0.07 ± 0.07	0.03 ± 0.16
		HERMES	-0.06 ± 0.08 (27)	-0.09 ± 0.08 (23)	-0.07 ± 0.06 (17)	0.03 ± 0.11 (14)	0.03 ± 0.09 (47)	-0.08 ± 0.09	-0.11 ± 0.09	-0.09 ± 0.08	0.01 ± 0.12	0.02 ± 0.10
	W0027	FIES	-0.09 ± 0.09 (25)	-0.08 ± 0.06 (21)	-0.04 ± 0.14 (15)	0.01 ± 0.07 (14)	-0.03 ± 0.16 (37)	-0.09 ± 0.10	-0.08 ± 0.07	-0.04 ± 0.15	0.01 ± 0.08	-0.03 ± 0.17
		HERMES	-0.03 ± 0.09 (27)	-0.09 ± 0.06 (23)	-0.06 ± 0.09 (17)	0.05 ± 0.07 (14)	0.03 ± 0.08 (46)	-0.07 ± 0.10	-0.13 ± 0.07	-0.10 ± 0.10	0.01 ± 0.09	-0.01 ± 0.09
	W0077	HERMES	-0.04 ± 0.10 (27)	-0.09 ± 0.08 (22)	-0.05 ± 0.05 (17)	0.04 ± 0.09 (14)	0.05 ± 0.11 (46)	-0.08 ± 0.11	-0.13 ± 0.09	-0.10 ± 0.07	-0.00 ± 0.10	0.00 ± 0.12
	W0137	FIES	-0.04 ± 0.09 (24)	-0.07 ± 0.08 (20)	-0.02 ± 0.14 (15)	-0.00 ± 0.08 (13)	-0.01 ± 0.17 (38)	-0.05 ± 0.11	-0.08 ± 0.09	-0.03 ± 0.15	-0.01 ± 0.09	-0.02 ± 0.17

Table B.4 Continued from previous page

Cluster	Star	Instr	[Ni/H]	[Cr/H]	[Si/H]	[Ca/H]	[Ti/H]	[Ni/Fe]	[Cr/Fe]	[Si/Fe]	[Ca/Fe]	[Ti/Fe]
		HERMES	-0.09 ± 0.09 (27)	-0.14 ± 0.06 (23)	-0.09 ± 0.06 (17)	0.00 ± 0.08 (13)	-0.06 ± 0.06 (45)	-0.06 ± 0.10	-0.11 ± 0.07	-0.07 ± 0.07	0.03 ± 0.09	-0.04 ± 0.08
	W0295	FIES	0.02 ± 0.13 (27)	-0.07 ± 0.21 (21)	-0.04 ± 0.17 (15)	0.14 ± 0.09 (14)	0.03 ± 0.18 (38)	-0.05 ± 0.14	-0.13 ± 0.22	-0.11 ± 0.17	0.08 ± 0.10	-0.03 ± 0.19
	W0311	HERMES	-0.04 ± 0.09 (27)	-0.09 ± 0.07 (23)	-0.06 ± 0.07 (17)	0.03 ± 0.08 (14)	-0.01 ± 0.09 (47)	-0.05 ± 0.10	-0.11 ± 0.09	-0.07 ± 0.09	0.02 ± 0.10	-0.03 ± 0.10
NGC1817	W0008	FIES	-0.17 ± 0.09 (26)	-0.20 ± 0.08 (22)	-0.14 ± 0.12 (15)	-0.06 ± 0.10 (13)	-0.13 ± 0.11 (38)	-0.05 ± 0.10	-0.08 ± 0.09	-0.02 ± 0.13	0.06 ± 0.11	-0.01 ± 0.12
	W0022	FIES	-0.17 ± 0.12 (24)	-0.12 ± 0.12 (19)	-0.15 ± 0.16 (15)	-0.03 ± 0.12 (14)	-0.10 ± 0.14 (34)	-0.10 ± 0.12	-0.05 ± 0.13	-0.08 ± 0.17	0.05 ± 0.13	-0.03 ± 0.15
	W0073	FIES	-0.11 ± 0.11 (25)	-0.15 ± 0.10 (22)	-0.08 ± 0.05 (14)	-0.05 ± 0.06 (14)	-0.02 ± 0.10 (38)	-0.04 ± 0.12	-0.09 ± 0.11	-0.01 ± 0.07	0.01 ± 0.08	0.04 ± 0.11
	W0079	FIES	-0.11 ± 0.13 (24)	-0.13 ± 0.10 (22)	-0.08 ± 0.12 (15)	-0.01 ± 0.11 (9)	-0.05 ± 0.17 (31)	-0.05 ± 0.14	-0.08 ± 0.11	-0.02 ± 0.13	0.05 ± 0.12	0.01 ± 0.18
	W0127	FIES	-0.14 ± 0.13 (26)	-0.15 ± 0.14 (21)	-0.09 ± 0.06 (14)	-0.03 ± 0.14 (13)	-0.04 ± 0.11 (37)	-0.04 ± 0.14	-0.06 ± 0.15	0.01 ± 0.08	0.06 ± 0.15	0.05 ± 0.12
NGC1907	W0062	HERMES	-0.08 ± 0.20 (26)	-0.03 ± 0.19 (21)	-0.06 ± 0.08 (16)	0.06 ± 0.13 (14)	0.02 ± 0.20 (43)	-0.05 ± 0.20	0.01 ± 0.20	-0.02 ± 0.10	0.10 ± 0.14	0.06 ± 0.20
	W0113	HERMES	-0.11 ± 0.10 (27)	-0.14 ± 0.09 (23)	-0.11 ± 0.08 (17)	0.01 ± 0.08 (14)	-0.07 ± 0.06 (43)	-0.08 ± 0.11	-0.11 ± 0.10	-0.07 ± 0.10	0.04 ± 0.09	-0.04 ± 0.08
	W0131	HERMES	-0.21 ± 0.14 (26)	-0.15 ± 0.18 (21)	-0.14 ± 0.07 (17)	-0.02 ± 0.10 (14)	-0.09 ± 0.15 (42)	-0.10 ± 0.14	-0.05 ± 0.19	-0.03 ± 0.08	0.08 ± 0.11	0.01 ± 0.15
	W0133	HERMES	-0.11 ± 0.11 (27)	-0.03 ± 0.20 (22)	-0.20 ± 0.09 (16)	-0.05 ± 0.13 (14)	-0.02 ± 0.15 (41)	-0.06 ± 0.12	0.03 ± 0.21	-0.14 ± 0.10	0.01 ± 0.14	0.03 ± 0.15
	W0256	HERMES	-0.13 ± 0.11 (27)	-0.12 ± 0.10 (23)	-0.10 ± 0.08 (15)	-0.06 ± 0.05 (14)	-0.03 ± 0.10 (48)	-0.05 ± 0.12	-0.05 ± 0.11	-0.02 ± 0.09	0.02 ± 0.07	0.04 ± 0.11
	W2087	HERMES	-0.41 ± 0.17 (24)	-0.58 ± 0.13 (22)	-0.29 ± 0.13 (17)	-0.23 ± 0.14 (14)	-0.24 ± 0.13 (47)	0.12 ± 0.18	-0.05 ± 0.14	0.24 ± 0.14	0.31 ± 0.14	0.29 ± 0.14
NGC2099	W007	HERMES	-0.01 ± 0.09 (25)	0.02 ± 0.13 (22)	-0.01 ± 0.09 (17)	0.07 ± 0.06 (14)	0.03 ± 0.10 (43)	-0.05 ± 0.10	-0.02 ± 0.14	-0.05 ± 0.10	0.03 ± 0.07	-0.01 ± 0.11
	W016	HERMES	0.01 ± 0.09 (26)	0.03 ± 0.10 (21)	0.03 ± 0.10 (17)	0.15 ± 0.07 (14)	0.07 ± 0.14 (43)	-0.08 ± 0.10	-0.06 ± 0.11	-0.06 ± 0.11	0.06 ± 0.09	-0.02 ± 0.15
	W031	HERMES	0.09 ± 0.13 (25)	0.12 ± 0.15 (20)	0.08 ± 0.09 (16)	0.20 ± 0.13 (14)	0.14 ± 0.16 (36)	-0.05 ± 0.13	-0.02 ± 0.16	-0.06 ± 0.10	0.06 ± 0.14	-0.00 ± 0.16
	W148	HERMES	0.03 ± 0.08 (25)	-0.01 ± 0.12 (21)	0.06 ± 0.08 (17)	0.11 ± 0.08 (14)	0.09 ± 0.15 (44)	-0.05 ± 0.10	-0.09 ± 0.13	-0.02 ± 0.10	0.03 ± 0.10	0.01 ± 0.16
	W172	HERMES	0.02 ± 0.11 (27)	0.00 ± 0.11 (21)	0.00 ± 0.05 (17)	0.11 ± 0.07 (14)	0.07 ± 0.15 (43)	-0.03 ± 0.12	-0.05 ± 0.12	-0.05 ± 0.07	0.05 ± 0.09	0.01 ± 0.16
	W401	HERMES	0.01 ± 0.08 (27)	-0.00 ± 0.10 (23)	0.05 ± 0.05 (17)	0.11 ± 0.07 (14)	0.05 ± 0.13 (44)	-0.07 ± 0.09	-0.09 ± 0.11	-0.04 ± 0.07	0.03 ± 0.08	-0.04 ± 0.14
	W488	HERMES	0.00 ± 0.08 (27)	0.01 ± 0.08 (23)	0.04 ± 0.06 (17)	0.09 ± 0.08 (14)	0.05 ± 0.11 (44)	-0.07 ± 0.10	-0.06 ± 0.10	-0.03 ± 0.08	0.02 ± 0.09	-0.02 ± 0.12
NGC2420	W041	FIES	-0.21 ± 0.13 (26)	-0.19 ± 0.13 (22)	-0.21 ± 0.10 (15)	-0.08 ± 0.15 (14)	-0.10 ± 0.14 (38)	-0.03 ± 0.14	-0.01 ± 0.14	-0.03 ± 0.11	0.10 ± 0.15	0.08 ± 0.15
	W076	FIES	-0.10 ± 0.10 (26)	-0.22 ± 0.10 (20)	-0.07 ± 0.13 (15)	-0.04 ± 0.13 (13)	-0.02 ± 0.11 (36)	-0.02 ± 0.11	-0.15 ± 0.11	-0.00 ± 0.14	0.03 ± 0.13	0.05 ± 0.12
	W091	FIES	-0.09 ± 0.15 (26)	-0.15 ± 0.17 (20)	-0.09 ± 0.07 (15)	-0.08 ± 0.13 (13)	-0.04 ± 0.11 (37)	-0.01 ± 0.16	-0.07 ± 0.18	-0.00 ± 0.09	0.00 ± 0.14	0.05 ± 0.12
	W111	FIES	-0.09 ± 0.13 (25)	-0.11 ± 0.25 (23)	-0.09 ± 0.14 (14)	-0.01 ± 0.14 (14)	0.01 ± 0.22 (41)	-0.03 ± 0.14	-0.06 ± 0.26	-0.04 ± 0.15	0.05 ± 0.15	0.07 ± 0.22
	W118	FIES	-0.15 ± 0.12 (26)	-0.22 ± 0.10 (22)	-0.11 ± 0.09 (15)	-0.08 ± 0.12 (14)	-0.11 ± 0.11 (40)	-0.03 ± 0.13	-0.09 ± 0.11	0.02 ± 0.10	0.04 ± 0.12	0.01 ± 0.12
	W174	FIES	-0.12 ± 0.13 (25)	-0.16 ± 0.15 (22)	-0.11 ± 0.11 (15)	-0.00 ± 0.11 (14)	-0.03 ± 0.12 (38)	-0.07 ± 0.14	-0.10 ± 0.15	-0.05 ± 0.12	0.05 ± 0.12	0.03 ± 0.13
	W236	FIES	-0.10 ± 0.11 (26)	-0.15 ± 0.14 (23)	-0.14 ± 0.11 (14)	-0.07 ± 0.13 (13)	-0.05 ± 0.14 (38)	0.00 ± 0.12	-0.05 ± 0.15	-0.04 ± 0.12	0.03 ± 0.14	0.05 ± 0.15
NGC2539	W229	HERMES	0.02 ± 0.10 (26)	0.02 ± 0.10 (22)	-0.01 ± 0.11 (17)	0.04 ± 0.09 (14)	0.06 ± 0.12 (45)	-0.05 ± 0.11	-0.04 ± 0.11	-0.07 ± 0.12	-0.02 ± 0.10	-0.00 ± 0.12
	W251	HERMES	0.08 ± 0.16 (26)	0.05 ± 0.18 (21)	0.01 ± 0.11 (17)	0.14 ± 0.09 (14)	0.15 ± 0.21 (45)	0.04 ± 0.16	-0.00 ± 0.19	-0.04 ± 0.12	0.09 ± 0.10	0.10 ± 0.22
	W346	HERMES	0.02 ± 0.15 (27)	0.00 ± 0.11 (22)	-0.01 ± 0.08 (17)	0.08 ± 0.07 (14)	0.09 ± 0.12 (46)	-0.05 ± 0.16	-0.06 ± 0.12	-0.07 ± 0.09	0.01 ± 0.09	0.02 ± 0.13
	W463	HERMES	0.01 ± 0.08 (25)	-0.00 ± 0.10 (22)	0.01 ± 0.06 (17)	0.11 ± 0.09 (13)	0.05 ± 0.07 (39)	-0.06 ± 0.09	-0.07 ± 0.11	-0.05 ± 0.07	0.04 ± 0.10	-0.01 ± 0.09
	W502	HERMES	0.05 ± 0.09 (26)	0.02 ± 0.11 (22)	0.01 ± 0.16 (17)	0.06 ± 0.09 (14)	0.10 ± 0.12 (43)	-0.02 ± 0.10	-0.06 ± 0.12	-0.07 ± 0.16	-0.02 ± 0.10	0.02 ± 0.13
NGC2682	W084	HERMES	0.06 ± 0.09 (25)	0.00 ± 0.10 (22)	0.05 ± 0.09 (16)	0.15 ± 0.18 (14)	0.12 ± 0.16 (45)	-0.02 ± 0.10	-0.08 ± 0.11	-0.03 ± 0.10	0.07 ± 0.18	0.04 ± 0.17

Table B.4 Continued from previous page

Cluster	Star	Instr	[Ni/H]	[Cr/H]	[Si/H]	[Ca/H]	[Ti/H]	[Ni/Fe]	[Cr/Fe]	[Si/Fe]	[Ca/Fe]	[Ti/Fe]
	W141	HERMES	0.08 ± 0.12 (26)	-0.07 ± 0.09 (23)	0.06 ± 0.18 (17)	0.00 ± 0.11 (14)	0.07 ± 0.12 (48)	0.03 ± 0.13	-0.12 ± 0.11	0.01 ± 0.18	-0.05 ± 0.12	0.02 ± 0.13
	W151	HERMES	0.06 ± 0.08 (26)	-0.04 ± 0.07 (22)	-0.00 ± 0.07 (17)	0.00 ± 0.09 (14)	0.05 ± 0.09 (45)	0.02 ± 0.09	-0.07 ± 0.08	-0.04 ± 0.09	-0.04 ± 0.10	0.01 ± 0.10
	W164	HERMES	0.02 ± 0.10 (27)	-0.09 ± 0.09 (23)	-0.01 ± 0.09 (17)	-0.02 ± 0.08 (14)	0.01 ± 0.11 (47)	0.01 ± 0.11	-0.09 ± 0.10	-0.02 ± 0.10	-0.02 ± 0.10	0.00 ± 0.12
	W223	HERMES	0.00 ± 0.09 (27)	-0.14 ± 0.09 (23)	-0.01 ± 0.06 (17)	0.01 ± 0.10 (14)	-0.02 ± 0.10 (48)	-0.00 ± 0.10	-0.14 ± 0.10	-0.01 ± 0.07	0.01 ± 0.11	-0.03 ± 0.11
	W224	HERMES	0.10 ± 0.16 (27)	-0.06 ± 0.09 (23)	0.08 ± 0.07 (17)	0.05 ± 0.13 (14)	0.07 ± 0.16 (46)	0.01 ± 0.17	-0.15 ± 0.10	-0.01 ± 0.09	-0.04 ± 0.14	-0.02 ± 0.17
	W266	HERMES	0.02 ± 0.08 (26)	-0.06 ± 0.05 (23)	-0.02 ± 0.06 (17)	0.01 ± 0.06 (14)	0.03 ± 0.08 (46)	-0.00 ± 0.09	-0.08 ± 0.07	-0.04 ± 0.08	-0.01 ± 0.08	0.01 ± 0.09
	W286	HERMES	0.04 ± 0.10 (27)	-0.05 ± 0.08 (22)	-0.00 ± 0.09 (17)	0.04 ± 0.10 (14)	0.01 ± 0.10 (48)	-0.00 ± 0.11	-0.08 ± 0.10	-0.04 ± 0.10	0.01 ± 0.11	-0.03 ± 0.11
NGC6633	W100	HERMES	0.01 ± 0.08 (25)	-0.07 ± 0.10 (22)	-0.03 ± 0.07 (17)	0.07 ± 0.07 (14)	0.03 ± 0.11 (45)	-0.03 ± 0.09	-0.11 ± 0.11	-0.07 ± 0.08	0.03 ± 0.09	-0.01 ± 0.12
		FIES	-0.03 ± 0.17 (25)	-0.01 ± 0.12 (19)	0.06 ± 0.19 (14)	0.04 ± 0.14 (13)	0.05 ± 0.18 (38)	-0.11 ± 0.18	-0.08 ± 0.13	-0.01 ± 0.20	-0.03 ± 0.15	-0.02 ± 0.19
	W100	CAFE	-0.12 ± 0.08 (24)	-0.07 ± 0.12 (16)	-0.07 ± 0.07 (16)	0.01 ± 0.11 (14)	-0.03 ± 0.11 (39)	-0.08 ± 0.10	-0.02 ± 0.13	-0.02 ± 0.09	0.06 ± 0.12	0.02 ± 0.12
	W106	HERMES	0.00 ± 0.13 (27)	0.04 ± 0.11 (23)	-0.03 ± 0.06 (17)	0.14 ± 0.08 (14)	0.09 ± 0.14 (42)	-0.08 ± 0.14	-0.04 ± 0.12	-0.11 ± 0.08	0.06 ± 0.09	0.01 ± 0.15
		FIES	-0.02 ± 0.10 (25)	0.02 ± 0.14 (22)	-0.00 ± 0.16 (15)	0.16 ± 0.07 (13)	0.08 ± 0.22 (36)	-0.09 ± 0.11	-0.05 ± 0.14	-0.07 ± 0.17	0.09 ± 0.08	0.01 ± 0.23
	W119	HERMES	-0.02 ± 0.12 (26)	-0.03 ± 0.10 (23)	-0.06 ± 0.08 (17)	0.09 ± 0.08 (14)	0.06 ± 0.14 (42)	-0.05 ± 0.13	-0.07 ± 0.11	-0.09 ± 0.09	0.06 ± 0.09	0.03 ± 0.15
		FIES	-0.04 ± 0.12 (25)	-0.07 ± 0.14 (19)	-0.03 ± 0.12 (15)	0.03 ± 0.06 (13)	0.01 ± 0.20 (39)	-0.07 ± 0.13	-0.10 ± 0.15	-0.05 ± 0.12	0.00 ± 0.07	-0.02 ± 0.21
	W126	HERMES	-0.04 ± 0.09 (25)	-0.04 ± 0.10 (23)	-0.06 ± 0.08 (17)	0.06 ± 0.08 (14)	0.03 ± 0.08 (40)	-0.08 ± 0.10	-0.08 ± 0.11	-0.09 ± 0.09	0.02 ± 0.09	-0.00 ± 0.10
		FIES	-0.08 ± 0.09 (25)	-0.06 ± 0.12 (23)	-0.05 ± 0.16 (15)	0.08 ± 0.07 (14)	-0.05 ± 0.21 (33)	-0.07 ± 0.10	-0.05 ± 0.13	-0.04 ± 0.16	0.09 ± 0.09	-0.04 ± 0.21
NGC6705	W0660	HERMES	0.24 ± 0.16 (26)	0.11 ± 0.15 (23)	0.24 ± 0.15 (17)	0.17 ± 0.08 (14)	0.19 ± 0.15 (47)	0.05 ± 0.16	-0.09 ± 0.16	0.05 ± 0.16	-0.02 ± 0.10	-0.00 ± 0.16
	W0669	HERMES	0.31 ± 0.22 (23)	0.22 ± 0.31 (20)	0.38 ± 0.18 (13)	0.24 ± 0.16 (14)	0.24 ± 0.21 (42)	0.10 ± 0.23	0.01 ± 0.31	0.17 ± 0.19	0.03 ± 0.16	0.03 ± 0.21
	W0686	HERMES	0.18 ± 0.21 (25)	0.11 ± 0.29 (18)	0.24 ± 0.13 (13)	0.16 ± 0.14 (14)	0.20 ± 0.19 (40)	0.04 ± 0.21	-0.03 ± 0.29	0.10 ± 0.14	0.02 ± 0.15	0.06 ± 0.20
	W0779	HERMES	0.23 ± 0.16 (25)	0.12 ± 0.16 (23)	0.27 ± 0.20 (17)	0.24 ± 0.16 (14)	0.27 ± 0.20 (47)	0.04 ± 0.17	-0.07 ± 0.17	0.07 ± 0.21	0.05 ± 0.17	0.08 ± 0.21
		FIES	0.19 ± 0.19 (25)	0.04 ± 0.14 (21)	0.24 ± 0.13 (14)	0.19 ± 0.16 (14)	0.15 ± 0.18 (42)	0.02 ± 0.20	-0.14 ± 0.15	0.06 ± 0.14	0.01 ± 0.16	-0.02 ± 0.19
	W0916	HERMES	0.26 ± 0.23 (24)	0.26 ± 0.34 (19)	0.32 ± 0.16 (14)	0.34 ± 0.26 (14)	0.22 ± 0.21 (40)	0.09 ± 0.24	0.09 ± 0.34	0.15 ± 0.17	0.17 ± 0.27	0.05 ± 0.22
	W1184	HERMES	0.18 ± 0.17 (26)	0.10 ± 0.13 (22)	0.18 ± 0.11 (17)	0.17 ± 0.11 (14)	0.24 ± 0.20 (48)	0.05 ± 0.17	-0.03 ± 0.13	0.05 ± 0.12	0.05 ± 0.12	0.11 ± 0.20
		FIES	0.03 ± 0.19 (23)	-0.05 ± 0.10 (21)	0.07 ± 0.11 (14)	0.05 ± 0.12 (14)	0.05 ± 0.17 (41)	-0.00 ± 0.20	-0.08 ± 0.11	0.04 ± 0.12	0.01 ± 0.13	0.01 ± 0.17
	W1256	HERMES	0.06 ± 0.15 (26)	0.01 ± 0.10 (22)	0.11 ± 0.08 (17)	0.07 ± 0.11 (14)	0.15 ± 0.15 (47)	-0.01 ± 0.16	-0.07 ± 0.12	0.03 ± 0.09	-0.01 ± 0.12	0.07 ± 0.16
	W1423	HERMES	0.24 ± 0.17 (25)	0.07 ± 0.14 (22)	0.37 ± 0.16 (17)	0.11 ± 0.09 (14)	0.15 ± 0.21 (47)	0.08 ± 0.17	-0.10 ± 0.15	0.20 ± 0.17	-0.06 ± 0.10	-0.02 ± 0.22
		FIES	0.22 ± 0.18 (26)	0.14 ± 0.11 (22)	0.25 ± 0.14 (15)	0.19 ± 0.14 (14)	0.26 ± 0.18 (41)	-0.00 ± 0.19	-0.08 ± 0.12	0.03 ± 0.15	-0.03 ± 0.15	0.04 ± 0.19
NGC6791	W1794	FIES	0.15 ± 0.25 (26)	0.05 ± 0.22 (23)	0.19 ± 0.15 (14)	-0.01 ± 0.34 (14)	-0.00 ± 0.50 (42)	0.11 ± 0.26	0.01 ± 0.23	0.14 ± 0.17	-0.05 ± 0.34	-0.04 ± 0.50
	W2562	FIES	0.39 ± 0.53 (26)	0.26 ± 0.62 (21)	0.14 ± 0.20 (14)	0.07 ± 0.75 (13)	0.26 ± 0.56 (41)	0.15 ± 0.54	0.03 ± 0.62	-0.10 ± 0.21	-0.17 ± 0.75	0.03 ± 0.56
	W2579	FIES	0.26 ± 0.31 (26)	0.06 ± 0.27 (23)	0.32 ± 0.23 (15)	-0.02 ± 0.30 (14)	0.22 ± 0.34 (42)	0.09 ± 0.31	-0.11 ± 0.27	0.15 ± 0.24	-0.19 ± 0.30	0.05 ± 0.34
	W3363	FIES	0.32 ± 0.27 (24)	0.11 ± 0.21 (23)	0.31 ± 0.17 (15)	0.17 ± 0.20 (14)	0.32 ± 0.40 (41)	0.05 ± 0.28	-0.15 ± 0.21	0.04 ± 0.18	-0.10 ± 0.21	0.05 ± 0.40
	W3926	FIES	0.37 ± 0.28 (25)	0.07 ± 0.23 (22)	0.31 ± 0.23 (14)	0.18 ± 0.17 (14)	0.23 ± 0.31 (41)	0.14 ± 0.29	-0.15 ± 0.23	0.09 ± 0.24	-0.05 ± 0.18	0.01 ± 0.32
NGC6819	W333	HERMES	0.04 ± 0.08 (27)	-0.09 ± 0.11 (23)	0.03 ± 0.09 (17)	-0.02 ± 0.11 (14)	0.00 ± 0.14 (47)	-0.01 ± 0.09	-0.14 ± 0.12	-0.02 ± 0.10	-0.07 ± 0.12	-0.05 ± 0.15
	W386	HERMES	0.12 ± 0.09 (25)	0.05 ± 0.12 (23)	-0.03 ± 0.13 (17)	0.07 ± 0.16 (14)	0.18 ± 0.13 (46)	0.03 ± 0.10	-0.04 ± 0.13	-0.12 ± 0.14	-0.02 ± 0.17	0.09 ± 0.14

Table B.4 Continued from previous page

Cluster	Star	Instr	[Ni/H]	[Cr/H]	[Si/H]	[Ca/H]	[Ti/H]	[Ni/Fe]	[Cr/Fe]	[Si/Fe]	[Ca/Fe]	[Ti/Fe]
	W398	HERMES	0.05 ± 0.12 (27)	-0.06 ± 0.09 (23)	-0.01 ± 0.12 (17)	0.02 ± 0.10 (14)	0.05 ± 0.15 (47)	-0.02 ± 0.13	-0.13 ± 0.11	-0.08 ± 0.13	-0.05 ± 0.12	-0.02 ± 0.16
	W978	HERMES	0.05 ± 0.17 (26)	-0.04 ± 0.11 (23)	0.02 ± 0.08 (17)	0.03 ± 0.09 (14)	0.10 ± 0.15 (45)	-0.02 ± 0.18	-0.10 ± 0.12	-0.04 ± 0.09	-0.03 ± 0.10	0.04 ± 0.15
	W979	HERMES	0.11 ± 0.10 (27)	0.02 ± 0.13 (22)	0.09 ± 0.08 (17)	0.11 ± 0.12 (14)	0.15 ± 0.19 (46)	-0.03 ± 0.11	-0.12 ± 0.14	-0.05 ± 0.09	-0.03 ± 0.13	0.01 ± 0.20
	W983	HERMES	0.09 ± 0.09 (27)	-0.02 ± 0.13 (23)	0.07 ± 0.07 (17)	0.07 ± 0.12 (14)	0.11 ± 0.11 (47)	-0.03 ± 0.10	-0.14 ± 0.14	-0.05 ± 0.08	-0.06 ± 0.13	-0.02 ± 0.12
NGC6939	W130	HERMES	0.20 ± 0.22 (24)	0.18 ± 0.32 (18)	0.06 ± 0.27 (17)	0.30 ± 0.39 (11)	0.33 ± 0.39 (40)	-0.03 ± 0.23	-0.05 ± 0.32	-0.16 ± 0.27	0.08 ± 0.39	0.11 ± 0.39
	W145	HERMES	0.10 ± 0.13 (26)	0.07 ± 0.11 (23)	0.01 ± 0.19 (17)	0.12 ± 0.11 (14)	0.12 ± 0.17 (45)	-0.02 ± 0.14	-0.05 ± 0.12	-0.11 ± 0.20	0.00 ± 0.12	0.01 ± 0.18
	W170	HERMES	0.04 ± 0.13 (27)	0.06 ± 0.12 (23)	0.00 ± 0.11 (17)	0.15 ± 0.10 (14)	0.12 ± 0.13 (46)	-0.06 ± 0.13	-0.05 ± 0.13	-0.10 ± 0.12	0.05 ± 0.11	0.02 ± 0.14
	W214	HERMES	0.17 ± 0.12 (27)	0.02 ± 0.11 (23)	0.01 ± 0.11 (17)	0.14 ± 0.10 (14)	0.16 ± 0.17 (47)	0.01 ± 0.13	-0.15 ± 0.12	-0.16 ± 0.12	-0.03 ± 0.11	-0.01 ± 0.18
	W230	HERMES	0.02 ± 0.11 (27)	-0.04 ± 0.12 (23)	0.01 ± 0.09 (17)	0.09 ± 0.14 (14)	0.04 ± 0.13 (46)	-0.06 ± 0.12	-0.13 ± 0.13	-0.08 ± 0.10	0.00 ± 0.15	-0.04 ± 0.14
	W292	HERMES	0.01 ± 0.10 (27)	-0.08 ± 0.10 (23)	-0.04 ± 0.09 (17)	0.08 ± 0.14 (14)	0.07 ± 0.14 (46)	-0.03 ± 0.11	-0.13 ± 0.11	-0.09 ± 0.10	0.04 ± 0.15	0.03 ± 0.15
NGC6991	W034	CAFE	-0.14 ± 0.08 (25)	-0.12 ± 0.09 (17)	-0.08 ± 0.07 (15)	-0.03 ± 0.08 (13)	-0.02 ± 0.33 (36)	-0.07 ± 0.09	-0.06 ± 0.10	-0.02 ± 0.09	0.04 ± 0.09	0.05 ± 0.33
		FIES	0.02 ± 0.13 (27)	-0.05 ± 0.14 (22)	-0.03 ± 0.15 (15)	0.07 ± 0.11 (14)	0.05 ± 0.18 (37)	-0.03 ± 0.14	-0.11 ± 0.15	-0.08 ± 0.16	0.01 ± 0.12	-0.00 ± 0.19
	W043	CAFE	-0.07 ± 0.12 (26)	-0.07 ± 0.18 (16)	-0.07 ± 0.09 (16)	0.05 ± 0.09 (13)	0.03 ± 0.13 (38)	-0.05 ± 0.13	-0.05 ± 0.18	-0.05 ± 0.10	0.07 ± 0.10	0.05 ± 0.14
	W049	CAFE	-0.10 ± 0.09 (25)	-0.10 ± 0.12 (17)	-0.08 ± 0.07 (16)	-0.03 ± 0.20 (13)	0.03 ± 0.30 (36)	-0.06 ± 0.10	-0.06 ± 0.13	-0.05 ± 0.08	0.00 ± 0.20	0.07 ± 0.31
		FIES	-0.03 ± 0.06 (27)	-0.04 ± 0.08 (22)	-0.04 ± 0.07 (14)	0.02 ± 0.07 (13)	0.09 ± 0.09 (37)	-0.06 ± 0.07	-0.07 ± 0.09	-0.07 ± 0.09	-0.01 ± 0.09	0.05 ± 0.10
	W067	CAFE	-0.12 ± 0.12 (24)	-0.09 ± 0.17 (15)	-0.12 ± 0.10 (17)	0.00 ± 0.13 (13)	-0.01 ± 0.13 (39)	-0.06 ± 0.12	-0.03 ± 0.17	-0.05 ± 0.11	0.06 ± 0.13	0.06 ± 0.14
		FIES	-0.06 ± 0.11 (24)	-0.07 ± 0.10 (22)	0.00 ± 0.10 (15)	-0.03 ± 0.08 (13)	0.01 ± 0.11 (40)	-0.06 ± 0.12	-0.07 ± 0.11	-0.00 ± 0.11	-0.03 ± 0.09	0.00 ± 0.12
	W100	CAFE	-0.06 ± 0.15 (25)	-0.04 ± 0.11 (15)	-0.04 ± 0.07 (16)	0.08 ± 0.12 (14)	0.02 ± 0.16 (38)	-0.07 ± 0.15	-0.06 ± 0.12	-0.06 ± 0.09	0.06 ± 0.13	0.01 ± 0.17
	W131	CAFE	-0.05 ± 0.11 (27)	-0.05 ± 0.11 (17)	-0.04 ± 0.06 (16)	0.04 ± 0.06 (13)	0.06 ± 0.20 (35)	-0.06 ± 0.12	-0.06 ± 0.12	-0.05 ± 0.08	0.03 ± 0.07	0.05 ± 0.20
		FIES	-0.04 ± 0.13 (27)	-0.07 ± 0.07 (23)	-0.06 ± 0.09 (15)	0.00 ± 0.10 (14)	-0.01 ± 0.09 (39)	-0.07 ± 0.14	-0.10 ± 0.08	-0.09 ± 0.10	-0.02 ± 0.11	-0.04 ± 0.10
NGC7245	W045	FIES	0.26 ± 0.27 (26)	0.27 ± 0.21 (22)	0.14 ± 0.13 (15)	0.22 ± 0.28 (14)	0.37 ± 0.33 (36)	0.02 ± 0.28	0.04 ± 0.22	-0.10 ± 0.14	-0.01 ± 0.28	0.13 ± 0.33
	W055	FIES	0.03 ± 0.12 (27)	-0.00 ± 0.14 (22)	0.03 ± 0.08 (14)	0.16 ± 0.09 (14)	0.08 ± 0.12 (37)	-0.06 ± 0.13	-0.09 ± 0.15	-0.06 ± 0.09	0.07 ± 0.11	-0.01 ± 0.13
	W095	FIES	0.00 ± 0.27 (26)	-0.05 ± 0.25 (21)	-0.01 ± 0.09 (15)	0.02 ± 0.07 (13)	-0.03 ± 0.12 (38)	0.02 ± 0.28	-0.03 ± 0.26	0.00 ± 0.10	0.04 ± 0.09	-0.01 ± 0.13
	W178	FIES	0.02 ± 0.24 (26)	0.12 ± 0.28 (21)	-0.05 ± 0.10 (14)	0.07 ± 0.18 (14)	0.10 ± 0.24 (33)	-0.02 ± 0.25	0.08 ± 0.28	-0.09 ± 0.12	0.03 ± 0.19	0.06 ± 0.24
	W179	FIES	0.04 ± 0.13 (24)	0.02 ± 0.24 (22)	0.01 ± 0.12 (15)	0.02 ± 0.14 (14)	0.13 ± 0.17 (39)	-0.04 ± 0.14	-0.06 ± 0.25	-0.07 ± 0.13	-0.06 ± 0.15	0.05 ± 0.17
	W0205	FIES	0.13 ± 0.32 (26)	0.09 ± 0.33 (23)	0.12 ± 0.19 (14)	0.11 ± 0.21 (14)	0.25 ± 0.32 (40)	0.01 ± 0.33	-0.02 ± 0.33	0.01 ± 0.20	-0.01 ± 0.22	0.13 ± 0.32
NGC7762	W0002	HERMES	-0.00 ± 0.09 (27)	-0.07 ± 0.07 (23)	-0.04 ± 0.07 (17)	0.01 ± 0.06 (14)	0.02 ± 0.11 (46)	-0.05 ± 0.10	-0.11 ± 0.08	-0.09 ± 0.08	-0.03 ± 0.07	-0.02 ± 0.12
	W0003	HERMES	-0.01 ± 0.09 (27)	-0.08 ± 0.11 (22)	-0.07 ± 0.10 (17)	0.01 ± 0.10 (14)	0.02 ± 0.15 (48)	-0.00 ± 0.11	-0.07 ± 0.12	-0.06 ± 0.11	0.02 ± 0.11	0.03 ± 0.16
	W0084	HERMES	-0.02 ± 0.07 (26)	-0.02 ± 0.09 (23)	-0.02 ± 0.11 (17)	0.08 ± 0.07 (14)	0.09 ± 0.12 (46)	-0.08 ± 0.09	-0.08 ± 0.10	-0.09 ± 0.12	0.02 ± 0.08	0.03 ± 0.13
	W0110	HERMES	0.08 ± 0.10 (26)	0.03 ± 0.10 (23)	0.03 ± 0.07 (17)	0.07 ± 0.07 (14)	0.11 ± 0.11 (46)	-0.01 ± 0.11	-0.06 ± 0.11	-0.06 ± 0.08	-0.02 ± 0.09	0.02 ± 0.12
	W0125	HERMES	-0.02 ± 0.08 (27)	-0.04 ± 0.10 (23)	-0.07 ± 0.07 (17)	0.01 ± 0.08 (14)	0.01 ± 0.11 (46)	-0.03 ± 0.09	-0.05 ± 0.11	-0.08 ± 0.09	0.00 ± 0.09	-0.00 ± 0.12
	W0139	HERMES	0.02 ± 0.15 (25)	-0.14 ± 0.18 (23)	-0.03 ± 0.13 (17)	0.01 ± 0.14 (14)	-0.01 ± 0.11 (45)	0.01 ± 0.16	-0.15 ± 0.18	-0.04 ± 0.14	-0.01 ± 0.14	-0.02 ± 0.12
NGC7789	W05862	HERMES	-0.06 ± 0.11 (27)	-0.17 ± 0.13 (22)	-0.06 ± 0.12 (17)	0.01 ± 0.09 (14)	-0.02 ± 0.16 (45)	-0.05 ± 0.12	-0.16 ± 0.14	-0.05 ± 0.13	0.02 ± 0.11	-0.01 ± 0.16
	W07176	HERMES	0.01 ± 0.12 (27)	-0.04 ± 0.13 (23)	-0.01 ± 0.08 (17)	0.06 ± 0.09 (14)	0.07 ± 0.11 (46)	-0.07 ± 0.13	-0.12 ± 0.14	-0.09 ± 0.10	-0.02 ± 0.10	-0.01 ± 0.12

Table B.4 Continued from previous page

Cluster	Star	Instr	[Ni/H]	[Cr/H]	[Si/H]	[Ca/H]	[Ti/H]	[Ni/Fe]	[Cr/Fe]	[Si/Fe]	[Ca/Fe]	[Ti/Fe]
	W07714	HERMES	-0.00 ± 0.09 (25)	-0.04 ± 0.11 (23)	-0.03 ± 0.07 (17)	0.07 ± 0.07 (14)	0.04 ± 0.13 (45)	-0.06 ± 0.10	-0.09 ± 0.12	-0.08 ± 0.09	0.01 ± 0.09	-0.01 ± 0.14
	W08260	HERMES	-0.03 ± 0.13 (27)	-0.05 ± 0.11 (23)	-0.05 ± 0.10 (17)	0.01 ± 0.11 (14)	0.01 ± 0.15 (46)	-0.06 ± 0.13	-0.07 ± 0.12	-0.08 ± 0.11	-0.02 ± 0.12	-0.02 ± 0.15
	W08556	FIES	-0.03 ± 0.14 (25)	-0.06 ± 0.07 (23)	-0.03 ± 0.08 (15)	-0.00 ± 0.12 (13)	0.02 ± 0.12 (38)	-0.05 ± 0.15	-0.08 ± 0.08	-0.05 ± 0.09	-0.02 ± 0.13	0.00 ± 0.13
	W08734	FIES	0.11 ± 0.12 (27)	0.04 ± 0.11 (23)	0.07 ± 0.09 (15)	0.16 ± 0.12 (13)	0.14 ± 0.15 (38)	-0.04 ± 0.13	-0.11 ± 0.12	-0.08 ± 0.10	0.01 ± 0.13	-0.01 ± 0.16
	W10915	HERMES	0.02 ± 0.14 (26)	-0.04 ± 0.12 (23)	-0.04 ± 0.10 (17)	0.06 ± 0.08 (14)	0.04 ± 0.12 (43)	-0.06 ± 0.15	-0.11 ± 0.13	-0.12 ± 0.11	-0.01 ± 0.10	-0.03 ± 0.13
		FIES	0.04 ± 0.14 (27)	-0.02 ± 0.20 (22)	0.04 ± 0.13 (14)	0.04 ± 0.12 (14)	0.07 ± 0.20 (36)	-0.04 ± 0.15	-0.10 ± 0.21	-0.03 ± 0.13	-0.03 ± 0.13	-0.01 ± 0.21

Abadi, M. G. et al. (2003). «Simulations of Galaxy Formation in a Λ Cold Dark Matter Universe. II. The Fine Structure of Simulated Galactic Disks.» In: *ApJ* 597, pp. 21–34.

Aceituno, J. et al. (2013). «CAFE: Calar Alto Fiber-fed Échelle spectrograph.» In: *A&A* 552, A31, A31.

Adibekyan, V. Z. et al. (2012). «Chemical abundances of 1111 FGK stars from the HARPS GTO planet search program. Galactic stellar populations and planets.» In: *A&A* 545, A32, A32.

Ahumada, A. V. et al. (2013). «NGC 2849 and NGC 6134: two more BOCCE open clusters.» In: *MNRAS* 430, pp. 221–233.

Alam, S. et al. (2015). «The Eleventh and Twelfth Data Releases of the Sloan Digital Sky Survey: Final Data from SDSS-III.» In: *ApJS* 219, 12, p. 12.

Alcaino, G. (1965). «A photoelectric investigation of the galactic clusters IC 4665 and IC 4756.» In: *Lowell Observatory Bulletin* 6, pp. 167–172.

Allen, C. and A. Santillan (1991). «An improved model of the galactic mass distribution for orbit computations.» In: *Rev. Mexicana Astron. Astrofis.* 22, pp. 255–263.

Allende Prieto, C., D. L. Lambert, and M. Asplund (2001). «The Forbidden Abundance of Oxygen in the Sun.» In: *ApJ* 556, pp. L63–L66.

Alonso, A., S. Arribas, and C. Martínez-Roger (1999). «The effective temperature scale of giant stars (Fo-K5). II. Empirical calibration of T_{eff} versus colours and [Fe/H].» In: *A&A* 140, pp. 261–277.

Anders, F. et al. (2016). «Red giants observed by CoRoT and APOGEE: The evolution of the Milky Way's radial metallicity gradient.» In: *ArXiv e-prints*.

Andreuzzi, G. et al. (2004). «UBVI photometry of the intermediate-age open cluster NGC 6939.» In: *MNRAS* 348, pp. 297–306.

Andrievsky, S. M. et al. (2013). «Barium abundances in Cepheids.» In: *MNRAS* 428, pp. 3252–3261.

Anstee, S. D. and B. J. O'Mara (1991). «An investigation of Brueckner's theory of line broadening with application to the sodium D lines.» In: *MNRAS* 253, pp. 549–560.

Anthony-Twarog, B. J., B. A. Twarog, and L. Mayer (2007). «vbyCaHβ CCD Photometry of Clusters. VIII. The Super-Metal-Rich, Old Open Cluster NGC 6791.» In: *AJ* 133, pp. 1585–1598.

Anthony-Twarog, B. J. et al. (1990). «A CCD photometric analysis of the old open cluster NGC 2420.» In: *AJ* 99, pp. 1504–1535.

Antoja, T. et al. (2011). «Understanding the spiral structure of the Milky Way using the local kinematic groups.» In: *MNRAS* 418, pp. 1423–1440.

Antoja, T. et al. (2014). «Constraints on the Galactic bar from the Hercules stream as traced with RAVE across the Galaxy.» In: *A&A* 563, A60, A60.

Arcimis, A. T. (1901). *Astronomía popular. Descripción general del cielo*.

Arnould, M. and S. Goriely (2003). «The p-process of stellar nucleosynthesis: astrophysics and nuclear physics status.» In: *Phys. Rep.* 384, pp. 1–84.

Asplund, M. et al. (2009). «The Chemical Composition of the Sun.» In: *ARA&A* 47, pp. 481–522.

Balaguer-Núñez, L. et al. (2004). «New membership determination and proper motions of NGC 1817. Parametric and non-parametric approach.» In: *A&A* 426, pp. 819–826.

Balser, D. S. et al. (2011). «H II Region Metallicity Distribution in the Milky Way Disk.» In: *ApJ* 738, 27, p. 27.

Barklem, P. S. and B. J. O'Mara (1998). «The broadening of strong lines of Caˆ+, Mgˆ+ and Baˆ+ by collisions with neutral hydrogen atoms.» In: *MNRAS* 300, pp. 863–871.

Beaver, J. et al. (2013). «Strömgren-Hβ Photometry of the Rich Open Cluster NGC 6705 (M 11).» In: *PASP* 125, pp. 1412–1420.

Bedin, L. R. et al. (2006). «The absolute motion of the peculiar cluster NGC 6791.» In: *A&A* 460, pp. L27–L30.

Bensby, T., S. Feltzing, and I. Lundström (2004). «A possible age-metallicity relation in the Galactic thick disk?» In: *A&A* 421, pp. 969–976.

Bensby, T., S. Feltzing, and M. S. Oey (2014). «Exploring the Milky Way stellar disk. A detailed elemental abundance study of 714 F and G dwarf stars in the solar neighbourhood.» In: *A&A* 562, A71, A71.

Bergemann, M. et al. (2014). «The Gaia-ESO Survey: radial metallicity gradients and age-metallicity relation of stars in the Milky Way disk.» In: *A&A* 565, A89, A89.

Blackwell-Whitehead, R. J. et al. (2005). «Hyperfine Structure Measurements of Neutral Manganese with Fourier Transform Spectroscopy.» In: *ApJS* 157, pp. 402–409.

Blanco-Cuaresma, S. et al. (2014a). «Determining stellar atmospheric parameters and chemical abundances of FGK stars with iSpec.» In: *A&A* 569, A111, A111.

Blanco-Cuaresma, S. et al. (2014b). «The Gaia FGK benchmark stars. High resolution spectral library.» In: *A&A* 566, A98, A98.

Blanco-Cuaresma, S. et al. (2016). «How Much Can We Trust High-Resolution Spectroscopic Stellar Atmospheric Parameters?» In: *19th Cambridge Workshop on Cool Stars, Stellar Systems, and the Sun (CS19)*, p. 22.

— (2017). «How much can we trust high-resolution spectroscopic stellar chemical abundances?» In: *Highlights on Spanish Astrophysics IX*. Ed. by S. Arribas et al., pp. 334–337.

Böcek Topcu, G. et al. (2015). «The chemical compositions and evolutionary status of red giants in the open cluster NGC 752.» In: *MNRAS* 446, pp. 3562–3578.

Bonatto, C. and E. Bica (2003). «Mass segregation in M 67 with 2MASS.» In: *A&A* 405, pp. 525–530.

Bragaglia, A. and M. Tosi (2006). «The Bologna Open Cluster Chemical Evolution Project: Midterm Results from the Photometric Sample.» In: *AJ* 131, pp. 1544–1558.

Bragaglia, A. et al. (2001). «Metal Abundances of Red Clump Stars in Open Clusters. I. NGC 6819.» In: *ApJ* 121, pp. 327–336.

Bragaglia, A. et al. (2014). «Searching for Chemical Signatures of Multiple Stellar Populations in the Old, Massive Open Cluster NGC 6791.» In: *ApJ* 796, 68, p. 68.

Bressan, A. et al. (2012). «PARSEC: stellar tracks and isochrones with the PAdova and TRieste Stellar Evolution Code.» In: *MNRAS* 427, pp. 127–145.

Brogaard, K. et al. (2012). «Age and helium content of the open cluster NGC 6791 from multiple eclipsing binary members. II. Age dependencies and new insights.» In: *A&A* 543, A106, A106.

Cantat-Gaudin, T. et al. (2014a). «DOOp, an automated wrapper for DAOSPEC.» In: *A&A* 562, A10, A10.

Cantat-Gaudin, T. et al. (2014b). «The Gaia-ESO Survey: Stellar content and elemental abundances in the massive cluster NGC 6705.» In: *A&A* 569, A17, A17.

Cantat-Gaudin, T. et al. (2016). «Abundances and kinematics for ten anticentre open clusters.» In: *A&A* 588, A120, A120.

Cardelli, J. A., G. C. Clayton, and J. S. Mathis (1989). «The relationship between infrared, optical, and ultraviolet extinction.» In: *ApJ* 345, pp. 245–256.

Carlberg, J. K. (2014). «Rotational and Radial Velocities of 1.3-2.2 M $_{\odot}$ Red Giants in Open Clusters.» In: *AJ* 147, 138, p. 138.

Carraro, G., E. A. Semenko, and S. Villanova (2016). «Radial Velocities and Metallicities of Red Giant Stars in the Old Open Cluster NGC 7762.» In: *AJ* 152, 224, p. 224.

Carraro, G. et al. (2006a). «NGC 6791: An Exotic Open Cluster or the Nucleus of a Tidally Disrupted Galaxy?» In: *ApJ* 643, pp. 1151–1159.

— (2006b). «NGC 6791: An Exotic Open Cluster or the Nucleus of a Tidally Disrupted Galaxy?» In: *ApJ* 643, pp. 1151–1159.

Carrera, R. (2012a). «Analysis of the CN and CH Molecular Band Strengths in Stars of the Open Cluster NGC 6791.» In: *ApJ* 758, 110, p. 110.

— (2012b). «Radial velocities and metallicities from infrared Ca II triplet spectroscopy of open clusters . Berkeley 26, Berkeley 70, NGC 1798, and NGC 2266.» In: *A&A* 544, A109, A109.

Carrera, R. and E. Pancino (2011). «Chemical abundance analysis of the open clusters Berkeley 32, NGC 752, Hyades, and Praesepe.» In: *A&A* 535, A30, A30.

Carrera, R. et al. (2015). «Radial velocities and metallicities from infrared Ca ii triplet spectroscopy of open clusters. II. Berkeley 23, King 1, NGC 559, NGC 6603, and NGC 7245.» In: *A&A* 578, A27, A27.

Carrera, R. et al. (2017). «The open cluster King 1 in the second quadrant.» In: *A&A (submitted)*.

Casamiquela, L. et al. (2016). «The OCCASO survey: presentation and radial velocities of 12 Milky Way open clusters.» In: *MNRAS* 458, pp. 3150–3167.

— (2017). «OCCASO II. Physical parameters and Fe abundances for 18 Open Clusters.» In: *MNRAS (submitted)*.

Cescutti, G. et al. (2007). «Abundance gradients in the Milky Way for α elements, iron peak elements, barium, lanthanum, and europium.» In: *A&A* 462, pp. 943–951.

Cheng, J. Y. et al. (2012). «Metallicity Gradients in the Milky Way Disk as Observed by the SEGUE Survey.» In: *ApJ* 746, 149, p. 149.

Chiappini, C. (2009). «The chemical evolution of the Galactic thick and thin disks.» In: *The Galaxy Disk in Cosmological Context*. Ed. by J. Andersen et al. Vol. 254. IAU Symposium, pp. 191–196.

Chiappini, C., F. Matteucci, and D. Romano (2001). «Abundance Gradients and the Formation of the Milky Way.» In: *ApJ* 554, pp. 1044–1058.

Chiappini, C. et al. (2015). «Young [α/Fe]-enhanced stars discovered by CoRoT and APOGEE: What is their origin?» In: *A&A* 576, L12, p. L12.

Choo, K. J. et al. (2003). «Search for variable stars in the open cluster NGC 2539.» In: *A&A* 399, pp. 99–104.

Colavitti, E., F. Matteucci, and G. Murante (2008). «The chemical evolution of a Milky Way-like galaxy: the importance of a cosmologically motivated infall law.» In: *A&A* 483, pp. 401–413.

Collins, G. W. I. (2003). W H Freeman & Co, (2003).

Conrad, C. et al. (2014). «A RAVE investigation on Galactic open clusters. I. Radial velocities and metallicities.» In: *A&A* 562, A54, A54.

Cunha, K. et al. (2015). «Sodium and Oxygen Abundances in the Open Cluster NGC 6791 from APOGEE H-band Spectroscopy.» In: *ApJ* 798, L41, p. L41.

Daflon, S. et al. (2009). «Sulfur Abundances in the Orion Association B Stars.» In: *AJ* 138, pp. 1577–1583.

Dalton, G. et al. (2012). «WEAVE: the next generation wide-field spectroscopy facility for the William Herschel Telescope.» In: *Society of Photo-Optical Instrumentation Engineers (SPIE) Conference Series*. Vol. 8446. Society of Photo-Optical Instrumentation Engineers (SPIE) Conference Series, p. 0.

Davenport, J. R. A. and E. L. Sandquist (2010). «Death of a Cluster: The Destruction of M67 as Seen by the Sloan Digital Sky Survey.» In: *ApJ* 711, pp. 559–572.

De Silva, G. M. et al. (2015). «The GALAH survey: scientific motivation.» In: *MNRAS* 449, pp. 2604–2617.

Di Matteo, P. et al. (2011). «The formation of a thick disk through the heating of a thin disk: Agreement with orbital eccentricities of stars in the solar neighborhood.» In: *A&A* 525, L3, p. L3.

Dias, W. S. et al. (2002). «New catalogue of optically visible open clusters and candidates.» In: *A&A* 389, pp. 871–873.

Dias, W. S. et al. (2014). «Proper motions of the optically visible open clusters based on the UCAC4 catalog.» In: *A&A* 564, A79, A79.

Drimmel, R. and D. N. Spergel (2001). «Three-dimensional Structure of the Milky Way Disk: The Distribution of Stars and Dust beyond 0.35 R_{solar}.» In: *ApJ* 556, pp. 181–202.

Edvardsson, B. et al. (1993). «The Chemical Evolution of the Galactic Disk - Part One - Analysis and Results.» In: *A&A* 275, p. 101.

Feltzing, S., M. Fohlman, and T. Bensby (2007). «Manganese trends in a sample of thin and thick disk stars. The origin of Mn.» In: *A&A* 467, pp. 665–677.

Feltzing, S., J. Holmberg, and J. R. Hurley (2001). «The solar neighbourhood age-metallicity relation - Does it exist?» In: *A&A* 377, pp. 911–924.

Forbes, J., M. Krumholz, and A. Burkert (2012). «Evolving Gravitationally Unstable Disks over Cosmic Time: Implications for Thick Disk Formation.» In: *ApJ* 754, 48, p. 48.

Friel, E. D. (1995). «The Old Open Clusters Of The Milky Way.» In: *ARA&A* 33, pp. 381–414.

Friel, E. D., H. R. Jacobson, and C. A. Pilachowski (2010). «Abundances of Red Giants in Old Open Clusters. V. Be 31, Be 32, Be 39, M 67, NGC 188, and NGC 1193.» In: *AJ* 139, pp. 1942–1967.

Friel, E. D. et al. (2002). «Metallicities of Old Open Clusters.» In: *AJ* 124, pp. 2693–2720.

Frinchaboy, P. M. et al. (2006). «Photometry and Spectroscopy of Old, Outer Disk Star Clusters: vdB-Hagen 176, Berkeley 29, and Saurer 1.» In: *AJ* 131, pp. 922–938.

Frinchaboy, P. M. et al. (2013). «The Open Cluster Chemical Analysis and Mapping Survey: Local Galactic Metallicity Gradient with APOGEE Using SDSS DR10.» In: *ApJ* 777, L1, p. L1.

Fuhrmann, K. (2011). «Nearby stars of the Galactic disc and halo - V.» In: *MNRAS* 414, pp. 2893–2922.

Gaia Collaboration et al. (2016). «The Gaia mission.» In: *A&A* 595, A1, A1.

Gallart, C., M. Zoccali, and A. Aparicio (2005). «The Adequacy of Stellar Evolution Models for the Interpretation of the Color-Magnitude Diagrams of Resolved Stellar Populations.» In: *ARA&A* 43, pp. 387–434.

Geisler, D. et al. (2012). «The Unique Na:O Abundance Distribution in NGC 6791: The First Open(?) Cluster with Multiple Populations.» In: *ApJ* 756, L40, p. L40.

Geller, A. M., D. W. Latham, and R. D. Mathieu (2015). «Stellar Radial Velocities in the Old Open Cluster M67 (NGC 2682). I. Memberships, Binaries, and Kinematics.» In: *AJ* 150, 97, p. 97.

Geller, A. M. et al. (2008). «WIYN Open Cluster Study. XXXII. Stellar Radial Velocities in the Old Open Cluster NGC 188.» In: *AJ* 135, pp. 2264–2278.

Genovali, K. et al. (2013). «On the metallicity distribution of classical Cepheids in the Galactic inner disk.» In: *A&A* 554, A132, A132.

Genovali, K. et al. (2014). «On the fine structure of the Cepheid metallicity gradient in the Galactic thin disk.» In: *A&A* 566, A37, A37.

Genovali, K. et al. (2015). «On the α-element gradients of the Galactic thin disk using Cepheids.» In: *A&A* 580, A17, A17.

Gilmore, G. et al. (2012). «The Gaia-ESO Public Spectroscopic Survey.» In: *The Messenger* 147, pp. 25–31.

Gim, M. et al. (1998). «The Open Cluster NGC 7789. I. Radial Velocities for Giant Stars.» In: *PASP* 110, pp. 1172–1182.

Glushkova, E. V. and A. S. Rastorguev (1991). «Radial Velocities of Stars in Open Clusters.» In: *Soviet Astronomy Letters* 17, p. 13.

Glushkova, E. V. et al. (1998). «Investigation of the kinematics of young disk populations.» In: *A&A* 329, pp. 514–521.

Gonzalez, G. and G. Wallerstein (2000). «Elemental Abundances in the Inner Galaxy Open Cluster M11.» In: *PASP* 112, pp. 1081–1088.

Gratton, R. et al. (2006). «The Metallicity of the Old Open Cluster NGC 6791.» In: *ApJ* 642, pp. 462–469.

Gray, R. O. and C. J. Corbally (1994). «The calibration of MK spectral classes using spectral synthesis. 1: The effective temperature calibration of dwarf stars.» In: *AJ* 107, pp. 742–746.

Grevesse, N., M. Asplund, and A. J. Sauval (2007). «The Solar Chemical Composition.» In: *Space Sci. Rev.* 130, pp. 105–114.

Gustafsson, B. et al. (2008). «A grid of MARCS model atmospheres for late-type stars. I. Methods and general properties.» In: *A&A* 486, pp. 951–970.

Harmer, S. et al. (2001). «X-rays from the open cluster NGC 6633.» In: *MNRAS* 324, pp. 473–483.

Harris, G. L. H. and W. E. Harris (1977). «The Hyades-age cluster NGC 1817.» In: *AJ* 82, pp. 612–619.

Hawkins, K. et al. (2016a). «An accurate and self-consistent chemical abundance catalogue for the APOGEE/Kepler sample.» In: *A&A* 594, A43, A43.

Hawkins, K. et al. (2016b). «Gaia FGK benchmark stars: new candidates at low metallicities.» In: *A&A* 592, A70, A70.

Hayden, M. R. et al. (2014). «Chemical Cartography with APOGEE: Large-scale Mean Metallicity Maps of the Milky Way Disk.» In: *AJ* 147, 116, p. 116.

Hayden, M. R. et al. (2015). «Chemical Cartography with APOGEE: Metallicity Distribution Functions and the Chemical Structure of the Milky Way Disk.» In: *ApJ* 808, 132, p. 132.

Haywood, M. et al. (2013). «The age structure of stellar populations in the solar vicinity. Clues of a two-phase formation history of the Milky Way disk.» In: *A&A* 560, A109, A109.

Heger, M. L. (1922). «Further study of the sodium lines in class B stars.» In: *Lick Observatory Bulletin* 10, pp. 141–145.

Heiter, U. et al. (2014). «On the metallicity of open clusters. II. Spectroscopy.» In: *A&A* 561, A93, A93.

Heiter, U. et al. (2015a). «Atomic and molecular data for optical stellar spectroscopy.» In: *Phys. Scr* 90.5, 054010, p. 054010.

Heiter, U. et al. (2015b). «Gaia FGK Benchmark Stars: Effective temperatures and surface gravities.» In: *ArXiv e-prints*.

Henry, R. B. C. et al. (2010). «Abundances of Galactic Anticenter Planetary Nebulae and the Oxygen Abundance Gradient in the Galactic Disk.» In: *ApJ* 724, pp. 748–761.

Herbig, G. H. (1995). «The Diffuse Interstellar Bands.» In: *ARA&A* 33, pp. 19–74.

Herzog, A. D., W. L. Sanders, and W. Seggewiss (1975). «Membership and photometry of the open cluster IC 4756.» In: *A&AS* 19, pp. 211–234.

Hillebrandt, W. and J. C. Niemeyer (2000). «Type IA Supernova Explosion Models.» In: *ARA&A* 38, pp. 191–230.

Hinkel, N. R. et al. (2016). «A Comparison of Stellar Elemental Abundance Techniques and Measurements.» In: *ApJS* 226, 4, p. 4.

Hole, K. T. et al. (2009). «WIYN Open Cluster Study. XXIV. Stellar Radial-Velocity Measurements in NGC 6819.» In: *AJ* 138, pp. 159–168.

Holmberg, J., B. Nordström, and J. Andersen (2009). «The Geneva-Copenhagen survey of the solar neighbourhood. III. Improved distances, ages, and kinematics.» In: *A&A* 501, pp. 941–947.

Holtzman, J. A. et al. (2015). «Abundances, Stellar Parameters, and Spectra from the SDSS-III/APOGEE Survey.» In: *AJ* 150, 148, p. 148.

Hron, J. (1987). «Kinematics of young open clusters and the rotation curve of our Galaxy.» In: *A&A* 176, pp. 34–52.

Huang, Y. et al. (2015). «On the metallicity gradients of the Galactic disk as revealed by LSS-GAC red clump stars.» In: *Research in Astronomy and Astrophysics* 15, 1240, p. 1240.

Jacobson, H. R., E. D. Friel, and C. A. Pilachowski (2007). «Na, Al, and O Abundances of Open Clusters NGC 7142, NGC 6939, and IC 4756.» In: *ApJ* 134, pp. 1216–1230.

Jacobson, H. R., C. A. Pilachowski, and E. D. Friel (2011). «A Chemical Abundance Study of 10 Open Clusters Based on WIYN-Hydra Spectroscopy.» In: *ApJ* 142, 59, p. 59.

Jacobson, H. R. et al. (2016). «The Gaia-ESO Survey: Probes of the inner disk abundance gradient.» In: *A&A* 591, A37, A37.

Janes, K. A. (1979). «Evidence for an abundance gradient in the galactic disk.» In: *ApJS* 39, pp. 135–156.

Jeffries, R. D. et al. (2002). «Membership, metallicity and lithium abundances for solar-type stars in NGC 6633.» In: *MNRAS* 336, pp. 1109–1128.

Jenniskens, P. and F.-X. Desert (1994). «A survey of diffuse interstellar bands (3800-8680 A).» In: *A&AS* 106.

Jofré, P. et al. (2014). «Gaia FGK benchmark stars: Metallicity.» In: *A&A* 564, A133, A133.

Jofré, P. et al. (2015). «Gaia FGK benchmark stars: abundances of α and iron-peak elements.» In: *A&A* 582, A81, A81.

Jofré, P. et al. (2016). «Cannibals in the thick disk: the young α-rich stars as evolved blue stragglers.» In: *A&A* 595, A60, A60.

Jofre, P. et al. (2016). «Gaia FGK Benchmark stars: Opening the black box of stellar element abundance determination.» In: *ArXiv e-prints*.

Johnson, H. L. (1953). «Magnitudes and Colors in NGC 752.» In: *ApJ* 117, p. 356.

Katz, D. et al. (2004). «Spectroscopic survey of the Galaxy with Gaia- I. Design and performance of the Radial Velocity Spectrometer.» In: *MNRAS* 354, pp. 1223–1238.

Kharchenko, N. V. et al. (2005). «Astrophysical parameters of Galactic open clusters.» In: *A&A* 438, pp. 1163–1173.

Kharchenko, N. V. et al. (2013). «Global survey of star clusters in the Milky Way. II. The catalogue of basic parameters.» In: *A&A* 558, A53, A53.

Kiss, L. L. et al. (2001). «A variable star survey of the open cluster M 37.» In: *A&A* 376, pp. 561–567.

Korotin, S. A. et al. (2014). «Oxygen abundance distribution in the Galactic disc.» In: *MNRAS* 444, pp. 3301–3307.

Kos, J. et al. (2014). «Pseudo-three-dimensional maps of the diffuse interstellar band at 862 nm.» In: *Science* 345, pp. 791–795.

Kubryk, M., N. Prantzos, and E. Athanassoula (2015). «Evolution of the Milky Way with radial motions of stars and gas. I. The solar neighbourhood and the thin and thick disks.» In: *A&A* 580, A126, A126.

Kurucz, R. L. (2005). «ATLAS12, SYNTHE, ATLAS9, WIDTH9, et cetera.» In: *Memorie della Societa Astronomica Italiana Supplementi* 8, p. 14.

Kurucz, R. (1993). «SYNTHE Spectrum Synthesis Programs and Line Data.» In: *SYNTHE Spectrum Synthesis Programs and Line Data. Kurucz CD-ROM No. 18. Cambridge, Mass.: Smithsonian Astrophysical Observatory, 1993.* 18.

Lada, C. J. (2010). «The physics and modes of star cluster formation: observations.» In: *Philosophical Transactions of the Royal Society of London Series A* 368, pp. 713–731.

Lanzafame, A. C. and F. Spada (2015). «Rotational evolution of slow-rotators sequence stars.» In: *ArXiv e-prints*.

Lee, Y. S. et al. (2008). «The SEGUE Stellar Parameter Pipeline. II. Validation with Galactic Globular and Open Clusters.» In: *AJ* 136, pp. 2050–2069.

Lemasle, B. et al. (2007). «Detailed chemical composition of Galactic Cepheids. A determination of the Galactic abundance gradient in the 8-12 kpc region.» In: *A&A* 467, pp. 283–294.

Lemasle, B. et al. (2013). «Galactic abundance gradients from Cepheids. α and heavy elements in the outer disk.» In: *A&A* 558, A31, A31.

Lépine, J. R. D. et al. (2011). «Overlapping abundance gradients and azimuthal gradients related to the spiral structure of the Galaxy.» In: *MNRAS* 417, pp. 698–708.

Li, H. et al. (2015). «High-resolution spectroscopic studies of ultra metal-poor stars found in the LAMOST survey.» In: *PASJ* 67, 84, p. 84.

Liu, C. et al. (2017). «Determination of robust metallicities for metal-rich red giant branch stars.» In: *ArXiv e-prints*.

Luck, R. E. and U. Heiter (2005). «Stars within 15 Parsecs: Abundances for a Northern Sample.» In: *AJ* 129, pp. 1063–1083.

Ludwig, H.-G. et al. (2014). «3D modeling of stellar atmospheres and the impact on the understanding of the reliability of elemental abundances in stars as tracers of galactic chemical evolution.» In: *Setting the scene for Gaia and LAMOST*. Ed. by S. Feltzing et al. Vol. 298. IAU Symposium, pp. 343–354.

Maciejewski, G. and A. Niedzielski (2007). «CCD BV survey of 42 open clusters.» In: *A&A* 467, pp. 1065–1074.

Magic, Z. et al. (2013). «The Stagger-grid: A grid of 3D stellar atmosphere models. I. Methods and general properties.» In: *A&A* 557, A26, A26.

Magrini, L. et al. (2009). «The evolution of the Galactic metallicity gradient from high-resolution spectroscopy of open clusters.» In: *A&A* 494, pp. 95–108.

Magrini, L. et al. (2013). «FAMA: An automatic code for stellar parameter and abundance determination.» In: *A&A* 558, A38, A38.

Magrini, L. et al. (2014). «The Gaia-ESO Survey: Abundance ratios in the inner-disk open clusters Trumpler 20, NGC 4815, NGC 6705.» In: *A&A* 563, A44.

Magrini, L. et al. (2015). «The Gaia-ESO Survey: Insights into the inner-disc evolution from open clusters.» In: *A&A* 580, A85, A85.

Martig, M. et al. (2015). «Young α-enriched giant stars in the solar neighbourhood.» In: *MNRAS* 451, pp. 2230–2243.

Mathieu, R. D. et al. (1986). «Precise radial velocities of late-type stars in the open clusters M11 and M67.» In: *AJ* 92, pp. 1100–1117.

Matteucci, F., ed. (2001). *The chemical evolution of the Galaxy*. Vol. 253. Astrophysics and Space Science Library.

McNamara, B. J., N. M. Pratt, and W. L. Sanders (1977). «Membership in the open cluster M11.» In: *A&AS* 27, pp. 117–143.

McNamara, B. J. and S. Solomon (1981). «A proper motion membership analysis of the open cluster NGC 7789.» In: *A&A,Suplement* 43, pp. 337–351.

McWilliam, A. (1990). «High-resolution spectroscopic survey of 671 GK giants. I - Stellar atmosphere parameters and abundances.» In: *ApJS* 74, pp. 1075–1128.

Mermilliod, J. C., M. Mayor, and S. Udry (2008). «Red giants in open clusters. XIV. Mean radial velocities for 1309 stars and 166 open clusters.» In: *A&A* 485, pp. 303–314.

Mészáros, S. et al. (2013). «Calibrations of Atmospheric Parameters Obtained from the First Year of SDSS-III APOGEE Observations.» In: *AJ* 146, 133, p. 133.

Miglio, A. et al. (2013). «Galactic archaeology: mapping and dating stellar populations with asteroseismology of red-giant stars.» In: *MNRAS* 429, pp. 423–428.

Mikolaitis, Š. et al. (2014). «The Gaia-ESO Survey: the chemical structure of the Galactic discs from the first internal data release.» In: *A&A* 572, A33, A33.

Milliman, K. E. et al. (2014). «WIYN Open Cluster Study. LX. Spectroscopic Binary Orbits in NGC 6819.» In: *AJ* 148, 38, p. 38.

Milone, A. A. E. (1994). «The mean radial velocity of the open cluster NGC 6939.» In: *PASP* 106, pp. 1085–1090.

Minchev, I., C. Chiappini, and M. Martig (2013). «Chemodynamical evolution of the Milky Way disk. I. The solar vicinity.» In: *A&A* 558, A9, A9.

— (2014). «Chemodynamical evolution of the Milky Way disk. II. Variations with Galactic radius and height above the disk plane.» In: *A&A* 572, A92, A92.

Minchev, I. and B. Famaey (2010). «A New Mechanism for Radial Migration in Galactic Disks: Spiral-Bar Resonance Overlap.» In: *ApJ* 722, pp. 112–121.

Mochejska, B. J. and J. Kaluzny (1999). «Variable Stars in the Field of the Open Cluster NGC 7789.» In: *Acta Astronomica* 49, pp. 351–370.

Montgomery, K. A., L. A. Marschall, and K. A. Janes (1993). «CCD photometry of the old open cluster M67.» In: *ApJ* 106, pp. 181–219.

Mucciarelli, A. et al. (2013). «GALA: An Automatic Tool for the Abundance Analysis of Stellar Spectra.» In: *ApJ* 766, 78, p. 78.

Negueruela, I. et al. (2014). «CAFÉ-BEANS: An exhaustive hunt for high-mass binaries.» In: *ArXiv e-prints*.

Nidever, D. L. et al. (2014). «Tracing Chemical Evolution over the Extent of the Milky Way's Disk with APOGEE Red Clump Stars.» In: *ApJ* 796, 38, p. 38.

Nidever, D. L. et al. (2015). «The Data Reduction Pipeline for the Apache Point Observatory Galactic Evolution Experiment.» In: *ArXiv e-prints*.

Nilakshi and R. Sagar (2002). «A comprehensive study of the rich open star cluster NGC 2099 based on deep BVI CCD observations.» In: *A&A* 381, pp. 65–76.

Nordström, B. et al. (2004). «The Geneva-Copenhagen survey of the Solar neighbourhood. Ages, metallicities, and kinematic properties of
»14 000 F and G dwarfs.» In: *A&A* 418, pp. 989–1019.

Overbeek, J. C. et al. (2015). «NGC 7789: an Open Cluster Case Study.» In: *AJ* 149, 15, p. 15.

Pace, G. et al. (2010). «Abundances and physical parameters for stars in the open clusters NGC 5822 and IC 4756.» In: *A&A* 515, A28, A28.

Pancino, E. et al. (2010). «Chemical abundance analysis of the open clusters Cr 110, NGC 2099 (M 37), NGC 2420, NGC 7789, and M 67 (NGC 2682).» In: *A&A* 511, A56, A56.

Pandey, A. K. et al. (2007). «Stellar Contents of Two Intermediate Age Clusters: NGC 1912 and NGC 1907.» In: *PASJ* 59, pp. 547–558.

Pasquini, L. et al. (2008). «Solar twins in M 67.» In: *A&A* 489, pp. 677–684.

Pasquini, L. et al. (2011). «Gravitational redshifts in main-sequence and giant stars.» In: *A&A* 526, A127, A127.

Pasquini, L. et al. (2012). «Search for giant planets in M 67. I. Overview.» In: *A&A* 545, A139, A139.

Pichardo, B., M. Martos, and E. Moreno (2004). «Models for the Gravitational Field of the Galactic Bar: An Application to Stellar Orbits in the Galactic Plane and Orbits of Some Globular Clusters.» In: *ApJ* 609, pp. 144–165.

Pichardo, B. et al. (2003). «Nonlinear Effects in Models of the Galaxy. I. Midplane Stellar Orbits in the Presence of Three-dimensional Spiral Arms.» In: *ApJ* 582, pp. 230–245.

Pichardo, B. et al. (2012). «The Sun was Not Born in M67.» In: *AJ* 143, 73, p. 73.

Pietrinferni, A. et al. (2004). «A Large Stellar Evolution Database for Population Synthesis Studies. I. Scaled Solar Models and Isochrones.» In: *ApJ* 612, pp. 168–190.

Platais, I. (1991). «The studies of proper motions in the regions of open clusters. II - NGC 752.» In: *A&AS* 87, pp. 69–87.

Platais, I. et al. (2003). «WIYN Open Cluster Study. XVII. Astrometry and Membership to V=21 in NGC 188.» In: *AJ* 126, pp. 2922–2935.

Plez, B. (2012). *Turbospectrum: Code for spectral synthesis*. Astrophysics Source Code Library.

Pradhan, A. K. and S. N. Nahar (2011). *Atomic Astrophysics and Spectroscopy*. American Astronomical Society Meeting Abstracts.

Prša, A. et al. (2016). «Nominal Values for Selected Solar and Planetary Quantities: IAU 2015 Resolution B3.» In: *AJ* 152, 41, p. 41.

Ramírez, I. and C. Allende Prieto (2011). «Fundamental Parameters and Chemical Composition of Arcturus.» In: *ApJ* 743, 135, p. 135.

Randich, S., G. Gilmore, and Gaia-ESO Consortium (2013). «The Gaia-ESO Large Public Spectroscopic Survey.» In: *The Messenger* 154, pp. 47–49.

Raskin, G. et al. (2011). «HERMES: a high-resolution fibre-fed spectrograph for the Mercator telescope.» In: *A&A* 526, A69, A69.

Reddy, A. B. S., S. Giridhar, and D. L. Lambert (2012). «Comprehensive abundance analysis of red giants in the open clusters NGC 752, 1817, 2360 and 2506.» In: *MNRAS* 419, pp. 1350–1361.

— (2013). «Comprehensive abundance analysis of red giants in the open clusters NGC 2527, 2682, 2482, 2539, 2335, 2251 and 2266.» In: *MNRAS* 431, pp. 3338–3348.

Reid, I. N. et al. (2007). «Searching for Earth Analogs Around the Nearest Stars: The Disk Age-Metallicity Relation and the Age Distribution in the Solar Neighborhood.» In: *ApJ* 665, pp. 767–784.

Reid, M. J. et al. (2009). «Trigonometric Parallaxes of Massive Star-Forming Regions. VI. Galactic Structure, Fundamental Parameters, and Noncircular Motions.» In: *ApJ* 700, 137-148, pp. 137–148.

Reid, M. J. et al. (2014). «Trigonometric Parallaxes of High Mass Star Forming Regions: The Structure and Kinematics of the Milky Way.» In: *ApJ* 783, 130, p. 130.

Rocha-Pinto, H. J. et al. (2000). «Chemical enrichment and star formation in the Milky Way disk. I. Sample description and chromospheric age-metallicity relation.» In: *A&A* 358, pp. 850–868.

Rosvick, J. M. and D. A. Vandenberg (1998). «BV Photometry for the ˜2.5 Gyr Open Cluster NGC 6819: More Evidence for Convective Core Overshooting on the Main Sequence.» In: *AJ* 115, pp. 1516–1523.

Roškar, R. et al. (2008). «Riding the Spiral Waves: Implications of Stellar Migration for the Properties of Galactic Disks.» In: *ApJ* 684, L79, p. L79.

Rutten, R. J. (2003). *Radiative Transfer in Stellar Atmospheres*. Lecture Notes Utrecht University, (2003).

Sagar, R. and W. K. Griffiths (1998). «BVI CCD photometry of the distant open star clusters Berkeley 81, Berkeley 99, NGC 6603 and NGC 7044.» In: *MNRAS* 299, pp. 1–23.

Sakari, C. M. et al. (2011). «Detailed Chemical Abundances of Four Stars in the Unusual Globular Cluster Palomar 1.» In: *ApJ* 740, 106, p. 106.

Salaris, M., A. Weiss, and S. M. Percival (2004). «The age of the oldest Open Clusters.» In: *A&A* 414, pp. 163–174.

Sandage, A., L. M. Lubin, and D. A. VandenBerg (2003). «The Age of the Oldest Stars in the Local Galactic Disk from Hipparcos Parallaxes of G and K Subgiants.» In: *PASP* 115, pp. 1187–1206.

Sanders, W. L. (1972). «Membership of the open cluster NGC 6819.» In: *A&A* 19, pp. 155–158.

— (1973). «Membership of the open cluster NGC 6633.» In: *A&AS* 9, p. 213.

— (1977). «Membership of the open cluster M67.» In: *A&AS* 27, pp. 89–116.

Santos Jr., J. F. C., C. Bonatto, and E. Bica (2005). «Structure and stellar content analysis of the open cluster M 11 with 2MASS photometry.» In: *A&A* 442, pp. 201–209.

Santos, N. C. et al. (2009). «Metallicities for 13 nearby open clusters from high-resolution spectroscopy of dwarf and giant stars. Stellar metallicity, stellar mass, and giant planets.» In: *A&A* 493, pp. 309–316.

Sbordone, L. et al. (2004). «ATLAS and SYNTHE under Linux.» In: *Memorie della Societa Astronomica Italiana Supplementi* 5, p. 93.

Scott, J. E., E. D. Friel, and K. A. Janes (1995). «Kinematics of the old open cluster system.» In: *AJ* 109, pp. 1706–1715.

Sestito, P. et al. (2008). «Open clusters as key tracers of Galactic chemical evolution. III. Element abundances in Berkeley 20, Berkeley 29, Collinder 261 and Melotte 66.» In: *A&A* 488, pp. 943–958.

Smiljanic, R. et al. (2014). «The Gaia-ESO Survey: The analysis of high-resolution UVES spectra of FGK-type stars.» In: *A&A* 570, A122, A122.

Smith, V. V. et al. (2013). «Chemical Abundances in Field Red Giants from High-resolution H-band Spectra Using the APOGEE Spectral Linelist.» In: *ApJ* 765, 16, p. 16.

Smolinski, J. P. et al. (2011). «The SEGUE Stellar Parameter Pipeline. IV. Validation with an Extended Sample of Galactic Globular and Open Clusters.» In: *AJ* 141, 89, p. 89.

Sobeck, J. S., J. E. Lawler, and C. Sneden (2007). «Improved Laboratory Transition Probabilities for Neutral Chromium and Redetermination of the Chromium Abundance for the Sun and Three Stars.» In: *ApJ* 667, pp. 1267–1282.

Sofue, Y., M. Honma, and T. Omodaka (2009). «Unified Rotation Curve of the Galaxy – Decomposition into de Vaucouleurs Bulge, Disk, Dark Halo, and the 9-kpc Rotation Dip –.» In: *PASJ* 61, p. 227.

Soubiran, C., M. Odenkirchen, and J.-F. Le Campion (2000). «Fundamental properties of the open cluster NGC 2355.» In: *A&A* 357, pp. 484–494.

Soubiran, C. et al. (2008). «Vertical distribution of Galactic disk stars. IV. AMR and AVR from clump giants.» In: *A&A* 480, pp. 91–101.

Stanghellini, L. and M. Haywood (2010). «The Galactic Structure and Chemical Evolution Traced by the Population of Planetary Nebulae.» In: *ApJ* 714, pp. 1096–1107.

Stetson, P. B. (2000). «Homogeneous Photometry for Star Clusters and Resolved Galaxies. II. Photometric Standard Stars.» In: *PASP* 112, pp. 925–931.

Stetson, P. B., H. Bruntt, and F. Grundahl (2003). «Homogeneous Photometry. III. A Star Catalog for the Open Cluster NGC 6791.» In: *PASP* 115, pp. 413–447.

Stetson, P. B. and E. Pancino (2008). «DAOSPEC: An Automatic Code for Measuring Equivalent Widths in High-Resolution Stellar Spectra.» In: *PASP* 120, pp. 1332–1354.

Subramaniam, A. and B. C. Bhatt (2007). «Photometric study of distant open clusters in the second quadrant: NGC 7245, King 9, King 13 and IC 166.» In: *MNRAS* 377, pp. 829–834.

Subramaniam, A. and R. Sagar (1999). «Multicolor CCD Photometry and Stellar Evolutionary Analysis of NGC 1907, NGC 1912, NGC 2383, NGC 2384, and NGC 6709 Using Synthetic Color-Magnitude Diagrams.» In: *AJ* 117, pp. 937–961.

Sung, H. et al. (1999a). «UBVI CCD photometry of M11 - II. New photometry and surface density profiles.» In: *MNRAS* 310, pp. 982–1001.

— (1999b). «UBVI CCD photometry of M11 - II. New photometry and surface density profiles.» In: *MNRAS* 310, pp. 982–1001.

Tautvaišienė, G. et al. (2015). «The Gaia-ESO Survey: CNO abundances in the open clusters Trumpler 20, NGC 4815, and NGC 6705.» In: *A&A* 573, A55, A55.

Taylor, M. B. (2005). «TOPCAT & STIL: Starlink Table/VOTable Processing Software.» In: *Astronomical Data Analysis Software and Systems XIV*. Ed. by P. Shopbell, M. Britton, and R. Ebert. Vol. 347. Astronomical Society of the Pacific Conference Series, p. 29.

Telting, J. H. et al. (2014). «FIES: The high-resolution Fiber-fed Echelle Spectrograph at the Nordic Optical Telescope.» In: *Astronomische Nachrichten* 335, p. 41.

Thevenin, F. (1998). «VizieR Online Data Catalog: Chemical Abundances in Late-Type Stars (Thevenin, 1998).» In: *VizieR Online Data Catalog* 3193.

Tofflemire, B. M. et al. (2014). «WIYN Open Cluster Study. LIX. Radial Velocity Membership of the Evolved Population of the Old Open Cluster NGC 6791.» In: *AJ* 148, 61, p. 61.

Twarog, B. A. (1980). «The chemical evolution of the solar neighborhood. II - The age-metallicity relation and the history of star formation in the galactic disk.» In: *ApJ* 242, pp. 242–259.

Twarog, B. A., K. M. Ashman, and B. J. Anthony-Twarog (1997). «Some Revised Observational Constraints on the Formation and Evolution of the Galactic Disk.» In: *AJ* 114, p. 2556.

Valitova, A. M. et al. (1990). «Radial Velocities of Stars in the Field of the Open Cluster IC4756.» In: *Soviet Astronomy Letters* 16, p. 301.

VandenBerg, D. A. et al. (2012). «Models for Metal-poor Stars with Enhanced Abundances of C, N, O, Ne, Na, Mg, Si, S, Ca, and Ti, in Turn, at Constant Helium and Iron Abundances.» In: *ApJ* 755, 15, p. 15.

Villalobos, Á. and A. Helmi (2008). «Simulations of minor mergers - I. General properties of thick discs.» In: *MNRAS* 391, pp. 1806–1827.

Vogel, K. W. et al. (2003). «WIYN Open Cluster Study: Precision UBVRI CCD Photometry of the Open Cluster NGC 2539.» In: *American Astronomical Society Meeting Abstracts*. Vol. 35. Bulletin of the American Astronomical Society, p. 1228.

Yadav, R. K. S. et al. (2008). «Ground-based CCD astrometry with wide-field imagers. II. A star catalog for M 67: WFI@2.2 m MPG/ESO astrometry, FLAMES@VLT radial velocities.» In: *A&A* 484, pp. 609–620.

Yong, D., B. W. Carney, and E. D. Friel (2012). «Elemental Abundance Ratios in Stars of the Outer Galactic Disk. IV. A New Sample of Open Clusters.» In: *AJ* 144, 95, p. 95.

Yong, D. et al. (2016). «GRACES observations of young [α/Fe]-rich stars.» In: *MNRAS* 459, pp. 487–495.

Zhao, J. et al. (1985). «Special issue for tables of membership of 42 open clusters.» In: *Shangai Obs. Akademia Sinica*, p. 4.

Zuckerman, B. and M. A. Malkan (1996). *The origin and evolution of the universe*.

van Altena, W. F. and B. F. Jones (1970). «Membership of the intermediate-age open cluster NGC 2420.» In: *A&A* 8, pp. 112–116.

van der Kruit, P. C. and K. C. Freeman (2011). «Galaxy Disks.» In: *ARA&A* 49, pp. 301–371.

von Hippel, T. and A. Sarajedini (1998). «WIYN Open Cluster Study. I. Deep Photometry of NGC 188.» In: *AJ* 116, pp. 1789–1800.